An Observational Study of Shock-Cloud Interaction in the Young VHE γ-ray SNR RX J1713.7−3946; Evidence for Cosmic-Ray Acceleration

Hidetoshi (Nagai) Sano

Department of Physics
Nagoya University

2013

Acknowledgements

First of all, I would like to express my deepest gratitude to Prof. Yasuo Fukui, my supervisor, for guiding and leading me throughout the five years at Nagoya University. I'm grateful for his great encouragement in various aspects during my researches. I have learned a lot of things; especially what is necessary in order to become a good scientist and professor. I'm truly a lucky person that I'm able to study under his supervision.

I would like to express my thankfulness Prof. Kengo Tachihara who gave me enormous help for the research and activities on the laboratory. I'm also grateful to Profs. Hiroaki Yamamoto and Takeshi Okuda who taught me some basic knowledge for operating and contracting of the radio telescope. My grateful thanks are due to Prof. Akiko Kawamura who gave me huge help and long-term support. I also thanks to Dr. Takahiro Hayakawa who supported for maintenance and management in many computers for analyzing and helped me in a scientific outreach. I grateful to Dr. Kazufumi Torii who taught me how to analyze CO data and significant contributed on the data analyzing. I gratitude Dr. Toshihisa Kuwahara who taught me a development of the observational device to be installed in NANTEN2. I'd like to acknowledged Profs. Hideo Ogawa, Akira Mizuno, Toshikazu Onishi, Norikazu Mizuno, and developers of the NANTEN2 telescope.

I'm deeply thankful to Profs. Takaaki Tanaka and Hironori Matsumoto who taught me how to analyze the X-ray data from A to Z and gave me in-depth discussion. I sincere gratitude to Profs. Gavin Rowell and Felix Aharonian who taught me the method for using a γ-ray data and gave me invaluable contribution. I heartfelt gratitude to Profs. Tsuyoshi Inoue, Shu-ichiro Inutsuka, and Ryo Yamazaki who tremendous supported our observational results with the numerical simulations and extensive discussions. I would like to appreciate Profs. Jürgen Stutzki, Frank Bertoldi, Leo Bronfman, Bon-Chul Koo, Arnold Benz, and Michael Burton's contribution when submitted my first refereed paper.

I would like to express my gratitude to all the graduate/under graduate students of our laboratory for a kind help and enjoying the activities on the laboratory; Natyuta Moribe, Ryuji Okamoto, Rei Enokiya, Satoshi Yoshiike, Tatsuya Fukuda, Keisuke Hasegawa, Sho Soga, Shigeki Shimizu, Taichi Nakashima, Masashi Wada, Momo Hattori, Yusuke Hattori, Tsukasa Usui, Keiko Yokoyama, Makio Ito, Yuta Takeuchi, and Sayaka Mochizuki. Thanks are also due to Kaori Tomida, Noriko Suzuki, Noriko Ikagawa, and Reiko Abe for their encouragement in various aspects.

I acknowledge financial support from the Japan Society for the Promotion of Science.

Finally, I thank all my friends and family, especially my wife, for helping and encouraging me in various aspects throughout my research, and my life.

Abstract

The origin of cosmic-rays and their efficient acceleration have been one of the most important issues of the modern astrophysics since their discovery in 1912. Supernova remnants (SNRs) are one of the most energetics sources in our Galaxy and their shock waves are thought to be the site of producing cosmic-rays below *knee* energy. Although cosmic-ray elections are confirmed to be accelerated in many SNRs by detections of synchrotron X-rays, origin of these protons, main component of cosmic-rays, are still not clear. To understand those open questions, we focused on the connection between the high energy radiations (X- and γ-rays) and interstellar gas associated with the SNRs. It is because the X- and γ-rays are produced by the interaction among the cosmic-rays accelerated in shock waves, interstellar gas, and interstellar magnetic fields. In present thesis, therefore, we have shown the shock-cloud interaction of the young γ-ray SNR RX J1713.7−3946 on the basis of the multi-wavelength study.

We observed a distribution of molecular gas with multi-J CO transitions toward the SNR RX J1713.7−3946 using the NANTEN/NANTEN2, ASTE telescopes and revealed the detailed physical conditions of the interstellar gas interacting with the SNR. We newly identified 9 CO clumps and a HI clump and derived these physical parameters (peak position, intensity, velocity, mass etc.). Specially, the most prominent CO peak "clump C" has also shown a strong density gradient consistent with an average density distribution of $r^{-2.2\pm0.4}$ (r is the radius of clump C) and definite bipolar outflow structure. Therefore, we have concluded that the clump C is containing the protostellar core(s) and is survived SNR shock erosion, since the shock propagation speed is stalled in the dense clump.

In a morphological study between the CO/HI clumps and *Suzaku* X-rays, we found that the X-rays are enhanced around the CO/HI clumps in sub-pc scale. Numerical simulations indicate that the magnetic field is amplified around dense CO/HI clumps as a result of enhanced turbulence induced by the shock-cloud interaction (Inoue et al., 2009, 2012). We concluded that these interstellar gas clumps are formed by a strong stellar wind from the progenitor of the SNR at some Myr ago and is now interacting with the SNR shock waves, which enhanced magnetic field and also lead to efficient acceleration in additional to the diffusive shock acceleration (DSA), which is classical model of shock acceleration.

In order to determine the origin of very high energy (VHE; Energies $E > 100$ GeV) γ-rays whether cosmic-ray protons (p-p collision; hadronic process) or electrons (inverse Compton scattering; leptoic process) in RX J1713.7−3946, we have carried out a detailed spacial comparison between the total interstellar gas and the VHE γ-rays. If the hadronic process is working, we expect that the γ-ray distribution mimics that of the interstellar gas. We tried to reveal the distribution of total interstellar protons using NANTEN ^{12}CO(J=1–0) and ATCA & Parkes HI datasets and compared it with VHE γ-ray distribution. As s result, we obtained an extremely well spacial correspondence between the total interstellar gas density and VHE γ-ray emission by similar factors, and concluded that the VHE γ-rays are hadronic origin. We have also estimated the total energy of cosmic-ray protons $W_{\rm tot} = (0.8\text{–}2.3) \times 10^{48}$ erg, 0.1% of the total energy of typical supernova explosion with the averaged interstellar gas density ~ 130 cm^{-3}. This result is strong evidence for the cosmic-ray proton acceleration close to *knee* energy in the SNR for the first time.

In addition to these morphological studies, we have revealed the spacial distributions of synchrotron X-ray parameters (absorbing column density $N_{\rm H}$(X-ray), photon index Γ, and absorption-corrected flux) using the *Suzaku* archival datasets, which is comparable to the structures of interstellar gas. The distribution of $F_{3-10{\rm keV}}$ and $N_{\rm H}$(X-ray) has shown a good correlation with that of interstellar gas and visual extinction, respectively. The Γ map, which also varies from 2.1 to 2.9 within the SNR and has prominent six dips (low Γ values). the They are accelerating the cosmic-ray electrons efficiently and are located not only gas rich region in the west, but also gas poor region in the east. We found that the trend can describe the interstellar gas distribution because the efficient acceleration of cosmic-ray electrons is depend on the shock speed $v_{\rm sh}$ and the turbulent motion (Zirakashvili & Aharonian, 2007). Spatially, the gas rich region became slow $v_{\rm sh}$ and high turbulent generated by the shock interaction (Inoue et al., 2012). On the other hand, the gas poor region has fast $v_{\rm sh}$ and low turbulent motion. Considering these situations, both gas rich and poor regions can also accelerate the cosmic-ray electrons efficiently. Therefore, we concluded that the interstellar gas plays an important role in efficient acceleration of the cosmic-ray electrons.

Finally, we discuss future prospects consisting of five science themes, which are including the potential of detection of thermal X-rays in the non-thermal SNRs such as RX J1713.7−3946.

Contents

List of Figures

List of Tables

Chapter 1

Introduction

1.1 Background

Cosmic-rays are charged and very energetic particles, main elements of which are protons, with ∼10% of Helium, and 1% of electrons and ionized nuclei. To understand the origin and acceleration mechanism of the cosmic-rays has been one of the most important issues of the modern astrophysics since 100 years ago. The reason for the importance is because the cosmic-rays are one of the primary components of high energy particles (see Table 1.1). Cosmic-rays, therefore affect heating and ionization of the interstellar medium (ISM). However, the site of galactic cosmic-rays acceleration ($E < 3{\times}10^{15}$ eV) is still not clear.

Supernova remnants (SNR) are the most likely candidates for the acceleration site below the *knee* energy, because they are almost the only energy sources satisfactory explain the cosmic-ray production rate in the Galaxy (see the Chapter 1.2 and 1.3). The theory of diffusive shock acceleration (DSA, see Chapter 1.3.2 in details) in SNRs can explain efficient particle acceleration and the observed cosmic-ray spectrum. Unfortunately, the site of production/acceleration of cosmic-rays cannot be observed directly due to the interstellar magnetic fields as the gyro radius of cosmic-rays is much less than the distance from us to sources.

Most important breakthrough to understand was the discovery of the non-thermal X-ray radiation from the young SNR SN1006, which was obtained by the *ASCA* X-ray observatory (Koyama et al., 1995). The observation revealed that the synchrotron X-rays are produced by Tera electron volt (10^{12} eV; hereafter TeV) electrons. Afterwards, detections of the synchrotron X-rays from other SNRs followed (e.g., Koyama et al., 1997; Slane et al., 2001; Tian et al., 2010) and it is confirmed that the cosmic-ray

TABLE 1.1: Energy Densities in the Local Interstellar Space

Interstellar Component	Energy Density (eV cm^{-3})	Note
Cosmic Microwave Background (CMB)	0.265	(1)
Far-infrared radiation from dust	0.31	(2)
Starlight ($h\nu$ <13.6 eV)	0.54	(2)
Thermal kinematic energy $(3/2)nkT$	0.49	(3)
Turbulent kinematic energy $(1/2)\rho v^2$	0.22	(4)
Magnetic energy $B^2/8\pi$	0.89	(5)
Cosmic-rays	1.39	(6)

Notes. (1): For $T_{\rm CMB}$ = 2.725 K (Fixsen, 2009), (2): Chapter 12 in Draine (2011), (3): For nT = 3800 cm^{-3} (see also Draine, 2011), (4): For $n_{\rm H}$=30 cm^{-3}, v = 1 km s^{-1}, (5): For median $B_{\rm tot} \sim 6\mu$G (Heiles & Crutcher, 2005), (6): Chapter 13 in Draine (2011).

electrons have been accelerated in the SNRs. Second observational breakthrough was imaging of very high energy (VHE; Energies $E > 100$ GeV) γ-rays from the young SNRs (e.g., Aharonian et al., 2004, 2007) obtained by the atmospheric Cherenkov telescopes (H.E.S.S., CANGAROO, MAGIC etc.). The VHE γ-rays are suggested to be produced by TeV electrons and/or protons through the interactions with photon field (inverse Compton scattering with the cosmic-ray electrons; hereafter the leptonic origin scenario, see Chapter 1.4.2) and/or interstellar protons (π^0-decay with the cosmic-ray protons; hereafter the hadronic origin scenario, see Chapter 1.4.3). Thanks to the synchrotron X-rays and γ-ray observations, we are now able to study the physical properties of cosmic-ray acceleration. However, we still have problems about cosmic-ray acceleration in the SNRs below;

Q.1 How the cosmic-rays are accelerated efficiently in the young (age$\sim$2000 yr) SNRs?

Q.2 Which is the dominant process in the VHE γ-ray SNRs, hadronic or leptonic origin?

Q.3 How is the relationship between cosmic-ray acceleration and surrounding material of SNRs.

Regarding the first question, according to observational results, the power law index of synchrotron X-ray spectra (so called "photon index" Γ) are different from region to region in the SNR (e.g., Cassam-Chenaï et al., 2004; Tanaka et al., 2008; Bamba et al., 2012). In other words, the variation of Γ indicates that an acceleration efficiency of cosmic-ray electrons varies with some conditions. But it is not known exactly what causes the variety.

For the second generation, the broad band spectra from X-rays to γ-rays allow us to make a comparative study between the observational results and theoretical ones. They bring successful results and improved our understanding of cosmic-ray properties. However, in most cases, we have no evidence either of the two models (i.e., both hadronic and leptonic dominant models; see also Figure 1.11) explain the observed facts. Furthermore, If the SNR is interacting the inhomogeneous ISM gas, the hadronic γ-ray emissions are indistinguishable from leptonic one (Inoue et al., 2012). The real ISM environment is not uniform, but most theoretical model is assuming the uniform ISM. Therefore, the sources of cosmic-ray protons are still not firmly identified.

Third, some of γ-ray SNRs associate with the dense ISM gas (see Chapter 1.5). The SNR shock waves ($\sim$3000–10000 km s^{-1}) must affect the ISM gas through the physical interaction, but the detailed mechanisms are not studied well. The shock waves also produce cosmic-ray particles according to the DSA model. Therefore making the interaction mechanisms clear , we will have better understandings of cosmic-ray acceleration mechanisms.

In present thesis, I show the observational answers to the questions Q.1, Q.2, and Q.3. In Chapter 1, I review the Galactic cosmic-rays and its acceleration mechanisms. Additionally, I summarize previous study of SNRs interacting with the ISM. In particular, I focus on the young and VHE γ-ray bright SNR RX J1713.7$-$3946. Chapter 2 gives a relationship between the non-thermal X-ray radiation and the ISM (Q.1 and Q.3). Chapter 3 shows evidence for acceleration of cosmic-ray protons in the SNR RX J1713.7$-$3946 (Q.2). Chapter 4 describes the mechanism of efficient cosmic-ray acceleration. In Chapter 4, I summarize our results and refer to the future prospects.

1.2 Cosmic-Rays

It is a longstanding question how cosmic-rays are accelerated in the universe since the first detection by Victor F. Hess. In 1912, he found that ionization rate of the atmosphere increases as he went as up higher with a balloon. The radiation was named "Hohenstrahlung"–it came to be called "cosmic-ray"– and it is the first detection of ionizing radiation from extraterrestrial sources. Around 1930's, the radiation was considered to be high energy γ-rays and/or positive by charged particles.

Today, as described above, we know cosmic-rays are charged particles, which are mainly protons, with $\sim$10% of Helium, and 1% of electrons and ionized nuclei. The energy spectrum of cosmic-rays are now known to extend beyond 10^{20} eV and is described with

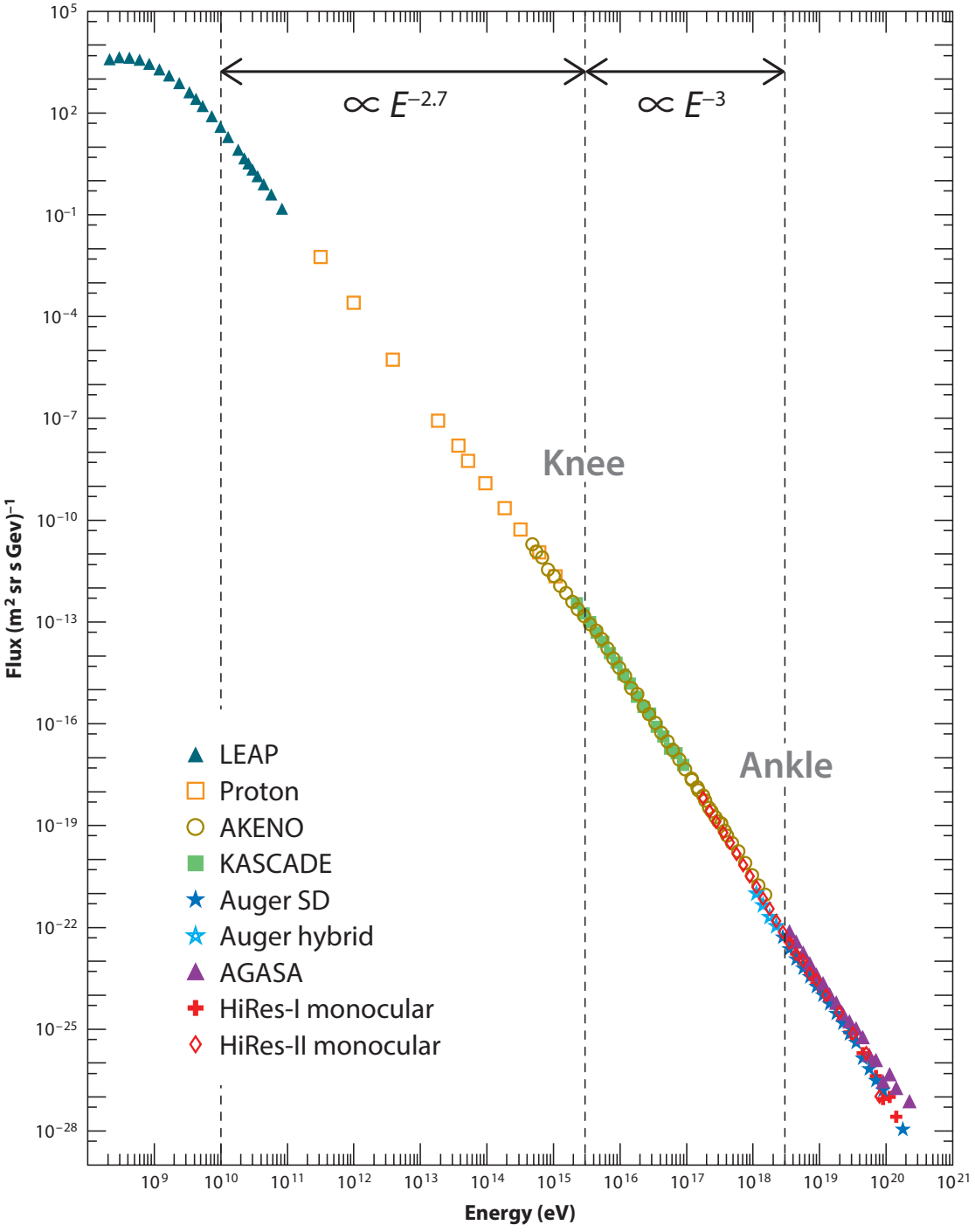

FIGURE 1.1: The energy spectrum of cosmic-rays (Beatty & Westerhoff, 2009).

a power-law function below;

$$dN(E) \propto E^{-p} dE \tag{1.1}$$

where N is the number of particles with the kinematic energy of E. The spectral index p lies in the range about 2.2–3.0. Figure 1.1 shows the energy spectrum of cosmic-rays around the earth (Beatty & Westerhoff, 2009). We clearly see two turn-over in the energy spectra; one is $E \sim 3 \times 10^{15}$ eV (so called *knee*) and the other is $E \sim 3 \times 10^{18}$ eV (so called *ankle*). The spectral index is ~ 2.7 in the energy range between 10^{10} and the *knee*, and become ~ 3 in the energy range between the *knee* and *ankle*. The spectral index of above *knee* is not determined yet.

In the present thesis, galactic cosmic-rays are defined as high energy particles below the *knee* energy and their origin is supposed to be the galactic sources. The gyro-radius $r_{\rm gyro}$ of a relativistic particle is given by

$$r_{\rm gyro} \sim \frac{1}{Z} \left(\frac{E}{10^{15}\ {\rm eV}} \right) \left(\frac{B}{1\ \mu{\rm G}} \right)^{-1} {\rm pc}, \tag{1.2}$$

where Z is the atomic number of nucleus, E is the kinematic energy, and B is the magnetic field strength. if we adopt $E = 10^{15}$ eV, $Z = 1$, and $B = 3$ μG (typical value of the interstellar magnetic field), cosmic-ray proton has a $r_{\rm gyro} \sim 0.3$ pc. Therefore, the interstellar magnetic field can confine the cosmic-rays ($E < 3 \times 10^{15}$ eV) within the Galaxy, whose radius and scale hight are roughly 15 kpc and 300 pc, respectively. Particles at energy around the *ankle*, which is popularly thought to be accelerated in extragalactic source (e.g., active galactic nuclei, gamma-ray burst, radio galaxy; see Figure 1.2). Incidentally, a cosmic-ray proton has an energy around 10^{20} eV, which can interact with the cosmic microwave background and loses energy due to the pion production. Therefore, no particle are expected to be observed above $\sim 10^{20}$ eV. This effect is so called Greisen Zatsepin Kuzmin (GZK) cut-off.

1.3 Cosmic-Ray Acceleration in Supernova Remnants

1.3.1 Kinetic Energy Budget

Supernova remnants (SNRs) are the most promising sources of galactic cosmic-ray accelerator (e.g., Ginzburg & Syrovatskii, 1964). It is because the collision-less shock waves are very powerful in the galactic sources satisfying the kinetic energy needed to explain the injection rate of the cosmic-rays. The required injection rate of cosmic-rays ($L_{\rm CR}$)

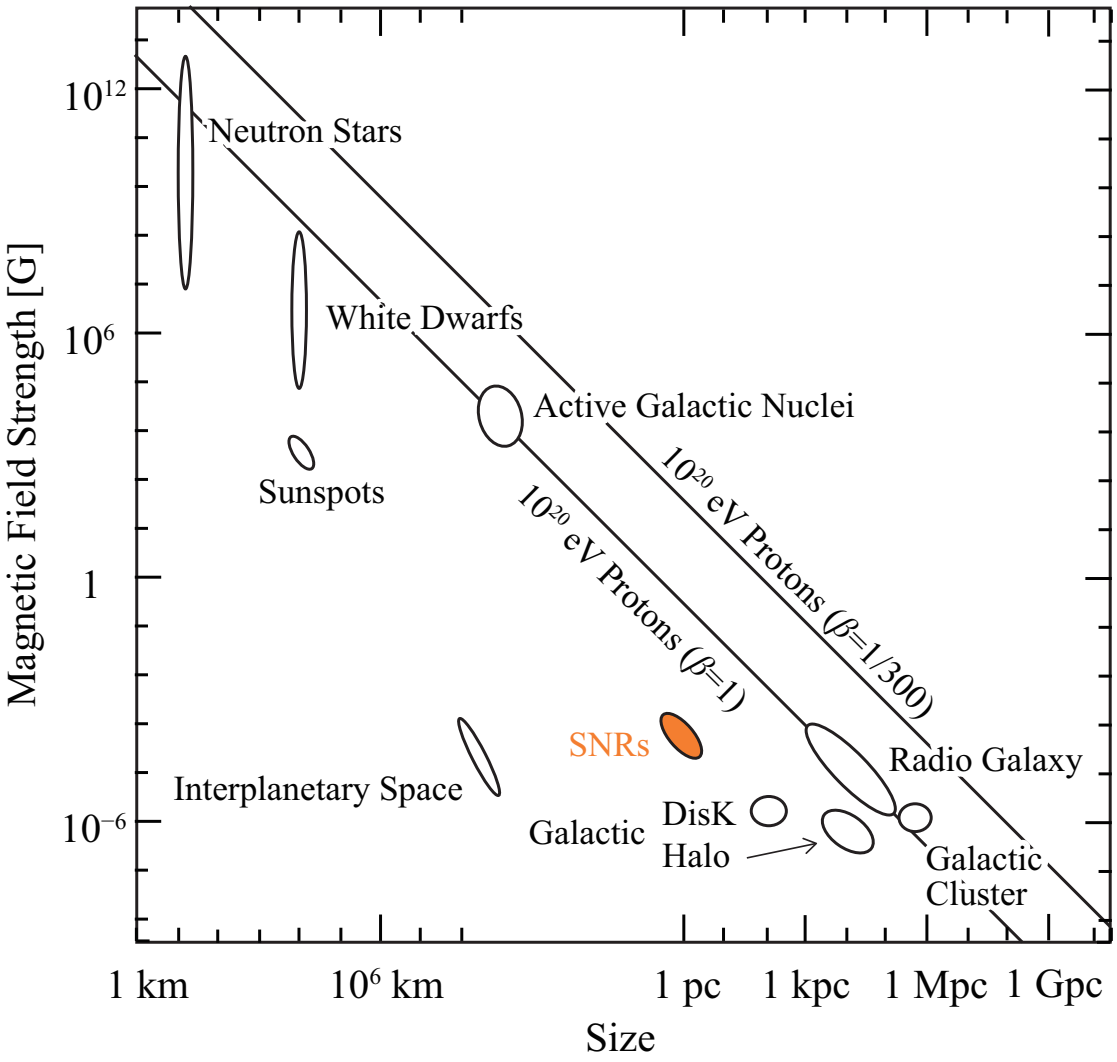

FIGURE 1.2: Hillas diagram (Hillas, 1984).

is estimated to be

$$L_{\rm CR} = \frac{V\,\varepsilon_{\rm CR}}{\tau_{\rm esc}} \sim 10^{41}\ {\rm erg\ s^{-1}}, \tag{1.3}$$

where $V = \pi R^2 h \sim 4 \times 10^{66}$ cm^{-3} is the volume of the Galactic disk with radius R ∼15 kpc and thickness h ∼200 pc, and $\varepsilon_{\rm CR} = 1.39$ eV cm^{-3} $= 2.2{\times}10^{-12}$ erg cm^{-3} is the energy density of cosmic-rays (see also Table 1.1), and $\tau_{\rm esc} \sim 3 \times 10^6$ yr is the escape time scale defined as $\tau_{\rm esc} = \mu/\rho c$ (e.g., Gabici, 2013, , μ is the).

On the other hand, the total power of supernova explosion $P_{\rm SNR}$ is given by

$$P_{\rm SNR} = \frac{E_{\rm SN}}{f_{\rm SN}} \sim 10^{42}\ {\rm erg\ s^{-1}}, \tag{1.4}$$

where $E_{\rm SN} = 10^{51}$ erg is the typical supernova explosion energy, and $f_{\rm SN} \sim 30$ yr is

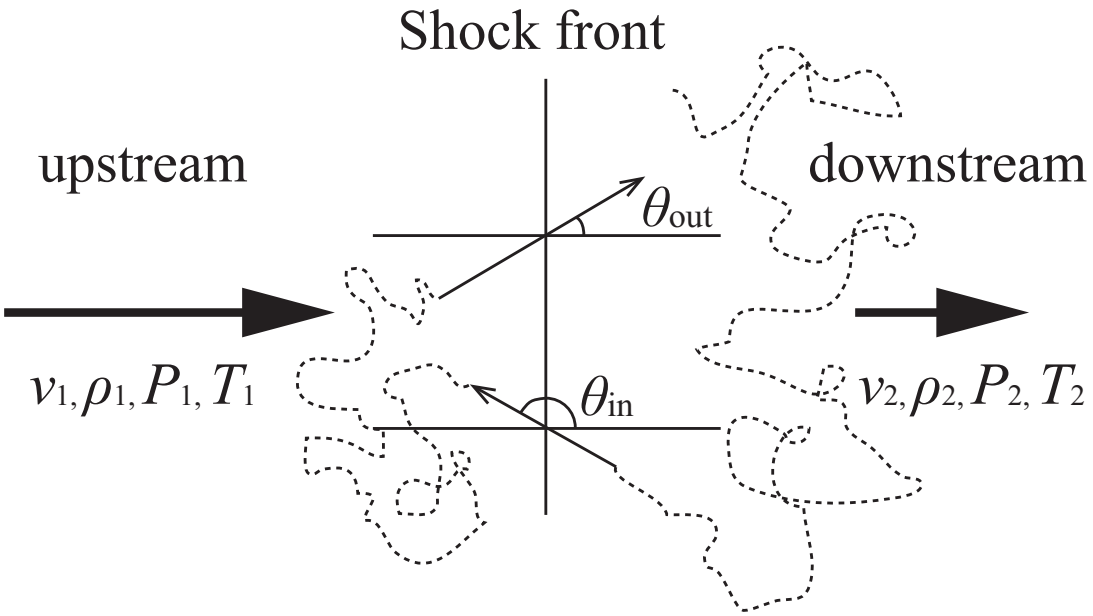

FIGURE 1.3: Schematic view of the diffusive shock acceleration. The dashed lines indicate the locus of cosmic-rays.

the supernova rate in the Galaxy ($\sim$ 3 events / century). Therefore, if the galactic cosmic-rays are accelerated in SNRs, $\sim$10% of each supernova energy is transferred to cosmic-rays.

1.3.2 Diffusive Shock Acceleration

As described above, galactic cosmic-rays are accelerated by shock waves in SNRs. In this case, collision-less shock waves are cased by supersonic plasma flows. Here, we defined a upstream fluid flowing towards the shock front with a velocity v_1, density ρ_1, pressure P_1, temperature T_1, and a downstream are beyond the shock front with a velocity v_2, density ρ_2, pressure P_2, temperature T_2 (see Figure 1.3). Then, fluids meet the following equations (so called Rankine-Hugnoiot equation):

$$\rho_1 v_1 = \rho_2 v_2 \tag{1.5}$$

$$P_1 + \rho_1 v_1^2 = P_2 + \rho_2 v_2^2 \tag{1.6}$$

$$\rho_1 v_1 \left(\frac{v_1^2}{2} + \frac{P_1}{\rho_1} + u_1 \right) = \rho_2 v_2 \left(\frac{v_2^2}{2} + \frac{P_2}{\rho_2} + u_2 \right), \tag{1.7}$$

where u_1 and u_2 are the internal energy of upstream and downstream fluids, respectively. Here, c_s is the sound velocity $c_s = \sqrt{\gamma P/\rho}$, where γ is the ratio of the heat capacity with constant pressure C_P to that with constant volume C_V. Then, writing $P + \rho v^2 = P(1 + \gamma M^2)$ with the Mach number $M = v/c_s$ the down stream / upstream ratios of

density, pressure, and temperature are written as:

$$\frac{\rho_2}{\rho_1}\quad\left(=\frac{v_1}{v_2}\right) = \frac{(\gamma+1)M_1^2}{(\gamma-1)M_1^2+2}\equiv r \tag{1.8}$$

$$\frac{P_2}{P_1} = \frac{2\gamma M_1^2-(\gamma-1)}{\gamma+1} \tag{1.9}$$

$$\frac{T_2}{T_1} = \frac{[2\gamma M_1^2-(\gamma-1)][(\gamma-1)\gamma M_1^2+2]}{(\gamma+1)^2M^2}. \tag{1.10}$$

where r is so called compression ratio. For the strong shock $M \gg 1$, it is given as:

$$r=\frac{\gamma+1}{\gamma-1}. \tag{1.11}$$

For a monoatomic gas, $\gamma = 5/3$, we obtain a constant value of $r = 4$, whereas the density increases $\rho_2 = 4\rho_1$ and velocity decreases $v_2 = v_1/4$ after the passage of the hock front.

Considering the case of cosmic-rays traveling through the shock wave from downstream to upstream with an angle $\theta_{\rm in}$ and from upstream to downstream with an angle $\theta_{\rm out}$ to a normal direction of shock front (= one round trip). The energy gain per one round trip ΔE is given by

$$\Delta E = \frac{v_1-v_2}{c}\,(\cos\theta_{\rm in}-\cos\theta_{\rm out})E. \tag{1.12}$$

Here, c is the light speed, $\theta_{\rm in}$ and $\theta_{\rm out}$ are constrained as $\pi/2 < \theta_{\rm in} < \pi$ and $0 < \theta_{\rm out} < \pi/2$. The cosmic-rays are considered to have homogeneous distribution for angle. Therefore, we can estimate the average $\cos\theta_{\rm in}$ and $\cos\theta_{\rm out}$ for cosmic-ray crossing the shock front:

$$<\cos\theta_{\rm in}> = \frac{\int_{\pi/2}^{\pi}\cos^2\theta_{\rm in}\sin\theta_{\rm in}d\theta}{\int_{\pi/2}^{\pi}\cos\theta_{\rm in}\sin\theta_{\rm in}d\theta} = -\frac{2}{3} \tag{1.13}$$

$$<\cos\theta_{\rm out}> = \frac{\int_{0}^{\pi/2}\cos^2\theta_{\rm out}\sin\theta_{\rm out}d\theta}{\int_{0}^{\pi/2}\cos\theta_{\rm out}\sin\theta_{\rm out}d\theta} = \frac{2}{3}. \tag{1.14}$$

Then, the averaged energy gain on a round trip is calculated to be

$$<\Delta E>=\frac{4(v_1-v_2)}{3c}E. \tag{1.15}$$

This equation indicates that the cosmic-ray particles gain energy through a round trip over a shock front. After n times round trips, the averaged energy gain E_n is descried

as:

$$\begin{aligned} E_n &= E_0\left(1+\frac{4(v_1-v_2)}{3c}\right)^n \\ &\sim E_0\exp\left(\frac{4(v_1-v_2)}{3c}n\right). \end{aligned} \tag{1.16}$$

Here, E_0 is initial energy. Therefore, the kinetic energy continues to increase as long as the cosmic-ray particles stay around the shock front. However, the particles will escape out from the shock front with a certain probability per round trip. We consider the escape probability $P_{\rm escape}$. In the downstream fluid, the averaged velocity crossing the shock front is $c/4$ if we assumed $v_1 \sim c$. Then, the total flux of particles crossing the shock is $N_p c/4$, where N_p is the number density of particles. Here, the number of escaped cosmic-rays due to the convection motion is Nv_2. Hence, the probability of the escaping particle is derived as $Nv_2/(Nc/4) = 4v_2/c$ in a round trip. Therefore, the escape probability $P_{\rm escape}$ from the shock waves after n times round trips is

$$\begin{aligned} P_{\rm escape} &= \frac{4v_2}{c}\times\left(1-\frac{4v_2}{c}\right)^n \\ &\sim \frac{4v_2}{c}\exp\left(-\frac{4v_2}{c}n\right). \end{aligned} \tag{1.17}$$

By using equations 1.16 and 1.17, the energy spectrum of accelerated particles dN/dE is given by

$$\frac{dN}{dE} \propto E^{-\frac{3v_2}{v_1-v_2}-1} = E^{-\alpha}, \tag{1.18}$$

where spectral index $\alpha = (r+2)/(r-1)$. In the case of extreme high speed shock, $r = 4$ and the spectral index $\alpha = 2.0$ are given. The value of spectral index agree very well with the cosmic-ray spectrum around the earth[1].

The next important question is "what is the maximum energy to accelerate by DSA". To estimate the maximum energy, we need to evaluate the acceleration times scale $t_{\rm acc}$. This can be described as:

$$t_{\rm acc} = \Delta t\left\langle\frac{E}{\Delta E}\right\rangle = \frac{3c}{4(v_1-v_2)}\Delta t. \tag{1.19}$$

Here, Δt is the time needed for a round trip. The time Δt can be decomposed into the staying time of upstream and downstream. Therefore, Δt is given by

$$\Delta t = \frac{4D_1}{v_1 c}+\frac{4D_2}{v_2 c}, \tag{1.20}$$

[1]The observed spectral index is 2.7, which is larger than $\alpha = 2.0$. However, It can be described that the higher cosmic-ray energy, the more rapidly they escape from the Galaxy.

where D_1 and D_2 are the diffusion coefficient in upstream and downstream, respectively. For simplification, we assumed $D_1 = D_2 = D$ and strong shock ($v_1 = 4v_2 = v_s$). In this case, diffusion coefficient D is expressed as:

$$D = \frac{c\, r_{\rm gyro}}{3}\,\eta, \tag{1.21}$$

where $r_{\rm gyro} = E/(Z_e B)$ (Z_e indicates the charge of accelerated particle) is the gyro radius and η (≥ 1) $= (B/\delta B)^2$ is the degree of magnetic field fractionation so called "gyro factor"[2]. Therefore, the equation 1.21 can be rewritten in the form below:

$$t_{\rm acc} = \frac{20}{3}\,\frac{c}{v_s^2}\,\frac{E}{Z_e\, B}\,\eta. \tag{1.22}$$

Here, we estimate the maximum energy of cosmic-rays in SNR by the shock waves. Since the age of an SNR can be approximated as $t_{\rm age} = R/v_s$ (R is the radius of the SNR), the maximum energy $E_{\rm max}$ is given by

$$\begin{aligned} E_{\rm max} &= \frac{E}{t_{\rm acc}}\, t_{\rm age} \\ &= \frac{3}{20}\,\frac{v_s}{c}\,\frac{Z_e\, B\, R}{\eta} \\ &\sim 100 \times \eta^{-1}\, Z_e \left(\frac{v_s}{5000\ {\rm km\ s^{-1}}}\right)\left(\frac{B}{10\ \mu{\rm G}}\right)\left(\frac{R}{10\ {\rm pc}}\right) {\rm TeV}. \end{aligned} \tag{1.23}$$

Therefore, the cosmic-rays can be accelerated up to ∼100 TeV in the typical young SNRs.

1.4 Radiative Processes of High Energy Cosmic-Rays

Accelerated cosmic-rays can be observed by their non-thermal emissions which are produced by many physical processes with the energy loss of cosmic-rays. In this section, we introduce the radiative (energy loss) process of cosmic-rays.

1.4.1 Synchrotron Radiation

Relativistic charged electrons emit the synchrotron radiation with its helical motion in magnetic field. The total power per unit frequency emitted by a single electron is

[2]The situation $\eta = 1$ corresponds "Bohm diffusion limit", which indicates the most efficient accelerating state.

described below (e.g., Rybicki & Lightman, 1979):

$$P(\omega) = \frac{\sqrt{3}}{2\pi} \frac{q_e^3 B \sin\alpha}{m_e c^2} F\left(\frac{\omega}{\omega_c}\right), \tag{1.24}$$

where B is magnetic field strength, q_e and m_e are the charge and mass of electron, respectively. The parameter α is the pitch angle between the electron and the magnetic field. The characteristic synchrotron photon energy ε_c is given by

$$\varepsilon_c = \frac{3}{2} \frac{\gamma^2 q_e B \sin\alpha}{mc}. \tag{1.25}$$

The function $F(\omega/\omega_c)$ is also defined as

$$F\left(\frac{\omega}{\omega_c}\right) = \frac{\omega}{\omega_c} \int_{\omega/\omega_c}^{\infty} K_{5/3}(\xi) d\xi, \tag{1.26}$$

where $K_{5/3}$ is the modified Bessel function. The asymptotic forms for the small and large values of ω/ω_c are:

$$F\left(\frac{\omega}{\omega_c}\right) \sim \begin{cases} \frac{4\pi}{\sqrt{3}\,\Gamma(1/3)} \left(\frac{\omega/\omega_c}{2}\right)^{1/3}, & (x \ll 1) \\ \left(\frac{\pi}{2}\right)^{1/2} e^{-\omega/\omega_c} \left(\frac{\omega}{\omega_c}\right)^{1/2}, & (x \gg 1) \end{cases} \tag{1.27}$$

An integration of Equation 1.24 over the frequencies, we obtain the total emitted power $P_{\rm synch}$ as:

$$P_{\rm synch} = \frac{4}{3} \sigma_{\rm T} c \beta^2 \gamma^2 U_{\rm B}, \tag{1.28}$$

where $\sigma_{\rm T} (= 8\pi r_0^2/3)$ is the Thomson cross section and $U_{\rm B} (= B^2/8\pi)$ is the magnetic energy density. This value $P_{\rm synch}$ is also called "energy loss rate" $(dE/dt)_{\rm synch} = -P_{\rm synch}$.

We have hitherto described only a case of one cosmic-ray electron. In reality, the synchrotron spectrum consists of radiation from a lot of cosmic-ray electrons. Let us take the number density of electrons with the energies from E to $E + dE$. It can be approximately expressed below:

$$N(E)dE = CE^{-p}dE, \tag{1.29}$$

where C is the constant varying with the pich angel. In order to obtain the synchrotron spectrum, we sum up the electrons with different energies. Then, the total power per

unit volume per unit frequency $P_{\rm tot}$ is derived as (Abramowitz & Stegun, 1965):

$$P(\omega)_{\rm tot} = \int P(\omega)N(E)dE \tag{1.30}$$

$$= \frac{\sqrt{3}\,q_e^3 CB\sin\alpha}{2\pi m_e c^2(p+1)}\,\Gamma\left(\frac{p}{4}+\frac{19}{12}\right)\Gamma\left(\frac{p}{4}-\frac{1}{12}\right)\left(\frac{m_e c\omega}{3q_e B\sin\alpha}\right)^{-(p-1)/2}. \tag{1.31}$$

Here, Γ is the Gamma function. The parameters in this equation are constant expect for B and ω, then we have

$$P(\omega)_{\rm tot} \propto AB^{(p+1)/2}\,\omega^{-(p-1)/2}, \tag{1.32}$$

where A is a constant. Therefore, the spectral index s is related to the accelerated electron distribution index p by

$$s = \frac{p-1}{2}. \tag{1.33}$$

Then, we obtain a photon index Γ of a power-law spectrum of the synchrotron X-rays, defined by $P(\omega)_{\rm tot} = \omega I(\omega)_{\rm tot} \propto \omega^{-\Gamma}$, is

$$\Gamma = \frac{p+1}{2} \tag{1.34}$$

Finally, we also note the energy of synchrotron X-ray photons ε in the young SNRs which is described below (Aharonian et al., 2007):

$$\varepsilon = \frac{2.2\ {\rm keV}}{\eta(1+\kappa^{1/2})^2}\left(\frac{v_1}{3000\ {\rm km\ s^{-1}}}\right)^2\frac{16}{\gamma_s^2}, \tag{1.35}$$

where κ is the ratio of the magnetic field upstream to the magnetic field downstream, and $\gamma_s = 3r/(r-1)$ is the power-law index of particles accelerated at the absence of energy losses with compression ratio r. In the regime of the Bohm diffusion, let us substitute $\kappa = 1$ and $\gamma_s = 4$ (see Chapter 1.3.2) in Equation 1.36,

$$\varepsilon = 0.55 \times \eta^{-1}\left(\frac{v_1}{3000\ {\rm km\ s^{-1}}}\right)^2 ({\rm keV}). \tag{1.36}$$

This equation indicates that the photon energy of synchrotron X-rays can be determined only by the shock speed v_1 and gyro-factor η.

1.4.2 Inverse Compton Scattering

Relativistic cosmic-ray electrons also contribute to the origin of γ-rays through the scattering of low-energy photons (e.g., cosmic microwave background; hereafter CMB) up

to the higher energy. The radiation mechanism is called "inverse Compton scattering". The energy of scattered interstellar photon $\varepsilon' = h\nu'$ is described as:

$$\varepsilon' = \frac{4}{3}\gamma^2\varepsilon_0, \tag{1.37}$$

where γ is the Lorentz factor and $\varepsilon_0 = h\nu$ is the initial energy of the interstellar photon. For instance, in the case of an electron of 10 TeV ($\gamma = 2 \times 10^7$) scatters a CMB photon ($\varepsilon_0 = 2.725$ K $= 2.348{\times}10^{-4}$ eV; see Table 1.1), the scattered photon energy is calculated as 250 GeV. This photon energy corresponds to the energy band of γ-rays, therefore, the γ-ray emitting process is so called "Leptonic process" distinguished from the π^0-decay ("Hadronic process") γ-rays (see Chapter 1.4.3).

The total power emitted by a single electron via inverse Compton scattering is described as (e.g., Rybicki & Lightman, 1979):

$$P_{\rm IC} = \frac{4}{3}\sigma_{\rm T} c\beta^2\gamma^2 U_{\rm photon}, \tag{1.38}$$

where $U_{\rm photon}(= n_{\rm photon}\varepsilon_0)$ is the energy density of the seed photons. We note that the Thomson scattering is only valid in case of $\gamma\varepsilon_0 \gg mc^2$. By using Equation 1.28, we the obtain the relationship:

$$\frac{P_{\rm synch}}{P_{\rm IC}} = \frac{U_{\rm B}}{U_{\rm photon}}. \tag{1.39}$$

The ratio of the radiative losses cased by the synchrotron emission to the inverse Compton scattering is the same as that of the energy density of magnetic field to the photon energy density. Therefore, we can determine the strength of magnetic fields directly comparing with $P_{\rm synch}$ and $P_{\rm IC}$ in the case of leptonic origin γ-rays alone.

1.4.3 π^0-Decay Emission

The accelerated cosmic-ray protons also emit γ-rays via π^0-decay process as:

$$p({\rm CR}) + p({\rm ISM}) \rightarrow p + p + \pi^0, \tag{1.40}$$

$$\pi^0 \rightarrow 2\gamma, \tag{1.41}$$

where p(CR) and p(ISM) are accelerated cosmic-ray proton and interstellar proton, respectively. We here noted that the kinematic energy of cosmic-ray proton $E_{\rm kin} = E_{\rm p} - m_{\rm p}c^2$ should exceed ~280 MeV. The created π^0 decays to two photons with the mean lifetime $\sim 8.4 \times 10^{-17}$ s. Each photon has 67.5 MeV (a quantity of half energy of π^0) in a static system and have opposite kinematic directions each other. However, the

photons energy increases, because π^0 obtain a part of the kinematic energy of cosmic-ray proton. Therefore, this process, so called "hadronic process", is important for the γ-ray production in the universe. These ideas were first proposed by Hayakawa (1952) and is widely recognized among international researchers.

The γ-ray emissivity $q_\gamma(E_\gamma)$ with energy of E_γ for an arbitrary spectrum of proton is given by (Aharonian & Atoyan, 1996),

$$q_\gamma(E_\gamma) = 2 \int_{E_{\rm min}}^{\infty} \frac{q_\pi(E_\pi)}{\sqrt{E_\pi^2 - {m_\pi}^2 c^4}} dE_\pi. \tag{1.42}$$

Here, E_π and m_π are kinematic energy and mass of π^0, respectively. $E_{\rm min}$ is the minimum energy of 2γ production from π^0 mesons and $q_\pi(E_\pi)$ is the π^0 spectrum as below:

$$q_\pi(E_\pi) = \frac{c n_{\rm H}}{f_\pi} \sigma_{\rm pp} \left(m_{\rm p} c^2 + \frac{E_\pi}{f_\pi} \right) E_{\rm p} \left(m_{\rm p} c^2 + \frac{E_\pi}{f_\pi} \right), \tag{1.43}$$

where $n_{\rm H}$ is the ambient interstellar gas density, f_π is the mean fraction of the kinetic energy of the proton transferred to the secondary meson per collision, and $E_{\rm p}$ is the energy distribution of the protons. Here, $\sigma_{\rm pp}(E_{\rm p})$ is the interaction cross section between cosmic-ray proton with $E_{\rm kin} \geq 1$ GeV and can be approximated as:

$$\sigma_{\rm pp}(E_{\rm p}) \sim 30[0.95 + 0.06 \ln(E_{\rm kin})/1 \text{ GeV}] \text{ mb}. \tag{1.44}$$

Here, we use typical values $\sigma_{\rm pp}(E_{\rm p}) \sim 40$ mb and $f_\pi \sim 0.45$ (e.g., Gabici, 2013). Then, the cooling time scale of protons via hadronic process $t_{\rm pp}$ is described as:

$$t_{\rm pp} = (n_{\rm H} \sigma_{\rm pp} f_\pi c)^{-1} \sim 6 \times 10^7 \left(\frac{n_{\rm H}}{1 \text{ cm}^{-3}} \right) \text{ yr}. \tag{1.45}$$

Therefore, the initial spectrum of the accelerated cosmic-ray protons is expected to unchanged.

Next, let us consider the difference of energy spectrum between the cosmic-ray protons and observed γ-rays. The energy of γ-rays produced by the hadronic process E_γ is proportional to the cosmic-ray proton energy $E_{\rm p}$ as $E_\gamma = h\nu \sim 0.1 E_{\rm p}$. In order to calculate the total energy of γ-rays F_ν, we assume the energy distribution of cosmic-ray protons as:

$$N_{\rm p}(E_{\rm p}) dE_{\rm p} = C E_{\rm p}^{-p} dE_{\rm p}, \tag{1.46}$$

where C is a constant. The total energy of γ-rays F_ν is given by:

$$\begin{aligned} F_\nu d\nu &= \int (0.1E_{\rm p}) C E_{\rm p}^{-p} dE_{\rm p} && (1.47)\\ &= Ch \int (10h\nu)^{1-p} d\nu && (1.48)\\ F_\nu &\propto \nu^{1-p}. && (1.49) \end{aligned}$$

Then, the photon index Γ is given by,

$$\Gamma = p. \quad (1.50)$$

Therefore, observed γ-ray spectrum via hadronic process almost reproduces the parent proton spectrum with a factor of ~ 0.1 lower energies. Consequently, observing the hadronic γ-ray emission is conducive to direct measurement of cosmic-ray properties.

Finally, we introduce the relationship between the F_ν and the interstellar gas density $n_{\rm H}$. Given the total energy of accelerated protons $W_{\rm p}$, we obtain

$$\begin{aligned} F_\nu &= \frac{1}{4\pi d^2}\left(\frac{W_{\rm p}}{t_{\rm pp}}\right),\\ F_\nu &\propto \left(\frac{W_{\rm p}\, n_{\rm H}}{d^2}\right), && (1.51) \end{aligned}$$

where d is the distance to source. Therefore, the γ-ray flux is proportional to the interstellar gas density. This fact strongly suggests that the spatial distribution of hadronic γ-rays have correlation with the interstellar gas distribution.

1.5 Associated SNRs with the Interstellar Gas

SNRs have a profound influence on the surrounding ISM via shock interaction, which affects the evolution of SNRs. It is therefore important to study the detailed physical properties of the interaction between SNRs and ISM, in order to understand the physics of shock interaction. In this section, we summarize the previous studies of the SNR-ISM interaction.

1.5.1 Overview of Previous Studies

The physical interaction between the SNR shocks and the surrounding interstellar gas has studied since several ten years ago. These studies mainly discussed shock compression (+acceleration) of the interstellar gas (e.g., Seta et al., 1998) and low-mass star

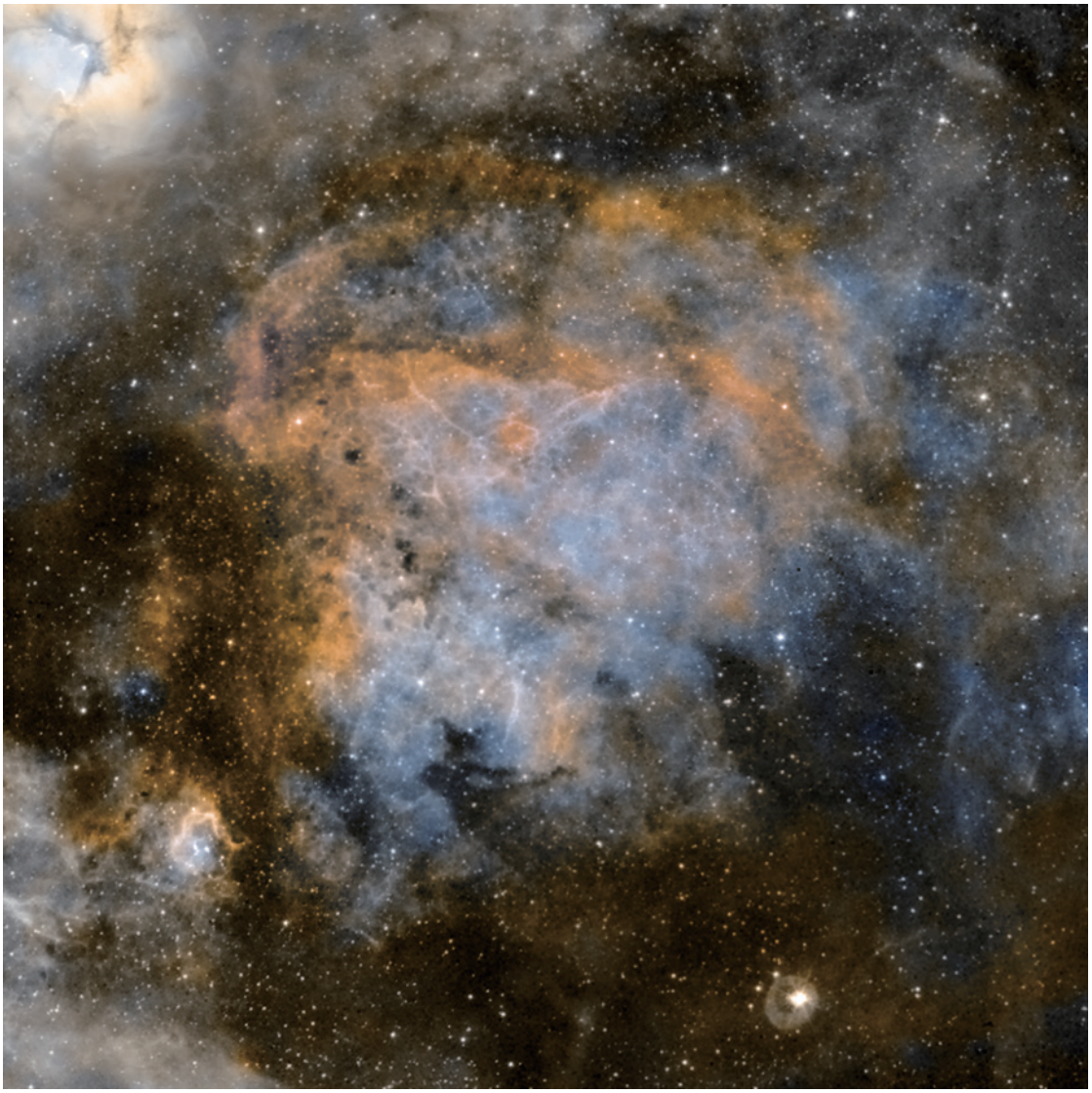

FIGURE 1.4: The three color composite image of the middle-aged SNR W28: orange is the radio continuum obtained by the Very Large Array (Dubner et al., 2000), gray is the optical light by the Cerro Tololo Inter-American Observatory (Keohane et al., 2005), and blue is X-rays taken by *ROSAT* (Rho & Borkowski, 2002).

formations trigged by the SNR shock waves (e.g., Fukui et al., 1999). The physical conditions of shocked gas are already revealed in some middle-aged SNRs whose age is several 10,000 yr (e.g., Denoyer, 1979; Wootten, 1977, 1981).

Recently, the comparative study between the high energy emission and the interstellar gas is again attracting the attention from the viewpoint of an efficient cosmic-ray accelerations in conjunction the γ-ray origin. Figure 1.4 shows one of the middle-aged SNR W28, which is emitted in radio continuum, thermal X-rays, and γ-rays (e.g., Brogan et al., 2006; Rho & Borkowski, 2002; Aharonian et al., 2008; Abdo et al., 2010). In particular, it has been actively debated whether the VHE γ-rays are hadronic origin

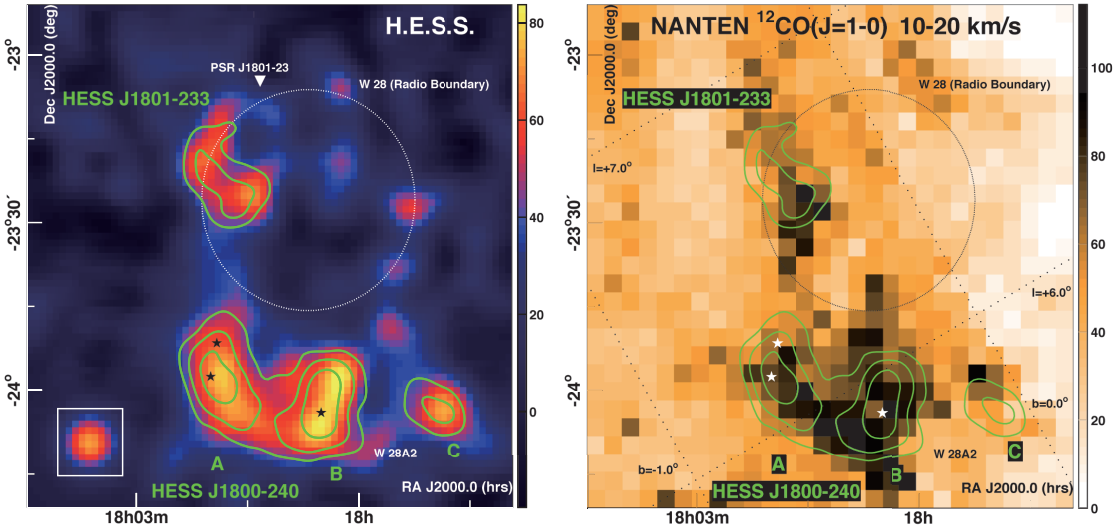

FIGURE 1.5: Distributions of H.E.S.S. VHE γ-rays (left panel) and NANTEN ^{12}CO(J=1–0) emission (right panel) toward W28 (Aharonian et al., 2008). The green contours show the VHE γ-ray significance levels of 4, 5, and 6 σ. The dashed circles indicate a boundary of radio continuum (Brogan et al., 2006). We can easily confirm clear correlation between the VHE γ-rays and the interstellar gas.

or not. Generally, it is difficult to distinguish the hadronic and leptonic γ-rays from the only spectral study by using the DSA model due to many free parameters (e.g., magnetic field strength) and some unrealistic approximation (e.g., assuming homogeneous gas density). However, if the γ-rays are hadronic origin, the spatial distribution of γ-ray flux is proportional to the CO maps because the CO integrated intensity can be convert to the molecular hydrogen density (see also Equation 1.51). The SNR W28 is also known that the shock waves are interacting with the dense molecular gas (e.g., Arikawa et al., 1999), hence Aharonian et al. (2008) compared the H.E.S.S. γ-ray with the NANTEN CO datasets. Figure 1.5 shows the intensity maps of VHE γ-rays and CO. The distribution of VHE γ-rays are extended to the outside of radio boundary and have four outstanding peaks. We can see clear correlation between the two images and the authors conclude that the VHE γ-rays are consistent with hadronic origin. Subsequently, *AGILE* and *Fermi* detected the GeV γ-rays and they estimate the total proton energy $W_{\rm p} = 2.3\text{–}3.3 \times 10^{49}$ erg (Giuliani et al., 2010; Abdo et al., 2010). The acceleration rate, $W_{\rm p}/E_{\rm SN}$ ~2–3% is less than the estimation in Chapter 1.3.1 (~ 10%) and quite reasonable. Most recently, Yoshiike et al. (2013, 2014) also studied same comparison in the middle-aged SNRs W44, IC443, and W51C and the authors obtained similar results as W28 ($W_{\rm p}/E_{\rm SN}$ ~1%). These results indicate that the middle-aged SNRs emitting in γ-rays are one of the main components of cosmic-ray proton accelerator.

Unfortunately, it is not enough to explain the cosmic-ray spectrum below the *knee* energy because the middle-aged SNRs can not accelerate cosmic-ray protons to $E_{\rm p} \sim 10^{15}$ eV.

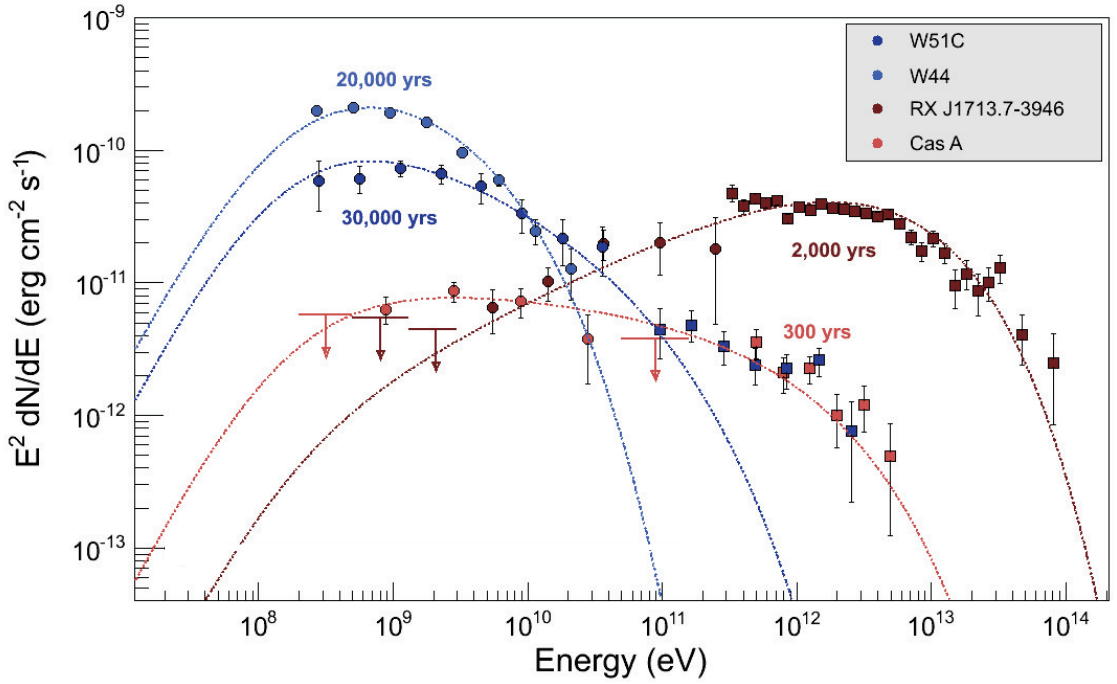

FIGURE 1.6: Spectral energy distribution of γ-rays toward typical four SNRs (Funk, 2012). The filled circles and squares correspond to the observed points of GeV and VHE γ-rays, respectively. Each dashed line indicates the expected energy spectrum by the DSA model.

Figure 1.6 shows the energy spectrum of the middle-aged SNRs (W51C and W44) and the young SNRs (RX J1713.7−3946 and Cas A). In the middle-aged SNRs, the maximum energy of expected γ-ray spectrum is $\sim 10^{11}$–10^{12} eV. On the other hand, the maximum energy of young SNRs reaches $\sim 10^{13}$–10^{14} eV. The energy of cosmic-ray protons $E_{\rm p}$ is $\sim$10 times higher than γ-ray energy and hence RX J1713.7−3946 is the best candidate of cosmic-ray accelerator at $E_{\rm p} \sim 10^{15}$ eV. Therefore, the young SNRs RX J1713.7−3946 is the best target to observe for the understanding efficient acceleration of cosmic-ray protons above the *knee* energy.

1.5.2 Previous Studies of the Young SNR RX J1713.7−3946

Young SNR RX J1713.7−3946 (also known as G347.3−0.5) is the best target for clarifying efficient cosmic-ray acceleration, because the SNR emits strong synchrotron X-rays and GeV–VHE γ-rays with a shell like structure (e.g., Acero et al., 2009; Abdo et al., 2011; Aharonian et al., 2007, see also Figure 1.7). However, the origin of γ-rays has not been revealed yet whether hadronic or leptonic (discussed later). The SNR has a large apparent diameter ($\sim$1 deg) and is located relatively close to the Galactic center at (l, b) = (347.3, −0.5) where contamination by the Galactic foreground/background is heavy at any wavelength (see Figure 1.8). Therefore, RX J1713.7−3946 was not known as

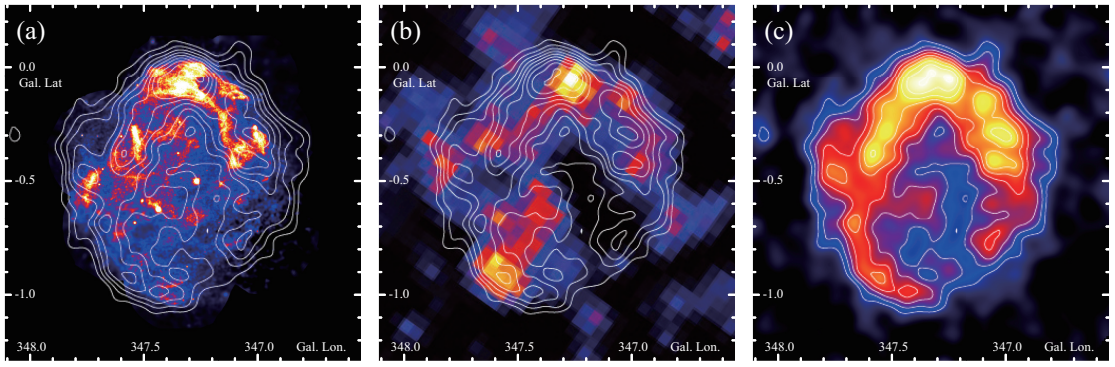

FIGURE 1.7: Distribution of (a) *XMM-Newton* X-rays (Acero et al., 2009), (b) *Fermi* GeV γ-rays (Abdo et al., 2011), and (c) H.E.S.S. VHE γ-rays (Aharonian et al., 2007) toward the SNR RX J1713.7−3946. White contours show the H.E.S.S. VHE γ-ray intensity and are plotted every 20 smoothed counts from 20 smoothed counts.

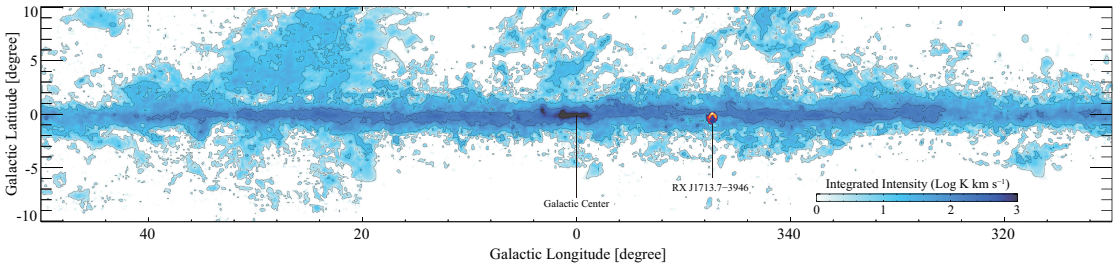

FIGURE 1.8: Distribution of ^{12}CO(J=1–0) in the Galaxy taken by the Cfa 1.2-m telescopes and the NANTEN telescope (Dame et al., 2001; Mizuno & Fukui, 2004). Overlaid is the VHE γ-ray emission toward RX J1713.7−3946 with H.E.S.S (Aharonian et al., 2007).

an SNR in the radio continuum radiation and was discovered in X-ray by the *ROSAT* for the first time (Pfeffermann & Aschenbach, 1996). After that, Koyama et al. (1997) showed that the X-ray emission is by the synchrotron radiation with no thermal features using the *ASCA* satellite (formerly named Astro-D) and derived a distance of 1 kpc based on a relatively small X-ray absorption $N_{\rm H}$(X-ray), corresponding to an HI column density of $(6.2 \pm 1) \times 10^{21}$ cm^{-2} for the northwest rim. Coincidentally, Wang et al. (1997) pointed out a possibility that RX J1713.7−3946 is the remnant of an AD393 guest star as recorded in Sung Shu by Shen (AD500) and strongly supported a short distance of ∼1 kpc and age of ∼1600 yr. Slane et al. (1999) suggested the possible association of a molecular cloud named "cloud A", and its the local standard of rest (LSR) velocity $V_{\rm LSR}$ ∼90 km s^{-1} from the observations of ^{12}CO(J=1–0) emission line at 8.8′ resolution suggests a large distance of 6.3±0.4 kpc. The authors also mentioned that an enhanced value of the CO J=2–1/J=1–0 line ratio ∼ 2.0 in cloud A indicates the physical interaction with the SNR shock waves. Today, we confirmed that the distance to RX J1713.7−3946 is ∼1 kpc from us (e.g., Fukui et al., 2003) and yet, in the late 90's, it has not been cleared yet. The decisive evidence of smaller distance is brought from a result

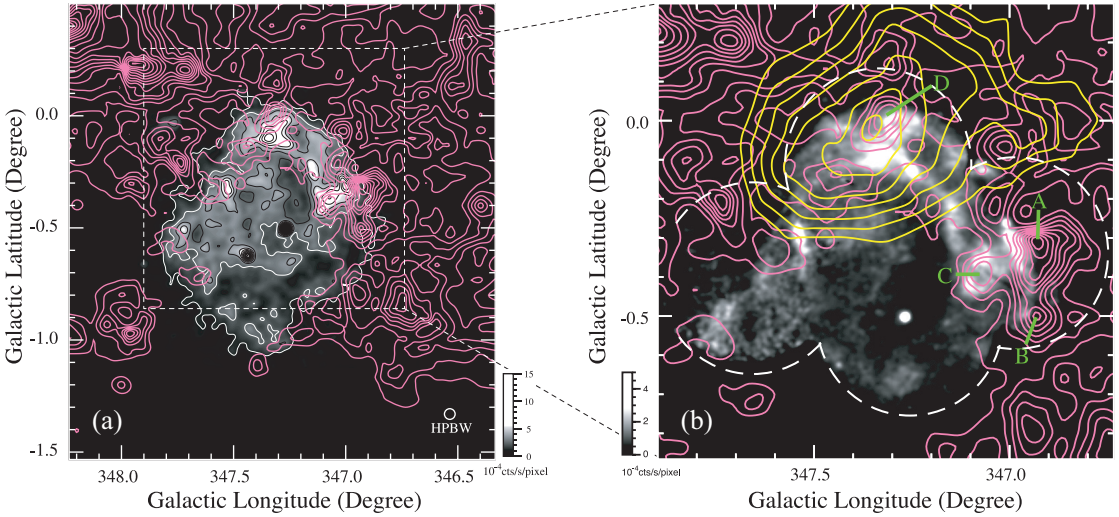

FIGURE 1.9: (a) Intensity distribution of *ROSAT* X-ray image superposed with the NANTEN CO contours (Fukui et al., 2003). (b) Close-up view of RX J1713.7−3946 with *XMM-Newton* X-rays superposed with the NANTEN CO contours (magenta) and CANGAROO VHE γ-rays Fukui et al. (2003).

of NANTEN CO survey (Mizuno & Fukui, 2004) in 2003. Fukui et al. (2003) revealed a detail structure of CO in RX J1713.7−3946 at finer resolution $\sim 2.7'$ and discovered definitely interacting molecular clouds at $V_{\rm LSR}$ ∼7 km s^{-1}, which corresponds to a distance of 1 kpc from us. Figure 1.9 shows the *ROSAT* X-ray image overlaid with the NANTEN ^{12}CO(J=1–0) contours in the velocity range from −11 to −3 km s^{-1}. The authors found that the CO emission delineates the outer boundary of the SNR expect for the southeast region and its peaks (named A to D in Figure 1.9b) is good spatial corresponding with the X-ray intensity peaks, especially in western region (upper right in Figure 1.9). The correlation suggests that the SNR shock waves are strongly interacting with the ISM. Additionally, they also found that cloud A shows worse spatial contact with the edge of the SNR and molecular peak C has a broad wing like component probably cased by the shock interaction. Therefore, the authors concluded that the kinematic distance and age are 1 kpc and ∼1600 yr, respectively. The physical parameters are consistent with the previous studies (Pfeffermann & Aschenbach, 1996; Koyama et al., 1997; Wang et al., 1997) and supported by many studies by using CO and X-rays (e.g., Moriguchi et al., 2005; Cassam-Chenaï et al., 2004). In the present thesis, I use these values.

The γ-ray radiation from the northwest rim of SNR RX J1713.7−3946 is detected by CANGAROO 3.8-m atmospheric imaging Cerenkov telescope for the first time (Muraishi et al., 2000). The authors discussed the emitting process and conclude that the VHE γ-rays are dominated by leptonic origin (inverse Compton scattering), but Fukui et al. (2003)'s results suggested that the spacial correlation between the CO peak D and

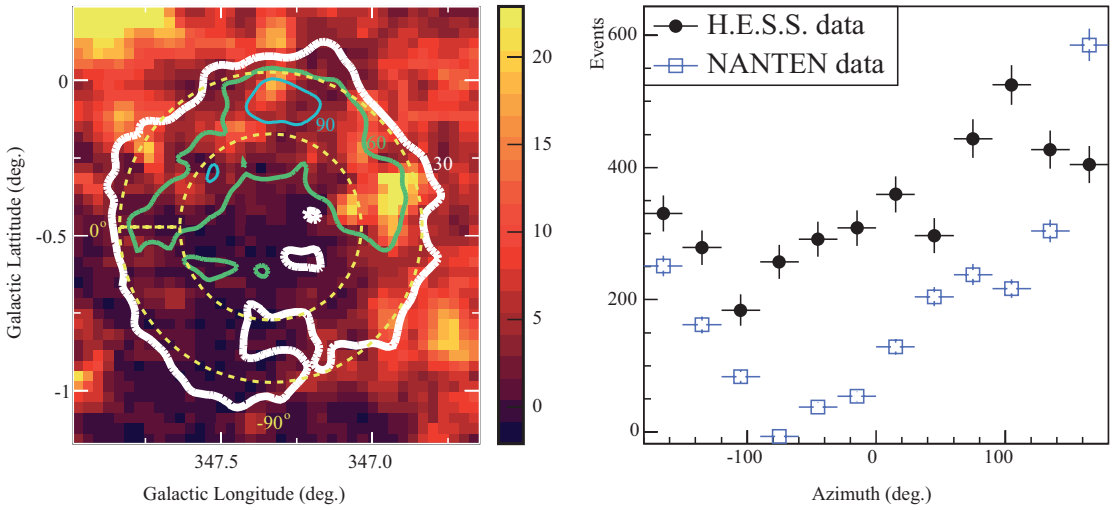

FIGURE 1.10: The comparison between the H.E.S.S. VHE γ-rays and NANTEN CO (Aharonian et al., 2006b). Left panel shows the map of NANTEN CO image overlaid the H.E.S.S. VHE γ-ray contours. The contour levels are 30, 60, and 90 smoothed counts. Right panel shows azimuth profile plot of VHE γ-rays and CO between the two dashed yellow circle shown in the left panel.

VHE γ-rays gives convincing evidence for the hadronic origin (see the yellow contours in Figure 1.9b). More detailed studies of VHE γ-ray origin are performed by Aharonian et al. (2004, 2006b, 2007) with the H.E.S.S. observations. The authors revealed shell-like morphology of VHE γ-rays and compared it with the NANTEN CO distribution (Aharonian et al., 2006b, ; see Figure 1.10). If the hadronic process is working, we expect that the azimuthal profile ofγ-rays is approximately proportional to that of the CO intensity. As a result, the comparative study was successful for a global agreement between the two measurements. However, the authors found that the correlation is not complete in the sense that the southeastern-rim (60–90 deg in azimuth plot) of the VHE γ-ray shell has no counterpart in CO. Therefore, although the hadronic process is the most likely origin of the VHE γ-rays in the SNR, more detail investigations are required.

From here on out, I describe recent progress of X-ray, GeV γ-rays (and the origin of γ-rays), and numerical simulations in RX J1713.7−3946. After the 21st century began, the X-ray properties of RX J1713.7−3946 are gradually revealed by using three space telescope, *XMM-Newton*, *Suzaku*, and *Chandra*. Cassam-Chenaï et al. (2004) has presented spatial distribution of absorbing column density $N_{\rm H}$(X-ray) and photon index Γ obtained by *XMM-Newton*. The maps do not have fine resolution enough to compare with the ISM structures, but the map of $N_{\rm H}$(X-ray) has revealed strong variations over the whole SNR (0.4×10^{22} cm$^{-2} \leq N_{\rm H}$(X-ray) $\leq 1.1 \times 10^{22}$ cm^{-2}). The authors carried out a careful analysis of X-ray absorption using a coarse resolution of CO map (Dame et al., 2001), HI, and star counting method, which favors a shorter distance ($d = 1.3 \pm$

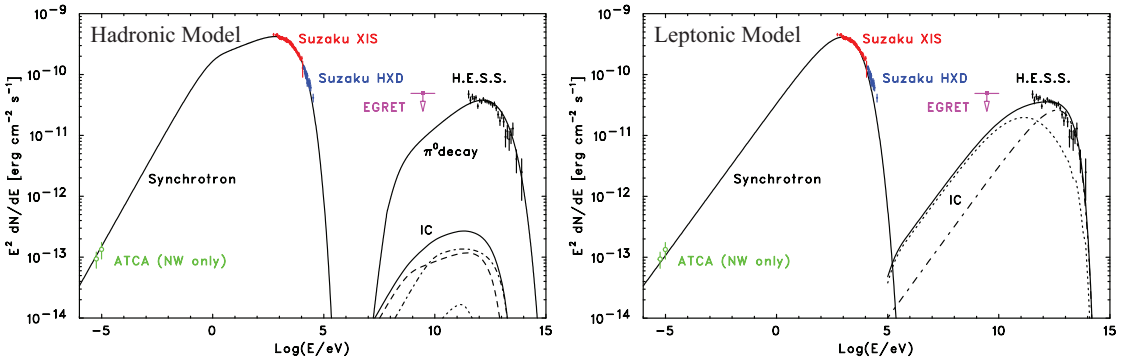

FIGURE 1.11: Spectral energy distribution of RX J1713.7−3946 with a hadronic and leptonic models (Tanaka et al., 2008). The hadronic model is assumed high magnetic field $B = 200\mu$G. The dash-dotted line, dashed line, and soiled lines in the leptonic model are indicate pure inverse Compton (IC) component, 2nd IC component with seed photon of additional optical radiation, and the total, respectively.

0.4 kpc). Additionally, the value of photon index Γ has also shown the strong variation ($1.8 \leq \Gamma \leq 2.6$). This trend was well-supported by more detailed analysis of the *XMM-Newton* data (Hiraga et al., 2005; Acero et al., 2009). Cassam-Chenaï et al. (2004) also investigated a compact central object "1WGA J1713.4−3949" in the SNR and proposed that the point source is the compact relic of RX J1713.7−3946's supernova progenitor. Around the same time, *Chandra* revealed the filamentary structure (10″ scale) and its short time variability (∼1 yr) of the X-rays (Uchiyama et al., 2003, 2007). The variability was described as cased by rapid particle accelerations and cooling in ∼1 yr scale. It leads us to expect that, the cosmic-ray electrons should be accelerated efficiently (so called "Bohm diffusion regime''; Uchiyama et al., 2007), and the magnetic field strength is to be ∼ 1 mG (∼100 times higher than typical values in SNRs). Takahashi et al. (2008) and Tanaka et al. (2008) have discovered the hard synchrotron X-rays up to 40 keV from the SNR using *Suzaku*. The spectra are well fitted by interstellar absorbed power-law function with exponential cut-off. The authors concluded that the existence of cut-off indicates evidence for cosmic-ray electrons in the regime close to the Bohm diffusion limit (Tanaka et al., 2008, see also Chapter 1.3.2). It is not known what triggered the efficient acceleration.

Tanaka et al. (2008) also discussed the origin of VHE γ-rays by using broad band energy spectrum with *Suzaku* and H.E.S.S.. Figure 1.11 shows the spectral energy distribution of RX J1713.7−3946 for the hadronic and leptonic models. The DSA models could reproduce the observed data (*suzaku* XIS and HXD X-rays, and H.E.S.S. VHE γ-rays) by changing the unknown parameters, magnetic fields B and/or the amount of seed photons etc. According to the authors, the hadronic model is in favor than the leptonic one because the high magnetic field strength B ∼200 μG for the hadronic model is consistent

with Uchiyama et al. (2007), and the leptonic model assumes an unrealistic component of the optical radiation with an energy density of 140 eV cm^{-3} (typical radiation field is 0.54 eV; see also Table 1.1). Recently, the *Fermi* Large Area Telescope (LAT) revealed GeV γ-ray spectrum in the SNR (Abdo et al., 2011, see also the significance map in Figure 1.7) and the authors concluded that the GeV to VHE γ-ray emissions are the leptonic origin.

Most recently, Inoue et al. (2009, 2012) presented magnetohydrodynamic (MHD) numerical simulations of the shock interaction with molecular and atomic gas. They indicate that the interaction between the shock waves and the **clumpy interstellar gas** excite turbulence which amplifies the magnetic field around the clumps (Inoue et al., 2009, 2012). The authors also suggested that in the case of amplified the magnetic field, the photon index of the hadronic γ-ray emission ($p - 1/2$) is the same as that of the inverse Compton emission $(p + 1)/2$ when $p = 2$, and thus the spectra in the two scenarios are indistinguishable from the γ-ray observation alone. Comparison of the spatial distribution between the γ-rays and the interstellar gas is the only way to distinguish whether their origins are hadronic or leptonic.

1.6 Thesis Outline

Considering the history of studies on RX J1713.7−3946, it is now necessary in detail to study the interaction between the SNR shock waves and its surroundings[3] to understanding the origin of γ-rays and efficient mechanism of cosmic-ray accelerations.

Therefore, the present thesis gives a decisive answer to the above issues by using the CO, X-rays, and γ-rays dataset. Chapter 2 gives the quantitative relationship between the synchrotron X-rays (= cosmic-ray electrons) and the interstellar gas and presents the magnetic amplification due to the shock-cloud interaction. Chapter 3 shows evidence the cosmic-ray proton acceleration comparing the VHE γ-rays and total interstellar gas (both CO and HI). Chapter 3 proposes a scenario that the efficient acceleration of cosmic-ray electrons are cased by the shock-cloud interaction. In Chapter 4, we summarize our results and refer to the future prospects.

[3]We note that the magnetic fields strength is already known to ∼1 mG by Uchiyama et al. (2007), although it was measured in a small region of ∼ 10 $arcsec^2$. Therefore, the overall magnetic field strength in the SNR is still unknown.

Chapter 2

Non-Thermal X-ray Enhancement around Dense Gas Clumps

2.1 Background

Supernova remnants (SNRs) have a profound influence on the interstellar medium (ISM) via shock interaction and injection of heavy elements. The dynamical interaction also affects the evolution of SNRs through the distortion of the shell morphology, if the ISM is dense enough. It is therefore important to study the detailed physical properties of the interaction between SNRs and ISM, in order to understand what can occur.

RX J1713.7−3946 is one of the unique SNR emitting very-high-energy (VHE, Energies $E > 100$ GeV) γ-rays and X-rays, which is likely emitted by cosmic-ray particles accelerated in the SNR via diffusive shock acceleration (DSA; see detail for Chapter 1.3.2). It is noteworthy that the X-rays of the SNR are purely non-thermal synchrotron emission, indicating that the cosmic-ray electrons are accelerated in the SNR up to the 10 TeV range; there are only two SNRs except for RX J1713.7−3946, which show such non-thermal X-rays, RX J0852.0−4622 (Vela Jr.) and HESS J1731−347, known to date (e.g., Koyama et al., 1997; Slane et al., 2001; Tian et al., 2010). Detailed theoretical modeling of these high-energy radiation has been made over a wide range of physical parameters appropriate for the SNR, and has shown that the observed properties of high energy radiation are reproduced under reasonable sets of physical parameters relevant for the cosmic-ray acceleration (e.g., Zirakashvili & Aharonian, 2007, 2010). It is thus becoming more and more important to constrain observationally the physical parameters of the SNR, like the magnetic field, and their distributions.

The molecular clumps interacting with the SNR was discovered in the ^{12}CO(J=1–0) emission in $V_{\rm LSR}$, the velocity with respect to the local standard of rest, around −7 km s^{-1} as mentioned in Chapter 1.5.2. The result shows that the distribution of the

CO emission in RX J1713.7−3946 well correlates with the X-ray distribution in pc scale(Fukui et al., 2003, see Figure 1.9 in Chapter 1.5.2); the northwestern rim of the X-ray coincides with the most prominent CO peaks (Fukui et al., 2003; Moriguchi et al., 2005; Fukui, 2008). This X-ray distribution is now interpreted theoretically as caused by the interaction between the shock front and the molecular clumps as modeled in the magneto-hydrodynamical (MHD) numerical simulations by Inoue et al. (2009, 2012). The correlation provides a robust verification of the physical association of the CO clumps with the non-thermal X-ray shell. **However, there hasn't been quantitative study to clarify the connection among the X-rays, ISM clumps, and accelerated cosmic-ray electrons.**

Additionally, in the course of the above studies Fukui et al. (2003) found that CO peak C shows broad CO wings and suggested that the wings may result from dynamical acceleration by the SNR blast wave. Such broad molecular wings are found in several SNRs including IC443, W44, W28, etc. (e.g., Denoyer, 1979; Wootten, 1977, 1981). Moriguchi et al. (2005) showed that the ^{12}CO(J=3–2) distribution in peak C shows a hint of a bipolar nature being associated with an infrared compact source with the spectrum of a protostar. This may indicate an alternative possibility that the broad wings are driven by the outflow from a protostar but are not due to the shock interaction. It is an open question whether the SNR is accelerating molecular gas to high velocities in peak C. It is therefore important to clarify whether the CO broad wings are due to the blast-wave acceleration or due to protostellar activity in our efforts to better understand the interaction.

In this Chapter, we establish the connection between the synchrotron X-rays and the surrounding ISM distribution. The present work is aimed at better understanding the SNR shock-cloud interaction and establishing thereby the origin of the distribution of the synchrotron X-rays in the SNR. This study will be extended to the other SNRs with non-thermal features, allowing us to deepen our understanding on the role of the interacting ISM in the high energy radiation and in the cosmic-ray acceleration. In the present paper we show a comparison of the spatial distribution among CO, HI and X-rays over the whole SNR in order to clarify the relationship between dense gas and the high-energy electrons. Furthermore, we reveal the molecular properties of the core and broad wings in peak C and the other cloud cores nearby in RX J1713.7−3946.

2.2 Datasets of CO, HI, and X-rays

2.2.1 CO

We carried out ^{12}CO(J=2–1, 4–3) and ^{13}CO(J=2–1) observations with the NANTEN2 4-m sub-mm telescope of Nagoya University installed at Pampa La Bola (4865 m above the sea level) in the northern Chile.

The ^{12}CO(J=2–1) and ^{13}CO(J=2–1) data at 230 GHz were conducted from August to November in 2008. The front end was a 4 K cooled double sideband (DSB) receiver and a typical system temperature was ∼250 K in the single sideband (SSB) including the atmosphere toward the zenith. The telescope had an angular resolution (FWHM) of 90″ at 230 GHz. We used an acoustic optical spectrometer having 2048 channels with a bandwidth of 390 km s^{-1} and resolution per channel of 0.38 km s^{-1}. Observations in ^{12}CO(J=2–1) were carried out in the on-the-fly (OTF) mode with an integration time of 1.0 s or 2.0 s per grid, and provided a Nyquist-sampled 30″ grid dataset. The telescope had a beam size of 90” at 230 GHz. The ambient temperature load was employed for the intensity calibration. The absolute intensity scale was estimated by observing the Ori KL object [$5^{\rm h}35^{\rm m}14\overset{\rm s}{.}52; -5°22'28\overset{''}{.}2$ (J2000)] (Schneider et al., 1998) for ^{12}CO(J=2–1) line and the main beam efficiency, $\eta_{\rm mb}$, was estimated to be 0.83. The rms noise fluctuations with 1.0 s and 2.0 s integrations were better than 0.66 K and 0.51 K per channel, respectively. The pointing accuracy was estimated to be better than ∼15″ by observing Jupiter every two hours. The image was smoothed with a Gaussian kernel with FWHM of 60″. Observations in ^{13}CO were also carried out in the OTF mode for the area of 22 arcmin^2 including the peaks A, B, C, and D (Moriguchi et al., 2005) with an integration time of 2.0 s, and provided a Nyquist-sampled 30″ grid dataset. The pointing was checked by observing the Jupiter every two hours and was found to be as accurate as ∼15″. The rms noise fluctuations better than 0.68 K par channel. The ambient temperature load was also employed for the intensity calibration. The absolute intensity was calibrated by observing Oph EW4 [$16^{\rm h}26^{\rm m}21\overset{\rm s}{.}92; -24°25'40\overset{''}{.}4$ (J2000)] (Kulesa et al., 2005).

Observations in ^{12}CO(J=4–3) were carried out from November to December 2007 covering a 9 arcmin^2 region including peak C and toward a point in peak A. The telescope had a beam size of 38″ at 460 GHz as measured by observing Jupiter. The front end was a SIS receiver having SSB temperature of 300 K including the atmosphere toward the zenith. The typical rms noise fluctuations were 0.28 K per channel. The absolute intensity calibration is as described by Pineda et al. (2008).

In addition, we used the ^{12}CO(J=1–0) data at 115 GHz taken with the NANTEN 4-m telescope which were already published in Moriguchi et al. (2005). The angular resolution of the data was 2′.6 (FWHM) and the velocity resolution and rms noise fluctuations are 0.65 km s^{-1} and 0.3 K, respectively. Observations were carried out in the position-switching mode with a 2′ grid spacing (for more detailed information, see also Moriguchi et al., 2005). The ^{12}CO(J=2–1) data were used for comparison with the X-ray images, while the ^{12}CO(J=1–0) data mainly for estimating molecular mass from the integrated ^{12}CO intensity $W(^{12}\mathrm{CO})$ (K km s^{-1}) by using a relationship, $N(\mathrm{H_2}) = X_{\mathrm{CO}} \cdot [W(^{12}\mathrm{CO})$ (K km s^{-1})] (cm^{-2}), where an X_{CO} factor of 2.0×10^{20} (cm^{-2} (K km s^{-1})$^{-1}$) is adopted (Bertsch et al., 1993).

Together with the data above, we made use of the data by Moriguchi et al. (2005). They observed the peaks A, C, and D with the ASTE sub-mm telescope in ^{12}CO(J=3–2) in November, 2004. The data were taken by a position switching mode with a 30″ grid spacing with 23″ beam. The spectrometer was an AOS with 450 km s^{-1} band width and 0.43 km s^{-1} resolution. The system temperature was 300–400 K (DSB) and the typical rms achieved is 0.4–0.9 K with 30 s integration.

These observed areas are shown in Figure 2.1.

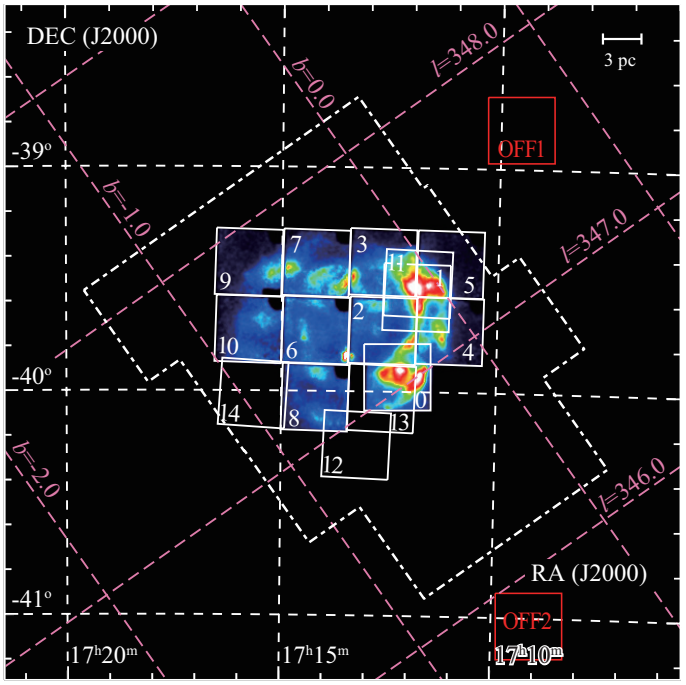

FIGURE 2.1: *Suzaku* FoV of each observation toward RX J1713.7−3946 overlaid on the *Suzaku* XIS 0+2+3 mosaic image (1–5 keV) taken from Tanaka et al. (2008). The small squares correspond to the FoV of the XIS. The numbers indicated in the XIS FoV are pointing IDs used throughout this paper (see also Table 2.1). We also show the observed area in the ^{12}CO(J=1–0, 2–1, 3–2, 4–3) and ^{13}CO(J=2–1) enclosed by the white, red, green, yellow, and orange dash-dotted lines, respectively.

2.2.2 HI

The 21 cm HI spectral data were taken from the Southern Galactic Plane Survey (SGPS; McClure-Griffiths et al., 2005) with the Australia Telescope Compact Array (ATCA) combined with the 64-m Parkes Radio Telescope. The combined beam size and the grid spacing of the dataset are 2′.2 and 40″, respectively. The velocity resolution and typical rms noise fluctuations were 0.82 km s^{-1} and 1.9 K, respectively. We applied the correction for the HI self-absorption by following the previous analysis of the cold HI gas without CO emission (see Chapter 3.3.3.3).

2.2.3 X-rays

We used *Suzaku* archive data of RX J1713.7−3946 taken from Data Archives and Transmission System (DARTS at ISAS/JAXA). The observations performed 15 pointings toward the main features and 2 OFF pointings of RX J1713.7−3946 and were published by Takahashi et al. (2008) and Tanaka et al. (2008) expect for the 4 pointings observed in 2010 February. Previous and current observations are summarized in Table 2.1, and the FoV of each observation is shown in Figure 2.1. Active detector systems aboard the *Suzaku* satellite are the X-ray Imaging Spectrometer (XIS; Koyama et al., 2007) and the Hard X-ray Detector (HXD; Takahashi et al., 2007). The XIS consists of four CCD cameras placed at the foci of X-ray Telescopes (XRTs; Serlemitsos et al., 2007). We analyzed only XIS data in the present paper. The spaced-row charge injection (SCI; Nakajima et al., 2008; Uchiyama et al., 2009) was used in the latter 4 pointings (see also Table 2.1). Unfortunately, XIS 2 was on closed access since 2006 November 9, possibly owing to a micrometeorite damage. XIS 0 showed an anomaly in Segment A on 2009 June 23. Thus, for the data in the latter 4 pointings we used XIS 0 (expect for Segment A), XIS 1 and XIS 3. We used "cleaned event files" processed and screened by versions 2.0 or 2.4 *Suzaku* pipeline depending on observation dates. First, we created the photon count images from the cleaned event files in the energy bands 1–5 keV and 5–10 keV. Here, we subtracted the non X-ray background (NXB) using **xisnxbgen**, which estimates NXB count rate based on night Earth observation data. Then, we corrected for XRT vignetting effects by simulating flat field images with **xissim** (Ishisaki et al., 2007). Additionally, we masked the region of ^{55}Fe calibration sources in the energy band 5–10 keV. Finally, we smoothed the images by using a Gaussian kernel with a FWHM of 45″. We performed data reduction with the version 6.11 of the HEAsoft tools.

TABLE 2.1: Summary of the *Suzaku* archive data of RX J1713.7−3946

Pointing ID	ObsID	α_{J2000} (h m s)	δ_{J2000} (° ′ ″)	XIS Exp. (ks)	Date	SCI
0.....	100026010	17 12 17.0	−39 56 11	69	2005 September 26	OFF
1.....	501063010	17 11 51.5	−39 31 13	18	2006 September 11	OFF
2.....	501064010	17 12 38.0	−39 40 14	21	2006 September 11	OFF
3.....	501065010	17 12 38.2	−39 22 15	22	2006 September 11	OFF
4.....	501066010	17 11 04.5	−39 40 10	21	2006 September 12	OFF
5.....	501067010	17 11 05.1	−39 22 10	21	2006 September 12	OFF
6.....	501068010	17 14 11.6	−39 40 14	21	2006 September 13	OFF
7.....	501069010	17 14 11.4	−39 22 15	18	2006 September 19	OFF
8.....	501070010	17 14 11.8	−39 58 14	21	2006 September 19	OFF
9.....	501071010	17 12 17.6	−39 18 50	21	2006 September 20	OFF
10.....	501072010	17 15 44.5	−39 40 10	20	2006 October 5	OFF
11.....	504027010	17 11 50.8	−39 31 00	62	2010 February 15	ON
12.....	504028010	17 13 14.0	−40 14 22	19	2010 February 16	ON
13.....	504029010	17 12 39.8	−40 01 50	21	2010 February 17	ON
14.....	504030010	17 15 39.0	−40 00 47	22	2010 February 17	ON
OFF1.....	100026020	17 09 31.9	−38 49 24	35	2005 September 25	OFF
OFF2.....	100026030	17 09 05.1	−41 02 07	38	2005 September 28	OFF

Notes. The details of pointing ID from 0 to 10, OFF1 and OFF2 are also shown in Takahashi et al. (2008) and Tanaka et al. (2008)..

2.3 Analysis

2.3.1 Large-scale CO, HI, and X-ray distributions

Figure 2.2 shows mosaic images of RX J1713.7−3946 which were constructed by using the data from XIS 0+1+2+3. Figures 2.2a and 2.2b show the soft band (1–5 keV) and hard band (5–10 keV) images, respectively. The unit for the images is 10^{-4} counts s^{-1} $pixel^{-1}$, and the pixel size is $\sim$16.7″. We find that the soft- and hard-band images are very similar with each other, which is already discussed in the previous study by Tanaka et al. (2008). Figure 2.2 shows the western rim clearly as well as several peaks of $\sim 10 \times 10^{-4}$ counts s^{-1} $pixel^{-1}$ in the northern rim and inside the SNR. In the soft band image, thick white circles indicate locations of the two bright point-like sources toward the inner part of the SNR. The left one is associated with a Wolf-Rayet star CD−39 11212B (Pfeffermann & Aschenbach, 1996), which corresponds to two X-ray point sources cataloged (1WGA J1714.4−3945 and EXO 1710−396; see also Table 2.2). The other one is thought to be a neutron star because of its X-ray spectral characteristics (Lazendic et al., 2003), which is cataloged as an X-ray point source (1WGA J1713.4−3949) and a pulsar (PSR J1713−3949). We also showed the modified color scale image in the energy band 1–5 keV, which enhances the regions of the low photon counts $\sim 7 \times 10^{-4}$ counts s^{-1} $pixel^{-1}$.

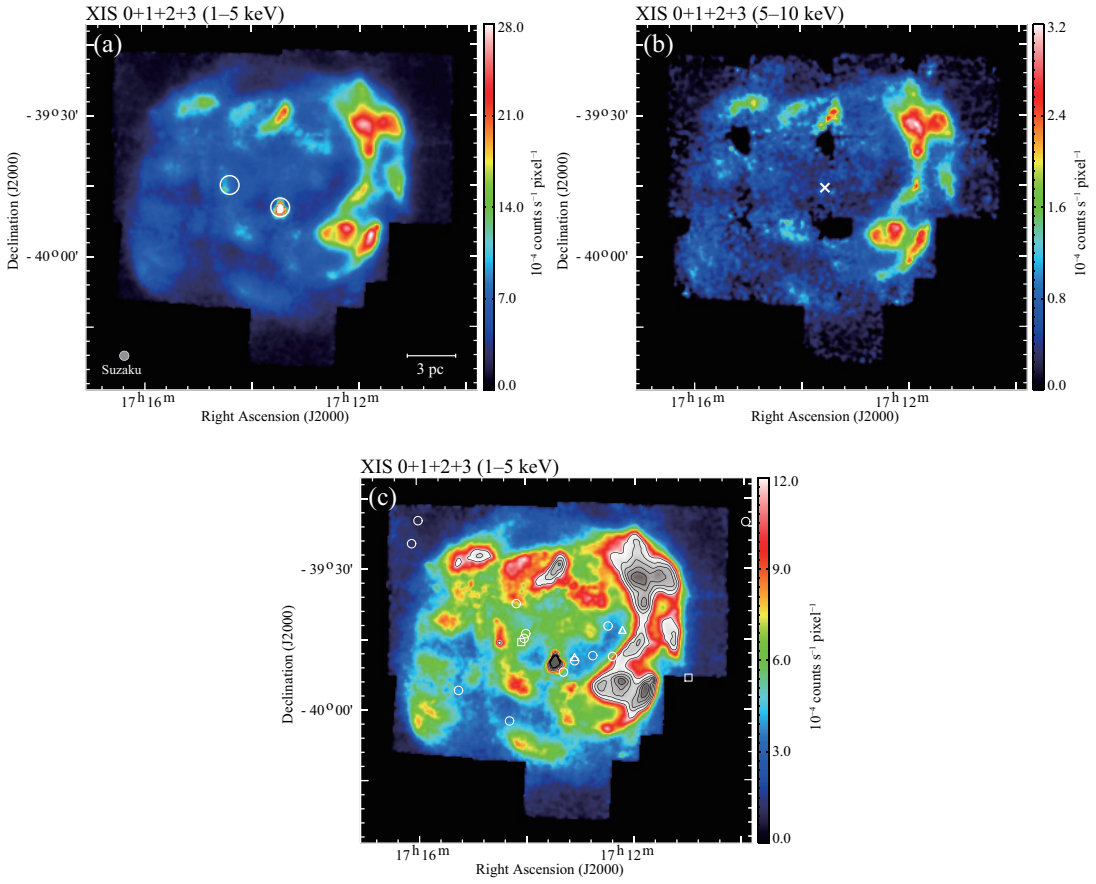

FIGURE 2.2: *Suzaku* XIS (XIS 0+1+2+3) mosaic images of RX J1713.7−3946 in the energy bands (a) 1–5 keV and (b) 5–10 keV. The color scale indicates the count rate on a linear scale. The color bar numbers are in units of 10^{-4} counts s^{-1} $pixel^{-1}$ with a pixel size of $\sim$16.7″. Both images are smoothed with a Gaussian kernel with FWHM of 45″. The positions of the two point-like sources are shown with large circles in (a) (see Table 2.2). (c) Same XIS mosaic image (1–5 keV) as (a), but the color scale is changed to emphasize the region of low photon counts below 12×10^{-4} counts s^{-1} $pixel^{-1}$. Above this level shown in gray scale, the lowest contour level and the contour interval are 12 and 4×10^{-4} counts s^{-1} $pixel^{-1}$, respectively. The small circles, triangles and squares show the position of seven X-rays point source, three pulsars and two Wolf-Rayet stars, respectively.

In addition to the localized peaks in X-rays, we find diffuse X-ray emission is extended inside the SNR. In order to estimate the level of this background X-rays in the 1–5 keV X-ray image, we show two histograms of the X-ray counts in Figure D1 (see Appendix D); one is for the whole region observed with *Suzaku* (Figure 2.1) and the other for the nine circles of 6-arcmin diameter without significant peaks inside the SNR (Figure D1). In the histogram inside the SNR, we find a peak at $\sim 3.86 \times 10^{-4}$ counts s^{-1} $pixel^{-1}$ and identify this level as the background within the SNR. On the other hand, we consider that a primary peak at $\sim 1.16 \times 10^{-4}$ counts s^{-1} $pixel^{-1}$ for the whole region indicates the background level outside the SNR. In Figure 2.2c we plotted the positions of the X-ray point sources, pulsars and Wolf-Rayet stars (Table 2.2) in order to test whether the X-ray distribution is influenced by these point sources. We see no excess toward

TABLE 2.2: Summary of the X-ray point sources toward RX J1713.7−3946

Name	$\alpha_{\rm J2000}$ (h m s)	$\delta_{\rm J2000}$ (° ′ ″)	Source Type	Ref.
WR 84	17 11 21.70	−39 53 22.2	Wolf-Rayet star†	1
CD−39 11212B	17 14 27.129	−39 45 47.25	Wolf-Rayet star	2
PSR J1712−3943A	17 12 35.0	−39 43 14	pulsar	3
PSR J1712−3943B	17 12 35.0	−39 43 14	pulsar	3
PSR J1713−3949	17 13 28	−39 49.0	pulsar†	4
EXMS B1709−397A	17 12 46	−39 48.9	X-ray point source	5
GPS 1709−396	17 12 51.0	−39 42 25	X-ray point source	6
EXMS B1709−397B	17 13 08	−39 48.7	X-ray point source	5
1WGA J1713.4−3949	17 13 28	−39 49.8	X-ray point source†	4, 7
CXOPS J171340.5−395213	17 13 40.5	−39 52 13	X-ray point source	8
EXO 1710−396	17 14 22	−39 44.0	X-ray point source‡	9
1WGA J1714.4−3945	17 14.4	−39 45	X-ray point source‡	10, 11

Notes. † and ‡ sources are connected with two X-ray point-like sources shown in Figure 2.2, respectively. (1) van der Hucht, 2001; (2) Cutri et al., 2003; (3) Burgay et al., 2006; (4) (Lazendic et al., 2003); (5) Reynolds et al., 1999; (6) Gottwald et al., 1995; (7) Landt & Bignall, 2008; (8) van den Berg et al., 2012; (9) Lu et al., 1996; (10) Slane et al., 1999; (11) Pfeffermann & Aschenbach, 1996.

the point sources in Figure 2.2c except for the two bright point-like sources marked in Figure 2.2a, and consider that X-ray features inside the SNR are not due to the point sources but are intrinsic to the SNR.

Figure 2.3 shows four overlays of the ^{12}CO(J=2–1) distribution and X-ray images in the two energy bands 1–5 keV (Figures 2.3a and 2.3b) and 5–10 keV (Figures 2.3c and 2.3d), respectively. A $V_{\rm LSR}$ range of CO from −20.2 to −9.1 km s^{-1} is shown in Figures 2.3a and 2.3c and that from −9.1 to 1.8 km s^{-1} in Figures 2.3b and 2.3d. These velocity ranges correspond to that of the interacting molecular gas (Fukui et al., 2012). Figure 2.3 indicates that CO and X-rays show a good correlation at a pc scale as already noted by Moriguchi et al. (2005). It is remarkable that most of the X-ray features are found toward CO clumps. The most outstanding X-rays are seen in the west of the shell, where the strongest CO emission is located (Figures 2.3b and 2.3d), and the second brightest X-rays are in the north of the shell where CO emission is also distributed (Figures 2.3a and 2.3c). The southern part of the CO emission appears to delineate the southern rim of the SNR (Figures 2.3b and 2.3d), while the eastern shell with weak X-rays has only a few small CO features (Figures 2.3b and 2.3d).

The CO distribution is highly clumpy. In order to make a detailed comparison with the X-rays, we cataloged CO clumps in the ^{12}CO(J=1–0) data in Figure A1 in Appendix A. We identified 22 CO clumps in total, which are selected by the following two criteria in the ^{12}CO(J=1–0) data; (1) the peak position is located within SNR boundary, (2) the peak brightness temperature is higher than 1 K, and (3) the total clump surface area defined as the region surrounded by the contour at half of the maximum integrated

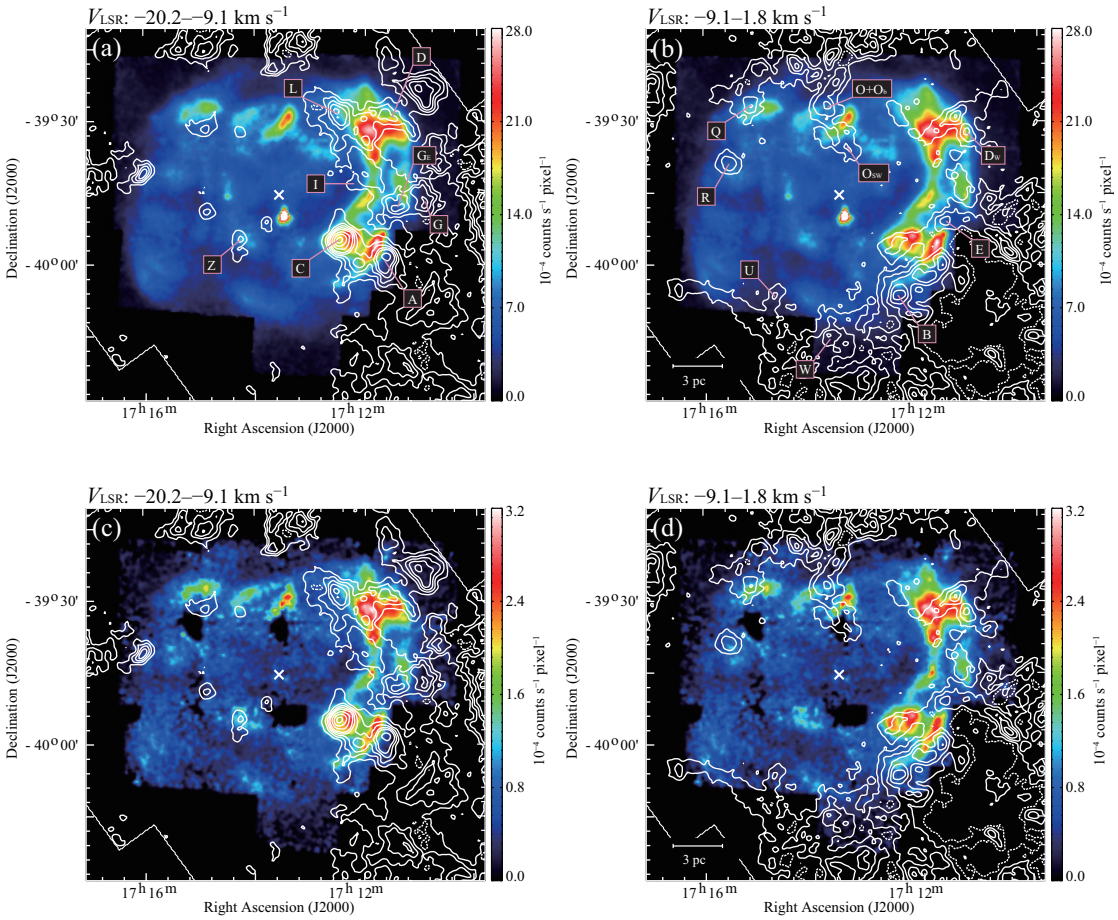

FIGURE 2.3: Pair of ^{12}CO(J=2–1) velocity channel maps (*white contours*) superposed on the *Suzaku* XIS mosaic image in two energy bands (a, b: 1–5 keV and, c, d: 5–10 keV) in color scale. The velocity ranges are (a, c) −20.2–−9.1 km s^{-1} and (b, d) −9.1–1.8 km s^{-1}, respectively. The lowest contour level and the contour interval of CO are 3.1 K km s^{-1} ($\sim 3\sigma$) in (b) and (d). In (a) and (c), the contour level are 3.1, 6.2, 9.3, 12.4, 15.5, 21.7, 27.9, 31.0 K km s^{-1}. The CO clumps discussed in Chapter 2.3.2 are indicated in the figure.

intensity is larger than a 3-beam area. We give their observed parameters in ^{12}CO(J=1–0) and ^{12}CO(J=2–1) in Table 2.3. 13 of them are identified either by Fukui et al. (2003) or Moriguchi et al. (2005). The rest of the clumps are newly identified in the present work. Most of the CO clumps have a single velocity component of line width $\sim$ 3–5 km s^{-1}. Only clump O (Moriguchi et al., 2005) has two velocity components of $\sim$7.5 km s^{-1} separation, and is divided into two clumps O and O_b. Five of them D_W, G_E, O_b, O_{SW} and Z have molecular mass higher than 50 $M_\odot$ (see also Table 2.3), and four of them C_E, Q_W, Z_{NW} and Z_{NE} have molecular mass less than 50 $M_\odot$. We focus hereafter on the 18 CO clumps which have molecular mass greater than 50 $M_\odot$ as shown in Figure 2.3, so that derivation of the physical parameters is ensured for a quantitative comparison with the X-rays (Chapter 2.2.3). Except for the five clumps C, I, L, O_{SW} and Z, which are located inside of the SNR boundary, most of the CO clumps (A, B, D, D_W, E, G, G_E, O, O_b, Q, R, U and W) are distributed on the outer boundary of the SNR shell.

TABLE 2.3: Properties of CO Clumps

Name	^{12}CO(J=1–0)						^{12}CO(J=2–1)					
	$\alpha_{\rm J2000}$ ($^{\rm h}$ $^{\rm m}$ $^{\rm s}$)	$\delta_{\rm J2000}$ ($^\circ$ $'$ $''$)	$T_{\rm R^*}$ (K)	$V_{\rm peak}$ (km s^{-1})	$\Delta V_{\rm LSR}$ (km s^{-1})	Mass ($M_\odot$)	$\alpha_{\rm J2000}$ ($^{\rm h}$ $^{\rm m}$ $^{\rm s}$)	$\delta_{\rm J2000}$ ($^\circ$ $'$ $''$)	$T_{\rm R^*}$ (K)	$V_{\rm peak}$ (km s^{-1})	$\Delta V_{\rm LSR}$ (km s^{-1})	
(1)	(2)	(3)	(4)	(5)	(6)	(7)	(8)	(9)	(10)	(11)	(12)	
A.....	17 11 35.9	−39 59 01.8	8.5	−10.3	4.8	686	17 11 38.4	−39 58 46.9	6.6	−10.0	4.5	
B.....	17 12 26.5	−40 06 06.3	4.2	−8.0	4.6	190	17 12 26.8	−40 05 55.5	3.3	−8.1	4.5	
C.....	17 12 25.9	−39 56 04.4	9.4	−12.0	3.8	397	17 12 27.0	−39 54 58.0	7.5	−11.9	4.6	
C$_{\rm E}$.....	17 13 01.3	−39 53 35.2	1.1	−9.1	1.6	10	17 12 57.4	−39 53 42.3	3.7	−8.8	1.4	
D.....	17 11 28.0	−39 30 37.6	4.0	−11.1	4.8	292	17 11 32.5	−39 30 03.9	3.3	−9.3	4.8	
D$_{\rm W}$.....	17 11 01.3	−39 34 17.6	2.3	2.4	3.3	137	17 11 34.3	−39 32 31.2	3.1	−1.1	6.0	
E.....	17 11 29.1	−39 50 38.5	2.0	−6.1	7.2	159	17 11 55.4	−39 51 07.2	2.0	−6.0	5.0	
G.....	17 10 55.6	−39 45 55.2	3.3	−10.8	8.0	307	17 10 56.3	−39 45 20.6	2.8	−11.5	4.8	
G$_{\rm E}$.....	17 11 27.1	−39 47 49.6	5.4	−12.8	2.6	168	17 11 21.0	−39 47 24.4	4.3	−12.3	2.7	
I.....	17 12 08.2	−39 43 43.3	1.8	−9.9	5.4	103	17 12 16.6	−39 43 22.8	1.3	−10.4	5.9	
L.....	17 12 25.8	−39 28 53.4	4.0	−12.0	5.7	370	17 12 30.2	−39 28 14.6	3.2	−11.7	6.0	
O.....	17 13 46.7	−39 27 49.8	1.1	−6.4	4.9	61	17 13 46.0	−39 26 28.6	1.2	−4.6	4.7	
O$_{\rm b}$.....	17 13 46.7	−39 27 49.8	1.9	1.1	3.4	80	17 13 46.0	−39 26 28.6	1.9	1.0	3.8	
O$_{\rm SW}$....	17 13 24.8	−39 37 08.6	2.8	−1.6	2.0	60	17 13 08.9	−39 36 43.2	3.5	−1.3	1.3	
Q.....	17 15 13.4	−39 25 06.2	2.9	−2.8	3.2	108	17 15 11.7	−39 26 47.4	2.8	−2.2	2.8	
Q$_{\rm W}$.....	17 14 49.3	−39 31 35.1	3.0	−14.3	2.4	46	17 14 53.0	−39 31 30.7	3.7	−14.1	1.8	
R.....	17 15 39.9	−39 38 34.6	4.1	−3.3	2.4	67	17 15 32.0	−39 39 28.5	3.2	−3.1	2.2	
U.....	17 14 34.2	−40 06 27.0	3.7	−4.8	1.3	58	17 14 13.4	−40 06 25.2	3.0	−4.6	1.3	
W.....	17 13 42.8	−40 16 40.7	5.0	−5.1	3.0	402	17 13 30.0	−40 15 03.6	3.3	−4.9	3.4	
Z.....	17 14 18.7	−39 56 55.1	2.6	−20.1	2.7	72	17 13 53.3	−39 54 46.8	2.9	−19.8	2.9	
Z$_{\rm NW}$....	17 13 45.0	−39 52 14.9	3.0	−19.8	2.6	36	17 13 45.6	−39 51 09.2	5.1	−19.8	1.8	
Z$_{\rm NE}$.....	17 14 57.4	−39 49 59.3	2.2	−20.0	3.3	31	17 14 53.3	−39 49 25.7	3.6	−19.6	2.5	

Notes. Col. (1): Clump name. Cols. (2–7) and (8–12): Observed properties of the ^{12}CO(J=1–0, 2–1) spectra obtained at the peak positions of the CO clumps. Cols. (2)–(3): Position of the peak CO intensity. Col. (4): Peak radiation temperature $T_{\rm R^*}$. Col. (5): $V_{\rm peak}$ derived from a single Gaussian fitting. Col. (6): FWHM line width $\triangle V_{\rm LSR}$. Col. (7): Total mass of the clumps derived by using the relation between the molecular hydrogen column density $N({\rm H_2})$ and the ^{12}CO(J=1–0) intensity $W(^{12}{\rm CO})$, $N({\rm H_2}) = 2.0 \times 10^{20} [W(^{12}{\rm CO})$ (K km s^{-1})] (cm^{-2}) (Bertsch et al., 1993). See also the text for more details. Cols. (8–12): The observed properties same with Cols. (2–6) for the ^{12}CO(J=2–1) spectra. The properties of A–C, D, E, G, I–O, Q and R–W derived from ^{12}CO(J=1–0) are shown by Moriguchi et al. (2005).

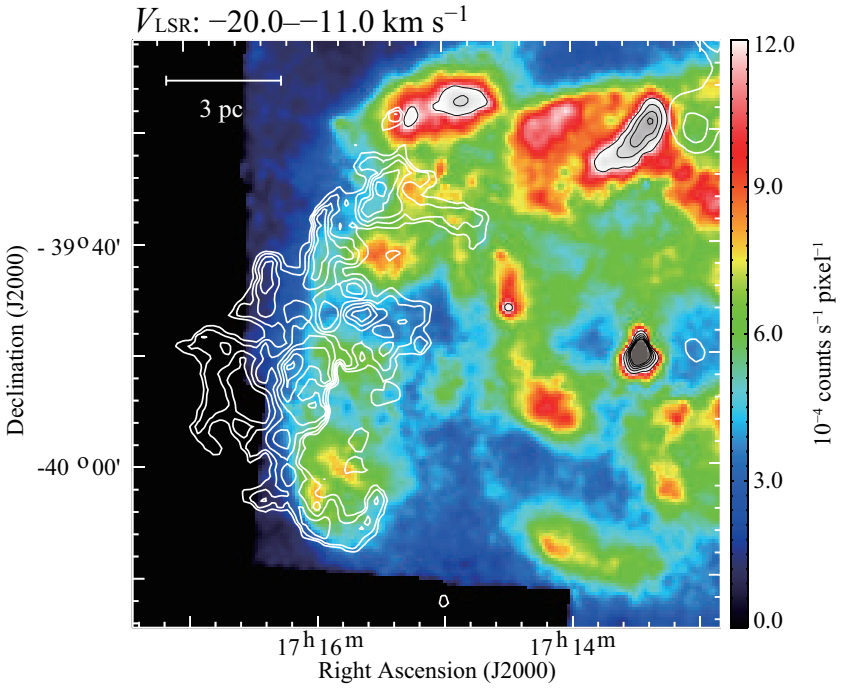

FIGURE 2.4: Same XIS mosaic image (1–5 keV) as Figure 2.2 (c) toward the the SE-rim. The white contours indicate the distribution of HI proton column density (self-absorption corrected; see also the text and Paper II). The lowest contour level and the contour interval in HI proton column density are 2.0 and 0.1 × 10^{21} cm^{-2}, respectively. The velocity range is −20.0–−11.0 km s^{-1}.

Finally, we compare the cold HI gas without CO with the X-rays in the southeast-rim of the SNR (hereafter SE-rim; see Chapter 3.3.3.3). The cold HI gas has density around 100 cm^{-3} and is likely interacting with the shock in a similar way to CO. Figure 2.4 shows an enlarged view in the SE-rim overlaid with the HI proton column density contours. The integration range is −20.0–−11.0 km s^{-1}. We apply the HI self-absorption by following the analysis in Chapter 3.3.3.3. The lowest contour level and the contour interval in the HI proton column density are 2.0 × 10^{21} cm^{-2} and 0.1 × 10^{21} cm^{-2}, respectively. It is remarkable that the HI distribution corrected for the self-absorption is complementary to the X-ray peaks in the low-photon-count region in the SE-rim.

2.3.2 Detailed Comparison with the X-Rays

We here make a detailed comparison of spatial distributions between CO/HI clumps and X-rays in images, radial and azimuthal distributions (Figures 2.5, 2.7 and 2.8).

In Figure 2.5 left and middle panels of each row, we show the images of the CO integrated intensity overlaid on the distributions of the soft (1–5 keV, left) and hard (5–10 keV, middle) X-rays. The crosses in each image indicate the center of gravity of the CO

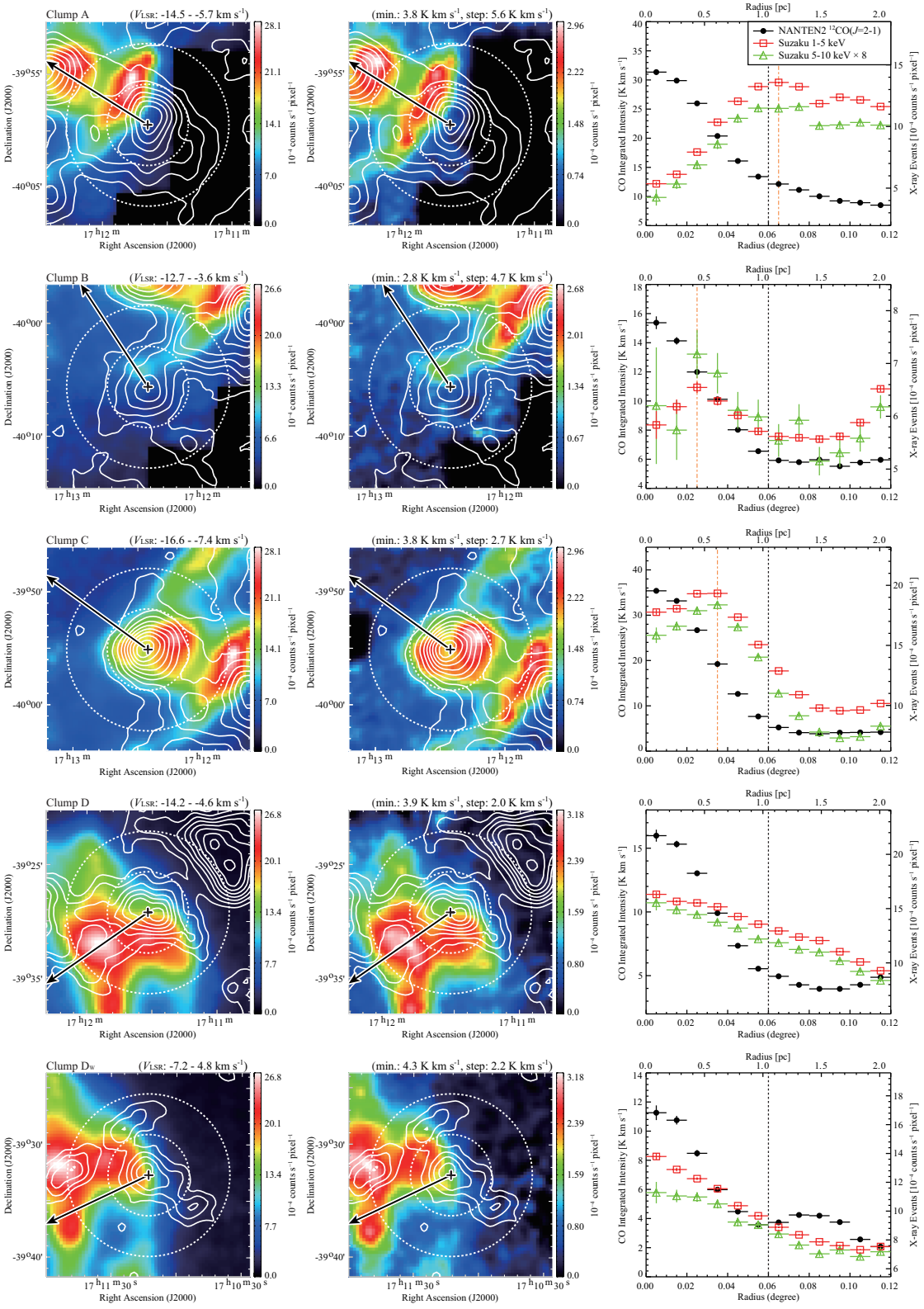

FIGURE 2.5: Distribution of ^{12}CO(J=2–1) emission (*white contours*) superposed on the *Suzaku* 1–5 keV (left) and 5–10 keV (right) images. Velocity range in integration and contour levels are shown in the top of left and middle panels, respectively. Each arrow indicates the direction of the center of the SNR. The crosses show the position of the center of gravity for each CO clump (see also Table 2.4). The dashed white circles represent radii 0.°06 and 0.°12 of the center of gravity for each CO clump. Right panels show the radial profiles around each molecular clump in the ^{12}CO(J=2–1) integrated intensity and *Suzaku* two energy bands (1–5 keV and 5–10 keV, in units of 10^{-4} counts s^{-1} pixel^{-1}) in Figure 2.2. The radial profiles from the 5–10 keV band has been scaled such that it has the same area as the 1–5 keV profile (scaled by a factor 8), for the sake of direct comparison. The orange dash-dotted lines indicate X-ray peak radius in the energy band 1–5 keV.

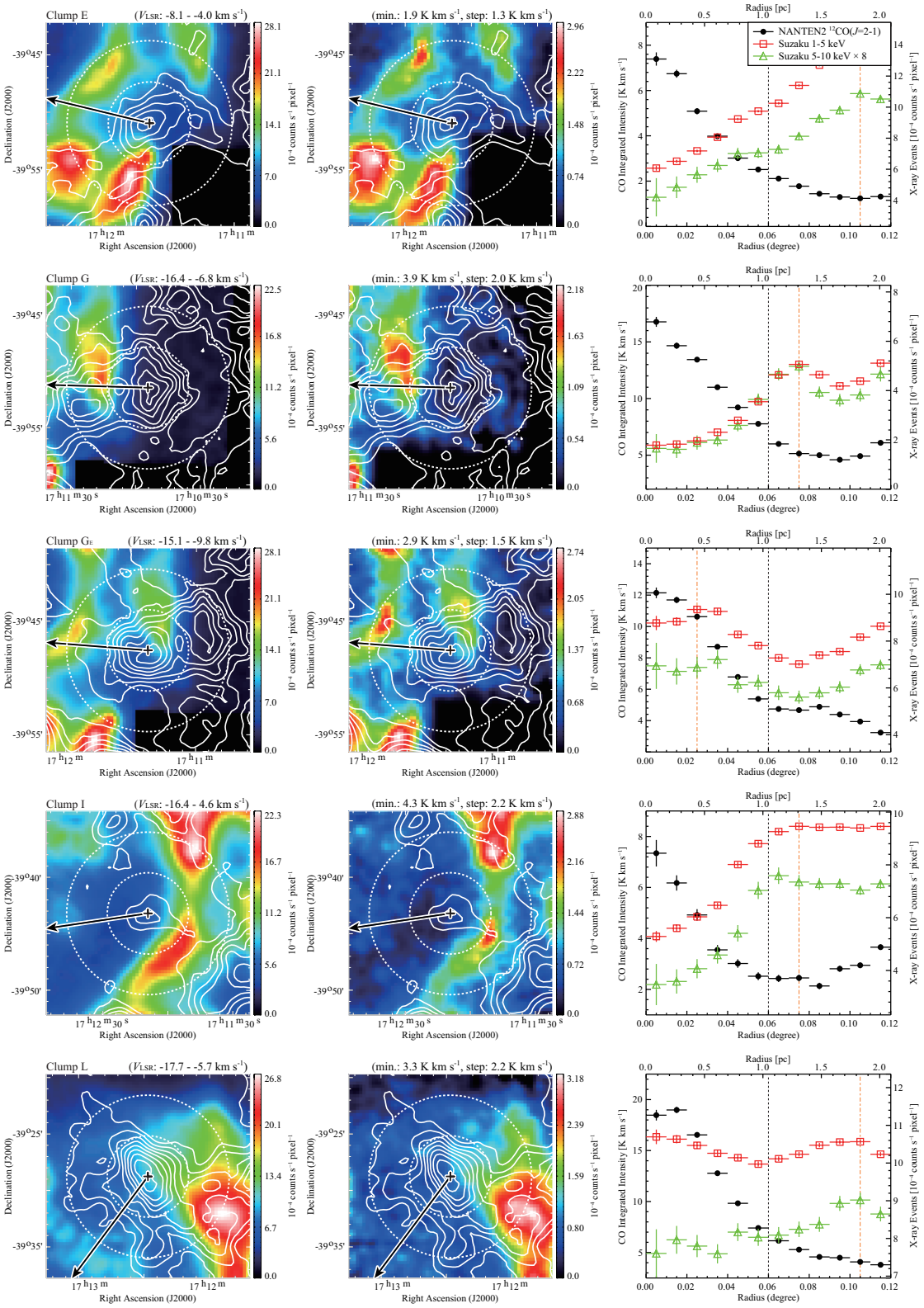

FIGURE 2.5: *continued.*

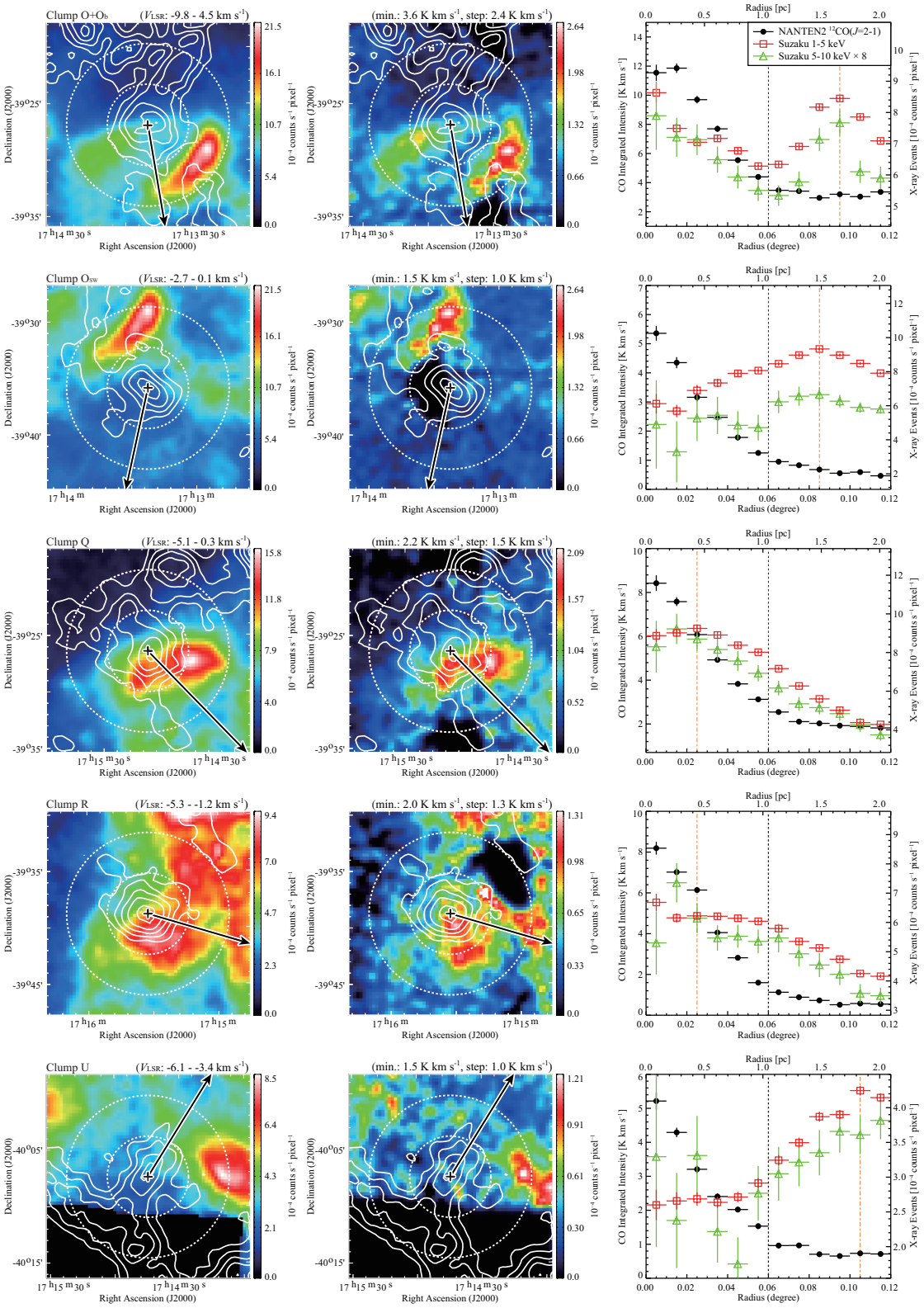

FIGURE 2.5: *continued.*

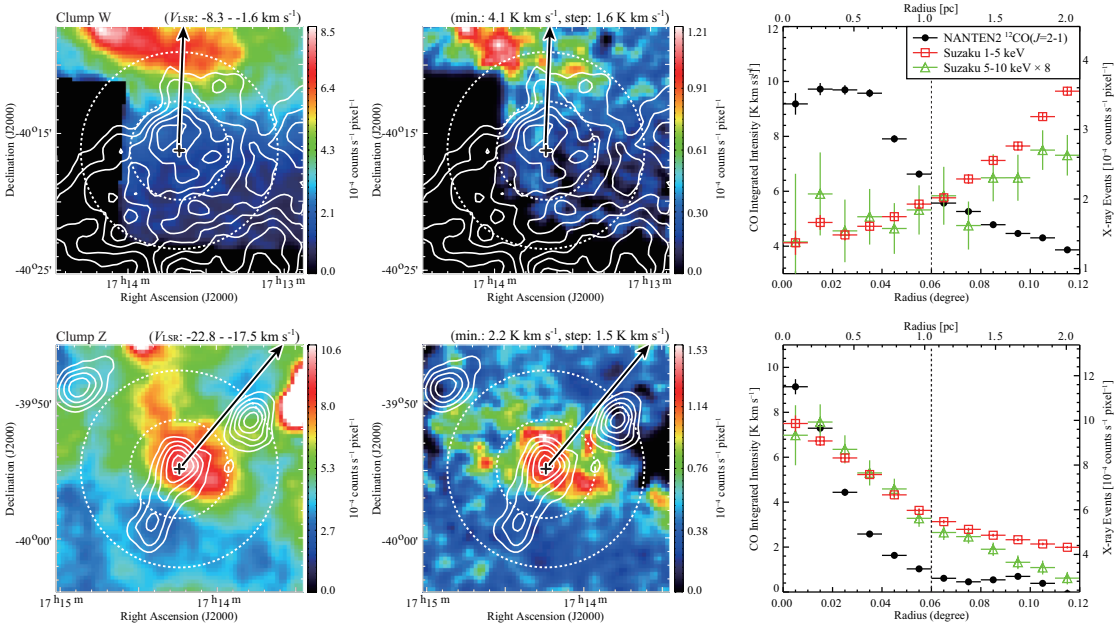

FIGURE 2.5: *continued.*

clumps listed in Table 2.4, which is somewhat different from the peak position in Table 2.2, and each arrow indicates the direction of the center of the SNR. The dashed white circles represent radii 0.°06 and 0.°12 of the center of gravity. We see a trend that the X-rays are enhanced toward the CO, while the CO peak generally shows offsets from the X-ray peak.

In Figure 2.5 right panels, we plot radial profiles of the CO integrated intensity and X-ray counts averaged at each radius for the 1–5 keV and 5–10 keV bands. In order to characterize quantitatively the radial distribution, we first identify the peak in the 1–5 keV radial distribution. In addition, we defined the separation from the center of gravity of CO clump to the X-ray peak in the radial distribution. 10 of the 17 clumps have peaks of the X-rays and positive X-ray slopes inside the peak in Figure 2.5. Clump W has no peak but also shows a clear positive X-ray slope. On the other hand, four of the CO clumps show negative slope and the other one show nearly flat slope. The radial distributions of the X-rays are generally smooth and monotonic so that linear approximation is reasonable in estimating the intensity gradients. Only the CO clumps O+O$_b$ show a complicated non-monotonic radial distribution of the X-rays, which may be due to blending of the two velocity components. We made least-squares fit to the X-rays by a straight line for simplicity for the 10 clumps within the peak, and for clump W and the other six clumps within a radius of 0.06 degrees. The values of the slope are listed in Table 2.5, and are shown as a histogram in Figure 2.6. 12 of the 16 clumps (75%) show positive slopes in the X-rays, indicating that the X-rays show decrease toward the

TABLE 2.4: Results of Radial and Azimuthal Distribution

Name	α_{J2000} (h m s)	δ_{J2000} (° ′ ″)	V_{LSR} (km s^{-1})	Radius (degree)	Separation (degree)	Peak Intensity ($\times10^{-4}$ counts s^{-1} pixel)	Angle (Fraction) (degree), (%)	Interacting Mass ($M_\odot$)
(1)	(2)	(3)	(4)	(5)	(6)	(7)	(8)	(9)
A.....	17 11 39.1	−39 59 22.2	−14.5– −5.7	0.050	0.065	18.50±0.07	−120–+120, (67)	460±60
B.....	17 12 25.3	−40 05 37.5	−12.7– −3.6	0.050	0.025	10.88±0.05	−150– +90, (67)	130±20
C.....	17 12 25.3	−39 55 07.4	−16.6– −7.4	0.040	0.035	19.64±0.07	−180–+180, (100)	400±30
D.....	17 11 31.9	−39 29 13.6	−14.2– −4.6	0.040	···	22.25±0.07	−150–+150, (83)	240±20
D$_W$.....	17 11 12.8	−39 32 43.5	−7.2– 4.8	0.040	···	21.18±0.07	−120– +90, (58)	80±11
E.....	17 11 38.7	−39 50 56.8	−8.1– −4.0	0.040	0.105	19.81±0.07	−180–+180, (100)	159±13
G.....	17 10 54.5	−39 46 25.7	−16.4– −6.8	0.050	0.075	11.81±0.09	−60– +60, (33)	100±30
G$_E$.....	17 11 22.2	−39 47 34.0	−15.1– −9.8	0.050	0.025	13.16±0.13	−150–+150, (83)	140±14
I.....	17 12 09.3	−39 43 11.9	−16.4– −4.6	0.030	0.075	14.22±0.07	−180–+180, (100)	103± 9
L.....	17 12 28.2	−39 28 45.9	−17.7– −5.7	0.045	0.105	19.91±0.07	−180–+180, (100)	370±30
O.....	17 13 48.9	−39 26 24.9	−11.3– −1.6	0.055	0.095	14.02±0.14	−120–+120, (67)	41± 5
O$_b$.....	17 13 46.9	−39 26 45.9	−4.6– 2.2	0.035	0.085	13.92±0.14	−120–+120, (67)	53± 7
O$_{SW}$.....	17 13 22.4	−39 35 50.6	−2.7– 0.1	0.030	0.085	14.5 ±0.2	−180–+180, (100)	60± 5
Q.....	17 15 09.6	−39 38 48.7	−5.1– 0.3	0.040	0.025	10.83±0.12	−150–+120, (75)	81± 9
R.....	17 15 32.4	−39 39 28.5	−5.3– −1.2	0.035	0.025	6.7 ±0.2	−150–+150, (83)	56± 6
U.....	17 14 44.5	−40 07 24.4	−6.1– −3.4	0.030	0.105	5.54±0.07	−90– 0, (25)	15± 5
W.....	17 13 40.2	−40 16 16.9	−8.3– −1.6	0.080	···	4.58±0.07	−30– +30, (17)	70±30
Z.....	17 14 14.3	−39 54 55.7	−22.8–−17.5	0.025	···	3.60±0.06	−150–+180, (92)	66± 6
HI SE-rim.....	17 16 09.3	−40 03 10.6	−20.0–−11.0	···	···	6.97±0.09	−90– +60, (42)	56±11
O+O$_b$.....	17 13 49.7	−39 26 54.9	−9.8– 4.5	0.040	0.095	14.03±0.14	−120–+120, (67)	94± 8
D+D$_W$.....	···	···	···	···	···	21.72±0.05	···	320±30
O+O$_b$+O$_{SW}$.	···	···	···	···	···	14.19±0.09	···	154±10
G+G$_E$.....	···	···	···	···	···	12.49±0.08	···	240±30
E+I.....	···	···	···	···	···	17.02±0.05	···	260±20

Notes. Col. (1): Clump name. Cols. (2)–(3): Position of the center of gravity with the ^{12}CO(J=2–1) integrated intensity (except for the SE-rim). Cols. (4): Integration range in velocity for the estimation of the ^{12}CO(J=2–1) or HI. (5): Radius of a CO clump defined as the radial distance from the center of gravity of a CO clump to the point where the intensity is at half maximum. (6) Separation of the X-ray peak from the center of gravity of each CO/HI clump. (7) X-ray peak intensity with the statistical error around each clump shown in Figure 2.8. (8) Azimuth angle range of the X-rays (1–5 keV) above the background level estimated in the Appendix A (see also Section 2.3.1). (9) Interacting clump mass defined as the total CO/HI mass within the azimuth angle range of the X-rays (1–5 keV) for each clump..

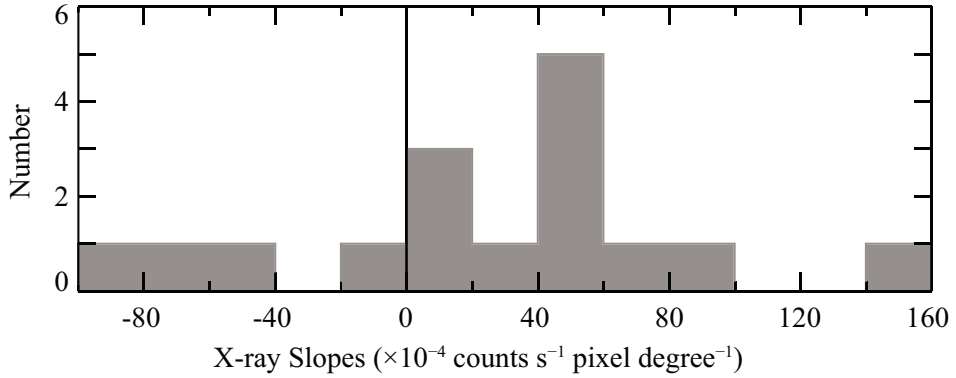

FIGURE 2.6: Histogram of the X-ray slope estimated by a linear fitting in the radial profile for each CO clump. The fitting ranges and results are shown in Table 2.5.

CO clump and are brightened in the surroundings of the CO clump. For the remaining 4 with negative or flat slopes except for clump Z, we also find clear relative enhancement of the X-rays in the surroundings of the CO clumps (in Figure 2.5 left and middle panels). Clump Z has no clear X-ray depression toward the center, while enhanced X-rays are seen in its surroundings (Figure 2.5 left and middle panels in the last low). We conclude that the enhanced X-rays around CO clumps are a general trend among the CO clumps, as is consistent with the previous result on clump C (Paper I). We note that the averaged behavior is that the CO clumps have a radius of 0.04 ± 0.01 degrees and the X-rays are distributed with a separation 0.07 ± 0.03 degrees from the center of each clump (see also Table 2.4).

In addition, we made a similar analysis on the cold HI in the SE-rim. The HI distribution estimated from self-absorption well delineates the outer boundary of the X-rays (Figure 2.7), and their relative distributions are similar to the case of clump A. The HI column density distribution is fairly flat having no clear peak. Instead of using the HI peak, we here draw a line passing through the center of the SNR and the soft X-ray peak, and define the HI column density peak on this line. The radial distributions are plotted centered on this HI peak. We find a trend similar to the CO clumps that the X-rays are clearly enhanced around the cold HI.

In Figure 2.8 top three panels show the same XIS mosaic images (1–5 keV) as in Figure 2.2c. The lines connecting the CO/HI clump positions (shown in Figures 2.5, 2.7 and Table 2.4) and the center of the SNR (l, b) = (347.°3, −0.°5) or ($\alpha_{\rm J2000}$, $\delta_{\rm J2000}$) = ($17^{\rm h}$ $13^{\rm m}$ $34^{\rm s}$, −39° 48′ 17″) are taken as the origins of the azimuth angle, which is measured counterclockwise. The azimuthal angular distribution of the X-rays around each CO/HI clump is estimated with respect to the direction of the center of the SNR. We measured the azimuthal angular extent of the X-rays in each clump in the 1–5 keV band image by adopting the background level inside the SNR as the threshold (Section 2.3.1). The results are shown in Figure 2.8 and Table 2.4. Figure 2.9 upper panel shows the range

TABLE 2.5: Fitting Results of the X-rays Radial Distribution

Name	Fitting Range (degree)	Slope ($\times 10^{-4}$ counts s^{-1} pixel degree^{-1})	Comments
(1)	(2)	(3)	(4)
A.....	0.00–0.07	+152± 2	positive slope with peak
B.....	0.00–0.03	+40±10	positive slope with peak
C.....	0.00–0.04	+56± 6	positive slope with peak
D.....	0.00–0.06	−59± 2	negative slope
Dw.....	0.00–0.06	−84± 3	negative slope
E.....	0.00–0.11	+82± 1	positive slope with peak
G.....	0.00–0.08	+57± 1	positive slope with peak
GE.....	0.00–0.03	+40±20	positive slope with peak
I.....	0.00–0.08	+70± 2	positive slope with peak
L.....	0.00–0.10	+2± 1	flat
O+Ob.....	...	...	...
Osw.....	0.00–0.09	+43± 3	positive slope with peak
Q.....	0.00–0.03	+20±20	positive slope with peak
R.....	0.00–0.03	−10±10	negative slope
U.....	0.00–0.10	+19± 1	positive slope with peak
W.....	0.00–0.06	+10± 2	positive slope with no peak
Z.....	0.00–0.06	−79± 4	negative slope

Notes. Col. (1): Clump name. Col. (2): Fitting range of X-rays in radial plot (see also the text for details). Col. (3): Slope of the fitted straight line of X-rays with 1 sigma error in the least-squares fitting. (4) Comments.

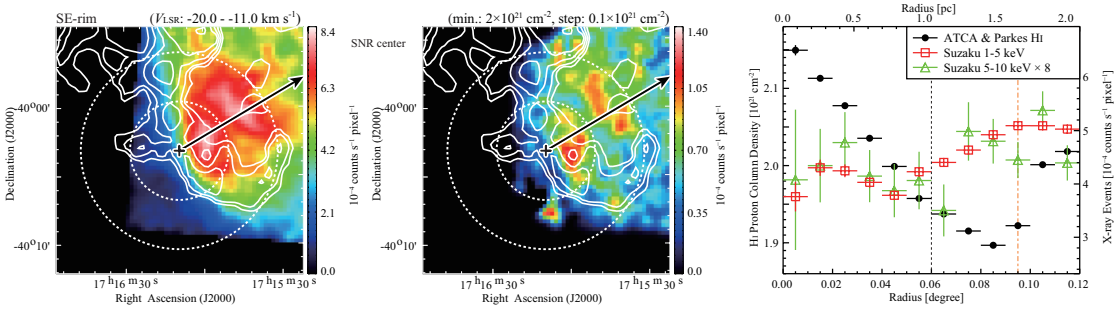

FIGURE 2.7: Distribution of the cold HI column density (*white contours*) superposed on the *Suzaku* images in the 1–5 keV (right) and 5–10 keV (middle) bands. Velocity range of integration and contour levels are shown in the top of the left and middle panels, respectively. Each arrow indicates the direction of the center of the SNR passing through the X-ray peak in the 1–5keV image. The crosses show the position which represents the cold HI clump and is determined as the crossing point of the HI cloud with the arrow, (α_{J2000}, δ_{J2000}) = (17^h 16^m 9.3^s, $-40°$ $3'$ $10.6''$) (see also the text). The dashed white circles represent radii of 0.°06 and 0.°12 centered on the crosses. Right panel shows the radial profile around the crosses in HI column density and the X-rays counts in the two energy bands (1–5 keV and 5–10 keV in Figure 2.2. The radial profile in the 5–10 keV band is scaled by a factor of 8 of the 1–5 keV band for the sake of direct comparison. The orange dash-dotted line indicates X-ray peak radius in the 1–5 keV band.

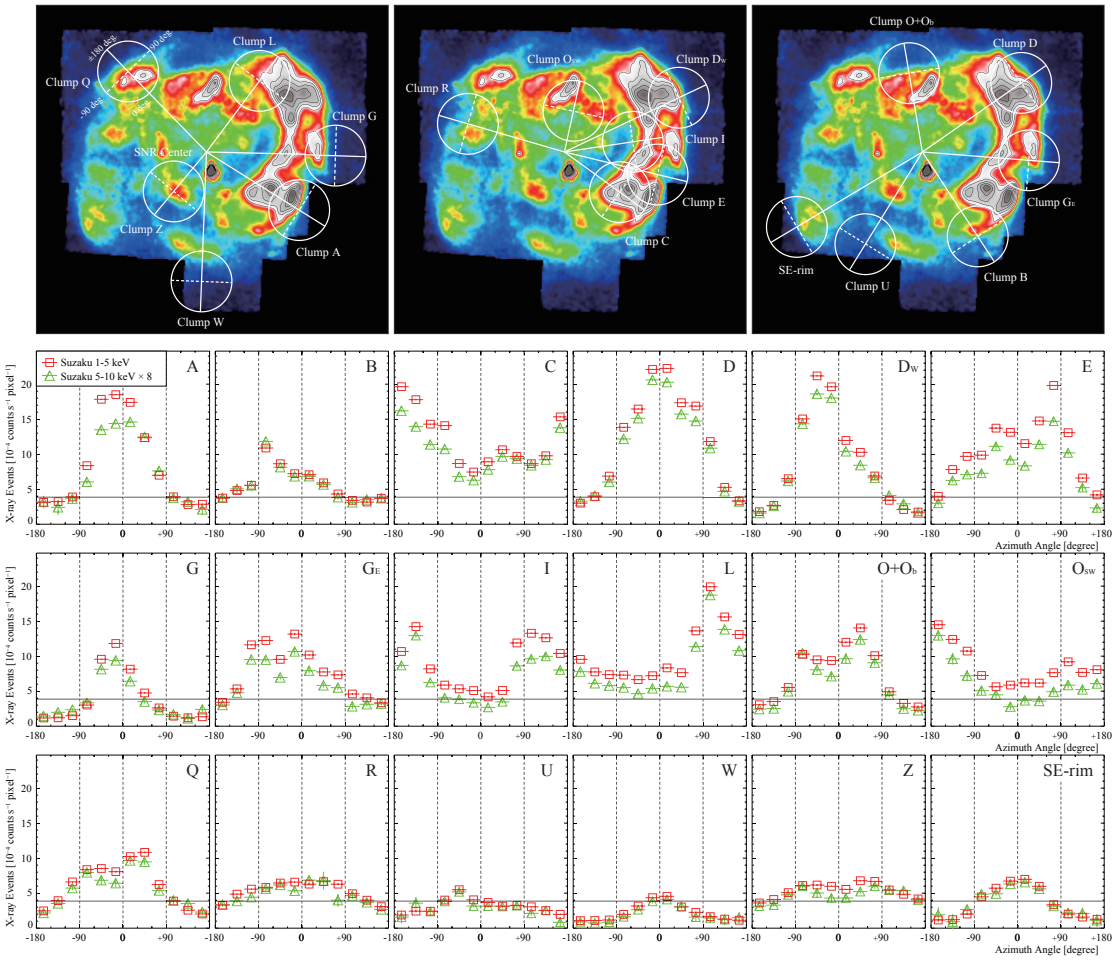

FIGURE 2.8: *top panels*: Same XIS mosaic image (1–5 keV) as Figure 2.2 (c). Overlaid white circles are centered on the center of gravity of each CO/HI clump. The azimuthal distribution of X-rays is averaged within each circle (radius = 0.°12). Each white solid straight line connects the centers of the circle and the SNR, and each dashed white line in the circle is vertical to the solid line. The azimuthal angle is measured from the solid line as the origin counterclockwise from −180 degrees to 180 degrees (e.g., clump Q in *top panel*). *other panels*: Azimuthal distributions of *Suzaku* XIS 1–5 keV (red square) and 5–10 keV (green triangles are scaled by a factor of 8) averaged in the circles for each clump. The horizontal solid lines indicate the background level of the X-rays estimated inside the SNR for the energy band 1–5 keV (see the text).

of angles and Figure 2.9 lower panel a histogram of the peak angle. The five clumps inside the SNR, clumps C, E, I, L and O$_{SW}$, are fully surrounded by the X-rays, which show a peak toward the azimuthal angle −180–−120 degrees (clumps C, I and O$_{SW}$) or +60–+120 degrees (clump E and L). These distributions indicate that the clumps inside of the SNR are surrounded by the enhanced X-rays, whereas those on the border of the SNR have enhanced X-rays only toward the center of the SNR. In Figure 2.9 lower panel we see a trend that the X-rays are enhanced at an azimuthal angle around 0, while scattering is large, ±60 degrees (clumps A, D, D$_W$, G, G$_E$, O+O$_b$, Q, R, U, W, Z and SE-rim). The histogram was fitted by a Gaussian function from −120 to 120 degrees, and we find that the best-fit parameters of center and sigma are 14±5 degrees and 51±5 degrees, respectively.

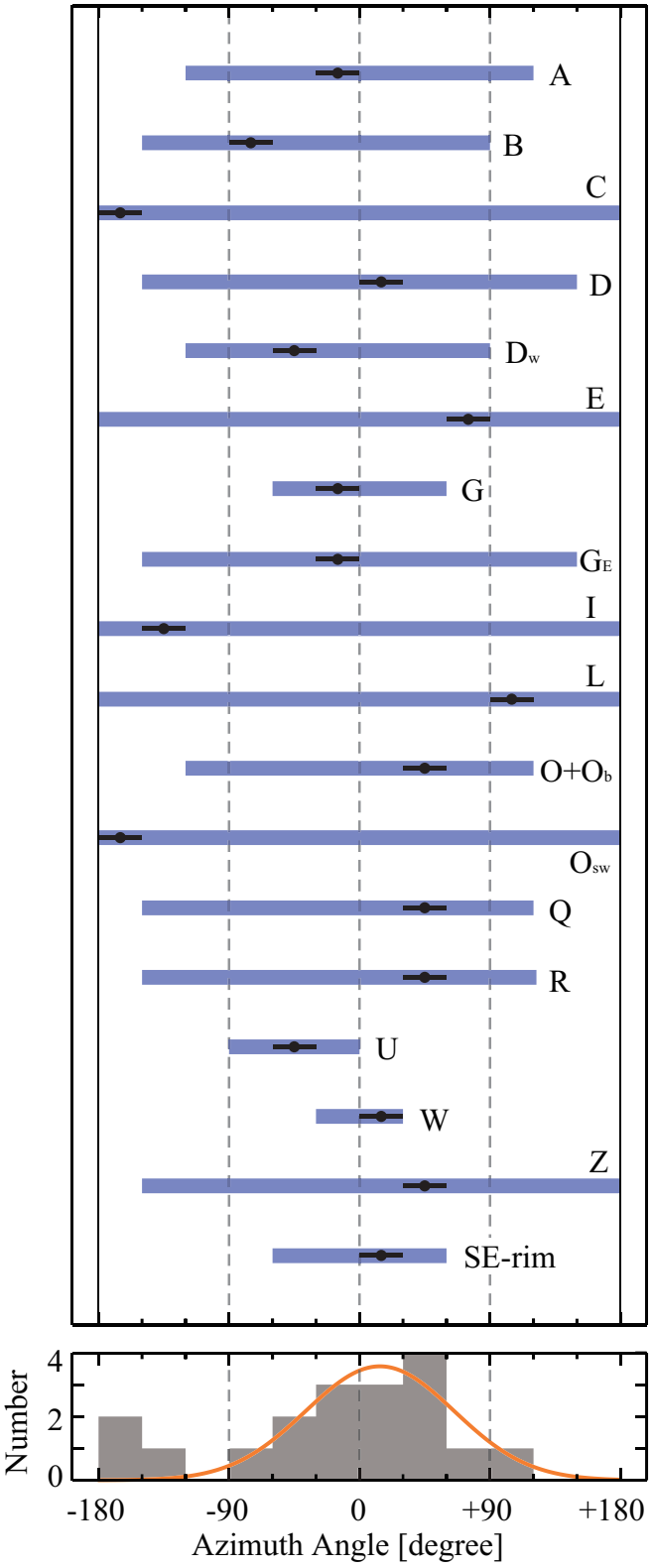

FIGURE 2.9: The azimuthal angular extent of the X-rays above the background level in each CO/HI clump for the 1–5 keV band image (*top panel*; see also Table 3). Each black dot indicates the angle of X-ray peak intensities in Figure 2.8. The histogram of the X-ray peak positions is shown in *lowest panel*. The red curve indicates the fitting result by a Gaussian function for the clumps from −90 degrees to +120 degrees.

2.3.3 Sub-millimeter Results; ^{12}CO(J=4–3) Distribution

We observed the ^{12}CO(J=4–3) transition in an area of 3.′0 × 3.′0 around clump C in equatorial coordinates and toward the peak position of Clump A. Figure 2.10 shows four images of clump C in the ^{12}CO(J=2–1, 3–2, and 4–3) and ^{13}CO(J=2–1) transitions, where the ^{12}CO(J=3–2) distribution is taken from (Moriguchi et al., 2005). The ^{12}CO(J=4–3) core is most compact and the size of the core increases toward the lower J transitions, suggesting a sharp intensity decrease with radius, since the higher J transitions have higher critical densities for collisional excitation.

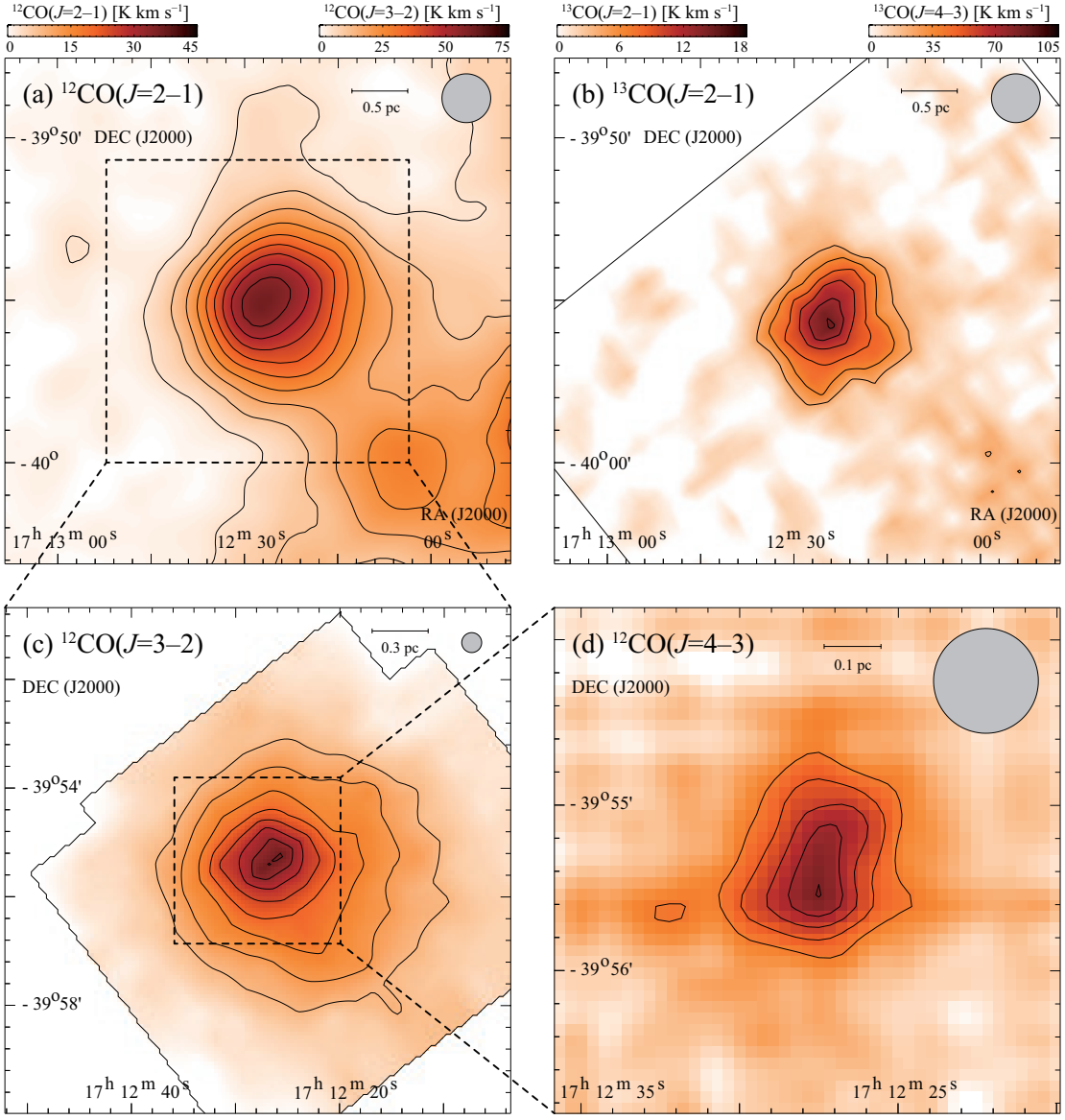

FIGURE 2.10: Intensity distributions of the ^{12}CO(J=4–3, 3–2, 2–1) and ^{13}CO(J=2–1) transitions of clump C. The velocity range is from −30 to 7 km s^{-1} in (d); from −20 to −7 km s^{-1} in (c); from −16.6 to −7.3 km s^{-1} in (a); and from −16 to −8 km s^{-1} in (b). The CO contours are every 10.2 K km s^{-1}($\sim 3.0\sigma$) from 41.6 K km s^{-1}($\sim 12.2\sigma$) in (d); every 5.0 K km s^{-1} ($\sim 5.3\sigma$) from 30.2 K km s^{-1} ($\sim 31.8\sigma$) in (c); every 3.8 K km s^{-1} ($\sim 4\sigma$) from 2.7 K km s^{-1} ($\sim 3\sigma$) in (a); and every 1.8 K km s^{-1}($\sim 2.6\sigma$) from 7.28 K km s^{-1} ($\sim 10.6\sigma$) in (d). The lowest contours are a half value of the peak intensity for each emission excepted for (a). The open cross shows the positions of the *IRAS* point source (see Table 2.6).

2.3.4 ^{12}CO(J=4–3) Broad Wings

Figure 2.11 shows that the broad ^{12}CO(J=4–3) wings first detected by Fukui et al. (2003) reveal a clear bipolar signature centered on *IRAS* 17089−3951 (Table 2.6) and on the peak position of the dense cloud core in clump C. The bipolarity verifies that the wings are driven by a protostar and are not driven by the SNR shock waves. The *IRAS* source position also shows a good correlation with an extended *Spitzer* sources at 8.28 μm (from IPAC Infrared Science Archive; Figure 2.11a). The wings toward clump C are also recognized in the present ^{12}CO(J=2–1) data in addition to the ^{12}CO(J=1–0) and ^{12}CO(J=3–2) transitions (Moriguchi et al., 2005), whereas the wing intensities of these lower-J transitions are more than a few times weaker than the ^{12}CO(J=4–3) wings. It is not clear if the other clumps A and D show sings of bipolar outflow either in the ^{12}CO(J=1–0) and ^{12}CO(J=3–2) data (Moriguchi et al., 2005) or in the present ^{12}CO(J=2–1) data.

We also find that the distribution of wing like components is complementary to the X-ray emission toward clump C. Figure 2.12 shows two overlays of ^{12}CO(J=4–3) wing component and X-ray images in two energy bands 1–5 keV (Figure 2.12a) and 5–10 keV (Figure 2.12a), respectively. First, clump C is surrounded by bright X-ray emission both on its east and west with a local minimum toward the center of the core (see also Figure

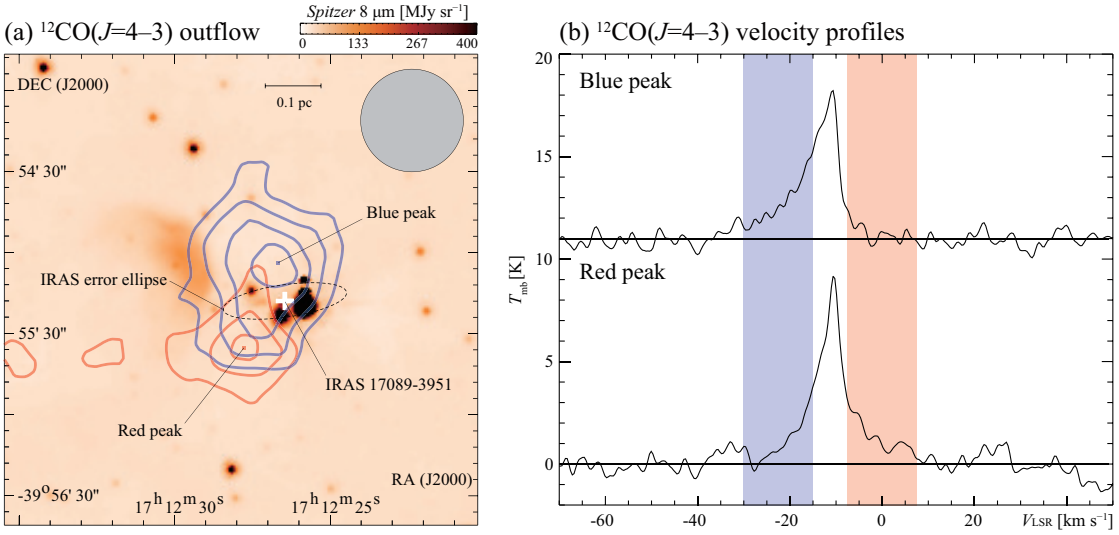

FIGURE 2.11: (a) Overlay map RX J1713.7−3946 *Spitzer* 8μm image in color scale (from GRIMPS Archive) and ^{12}CO(J=4–3) intensity contours taken by NANTEN2. The blue contours are from −30 to −15 km s^{-1} and the red contours from −8 to 7 km s^{-1}. The lowest contour level of the red and blue are 9.6 K km s^{-1} ($\sim 4\sigma$) for each. The contour interval of the black contour is 10.2 K km s^{-1} ($\sim 3\sigma$) and the others are 4.8 K km s^{-1} ($\sim 2\sigma$). Open cross and enclosed black dashed circle show the positions of the *IRAS* point source (see Table 2.6) and the 90% confidence region. (b) ^{12}CO(J=4–3) spectra covering a velocity range from −70 to 50 km s^{-1}. Painted areas with blue and red correspond to those color contours in (a).

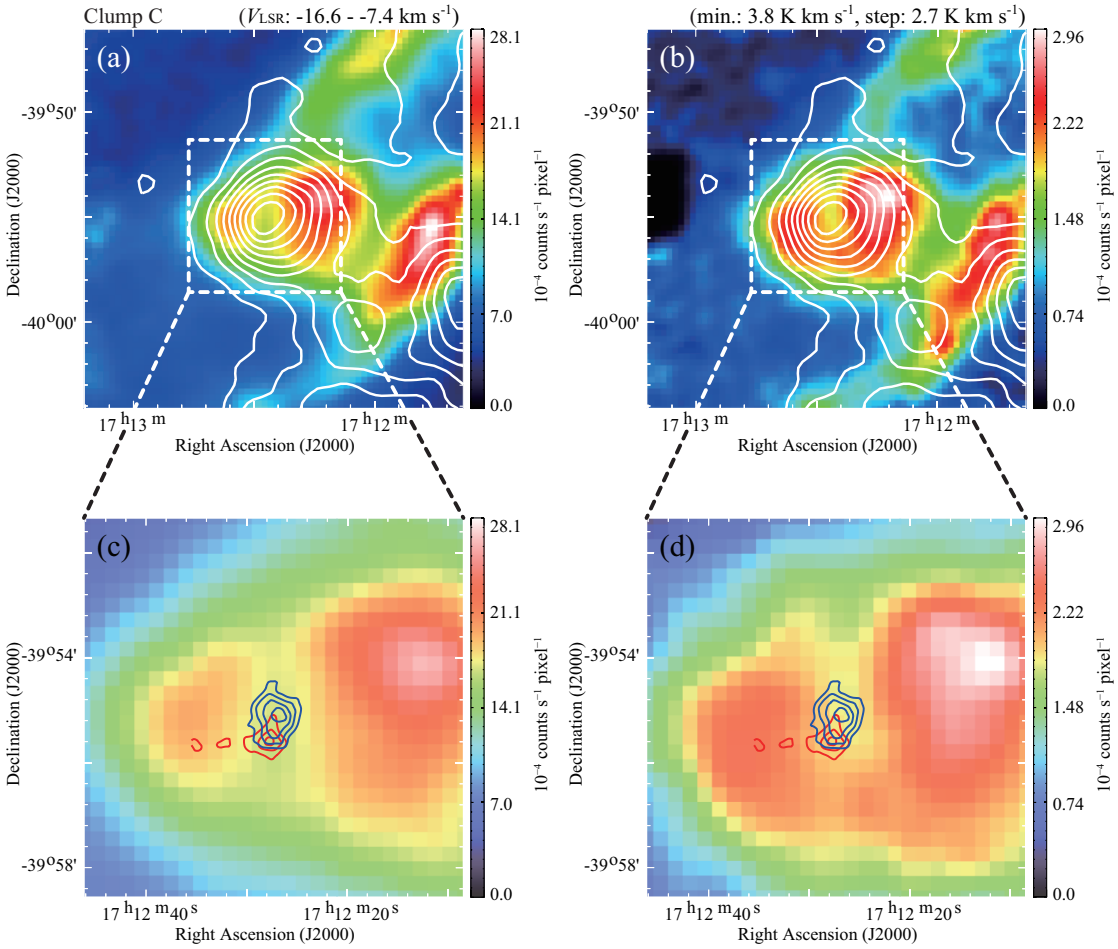

FIGURE 2.12: Distribution of ^{12}CO(J=2–1) emission (*white contours*) superposed on the *Suzaku* (a) 1–5 keV and (b) 5–10 keV images toward clump C. The velocity range and contour levels are the same as in Figure 2.5. (c) and (d) show the enlarged view in clump C overlaid with the ^{12}CO(J=4–3) intensity contours. The contours are the same as Figure 2.11a

2.5). Figure 2.12b shows a remarkable coincidence between the X-ray depression and the cloud core at a ∼0.1 pc scale. This depression is not due to interstellar absorption because we find similar distribution of X-ray in the higher energy band (5–10 keV) that is hardly absorbed (see Appendix E). Therefore, this morphology suggests that the X-ray emission is enhanced on the surface of the cloud core.

TABLE 2.6: Properties of *IRAS* point sources

Clump name (1)	*IRAS* point sources (2)	l (deg) (3)	b (deg) (4)	α(J2000) (^{h} ^{m} ^{s}) (5)	δ(J2000) ($^\circ$ $'$ $''$) (6)	semimaj $'$ (7)	semimin $'$ (8)	Posang deg. (9)	F_{12} (Jy) (10)	F_{25} (Jy) (11)	F_{60} (Jy) (12)	F_{100} (Jy) (13)	$L_{\rm IRAS}$ ($L_\odot$) (14)
A	17082-3955	346.94	-0.31	17 11 41.04	-39 59 11.21	23	5	98	5.4	3.8	17.5	138	137
C	17089-3951	347.08	-0.39	17 12 26.46	-39 55 17.98	23	6	98	4.4	13.0	98.5	234	311
D	17079-3926	347.31	0.01	17 11 25.59	-39 29 53.29	39	6	98	2.0	20.0	88.6	739	562

Notes. Cols. (1)–(2): Clump name (Moriguchi et al. 2005) and *IRAS* point source near the ^{12}CO(J=3-2) peaks. Cols. (3)–(6): Position of the *IRAS* sources. Cols. (7)–(9): Semimajour axis, semiminor axis, and position angle of the position error of the *IRAS* sources. Cols (10)–(13): Fluxes of 12, 25, 60, and 100 μm, respectively. Col. (14): *IRAS* luminosity estimated using formula of Emerson (1988). Col. (18). (see Cols. (2)–(4) and (10)–(15) are Moriguchi et al., 2005, Table 3)

2.4 Analysis of Detailed Molecular Properties

2.4.1 LVG Analysis

We shall use the large velocity gradient model of line radiation transfer to estimate density and temperature from the muti-J transitions of CO; i.e., ^{12}CO(J=3–2, 4–3) and ^{13}CO(J=2–1). We applied the large velocity gradient (LVG) analysis (Goldreich & Kwan, 1974; Scoville & Solomon, 1974) to estimate the physical parameters of the molecular gas toward clumps A and C by adopting a spherically symmetric uniform model having a radial velocity gradient dv/dr. The ^{12}CO(J=2–1) transition was not included in the analysis because the transition may be subject to self absorption due to low excitation foreground gas (e.g., Mizuno et al., 2010). We calculate level populations of ^{12}CO and ^{13}CO molecular rotational states and line intensities. The LVG model requires three independent parameters to calculate emission line intensities; i.e., kinetic temperature, density of molecular hydrogen and $X/(dv/dr)$. $X/(dv/dr)$ is the abundance ratio from CO to H_2 divided by the velocity gradient in the cloud. We use the abundance ratio [^{12}CO]/[^{13}CO] $\sim$75 (Güsten & Philipp, 2004) and [^{12}CO]/[H_2] $\sim 5\times10^{-5}$ (Blake et al., 1987), and estimate the mean velocity gradient between the peaks as $\sim$12.5 km s^{-1} pc^{-1}. Accordingly, we adopt that $X/(dv/dr)$ is 4.0×10^{-6} (km s^{-1} pc^{-1})$^{-1}$ for ^{12}CO.

In order to solve temperatures and densities which reproduce the observed line intensity ratio, we calculate chi-square χ^2 defined as below;

$$\chi^2 \quad = \quad \Sigma[(R_{\rm obs} - R_{\rm model})^2/\sigma] \tag{2.1}$$

where $R_{\rm obs}$ is the observed line intensity ratio between different excitation lines or different isotopes, $R_{\rm model}$ is the line ratio of the LVG calculations, σ is the standard deviation for $R_{\rm obs}$ in the analysis. The error in the observed intensity is estimated by considering the noise level of the observations and the calibration error. We assume that the error of calibration from T_A^* to $T_{\rm MB}$ is 10% for all the line intensities. The data used are derived from the line profiles in Figure 2.13 upper and three ratios are estimated for a 1.5 km s^{-1} velocity interval in the three peaks as listed in Table 2.7.

The lower panels of Figure 2.13 shows the results of fitting to the data obtained with a chi-square minimization approach to find the solution of temperature and density. Each locus of a black solid line surrounding the cross indicates the chi-square χ^2, which corresponds to the 95% confidence level of a chi-square distribution. The crosses denote the lowest point of chi-square. Additionally, we are able to reject each region outside the black solid line at the 95% confidence level. Table 2.7 summarizes the results of the LVG analysis. Density and temperature are relatively well constrained in clumps A and

TABLE 2.7: Results of LVG Analysis at Molecular clumps

Name	α_{J2000}	δ_{J2000}	^{12}CO		^{13}CO		
			J=3-2	J=4-3	J=2-1	$n(H_2)$	T_{kin}
	(°)	(°)	(K)	(K)	(K)	(10^4cm^{-3})	(K)
(1)	(2)	(3)	(4)	(5)	(6)	(7)	(8)
A	257.92	−40.00	6.6	2.1	1.9	$0.6^{+0.2}_{-0.1}$	10^{+1}_{-1}
C	258.12	−39.92	8.5	5.2	3.4	$1.1^{+0.6}_{-0.3}$	12^{+4}_{-1}

Notes. Col. (1): Clump name. Col. (2)–(3): Position of the observed point with the maximum ^{12}CO(J=3-2) intensity peak. Col. (4)-(6): Radiation temperature averaged to the line of sight over a velocity integral of 1.5 km s^{-1}. Col. (7): Density of molecular hydrogen. Col. (8): Kinetic temperature. The parameter, $X/(dV/dR)$= 4.0×10^{-6} (km s^{-1} pc^{-1})$^{-1}$, is used.

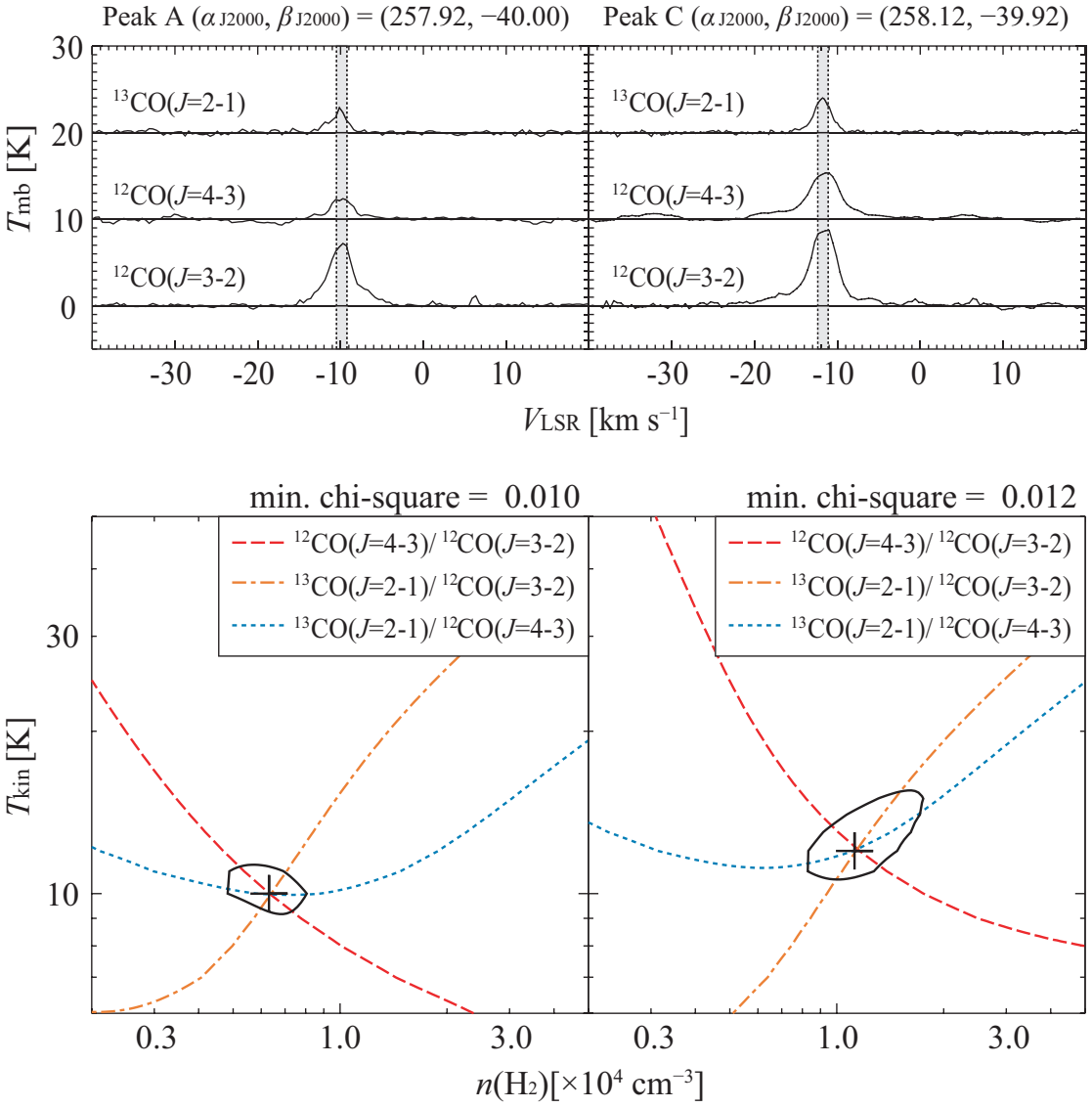

FIGURE 2.13: Results of an LVG analysis for molecular clumps A and C. *Top*: CO line profiles for each molecular peak are smoothed to 90″ by a Gaussian beam corresponding to the ^{13}CO(J=2–1) beam size. *Bottom*: Results of an LVG analysis for molecular peaks as indicated by the Top panels. Each locus of a black solid line surrounding the cross indicates the chi-square χ^2 of 3.84, which corresponds to the 95% confidence level of a chi-square distribution with one degree of freedom. The crosses denote the lowest point of chi-square.

C. The temperature of clumps A and C is in a range of 10–12 K and density is somewhat higher in clump C, $\sim 10^4$ cm^{-3}, than in clump A, $\sim 6 \times 10^3$ cm^{-3}.

2.4.2 The Density Distribution of Clump C

Clump C is associated with a dense cloud core with a strong intensity gradient (Figure 2.10). The total molecular mass of the core is estimated to be 400 $M_\odot$ from the ^{12}CO(J=1–0) integrated intensity (Moriguchi et al., 2005) for an X factor of 2.0×10^{20} [$W(^{12}\mathrm{CO})/(\mathrm{K\ km\ s^{-1}})$] (Bertsch et al., 1993). We shall derive the density distribution by employing a simple power-law analysis assuming a spherical symmetry. First, we de-convolve the intensity distribution in order to correct for the beam size. We assume the relation to derive a de-convolved core radius r in each transition; $r^2 = s^2 + r'^2$, where r, s and r' stand for the observed radius, the beam radius and the de-convolved radius, respectively, at a half power level of the peak intensity (Table 2.8). Then, we estimate the averaged density within r, $\overline{n(\mathrm{H_2})(< r)}$, so as to match the observed averaged integrated intensity to the LVG estimate within the radius by assuming kinetic temperature of 12 K and the same model parameters in Chapter 2.4.1. Considering the low luminosity of the *IRAS* source (300 $L_\odot$), we infer that the local temperature variation in the core is not significant and that a uniform temperature is a good approximation. The result is shown in Figure 2.14. This presents that the average density distribution is well approximated by a power law, $r^{-2.2\pm0.4}$. Such a steep density gradient is consistent with a star forming cloud core (Larson, 1969; Penston, 1969; Lizano & Shu, 1989; Onishi et al., 1999). The line width does not vary much among the different density regimes as shown in Figure 2.14, suggesting the infall motion is not very large. An alternative interpretation for the density distribution will be discussed later.

TABLE 2.8: Density Distribution and Core Radius for Peak C

	^{12}CO			^{13}CO
Property	J=2–1	J=3–2	J=4–3	J=2–1
Beam size (arcsec)	90	22	38	90
Core radius (pc)	0.62	0.44	0.23	0.32
Average brightness (K)	0.79	1.87	1.28	0.29
Number density (10^3cm^{-3})	0.33±0.05	1.51±0.23	3.55±0.53	1.78±0.27

Notes. Cols. Number density is derived by assuming T_{kin} = 12 K and $X/(dV/dR)$= 4.0×10^{-6} (km s^{-1} pc^{-1})$^{-1}$. We assume that the error of density caused by calibration from T_{A}^* to T_{MB} is ±15% for all intensities.

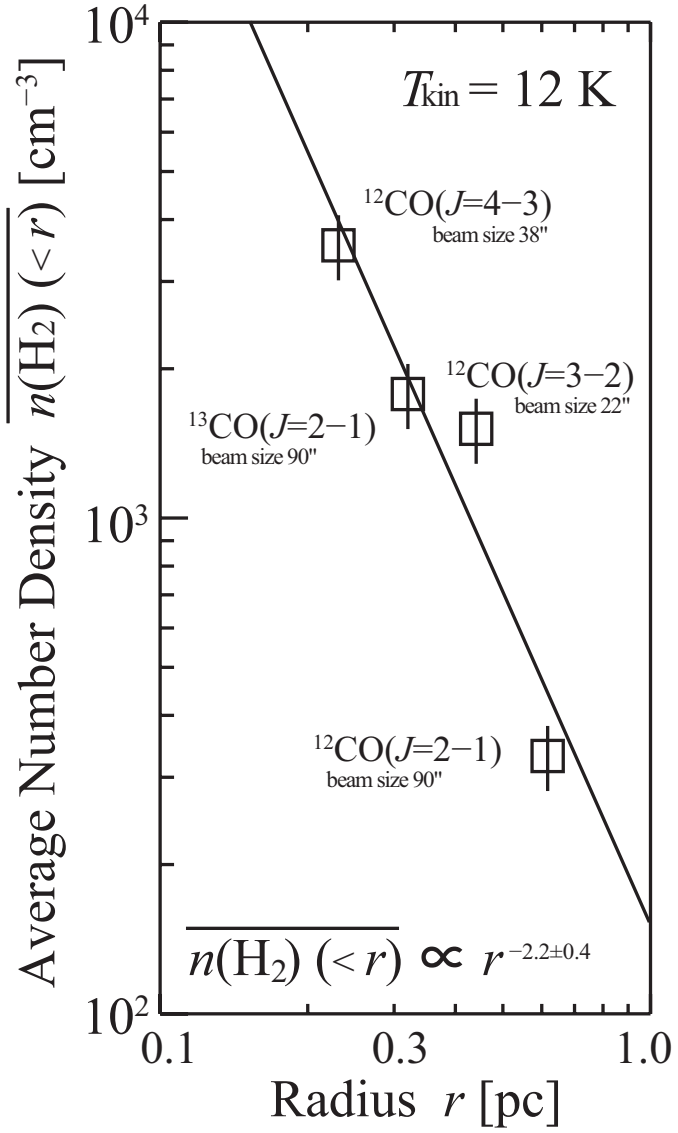

FIGURE 2.14: The molecular density distribution of clump C. The calculations are carried out for $T_{\rm kin}$ = 12 K (see Table 2.7). The solid line is a regression line obtained by least squares fitting. Error bars represent only those for the radiation temperature calibration,±15%. See Table 2.8. for further.

2.4.3 Physical parameters of the outflow

The bipolarity of the broad CO wings in Figure 2.11 verifies that the wings are caused by bipolar outflow driven by a protostar and is consistent with the compact dense core with a steep density gradient (Chapter 2.4.2). The physical parameters of the outflow are estimated by using the method described by (Moriguchi et al., 2005, Table 2.9). The average intensities of the red component are 8.9 K and 2.0 K for the ^{12}CO(J=2–1) and ^{12}CO(J=4–3) transitions in a velocity range from -8 km s^{-1} to -3 km s^{-1}. The density in the line emitting wings are then estimated to be $\sim 5\times10^3$ cm^{-3} from the line intensity ratio, ∼0.23, between the ^{12}CO(J=2–1) and ^{12}CO(J=4–3) transitions. The beam filling factor is estimated to be as small as 5% for an assumed excitation temperature of 12 K for the rotational levels of ^{12}CO. This result is similarly obtained from the blue component, that yields beam filling factor of $\sim$ 4%. Therefore, the CO wings represent highly clumped gas rather typical for outflows. The present ^{12}CO(J=4–3) data have verified that the wings represent outflow and showed that the ^{12}CO(J=4–3) wings are much more compact than the ^{12}CO(J=1–0) wings, indicating that the ^{12}CO(J=4–3) wings are denser outflow gas whose spatial extent is smaller than the lower density wings (Table 2.9, for the ^{12}CO(J=1–0) wings see Table 4 of Moriguchi et al., 2005). The most likely driving source of the outflow is the far infrared source *IRAS* 17089−3951. General properties for bipolar outflows are found elsewhere (e.g., Lada, 1985; Fukui, 1989; Fukui et al., 1993) and the present outflow is seen to be typical of an outflow associated with a low mass protostar in terms of its size and velocity.

TABLE 2.9: Outflow Properties at Clump C in ^{12}CO(J=4–3)

Property	Blue component	Red component
Integrated intensity (K km s^{-1})	17.5	14.7
Size (arcmin)	0.85	0.58
Size (pc)	0.25	0.17
ΔV (km s^{-1})	15	15
$t_{\rm dyn}$ (10^4 yr)	1.6	1.1

Notes. Integrated intensity is derived by summing the integrated intensities of the observed points in the area enclosed by a contour of 13.4 K within the velocity range of -30 km s^{-1} $\leq V_{\rm LSR} \leq -15$ km s^{-1} for blue-shifted component and 11.0 K within -8 km s^{-1} $\leq V_{\rm LSR} \leq 7$ km s^{-1} for red-shifted component, respectively. Size is defined as an effective diameter $= \sqrt{(A/\pi)} \times 2$, where A is the region enclosed by a contour of 13.4 K km s^{-1} and 11.0 K km s^{-1} for the blue-shifted and red-shifted component, respectively. ΔV is the velocity range of the wing component. The dynamical age, $t_{\rm dyn}$, is defined as $2R/\Delta V$.

2.5 Discussion

We present a general scenario following discussions given by Fukui et al. (2003) and Moriguchi et al. (2005). The progenitor of the SN was a high mass star formed some Myrs ago in the region, and which created a cavity in the ISM by its stellar wind. This is a star-forming region with a loose spatial association extended over a few 10 pc. The star formation in the clump C may have been triggered by the progenitor of the SNR (Koo et al., 2008; Desai et al., 2010). The progenitor star caused the supernova explosion 1600 yrs ago, as recorded in an ancient Chinese document (Wang et al., 1997) and the blast wave expanded into the cavity. The SNR is now interacting with the molecular clumps and this interacting layer is traced by the synchrotron X-rays, as supported by the good spatial anti-correlation with the CO clumps at a 0.1 pc scale.

We have compared the X-rays and the CO and HI dense clumps over the whole SNR, and present a schematic image of these results in Figure 2.15. This figure indicates that the CO and dense HI clumps form an inhomogeneous shell and that the X-rays are enhanced around all the clumps. We infer that the five CO clumps C, E, I, L and Osw survived the SNR blast waves, being now embedded within the SNR, while the other twelve CO clumps and the HI clump are shock-interacting on their inner side. As mentioned above, the ISM shell was formed over a timescale of Myr by the stellar winds of an OB star which experienced an SN explosion 1600 yr ago. Thus, the density in the cavity surrounded by the ISM shell is expected to be very low. The observational results also indicate that there is little dense gas left in the interior of the cavity (Figures 2.3 and A1). According to the numerical simulations which studied the interaction of the ISM with the strong stellar winds from an O-type star (Weaver et al., 1977), the gas density inside the evacuated wind bubble is ~ 0.01 cm^{-3}, which applies to the interior of the cavity.

The shock waves of the SNR first propagated in the stellar-wind cavity and then began interaction with the CO/HI clumps some 1000 yrs ago as given by the ratio of the shell thickness and the shock velocity, 3 pc / 3000 km s^{-1}. According to MHD numerical simulations by Inoue et al. (2012), the CO/HI clumps having density of $\sim 10^2$–10^3 cm^{-3} are surrounded by the interclump gas having density of ~ 1 cm^{-3} which is two orders of magnitude higher than that in the cavity. These authors show that the shock is stalled in the dense clumps. The shock velocity becomes $V_{\rm sh,clump} = V_{\rm sh,interclump}(n_{\rm interclump}/n_{\rm clump})^{0.5}$, where the interclump density $n_{\rm interclump} = 1$ cm^{-3} and the clump density $n_{\rm clump} = 10^2$–10^3 cm^{-3}. The shock velocity difference between the dense CO/HI clumps and the interclump gas will become a factor of $\sim$10–30. They calculated that the temperature of the shocked dense gas becomes much lower than the temperature in the post-shock diffuse gas, and argued that the thermal X-ray emission

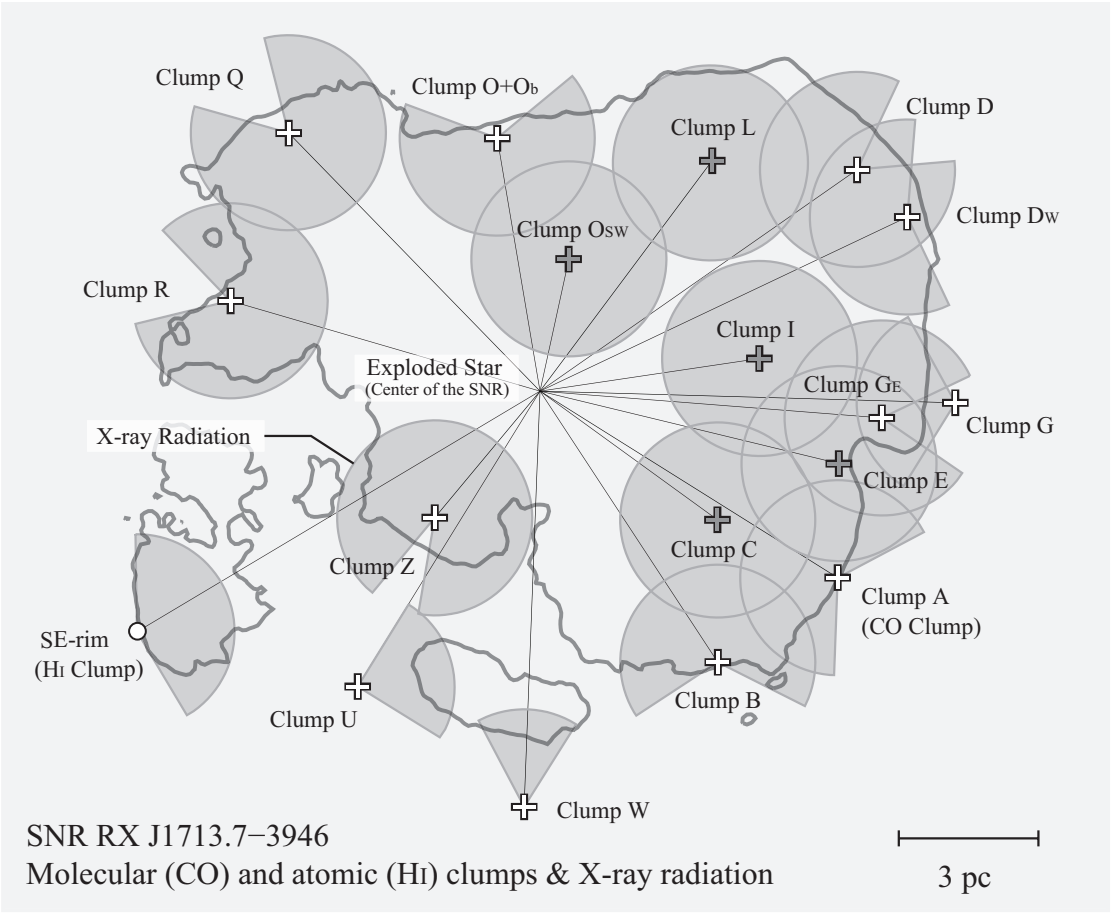

FIGURE 2.15: Schematic image of the distribution of the molecular (CO) clumps (open crosses), atomic (HI) clump (circle) and the X-rays (shaded partial or full circles) superposed on the *Suzaku* 1–5 keV X-ray outer boundary of the SNR (gray contours). The black open crosses (clumps C, I, E, L, and Osw) indicate those fully surrounded by the X-rays.

from the CO/HI clumps is strongly suppressed after the passage of the shock (see Section 4.3 of Inoue et al., 2012). The interclump gas does not emit significant thermal X-rays either, because the density $\sim$1 cm^{-3} is less than $\sim$2 cm^{-3}, the average density inside the SNR obtained from the upper limit of the thermal X-rays (Takahashi et al., 2008). Additionally, in this case, the penetrating depth in a typical timescale of the interaction $\sim$1000 yrs is then estimated to be $\sim$0.1 pc for n=10^3 cm^{-3} and $\sim$3 pc for n=1 cm^{-3}, respectively. Clump C has a present diameter of at least 0.6 pc at density of 10^3 cm^{-3} (Figure 2.14) and should have not been affected significantly by the shock penetration according to the argument above, whereas the ambient lower density gas is significantly disturbed and accelerated in a scale length of the SNR radius. We, therefore, infer that clump C (and other four clumps) is able to survive against the shock wave as originally suggested by Fukui et al. (2003), while the lower density ambient gas is significantly disturbed and accelerated.

An important consequence of the interaction is that the large velocity difference created

between the clumps and the interclump space induces turbulence, which leads to turbulent dynamo action. The magnetic field is then amplified to as high as 1 mG, which is consistent with the field strength derived from rapid time variation of the X-ray filaments (Uchiyama et al., 2007), while an alternative is that the fluctuations in the field orientation may explain the rapid time variation (Helder et al., 2012). The synchrotron flux integrated in the line of sight is proportional to $B^{1.5}$ if the spectral index of electrons p is 2.0 (e.g., Rybicki & Lightman, 1979). So, it is possible to enhance the X-ray radiation around the CO and HI clumps. It is known that the power of the synchrotron X-ray emission is not enhanced by magnetic field amplification due to the effect of synchrotron cooling, if the amplification takes place in the vicinity of the forward shock where electrons are being accelerated (e.g., Nakamura et al., 2012). In the present case, as discussed by Inoue et al. (2009, 2010, 2012), the magnetic field amplification owing to the shock-cloud interaction is effective at least 0.1 pc downstream of the shock front. This indicates that the synchrotron X-rays are emitted after the acceleration process, and thus the power of synchrotron X-ray is enhanced by the amplification. The observed power of the X-ray emission around the CO and HI clumps is 2–7 times higher than the background level inside the SNR. Then, the magnetic field around the CO and HI clumps is estimated to be 2–4 times higher than elsewhere in the SNR, if the X-ray enhancement is only due to the magnetic field amplification. The averaged magnetic field around the CO and HI clumps becomes 30–60 μG if the initial field is assumed to be 15 μG (e.g., Tanaka et al., 2008). The average field strength is also estimated by the width of synchrotron X-ray filaments as $\sim$100 μG (Bell, 2004; Hiraga et al., 2005; Ballet, 2006). Note that the dependence of the synchrotron flux on the magnetic field strength can be much more sensitive than the above-mentioned standard case, because the high-energy electrons that contribute the X-ray synchrotron emission can be in the cut-off regime (Bykov et al., 2008). Moreover, such enhanced magnetic field in turbulence may lead to more efficient acceleration than in the diffusive shock acceleration (Lazarian & Vishniac, 1999; Hoshino, 2012).

Finally, we discuss quantitative relationship between the CO/HI interacting clump mass and the X-ray enhancement. First, we estimate the interacting clump mass (column (9) of Table 2.8) with the shock waves as defined by the total CO/HI mass within the azimuth angle range of the X-rays with respect to the center of gravity (column (8) of Table 2.8). For the case in which two CO clumps have small separation (< 0.2 degrees) and the X-ray peak is situated between the CO clumps, we sum up the interacting clump masses and averaged the X-ray intensities (D+D$_{\rm W}$, O+O$_{\rm b}$+O$_{\rm SW}$, G+G$_{\rm E}$ and E+I; see also Table 2.8). In Figure 2.16, we plot the CO/HI interacting clump mass as a function the X-ray peak intensity. Here, we approximate the mass of the SE-rim to be 134 $M_\odot$ on the assumption that it has a large of 0.8 pc^2 along the X-ray boundary.

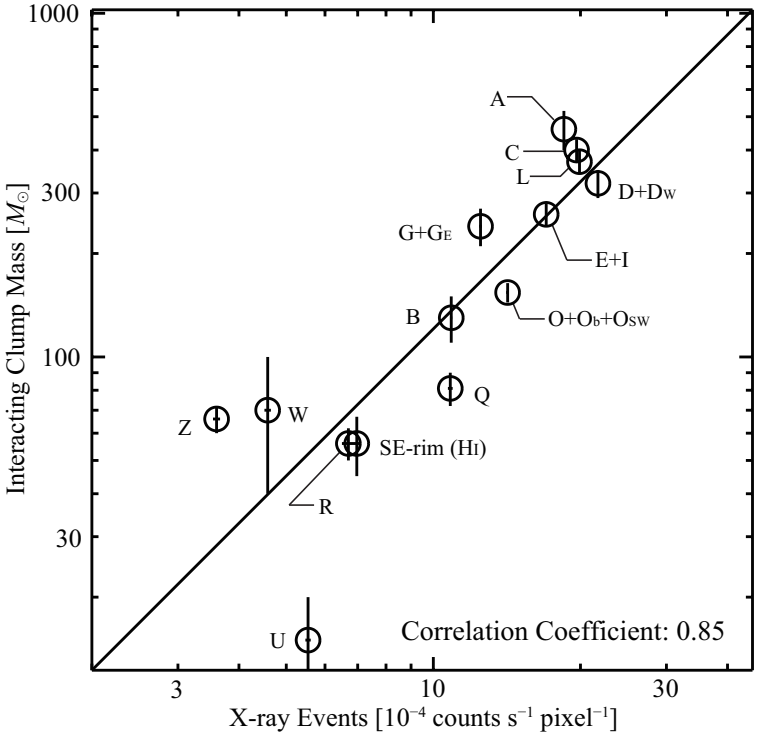

FIGURE 2.16: Correlation plot between the X-ray peak intensity in the azimuthal distributions derived in Figure 2.8 and the interacting clump mass with the shock waves, which is estimated by the CO or HI mass within the azimuth angle range of the X-rays for each clump (see for more details the text, and column (9) of Table 2.8). The linear regression by the least-squares fitting is shown by the solid line, where the correlation coefficient is ∼0.85 in double logarithm.

The result, shown in Figure 2.16, indicates that the correlation between the interacting clump mass and the X-ray intensity is good with a correlation coefficient of ∼0.85 in double logarithm. We conclude that intensity is roughly proportional to the interacting mass of each CO/HI clump at a pc scale. This result suggests that the ISM distribution is crucial in producing the non-thermal X-ray distribution in young SNRs.

2.6 Conclusions

We summarize the present work as follows;

1. We have shown that all the major CO and HI clumps with mass greater than 50 $M_\odot$ interacting with the shock waves in RX J1713.7−3946 are associated with the non-thermal X-rays. The X-rays are enhanced within ∼1 pc of the CO and HI peaks, whereas at smaller scales down to 0.1 pc the CO peaks tend to be anti-correlated with the X-rays which are decreased toward the CO and HI clumps. We

have shown a good correlation between the CO/HI clump mass interacting with the shock waves and the X-ray intensity.

2. Sub-millimeter results indicate that the core of clump C has a strong density gradient consistent with an average density distribution of $r^{-2.2\pm0.4}$, where r is the radius from the center of the core. The density and temperature, averaged over $90''$ (= 0.2 pc) are 0.8–1.7 $\times$ 10^4 cm^{-3} and 11–16 K, as derived from an LVG analysis. Clump C is also associated with a bipolar outflow as evidenced by the ^{12}CO(J=4–3) broad wings of at least 30 km s^{-1} velocity extent. Along with the far infrared spectrum, these identify the region as a site of recent low-mass star formation within Myr. This verifies the broad wings are not produced by the shock acceleration driven by the SNR as suggested before by Fukui et al. (2003). Clump A has density and temperature of 5–8 $\times$ 10^3 cm^{-3} and 9–11 K, somewhat lower than clump C. The *IRAS* sources in clump A and D are also likely protostars as noted by Moriguchi et al. (2005), because of the high density of these peaks.

3. The present findings in 1) are compared with numerical simulations of MHD in a realistic highly inhomogeneous density distribution by Inoue et al. (2009, 2012). These simulations indicate that the magnetic field is amplified around dense CO/HI clumps as a result of enhanced turbulence induced by the shock-cloud interaction. We interpret that thus-amplified magnetic fields enhance the X-ray intensity, which depends on the 1.5-th power of the magnetic field strength. Such enhanced magnetic field may also lead to efficient acceleration additional to the DSA. More comparative studies of distribution of the X-rays and the ISM will allow us to have a deeper insight into the origin of the X-ray distribution.

Chapter 3

Evidence for Acceleration of Cosmic-Ray Protons

3.1 Background

It is a longstanding problem how cosmic-ray protons, the major constituent of cosmic-rays are accelerated in interstellar space. SNRs are the most likely candidates for acceleration below Knee energy ($\sim 10^{15.5}$ eV) because the high-speed shock waves offer an ideal site for DSA (see detail for Chapter 1.3.2). The principal site of cosmic-ray proton acceleration is, however, not yet identified observationally in spite of a number of efforts to address this issue. Particularly, It's not clear whether the cosmic-ray protons have been accelerated to near Knee energy or not.

The young ($\sim$1600 yr) SNR RX J1713.7−3946 is one of the most promising candidate where the origin of the γ-rays may be established. The γ-rays higher than 10 TeV is detected here, suggesting that the cosmic-ray protons responsible may have energy close to the *knee*, if the γ-rays are produced by π^0-decay Aharonian et al. (2007) (hadronic process; see also Chapter 1.4.3). Furthermore, the SNR is interacting with the dense Molecular clumps (Fukui et al., 2003; Moriguchi et al., 2005, see also Chapter 2). Importantly, the associated molecular gas with the SNR opened a possibility to identify target protons where the hadronic process is working. **If the cosmic-ray density is nearly uniform, we expect the hadronic γ-ray distribution mimics that of the interstellar target protons** (see Equation 1.51). Some nearby molecular clouds show good spatial correlation with relatively high resolution γ-ray images, clearly verifying that the hadronic process is working to produce γ-rays in the cosmic ray sea (e.g., Ackermann et al., 2012). A detailed comparison between the ISM protons and the recent high-resolution γ-ray images of H.E.S.S. sources is useful to test the correlation, although such a test was not possible until recently in the preceding low resolution γ-ray observations at degree-scale resolution. Aharonian et al. (2006a) compared the

NANTEN CO distribution with the H.E.S.S. VHE (very high energy) γ-ray image and examined both leptonic and hadronic scenarios as the origin of the γ-rays. By adopting annular averaging of VHE γ-rays and CO in the shell (see Figure 1.10 in Chapter 1.5.2), these authors found that VHE γ-rays are fairly well correlated with CO, whereas the correlation is not complete in the sense that the southeastern rim of the VHE γ-ray shell has no counterpart in CO. The complete identification of target ISM protons thus remained unsettled in the hadronic scenario.

The γ-rays and X-rays are significantly enhanced toward the clumpy molecular gas at a pc scale as first shown by Fukui et al. (2003). A strong connection among the molecular gas, the γ-rays, the X-rays, and perhaps cosmic-rays is therefore suggested (Fukui et al., 2003; Fukui, 2008; Zirakashvili & Aharonian, 2010, and Chapter 2). Most of the previous models of the γ- and X-rays cited earlier assume more or less uniform density distribution of the ISM in the SNR, whereas the observations of the ISM indicate that the actual distribution is highly inhomogeneous, with density varying by a factor 100 or more around the SNR. In addition, Galactic-scale studies of γ-rays suggest that there is "dark gas" which is not detectable in CO or in HI but still contributes to the γ-rays and visual extinction (Grenier et al., 2005; Planck Collaboration et al., 2011). Such gas may be either cold HI or H_2 with no detectable CO. So, it is important to consider HI carefully in order to have a comprehensive understanding of the ISM protons. In the present paper, we shall use the term "dark HI" for observed HI with significantly lower brightness than the surroundings. So, "dark HI" does not mean "dark gas" above.

We here present a combined analysis of both the ^{12}CO(J=1–0) and HI datasets in order to clarify the distribution of the ISM protons and it compared with the VHE γ-ray distribution in RX J1713.7−3946. The present works will reveal the VHE γ-ray origin in the SNR and open a new approach to understanding the origin of galactic cosmic-rays.

3.2 Datasets of CO, HI, and VHE γ-rays

3.2.1 CO

The ^{12}CO(J=1–0) data at 2.6 mm wavelength were taken with NANTEN 4-m telescope in 2003 April and are identical with those published by Moriguchi et al. (2005). The system temperature of the SIS receiver was ∼250 K in the single side band including the atmosphere toward the zenith. The beam size of the telescope was $2'.6$ at 115 GHz and we adopted a grid spacing of $2'.0$ in these observations. The velocity resolution and rms noise fluctuations are 0.65 km s^{-1} and 0.3 K, respectively.

The ^{12}CO(J=2–1) data at 1.3 mm wavelength were taken with NANTEN2 4-m telescope in the period from August to November in 2008 and part of the dataset was shown by Chapter 2. The frontend was a 4 K cooled Nb SIS mixer receiver and the single-side-band (SSB) system temperature was ∼250 K, including the atmosphere toward the zenith. The telescope had a beam size of 90″ at 230 GHz. We used an acoustic optical spectrometers (AOS) with 2048 channels having a bandwidth of 390 km s^{-1} and resolution per channel of 0.38 km s^{-1}. Observations in ^{12}CO(J=2–1) were carried out in the on-the-fly (OTF) mode, scanning with an integration time of 1.0–2.0 s per point. The chopper wheel method was employed for the intensity calibration and the derived $T_{\rm rms}$ was better than 0.66 K and 0.51 K per channel with 1.0 s and 2.0 s integrations, respectively. An area of 2.25 deg^2 in a region of $346\overset{\circ}{.}7 \leq l \leq 348\overset{\circ}{.}2$ and $-1\overset{\circ}{.}3 \leq b \leq 0\overset{\circ}{.}4$ was observed.

Moriguchi et al. (2005) showed an analysis of the ^{12}CO(J=1–0) distribution over 100 km s^{-1} with a coarse velocity window of 10 km s^{-1} in order to test association with the SNR. These authors showed that the velocity range $V_{\rm LSR} = -20$ to 0 km s^{-1} has convincing signs of association with the SNR. We adopt in the present work the velocity interval, −20 to 0 km s^{-1}, for the associated ISM and present detailed ^{12}CO (J=1–0, 2–1) and HI data every 1 km s^{-1} (see Figure Appendix A.2).

3.2.2 HI

The HI data at 21 cm wavelength are from the Southern Galactic Plane Survey (SGPS; McClure-Griffiths et al., 2005) and combined from the Australia Telescope Compact Array (ATCA) and the Parkes Radio Telescope. The beam size of the dataset was 2′.2 and we adopted a grid spacing of 40″ toward the RX J1713.7-3946 in the current analysis. The velocity resolution and typical rms noise fluctuations were 0.82 km s^{-1} and 1.9 K, respectively.

3.2.3 VHE γ-rays

For the H.E.S.S. γ-ray data we used the combined H.E.S.S. image shown in Figure 2 of Aharonian et al. (2007). Data of 2004 and 2005 are used for this smoothed, acceptance-corrected gamma-ray excess image. The VHE image utilizes minimum three H.E.S.S. telescopes in event reconstruction to obtain a Gaussian standard deviation of $0\overset{\circ}{.}06$ or FWHM of $0\overset{\circ}{.}14$ (8′.3).

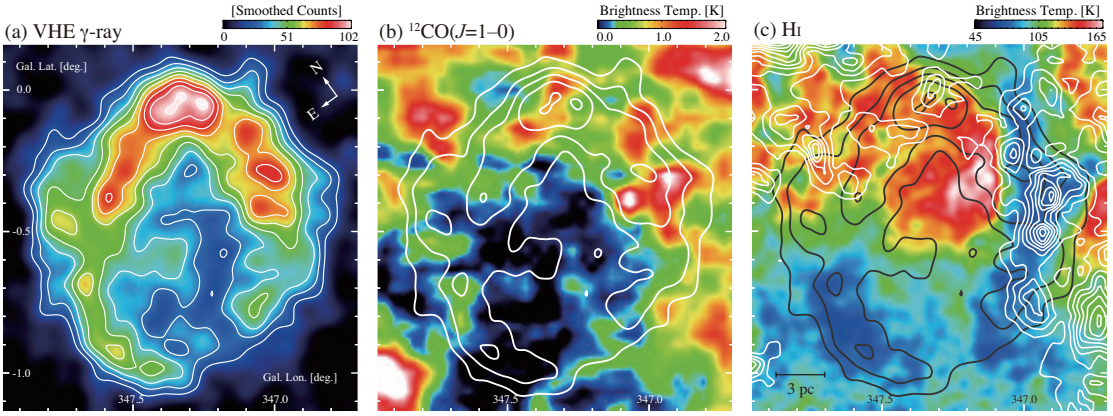

FIGURE 3.1: (a) The H.E.S.S. VHE γ-ray distribution of RX J1713.7−3946 in smoothed excess counts see Figure 2 of Aharonian et al., 2007. Note the use of Galactic coordinates to accentuate position relative to the Galactic plane. Contours are plotted every 10 smoothed counts from 20 smoothed counts. (b) Averaged brightness temperature distribution of ^{12}CO(J=1–0) emission in a velocity range of $V_{\rm LSR} = -20$ km s^{-1} to 0 km s^{-1} is shown in color (Fukui et al., 2003; Moriguchi et al., 2005). White contours show the H.E.S.S. VHE γ-ray distribution and are plotted every 20 smoothed counts from 20 smoothed counts. (c) Averaged brightness temperature distribution of HI emission obtained by ATCA and Parkes in a velocity range from $V_{\rm LSR} = -8$ km s^{-1} to -6 km s^{-1} (McClure-Griffiths et al., 2005) is shown in color. White contours show the ^{12}CO(J=1–0) brightness temperature integrated in the same velocity range every 1.0 K km s^{-1} ($\sim 3\sigma$).

3.3 Combined Analysis of the CO and HI Data

3.3.1 Distribution of CO and HI

Figure 3.1a shows VHE γ-ray distribution toward RX J1713.7−3946 obtained by H.E.S.S. and Figure 3.1b shows a velocity averaged distribution of ^{12}CO(J=1–0) overlaid on the VHE γ-ray distribution. The ^{12}CO(J=1–0) intensity becomes larger in the north to the Galactic plane than in the south and the most prominent features above 0.7 K are located in the northwest. The general ^{12}CO(J=1–0) distribution is shell-like associated with the γ-ray shell, showing weaker or no CO emission in part of the south. There are two regions where ^{12}CO(J=1–0) delineates particularly well the outer boundary of the shell in the southwest and east.

The ^{12}CO(J=2–1) distribution is qualitatively similar to the ^{12}CO(J=1–0) distribution (see Appendix Figure A2). A typical ratio of the J=2–1 / J=1–0 line intensities is $\sim$0.6, consistent with what are derived in the other molecular clouds without heat source (e.g. Ohama et al., 2010; Torii et al., 2011). We tentatively choose from Figure A2 in Appendix A, three major CO clouds, W, N, and SW, and three minor ones, E, NE, and SE, for the sake of discussion as schematically shown in Figure 3.2a, where we use ^{12}CO(J=2–1) data by taking an advantage of higher angular resolution.

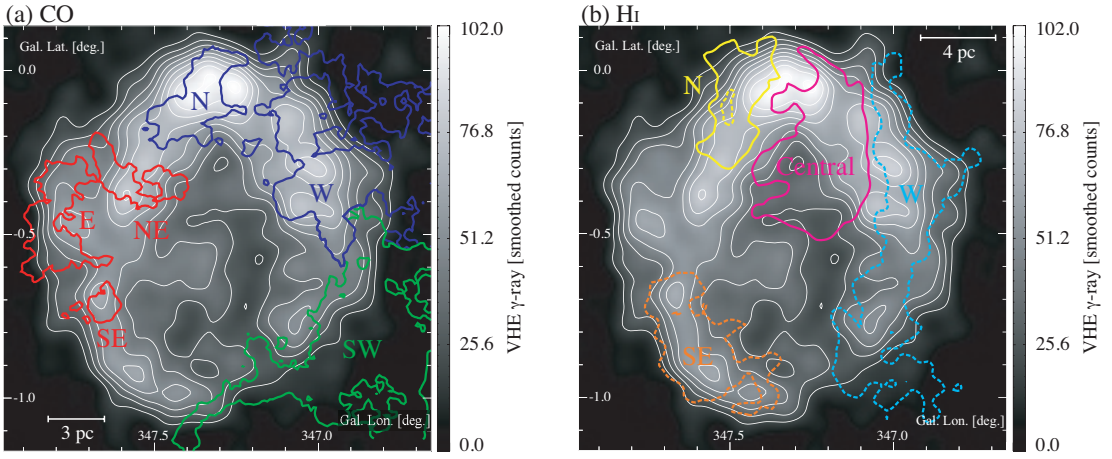

FIGURE 3.2: (a) Schematic of the identified ^{12}CO(J=2–1) clouds is shown in colored contours. The image and white contours show the VHE γ-ray distribution (Figure 3.1a). The integration velocity ranges are as follows; -8 to -2 km s^{-1} (contour level: 2.3 K km s^{-1}) for the SW cloud (CO), -17 to -5 km s^{-1} (contour level: 4.9 K km s^{-1}) for the W and N clouds (CO) and -6 to 0 km s^{-1} (contour level: 2.7 K km s^{-1}) for the NE, E and SE clouds (CO). (b) The locations of the identified HI clouds are shown in colored contours. The gray scale image and white contours show the VHE γ-ray distribution. The solid contours are for HI emission and the dashed contours are for dark HI. The integration velocity ranges are as follows; -8 to -2 km s^{-1} (contour level: 214 K km s^{-1}) for the W cloud (HI), -12 to -4 km s^{-1} (contour level: 780 K km s^{-1}) for the central and SE clouds (HI), and -14 to -11 km s^{-1} (contour level: 399 K km s^{-1}) for the N cloud (HI).

Figure 3.1c shows an overlay of the HI distribution superposed on the ^{12}CO(J=1–0) intensity in a velocity range of -8.0 to -6.0 km s^{-1}. The average HI brightness temperature ranges from 60 to 150 K and becomes higher toward the Galactic plane. The brightest HI of $\sim$150 K, the central cloud, is located toward the center of the SNR [(l, b)=(347.°25, $-0.°38$)] where little ^{12}CO(J=1–0) is seen. We find dark HI clouds of around 60 K in the west (W cloud) and in the southeast (SE cloud). These dark HI clouds are not due to absorption of the radio continuum radiation which is very weak toward the SNR (Lazendic et al., 2004). The dark HI W cloud well corresponds to the ^{12}CO(J=1–0) distribution, showing sharp edges both toward the east and west. The dark HI SE cloud has almost no counterpart in CO. The relatively bright HI emission is seen in the north of the SNR (N cloud). The N cloud tends to be located toward ^{12}CO(J=1–0) peaks, whereas the HI brightness shows a non-monotonic, more complicated behavior than in the W cloud. In the northeast, we find a rim of relatively lower HI brightness of $\sim$100 K toward (l, b)=(347.°5, $-0.°25$) that lies along the γ-ray shell. A schematic of the four main HI clouds is given in Figure 3.2b. The good correspondence of the HI clouds with the CO and the γ-rays supports that the HI is physically associated with the SNR.

In Figure 3.3 we show typical HI and CO profiles in the four main HI clouds. Figure 3.3 indicates that the HI emission is generally peaked at -10 km s^{-1} with small hints

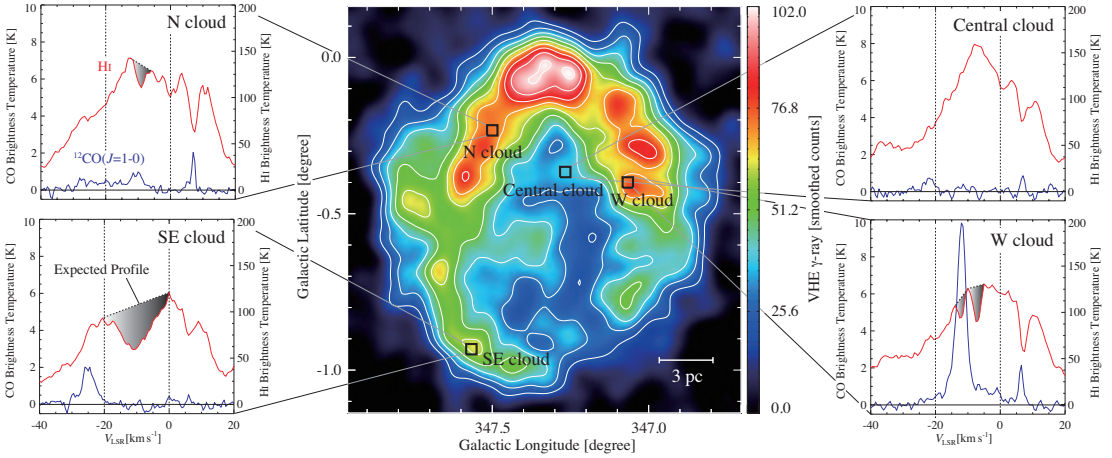

FIGURE 3.3: ^{12}CO(J=1–0) and HI profiles at the four HI clouds; the N cloud (l, b) = (347.°50, −0.°23), the SE cloud (l, b) = (347.°57, −0.°93), the central cloud (l, b) = (347.°27, −0.°37), and the W cloud (l, b) = (347.°07, −0.°40). The positions are denoted in the VHE γ-ray distribution. The shaded area shows expected profiles behind the self-absorption.

of saturation, confirming that the HI is associated with the SNR and is generally not optically thick. We find that narrow HI dips having depths of 20–30 K often correspond to ^{12}CO(J=1–0) emission features in the N and W clouds. The line widths of the narrow HI dips are as small as a few km s^{-1}. It is likely that these HI dips represent residual HI in cold CO gas seen as self-absorption. The broad HI dip in the SE cloud is also ascribed to self-absorption as argued into detail in Chapter 3.3.3.3 We show HI expected profiles of the background HI emission with a straight-line approximation as dashed areas in Figure 3 (e.g., Sato & Fukui, 1978).

3.3.2 Molecular Protons

In order to covert the ^{12}CO(J=1–0) intensity into the total molecular column density, we use an $X_{\rm CO}$ factor, which is defined as $X_{\rm CO}$ (cm^{-2}(K km s^{-1})$^{-1}$) = N(H$_2$) (cm^{-2})/W(^{12}CO) (K km s^{-1}). In order to derive an $X_{\rm CO}$ factor, the ^{12}CO(J=1–0) intensity is compared with the cloud dynamical mass (virial mass), or with the γ-rays produced via interaction of cosmic ray protons with molecular clouds. An $X_{\rm CO}$ factor therefore accounts for the total hadronic mass and is observationally uniform in the Galactic disk (e.g., Fukui & Kawamura, 2010). We here adopt an $X_{\rm CO}$ factor of 2.0×10^{20} W(^{12}CO) (cm^{-2}/K km s^{-1}) derived from the γ-rays and ^{12}CO(J=1–0) intensity in the Galaxy (Bertsch et al., 1993). We double the H$_2$ column density to derive the ISM protons in molecular form as shown in Figure 3.8a. Compared with the ^{12}CO(J=1–0) line, the ^{12}CO (J=2–1) line is not a common probe of the molecular mass. This is in part because the ^{12}CO(J=2–1) emission samples a smaller portion, having a higher

excitation condition, of a molecular cloud than traced by the ^{12}CO(J=1–0) emission. We estimate for instance that a typical fraction in area of the ^{12}CO(J=2–1) emission to the ^{12}CO(J=1–0) emission is about 70%–80% at the half-intensity level convolved to the same beam size in the present region from the CO data in Figure A2.

3.3.3 Atomic Protons

3.3.3.1 Optically Thin Case

We use the 21 cm HI transition to estimate the atomic proton column density. A usual assumption is that the HI emission is optically thin and the following relationship is used to calculate the HI column density:

$$N_{\rm p}({\rm HI}) = 1.823 \times 10^{18} \int T_L(V) dV \ \ ({\rm cm}^{-2}), \tag{3.1}$$

where $T_L(V)$ is the observed HI brightness temperature (K) (Dickey & Lockman, 1990). We note that this simple assumption is usually valid and apply Equation 3.1 to the regions where no HI dips are seen. It is certain that the narrow HI dips in the W and N clouds represent self-absorption by cold residual HI in CO gas from their exact coincidence with CO in velocity. The most prominent dark HI cloud, the SE cloud, shows large line-widths, not so common as self-absorption. We shall examine if the SE cloud represents self-absorption in the followings.

3.3.3.2 The Dark HI SE Cloud

We first show the integrated intensity image of the SE cloud in Figure 3.4a. The HI contours are every at 3.9σ noise level and shows significant details not apparent in Figure 3.1c, where a coarser color code is used. We find that the HI brightness variation is generally well correlated with the shell of VHE γ-rays in gray scale in the sense that HI brightness decreases toward the enhanced γ-rays. This trend lends a support for physical connection of the SE cloud with the γ-ray shell and may be interpreted as due to decrease in spin temperature with density increase in the self-absorbing HI gas (see Chapter 3.3.3.3). No ^{12}CO(J=1–0) emission is seen toward the SE cloud, expect for a possible small counterpart at (l, b) = (347.°64, $-$0.°72) and $V_{\rm LSR}$ = $-$6 to 0 km s^{-1} (Figure 3.2a and Figure A2), suggesting that density of the SE cloud is lower than the CO clouds.

3.4b shows a typical HI profile in the SE cloud having a deep and broad dip. The large velocity span of 20 km s^{-1} is not so common as a self-absorption feature; in nearby

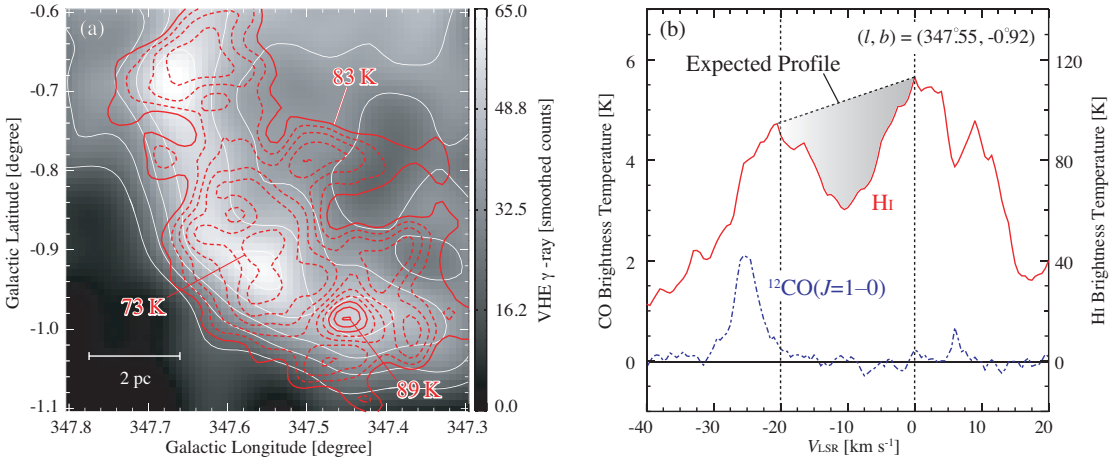

FIGURE 3.4: (a)The H.E.S.S. VHE γ-ray distribution toward the SE cloud (Aharonian et al., 2007). Red contours show averaged HI brightness temperature distribution in a velocity range from -15 km s^{-1} to -5 km s^{-1} (McClure-Griffiths et al., 2005). (b) The HI and ^{12}CO(J=1–0) spectra at (l, b) =(347.°55, $-0.°92$). The shaded area shows an expected HI profile.

dark clouds HI self-absorption is generally narrow with a few km s^{-1} in line width (e.g., Krčo & Goldsmith, 2010), whereas HI self-absorption as broad as 10 km s^{-1} is seen in giant molecular clouds (e.g., Sato & Fukui 1978). The SE cloud delineates the γ-ray shell (3.4a) and is possibly compressed gas by the wind of a high-mass star, the SN progenitor. We have investigated the velocity distribution of the SE cloud as given in Appendix A. We find that the SE cloud shows a strong velocity gradient which matches the blue-shifted part of an expanding swept-up shell. Such a shell is a natural outcome of the stellar-wind compression by the SN progenitor, supporting that the broad HI dip is ascribed to the acceleration of HI gas by the wind. A HI stellar-wind shell in Pegasus driven by an early B-type star indeed shows a line width as large as 15 km s^{-1} (Yamamoto et al., 2006), similar to that of the SE cloud. The difference from the narrow HI dips in the W and N clouds may be due to density; the SE cloud has lower density and is subject to stronger acceleration than the CO clouds with narrow HI dips (see for further discussion Chapter 3.4.1), whereas the CO clouds having higher density are less accelerated by the wind, making a systematic velocity gradient less clear in CO than in HI (see Figure B2).

Figure 3.5a shows the distribution of the extinction A_V toward RX J1713.7−3946 (Dobashi et al., 2005), and indicates that the SE cloud, as well as the rest of the shell, is traced by the enhanced optical extinction. This lends another support for the self-absorption interpretation of the SE cloud. Figure 3.5b shows the total (molecular and atomic) ISM proton column density both in the SNR (derived later in Chapter 3.3.4) and in the foreground within 1 kpc, which is supposed to correspond mainly to the optical extinction. The total proton column density N_p of $\sim 10^{22}$ cm^{-2} in Figure 3.5b

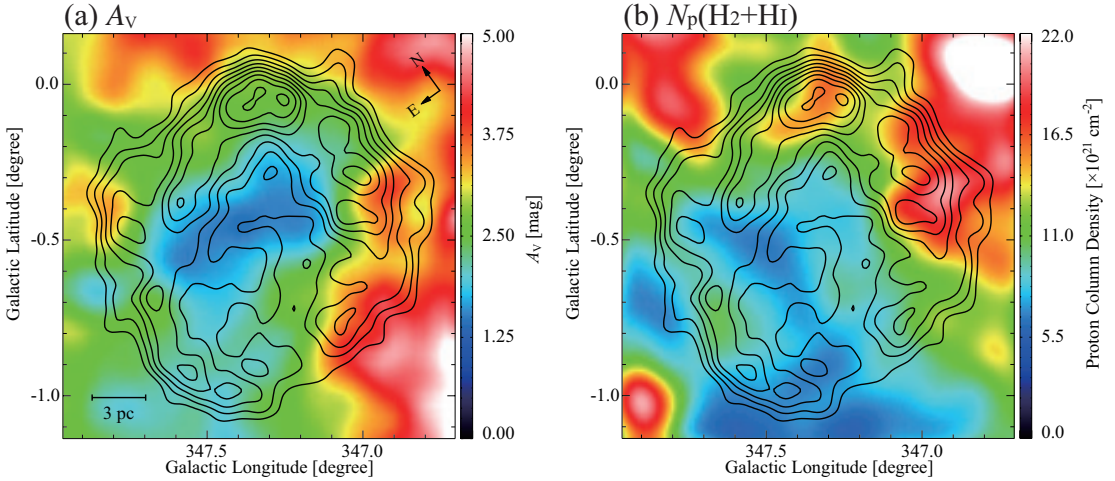

FIGURE 3.5: (a)A_V distribution (Dobashi et al. 2005) is shown in color. Contours are the same as in Figure 3.5a. (b) Distribution of column density of the total ISM protons estimated from both CO and HI in a velocity range from $V_{LSR} = -20$ to 10 km s^{-1}. Here the HI self-absorption is taken into account. Contours are the same as in Figure 3.5a).

corresponds to extinction of ∼4 mag if we adopt the relationship $N_p(\mathrm{cm}^{-2}) = 2.5\times10^{21} \cdot A_V$ (magnitude) (Jenkins & Savage 1974). The extinction toward the SE cloud is 2–3 mag in Figure 3.5a and is consistent with the HI self-absorption by considering the contamination by the foreground stars which tends to reduce A_V toward the Galactic plane.

In summary, we find it a reasonable interpretation that the SE cloud represents HI self-absorption associated with the SNR shell.

3.3.3.3 Analysis of the HI Self-absorption Dips

We shall briefly review some basic properties of HI gas in order to understand the behavior of HI brightness (e.g., Sato & Fukui, 1978). The spin temperature, T_s, of HI is ∼100 K or higher in warm neutral medium at particle density less than 10 cm^{-3}. T_s decreases with density from 100 K down to 10 K in a density range of 100–1000 cm^{-3} (e.g., Figure 2 in Goldsmith et al., 2007). The temperature decrease is mainly due to higher shielding of stellar radiation and increased line cooling.

It is well established that HI is converted into H_2 on dust surfaces with increasing of the gas column density and UV shielding and that H_2 is dissociated by cosmic rays and UV photons (e.g., Allen & Robinson, 1977). The equilibrium HI abundance is determined by the balance between formation and destruction of H_2 and the residual density of HI is about 10^{-2} that of H_2 in typical interstellar molecular clouds (Allen & Robinson, 1977; Sato & Fukui, 1978). We also note that the H_2 abundance should be time dependent

since the formation of H_2 is a slow process in the order of 10 Myr for density around 100 cm^{-3} (e.g., Allen & Robinson, 1977).

Based on the HI–H_2 transition, we interpret the dark HI in Figure 3.2b as representing the HI with lower T_s. The CO W cloud shows a good spatial coincidence with the dark HI W cloud as is consistent with the interpretation. The other prominent dark HI region, the SE cloud, shows no CO and we suggest that its density is lower and its T_s is higher than that in the CO W cloud. HI brightness $T_L(V)$ is expressed as follows (e.g., Sato & Fukui, 1978):

$$T_L(V) = T_s[1 - e^{-\tau(V)}] + T_L^{FG}(V) + [T_L^{BG}(V) + T_C^{BG}]e^{-\tau(V)} - (T_C^{FG} + T_C^{BG}), \quad (3.2)$$

where $T_L(V)$, T_s, $\tau(V)$, $T_L^{FG}(V)$, and $T_L^{BG}(V)$ are the observed HI brightness temperature, the spin temperature, the optical depth of cold HI in the cloud, and the foreground and background HI brightness temperature, respectively, at velocity V. T_C^{FG} and T_C^{BG} are the continuum brightness temperature at 21 cm wavelength in the foreground and background of the cloud, respectively. The radio continuum emission is weak in RX J1713.7−3946 (Lazendic et al., 2004), and T_C^{FG} and T_C^{BG} are nearly zero as compared with $T_L(V)$.

We are then able to estimate the HI column density of dark HI clouds. Figure 3.4b shows the HI self-absorption dip with the background HI emission interpolated by a straight line connecting the two shoulders at 0 and 20 km s^{-1}. This gives a conservative estimate because the actual background HI shape perhaps has a more intense peak at −10 km s^{-1} as seen in the northern area of the SNR. The spin temperature T_s of the dark HI gas is an unknown parameter. We estimate T_s to be less than ∼55 K from the lowest HI brightness at the bottom of the dip in Figure 3.4b and higher than ∼20 K, where the temperature of the CO clouds is ∼10 K (see Chapter 2.4.1). We estimate the absorbing dark HI column density to be N_p(HI) = 1.0×10^{21} cm^{-2} (optical depth = 0.8), 1.8×10^{21} cm^{-2} (optical depth = 1.1) and 3.1×10^{21} cm^{-2} (optical depth =1.5) for assumed three cases T_s = 30, 40 and 50 K, respectively, for the half-power line width Δv=10 km s^{-1}, where the HI optical depth $\bar{\tau}$ is estimated by Equation 3.2 and N_p(HI) by the following relationship;

$$N_p(\text{H I})\ (\text{cm}^{-2}) = 1.823 \times 10^{18}\, T_s\ (\text{K})\ \Delta v\ (\text{km s}^{-1})\ \bar{\tau}. \quad (3.3)$$

We shall here adopt T_s = 40 K and a corresponding dark HI optical depth of 1.1. A higher T_s gives a higher optical depth and vice versa. The relatively large optical depth around 1 is consistent with the fairly flat HI dip in Figure 3.4b, which suggests weak saturation. We also tested the effects of elevating the background HI by 15 K and found

a small change of 5×10^{20} cm^{-2}. The error is mainly introduced by the straight-line approximation and uncertainty in T_s of ∼10 K. We infer that the dark HI column density is accurate within a systematic error of $\sim 1 \times 10^{21}$ cm^{-2}.

The average HI density in the SE cloud is roughly estimated to be 150 cm^{-3} by dividing 1.8×10^{21} cm^{-2} by ∼4 pc, the line-of-sight length of the thick ISM shell, following the three-dimensional model described in Chapter 3.3.5. This density is significantly lower than the critical density for collisional excitation of the ^{12}CO (J=1–0) transition, ∼1000 cm^{-3}, consistent with no CO emission from the SE cloud and with low spin temperature around 40 K.

We also extended such an analysis to the regions with narrow HI dips associated with CO emission, where we adopt $T_s = 10$ K, the kinetic temperature of the CO gas. The small dips in these regions indicate that the HI optical depth is generally as low as ∼0.1 reflecting a small fraction of the residual HI in CO gas. We show the distributions of the peak optical depth of the HI self-absorption in Figure 3.6a, and the derived total HI column density distribution, the sum of the HI in emission and self-absorption in Figure 3.6b, where the SE cloud is significant. We shall hereafter refer to the dark HI of T_s = 40 K as "cool HI" and that of $T_s = 10$ K as "cold HI".

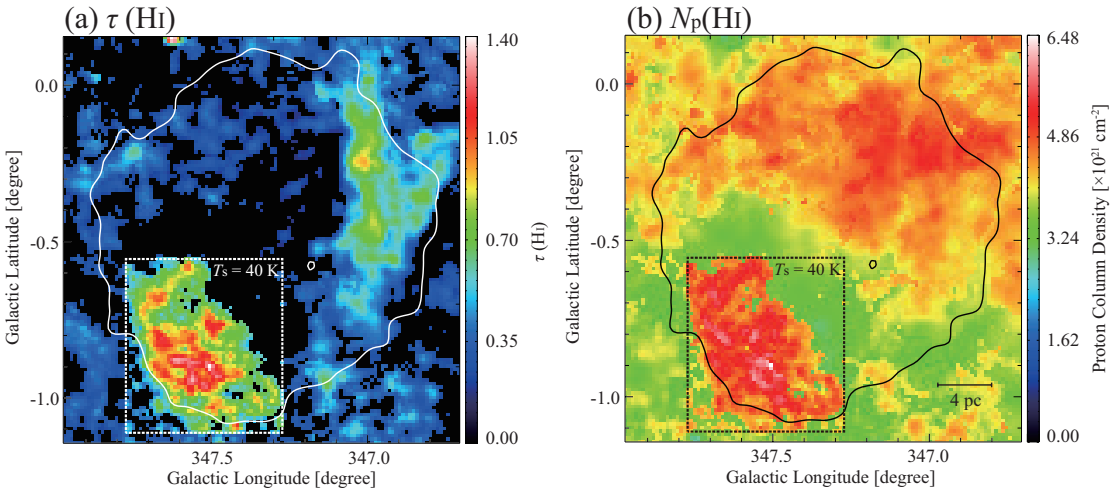

FIGURE 3.6: (a) Distribution of peak optical depth of the HI self-absorption. (b) Distribution of atomic proton column density, N_p(HI), estimated for the HI emission and self-absorption. The velocity range in both the figures is from −20 km s^{-1} to 0 km s^{-1}. Contours show the H.E.S.S. VHE γ-ray distribution (Aharonian et al., 2007) and are plotted at 20 smoothed counts. We assume spin temperatures T_s of 40 K and 10 K, inside and outside the dotted box toward the SE cloud, respectively.

3.3.4 Total ISM Protons

The number of the total ISM protons in the SNR is given by summing up the three components in a velocity range from -20 to 0 km s^{-1}; H_2 derived from ^{12}CO(J=1–0), dark HI (dips) and warm HI (emissions). The results are shown as spatial distributions in Figure 3.7. Figure 3.7a, 3.7b, 3.7c, and 3.7d, show $N_{\rm p}(H_2)$, $N_{\rm p}$(HI), $N_{\rm p}(H_2$+HI), and VHE γ-rays, respectively. We see that the total ISM protons $N_{\rm p}(H_2$+HI) show a shell-like shape similar to the VHE γ-rays which significantly improves the correlation with the γ-rays as compared with the case of molecular gas only. We therefore conclude that the contribution of HI is critical as well as H_2 in counting the ISM protons. We find that in the south the total ISM proton is dominated by the atomic gas, whereas in the north the molecular and atomic protons are both important. A more quantitative comparison will be given in Chapter3.3.5.2. Similar diagrams of the total ISM protons to Figure 3.7 are presented for the optically thin case for reference Figure C1 in Appendix C, where the shell-like distribution toward the SE cloud is missing.

3.3.5 The γ-Rays and the ISM Protons

3.3.5.1 Gamma-ray distribution

The VHE γ-ray distribution obtained by H.E.S.S. is a nearly circular-symmetric shell with some ellipticity elongated in the north–south direction. In order to gain an insight into the distribution of the γ-ray emissivity we undertake a simple analysis of the γ-ray distribution. We first adopt an elliptical annular ring in the analysis, while (Aharonian et al., 2006b) made a similar analysis by using a circular annular ring in correlating γ-rays and NANTEN CO intensity (see their Figure 17).

We estimated the radius of the γ-ray shell as defined at a half-intensity level of the peak γ-ray smoothed count every 15 deg for an assumed center. We averaged the radii in angle and minimized the sum of the squares of the deviation from the average. This process gives a central position to be $(l, b) = (347.^{\circ}34, -0.^{\circ}52)$. For this central position, we plotted the radius every 15 degrees and found that a sinusoidal distribution is a reasonable approximation as expected. Fitting this plot by a sinusoidal curve, we find that the shell is approximated by an elliptical shape with an aspect ratio of 1.1 whose major axis is almost in the north–south direction. This elliptical shape is adopted in Figure 3.8a.

Figure 3.9 shows the radial scatter of γ-ray smoothed counts and an averaged value shown by a step function in radius r every 0.05 deg. Here, we also adopted the elliptical

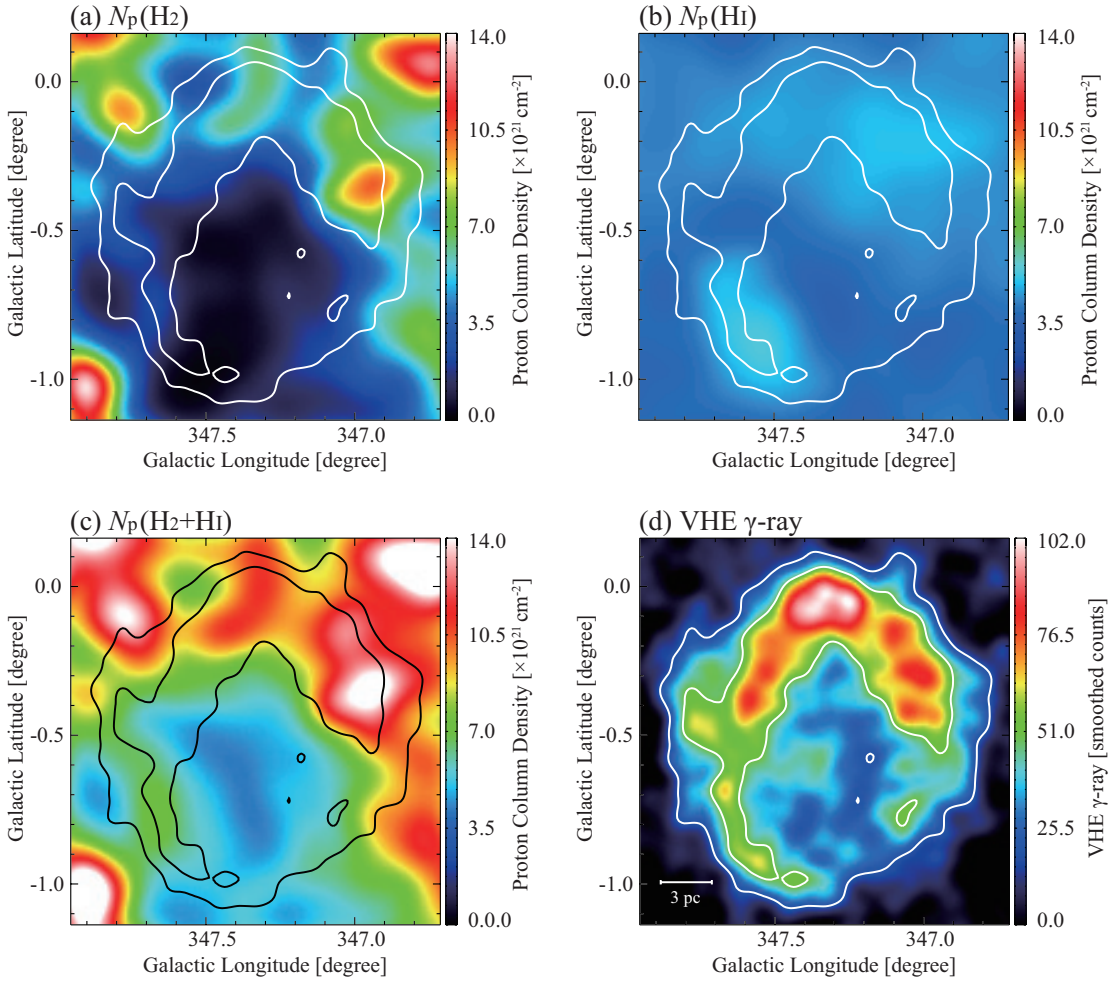

FIGURE 3.7: (a) Distributions of column density of ISM protons N_p estimated from ^{12}CO(J=1–0) $N_p(H_2)$, (b) HI emission with correction for the HI self-absorption N_p(HI) and, (c) sum of $N_p(H_2)$ and N_p(HI). All the data sets used here are smoothed to an HPBW of VHE γ-ray distribution with a Gaussian function. (d) VHE γ-ray distribution. Contours are plotted every 50 smoothed counts from 20 smoothed counts.

shape and normalized the radius to that of the major axis with the elliptical modification. After several trials of different functional forms, we found that a Gaussian radial distribution of the γ-ray emissivity per volume reproduces well the projected radial distribution in Figure 3.9. In the fitting we have two free parameters of the Gaussian shape, the peak radius r_0 and the sigma σ expressed as follows:

$$F(r) = A \times e^{-(r-r_0)^2/2\sigma^2}, \tag{3.4}$$

where A is a normalization coefficient. By requiring that the error in the fitting becomes minimum in the projected distribution shown by the step function, we found that $r_0 =$ 0.46 deg and $\sigma = 0.10$ deg give the best fit as shown in Figure 3.9. This distribution shows that the observed shell is consistent with a shell of a half-intensity thickness ∼0.24

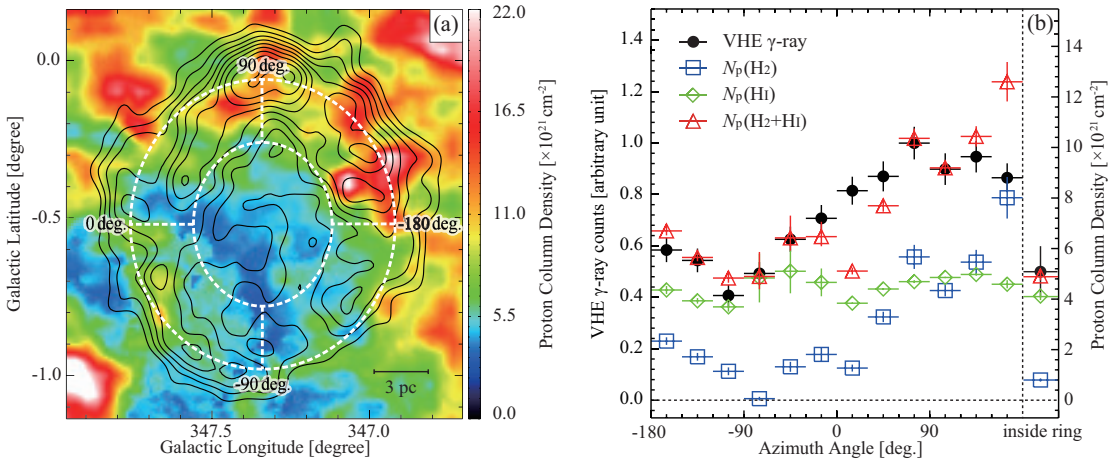

FIGURE 3.8: (a) Distributions of column density of the total ISM protons $N_{\rm p}({\rm H_2+HI})$ in a velocity range from -20 km s^{-1} to 0 km s^{-1}. Contours are the same as in Figure 3.1a. (b) Azimuthal distributions of $N_{\rm p}({\rm H_2})$, $N_{\rm p}({\rm HI})$, $N_{\rm p}({\rm H_2+HI})$, and VHE γ-ray smoothed counts per beam between the two elliptical rings shown in (a). The proton column densities are averaged values between the rings (see the text). Semimajor and semiminor radii of the outer ring are 0.°46 and 0.°42, respectively, and the radii of the inner ring are half of them. The same plots inside the inner ring are shown on the right side of (b).

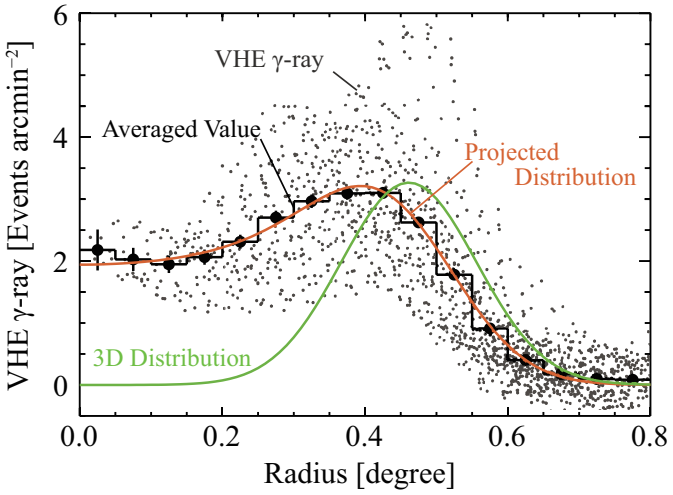

FIGURE 3.9: Radial distribution of VHE γ-ray radiation. Small dots show the distributions of all the H.E.S.S. data points and large filled circles with error bars show averaged values at each radius. We assume a 3D spherical shell with a Gaussian-like intensity distribution along its radius to approximate the VHE γ-ray distribution (see the text). The green line shows the estimated 3D Gaussian distribution and the red line shows its projected distribution. The peak radius and the full width at half maximum of the green line are estimated to be 0.°46 ($\sim$ 8.0 pc) and 0.°24 ($\sim$ 4.2 pc), respectively.

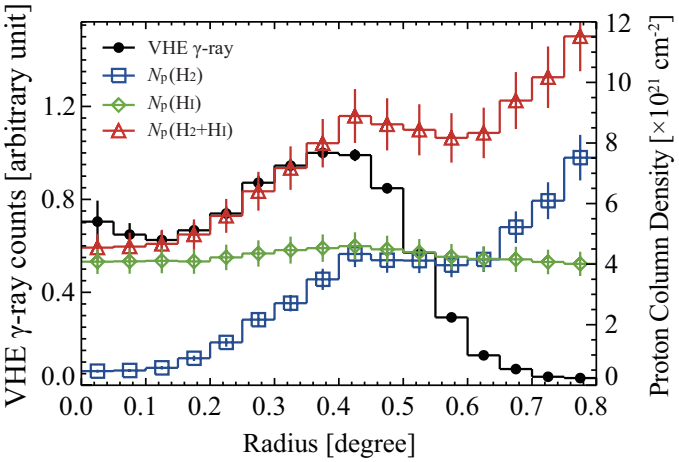

FIGURE 3.10: Radial distributions of averaged values of VHE γ-ray radiation, $N_p(H_2)$, $N_p(HI)$, and $N_p(H_2+HI)$. $N_p(H_2)$ and $N_p(HI)$ show column densities estimated from $^{12}CO(J=1–0)$ and HI, respectively, and $N_p(H_2+HI)$ shows the total ISM proton column density.

deg with nearly zero emissivity toward the center. This analysis indicates that the γ-rays are mainly emitted in a thick shell of 8.0 pc radius and 4.2 pc width at the half-intensity level with nearly zero emission from the inner part. A similar thick-shell model was also obtained by (Aharonian et al., 2006b). Numerical modeling of the γ-ray emission has been undertaken by several authors and indicates that the γ-ray emission has a rather steep gradient beyond the peak of the shell in either of the leptonic or hadronic scenario (e.g., Jun & Norman, 1996; Zirakashvili & Aharonian, 2010). The fitting to the H.E.S.S. data above shows that the gradient in the γ-ray distribution is not so steep toward the outside, which may be due to smearing in space by averaging. We shall not try a further elaborated analysis here due to the limiting angular resolution of H.E.S.S. which is $0.^{\circ}14$ deg (FWHM).

Figure 3.10 shows that the projected radial distribution of ISM protons follows a fairly similar distribution to the γ-rays inside the SNR. This is consistent with that the ISM distribution is also shell-like with an inner cavity as is consistent with the stellar wind shell discussed in Chapter 3.4.1; if the ISM has no cavity in the inner part, the projected distribution of the ISM should increase toward the center. We shall assume hereafter that the ISM distribution is also approximated by the same Gaussian shape as the γ-rays with a radius of 8.0 pc with a thickness of 4.2 pc at the half-intensity level.

3.3.5.2 Comparison between the γ-Rays and the ISM Protons

In the hadronic scenario, the target distribution should be correlated with the γ-ray distribution for a uniform cosmic-ray distribution. This correlation should be seen inside the shell of the SN shock which has a sharp gradient beyond its outer radius. We expect

that the ISM protons are distributed beyond the outermost edge of the shell where cosmic-ray protons cannot reach by diffusion. Beyond the SNR shock, the γ-ray emission profile may be influenced by components from the diffuse cosmic-ray background and by the energy dependent transport of escaping cosmic-rays from RX J1713.7−3946 into the clumpy ISM (e.g., Gabici et al., 2009; Casanova et al., 2010a,b). We are able to avoid possible effects of such cutoff by taking the radius of the correlation analysis well within the SNR shell where the cosmic-ray protons do not decrease in energy density.

The ISM proton distribution is shown in 3.8a with the two annular elliptical rings along the shell, where the size of the outer ring was chosen to meet the requirement above. Figure 3.8b shows a comparison between the ISM protons and γ-rays in the position angle shown in Figure 3.8a, where the vertical scale is adjusted so that the correspondence with the VHE γ-rays becomes optimum. Here, the error in the VHE γ-ray emission from the publicly available H.E.S.S. image is approximately (smoothed counts)$^{0.5}$. In Figure 3.8b, the uncertainty in the dark HI in the SE cloud, $1{\times}10^{21}$ cm^{-2}, is in the order of 10%–20% of the total. The total ISM proton density shows a good agreement with the VHE γ-ray angular distribution and also the central part in the inner ring. We recall that CO alone showed marked deficiency toward the SE cloud as compared with the γ-rays (see Figure 17 of Aharonian et al., 2006b). The present analysis indicates that the deficiency is recovered by including HI and has shown that the total gas of both atomic and molecular components has a good correlation with the VHE γ-rays in the annular ring. The total mass of the ISM protons responsible for the γ-rays is $2.0{\times}10^4$ $M_\odot$ over the whole SNR (radius 0.65 deg); the mass of molecular protons is $0.9{\times}10^4$ $M_\odot$ and that of atomic protons is $1.1{\times}10^4$ $M_\odot$, where we assume that the ISM protons interacting with the cosmic-ray protons is proportional to the VHE γ-rays (Chapter 3.3.5.1, Figure 3.10).

There are two points in Figure 3.8b, for which additional remarks may be appropriate. One is the point at an azimuth angle of 115 deg which may be estimated too low due to the lack of correction for the self-absorption because of the large velocity shift in the expanding shell (see Figure B1). Another is the point at an azimuth angle of 165 deg where the strong CO emission (peak A after Fukui et al., 2003) increases the proton column density, although the increased protons may not be interacting with the cosmic-ray protons beyond the SNR shock, leading to less γ-rays.

An independent test is made by the radial distribution of the ISM protons given in Figure 3.10, where an average taken over the same binning as the γ-rays in Figure 3.9 is shown by a step function, and the total ISM protons and γ-rays are superposed with the same proportional factor as adopted in Figure 3.8. Here, the error in the VHE γ-ray emission is approximately (oversampling-corrected total smoothed count)$^{0.5}$ normalized

to 1 (arcmin)^2. We see that the $N_{\rm p}$(H$_2$+HI) and γ-rays show a good agreement inside the shell and the γ-rays sharply decrease outside the shell. This offers another presentation of the good correlation between the γ-rays and the ISM protons.

We argue that the apparent anti-correlation between the HI brightness at the bottom of the dips and the γ-rays in the SE cloud (Figure 3.4) is consistent with that the HI dips are due to the cool and dense HI gas. The anti-correlation is interpreted that the spin temperature $T_{\rm s}$ of HI decreases with density (Chapter 3.3.3.3) and that the γ-rays increase with the ISM proton density locally in the SE cloud, demonstrating detailed correspondence between the γ-rays and the ISM protons which is mainly atomic. The small and narrow HI dips in the W and N clouds have the HI column density less than 10^{20} cm^{-2}, significantly lower than the typical molecular column density by two orders of magnitude. So, in most of the regions except for the SE cloud the HI column density is dominated by emission but not by self-absorption. For the sake of reference, we show a set of similar diagrams of ISM proton distributions for the optically thin case in Figures C2 and C1 in Appendix C, corresponding to Figures 3.8 and 3.10, respectively.

Before concluding this Chapter, we cautiously note that the cool/cold HI could not be estimated accurately, if the cool/cold HI is optically thick, if the cool/cold HI lies behind optically thick foreground HI in the line of sight, or if the background HI profile has a different shape from its neighbors. Such effects, while posing intrinsic limits for probing cool/cold HI, are relatively unimportant for nearby objects at a distance of 1 kpc or less where foreground HI is not important. The dark HI W and SE clouds are probably good examples where the cool/cold HI is well traced by the low HI brightness, whereas the N cloud with higher HI brightness may be partially affected by the foreground HI in the line of sight.

3.4 Discussion

3.4.1 The Evacuated Cavity by the Stellar Wind

It is likely that the CO shell in Figure 3.1b was formed over a timescale of Myr by the stellar wind of the progenitor, an OB star that exploded as a supernova (SN) 1600 yr ago. The total velocity span of the CO shell, $\sim$20 km s^{-1}, is much smaller than the SN shock speed and indicates that it takes Myr to form the shell of the ISM as roughly estimated by dividing the radius 9 pc by 10 km s^{-1}. Molecular gas expanding at 10 km s^{-1} can move only 0.01 pc in 1000 yr. Therefore, the current CO distribution has little been affected by the supernova explosion (SNe) and holds the initial condition before the shock interaction.

TABLE 3.1: A Comparison between RX J1713.7−3946 and Pegasus Loop

	RX J1713.7−3946[a]	Pegasus Loop[b]
Distance (kpc)	1	0.1
Diameter (pc)	17.4	25
Total mass of the ISM ($M_\odot$)	∼20000[c]	∼1500
Thickness of the ISM shell (pc)	∼4.2	∼5
Peak brightness of HI (K)	∼170	∼40
Line width of HI (km s^{-1})	∼20	∼16
Expansion velocity of the gaseous shell (km s^{-1})	∼10	∼7–9
Spectral type of the progenitor	B1 V/B0 V[d]	B2 IV

Notes. The Pegasus loop may consist of two shells and the mass should be regarded as an upper limit (Yamamoto et al., 2006).
[a] Fukui et al. (2003); Moriguchi et al. (2005)
[b] Yamamoto et al. (2006)
[c] Present work.
[d] Cassam-Chenaï et al. (2004)

While a stellar-wind shell with a known central star is not often observed elsewhere, one such example is the Pegasus loop found in ^{12}CO(J=1–0), HI, and dust emission at (l, b) = (109°, −45°) centered on a runway star HD886 (B2 IV) (Yamamoto et al., 2006). The Pegasus loop is located at ∼100 pc in a relatively uncontaminated environment outside the Galactic plane. No SNe occurred yet in this shell. A comparison between RX J1713.7−3946 and the Pegasus loop is given in Table 3.1. In Pegasus the swept-up shell of the ISM has a width of ∼5 pc for a radius of ∼18 pc and a total mass of ∼1500 $M_\odot$. The shell is mostly atomic and consists of 78 smaller ^{12}CO(J=1–0) clumps (see Figure 10 in Yamamoto et al., 2006). The clumped CO is a natural outcome of thermal/gravitational instability and seems common in such a shell. The shell is expanding at a total velocity span of 15 km s^{-1}. The HI density inside the shell is ∼1 cm^{-3} in the north, where the stellar wind evacuated the ISM over 1 Myr. The Pegasus loop is located in a somewhat lower-density environment than RX J1713.7−3946 and offers an insight into the initial condition of the ISM prior to the SNe in RX J1713.7−3946.

Inoue et al. (2009, 2012) carried out numerical simulations of the hydro-dynamical interaction between the shock wave and the highly inhomogeneous neutral gas to model the interaction in RX J1713.7−3946. The SN in RX J1713.7−3946 exploded in the cavity with average density less than 1 cm^{-3} (e.g., Zirakashvili & Aharonian, 2010; Morlino et al., 2009; Berezhko & Völk, 2008) and the dense shell with CO clumps remaining more or less as they were prior to the SNe. The SN shock front moves almost freely at ≥ 3000 km s^{-1} in the cavity in the early phase of ∼1000 yr and begins to interact with the dense and thick clumpy ISM wall swept-up by the stellar wind only in the last few 100 yr. The γ-ray shell is not strongly deformed, while we see some deviations of a pc-scale from a perfect circular shell, suggesting effects of recent dynamical interaction.

The interaction between molecular clumps and the shock is observed as the X-ray enhancement around dense molecular clumps at a spatial resolution higher than 0.5 pc. (see Chapter 2) showed that the molecular clump peak C is rim-brightened in X-rays, suggesting that it is a dense clump overtaken by the shock, and peak A (Fukui et al., 2003) is also X-ray-brightened only toward its inner edge, indicating the shock interaction at the inner boundary of peak A. Inoue et al. (2012) showed that the initial magnetic field B of 1 μG is amplified to 0.1–1 mG near dense clumps by the enhanced turbulence driven by the shock. The stronger magnetic field explains the X-ray enhancement as due to the enhanced synchrotron emission that is proportional to B^2, or, due to increased acceleration. Inoue et al. (2012) also showed that the shock speed v_s is significantly reduced locally with density n (cm^{-3}) such that v_s $\sim$3000 km s^{-1}/$\sqrt{n/n_0}$, where n_0 = 1 cm^{-3}. This dependence of v_s on density can explain the absence of thermal X-rays in the SNR because the molecular gas is too dense to be affected by the shock to emit thermal X-rays (Inoue et al., 2012). A uniform lower-density case with significant thermal X-rays by shock heating is presented by Ellison et al. (2010) but such a model is not applicable to the highly inhomogeneous ISM of RX J1713.7−3946 (Inoue et al., 2012, see also discussion in Section 4 of Ellison et al., 2010). The picture above is also consistent with that peak C, having density greater than 10^4 cm^{-3} (see Chapter 2.4.2), and has survived without erosion.

3.4.2 The γ-Ray Emission Mechanism

VHE γ-rays are emitted via two mechanisms, either leptonic or hadronic processes. The leptonic process explains γ-rays via the inverse Compton effect between cosmic-ray electrons and low energy photons. In the hadronic scenario, γ-rays are emitted by the decay of neutral pions which are produced in the high energy reactions between cosmic-ray protons and ISM protons. DSA is the most widely accepted scheme of particle acceleration (e.g., Bell, 1978; Blandford & Ostriker, 1978; Jones & Ellison, 1991; Malkov & Drury, 2001). The previous works on RX J1713.7−3946 show that the observed spectral energy distribution of γ-rays and X-rays is explained by either of the leptonic and/or hadronic mechanisms if DSA works to accelerate the particles (Aharonian et al., 2006b; Porter et al., 2006; Katz & Waxman, 2008; Berezhko & Völk, 2008; Ellison & Vladimirov, 2008; Tanaka et al., 2008; Morlino et al., 2009; Acero et al., 2009; Ellison et al., 2010; Patnaude et al., 2010; Zirakashvili & Aharonian, 2010; Abdo et al., 2011; Fang et al., 2011)

In the hadronic scenario, where the neutral pion decay determines the γ-rays via proton–proton reactions, the average density of the target protons is constrained by the total energy of cosmic-ray protons; the average target density greater than 0.1 cm^{-3} is required

to produce cosmic-ray protons having the total energy of 10^{51} erg, for the maximum energy of SNe, while higher target density is required for less cosmic-ray proton energy. In the leptonic scenario, where the inverse Compton process produces γ-rays, the critical parameter is the magnetic field which constrains the synchrotron loss timescale of cosmic-ray electrons; a magnetic field of order of 10 μG is usually required (e.g., Tanaka et al., 2008).

We here argue that the highly inhomogeneous distribution of the ISM, the cavity, and the dense and clumpy wall opens a possibility to accommodate the low-density site for DSA and the high-density target simultaneously as discussed into detail by (Inoue et al., 2012). A similar argument on the hadronic interaction between cosmic-ray protons with the ambient dense clouds has been presented by Zirakashvili & Aharonian (2010). In this picture, first, the cosmic rays are accelerated via DSA in the low-density cavity, and second, the cosmic-ray protons reach and react with the target protons in the dense wall to produce γ-rays. The main energy range of the cosmic-ray protons required for hadronic VHE γ-rays is 10–800 TeV (Zirakashvili & Aharonian, 2010). The penetration depth, $l_{\rm pd}$, of cosmic rays is expressed as follows (Inoue et al., 2012):

$$l_{\rm pd} \sim 0.1\eta^{1/2} \left(\frac{E}{10\ {\rm TeV}}\right)^{1/2} \left(\frac{B}{100\ \mu{\rm G}}\right)^{-1/2} \left(\frac{t_{\rm age}}{10^3\ {\rm yr}}\right)^{1/2} \ ({\rm pc}) \tag{3.5}$$

where E, B, and $t_{\rm age}$ are the particle energy, the magnetic field, and the age of the SNR. The parameter η is the so-called "gyro-factor" and has some ambiguity. In the SNR, it is reasonable to consider $\eta \sim$1 at least around the cloud (Uchiyama et al., 2007). Thus, the penetration depth of the protons in the above energy range is 0.3–2.8 pc for the magnetic field of 10 μG and 0.1–0.9 pc for 100 μG in a typical timescale of $\sim 10^3$ yr. The penetration depth of the cosmic-ray electrons is determined by taking $t_{\rm age}$ equal to the synchrotron loss timescale (e.g., Tanaka et al., 2008) in Equation 3.6 and becomes energy-independent for the X-ray emitting electrons of 1–40 TeV as follows:

$$l = 0.026\ \eta^{1/2} \left(\frac{B}{100\ \mu{\rm G}}\right)^{-3/2} \ ({\rm pc}). \tag{3.6}$$

We estimate l to be from 0.8 pc for 10 μG to 0.026 pc for 100 μG if $\eta = 1$. cosmic-ray protons can therefore reach and penetrate into the dense gas within pc-scale of the acceleration site to produce VHE γ-rays, while the cosmic-ray electrons stay relatively closer to the acceleration site, in particular, near the dense gas having strong magnetic field. This offers an explanation on the hadronic γ-ray production, and the correlation between the γ-rays and target protons in Figures 3.4, 3.8, and 3.10 is a natural outcome in the scenario (Inoue et al., 2012).

Gabici et al. (2007) discussed the importance of the energy-dependent interaction between cosmic-ray protons and molecular clouds, and Zirakashvili & Aharonian (2010) discussed that the γ-ray spectrum may not distinguish the leptonic and hadronic scenarios in case of RX J1713.7−3946 due to such energy dependence. Recently, *Fermi* Large Area Telescope (LAT) observations showed that the GeV spectrum of RX J1713.7−3946 is hard, similar to what is expected in the leptonic scenario, and Abdo et al. (2011) discussed that the hard spectrum may favor to the leptonic scenario. Inoue et al. (2012), however, argued that the hard *Fermi* LAT GeV spectrum is explained well also by the hadronic scenario as due to the energy-dependent penetration of cosmic-ray protons into the dense clouds and that the leptonic scenario is not unique to explain the spectrum. Inoue et al. (2012) confirmed that the γ-ray spectrum becomes similar both for the leptonic and hadronic scenarios, not usable to distinguish the two scenarios, as noted by Zirakashvili & Aharonian (2010) and concluded that the hadronic origin is testable only by comparing γ-rays with the ISM target distribution. The present results have demonstrated that the ISM proton distribution shows indeed a good spatial correspondence with the γ-rays by taking into account the contribution of the HI and match with the prediction by Zirakashvili & Aharonian (2010) and Inoue et al. (2012).

The total energy of cosmic-ray protons is estimated by the relationship between the total target protons and the observed γ-rays (2–400 TeV) after extrapolating the proton spectrum to 1 GeV as follows (Aharonian et al., 2006b):

$$W_{\rm tot} \sim (1-3)\times 10^{50}\left(\frac{d}{1\,{\rm kpc}}\right)^2\left(\frac{n}{1\,{\rm cm^{-3}}}\right)^{-1}\ ({\rm erg}), \tag{3.7}$$

where the distance to the source is $d \sim$1 kpc and the density of the target protons is n. The average density of ISM protons is calculated to be $\sim$130 cm^{-3} for the total mass of the ISM protons 2.0×10^4 $M_\odot$ over the whole SNR (radius 0.65 deg) as modeled in Figure 10 and the total cosmic-ray proton energy to be $\sim$(0.8–2.3) $\times$ 10^{48} erg by using Equation 3.7. This corresponds to $\sim$ 0.1% of the total energy release of SNe and may appear low. The other SNRs like W44 and W28 of a few to 10 times 1000 yr old have the total cosmic-ray proton energy in the order of 10^{49}–10^{50} erg (Abdo et al., 2010; Giuliani et al., 2010). We may speculate that the cosmic-ray protons become accumulated in a few times 10,000 yr to reach more than 10% of the SNe energy. This issue is to be further tested by examining cosmic-ray escaping from SNRs (e.g., Gabici et al., 2009; Casanova et al., 2010a,b).

To summarize the discussion, we have shown that a combined analysis of CO and HI provides a reasonable candidate for the target ISM protons and thereby lends a new support for the hadronic scenario. We should note that the present analysis offers one

of the necessary conditions for the hadronic scenario for uniform cosmic-ray proton distribution, but it is not a full verification of the hadronic scenario and does not rule out leptonic components. We need to acquire additional observations before fully establishing the hadronic scenario, including better determination of the magnetic field and higher angular resolution images of γ-rays at least comparable to that of the ISM. Cherenkov Telescope Array will provide such images in future. We discussed that the observed highly inhomogeneous distribution of the ISM plays an essential role in the γ-ray production; DSA works in highly evacuated cavity and the accelerated cosmic-ray protons travel over a pc to interact with the surrounding dense ISM protons. It is important to develop a similar analysis of both HI and CO in the other similar objects like RX J0852.0−4622 (Vela Jr.), RCW 86, and HESS J1731−347. Such works are in progress based on the NANTEN2 observations and high-resolution HI interferometry.

3.5 Conclusions

We summarize the main conclusions as follows;

1. A new analysis of CO and HI has revealed that the VHE γ-ray SNR RX J1713.7−3946 is associated with a significant amount of HI gas without H_2 derived from CO. This HI gas is relatively dense and cold and detectable mainly as HI emission. We have also identified regions where HI is observed as dark HI in self-absorption dips and derived the total ISM proton column density over the SNR. The HI plus H_2, the total ISM protons, provides one of the necessary conditions, target protons, in the hadronic origin of the γ-rays. Such target ISM protons have not been identified in the previous study that took into account only H_2, although the present finding alone does not exclude the leptonic origin.

2. For an annular pattern around the VHE γ-ray shell, we compared the total ISM proton distribution with the VHE γ-ray distribution and found that they show reasonably good correspondence, varying by similar factors. The inclusion of the atomic protons observed as the HI self-absorption dips is essential particularly in the southeast of the γ-ray shell. The interpretation of HI self-absorption dips is also supported by the enhanced optical extinction toward the southeast rim.

3. The cavity surrounding the SNR was created by the stellar wind of the SN progenitor. The inside of the cavity is of low density with <1 cm^{-3} while the cavity wall consists of the dense and clumpy atomic or molecular target protons of $\geq$100–1000 cm^{-3}. The DSA in the highly inhomogeneous ISM offers a reasonable mechanism of particle acceleration in the low-density cavity and the dense wall acts as the

target for γ-ray production by the cosmic-ray protons. Hydro-dynamical numerical simulations of the interaction have shown detailed physical processes involved (Inoue et al., 2012).

4. By considering the other pieces of the observational and theoretical works accumulated thus far, the present results make the hadronic interpretation much more comfortable in RX J1713.7−3946. The current energy of the total cosmic-ray protons is estimated to be $\sim 10^{48}$ erg, 0.1% of the total energy of SNe, if we assume that the γ-rays are all produced by the hadronic process.

Chapter 4

Evidence for Efficient Acceleration of Cosmic-Rays

4.1 Background

As described above, SNR RX J1713.7−3946 is one of the best target from which both non-thermal X-rays and VHE γ-rays are detected. In particular, It is noteworthy that the X-rays are purely non-thermal synchrotron emission, indicating that the cosmic-ray electrons are accelerated in the SNR up to the 10 TeV range. The X-ray spectra are well fitted with a absorbed power-law function of photon index $\Gamma = 2.2$–2.4 and interstellar absorbing column density $N_{\rm H}$(X-ray) = 0.6–0.8$\times 10^{22}$ cm^{-2} (e.g., Cassam-Chenaï et al., 2004; Tanaka et al., 2008; Acero et al., 2009). This variation of of Γ and $N_{\rm H}$(X-ray) become a key component to understanding the efficient acceleration of cosmic-ray electrons. However, It is not known how the variation to be formed.

We have discovered the strong connection between the ISM clumps and non-thermal X-ray distributions (see Chapter 2). In this Chapter, we focus on the spectral distribution of X-rays. Specifically, we reveal the spatial distribution of photon index Γ, absorbing column density $N_{\rm H}$(X-ray), and X-ray flux in the same scale as ISM distribution. This work is aimed at better understanding the efficient acceleration around the dense gas materials.

4.2 Observations and Data Reductions

4.2.1 X-rays

4.2.1.1 Details of the datasets

We analyzed the X-ray dataset archive obtained by *Suzaku* (Data Archives and Transmission System; DARTS at ISAS/JAXA). This dataset consists of 17 pointings taken at 2005 September (SWG; 3 pointings), 2006 September and October (AO1; 10 pointings), 2010 February (AO4: 4 pointings) and we mainly used 15 pointing of ON sources (see also Figure 2.1). These data were already analyzed and published elsewhere (Takahashi et al., 2008; Tanaka et al., 2008, and Chapter 2) as summarized in Table 2.1 and Figure 2.1.

On board *Suzaku* are two active detectors, X-ray Imaging Spectrometer (XIS; Koyama et al., 2007) for imaging soft X-rays (0.2–12 keV) and Hard X-ray Detector (HXD; Takahashi et al., 2007) for hard X-rays (10–600 keV). In the present work, we deal with only the data taken with XIS. XIS consists of four CCDs located at the focus of X-ray Telescopes (XRTs; Serlemitsos et al., 2007); three of them are "Front-illuminated CCDs" (FI CCD; XIS 0, 2, and 3) and the other is "back-illuminated CCD" (BI CCD; XIS 1). Spaced-row charge injection technique (SCI; Nakajima et al., 2008; Uchiyama et al., 2009) was applied only to the four pointings in 2010 February. Unfortunately, XIS 2 was damaged by a micrometeorite hit on 2006 November 9 and the 2010 data in February consists of only XIS 0, 1, and 3. Subsequently, Segment A of XIS 0 was found to have anomaly on 2009 June 23 and Segment B was noticed to show charge leakage in part. We therefore used only the data from Segments C and D. We used Software HEASoft version 6.11 with pipeline processing version 2.0 or 2.4 and with standard event selection criteria (cleaned event files).

4.2.1.2 Imaging

The X-ray images are those used in Figure 2.1. Figure 4.1 shows XIS mosaic image (1–5 keV) in RX J1713.7−3946. Color scheme is in a square-root scale in 10^{-4} counts s^{-1} $pixel^{-1}$ (pixel size is $\sim$16.7″) smoothed with a Gaussian kernel with FWHM $\sim$45″. This image is subtracted for non X-ray background (NXB) and corrected for the vignetting effect by XRT (see more details in Chapter 2.2.3).

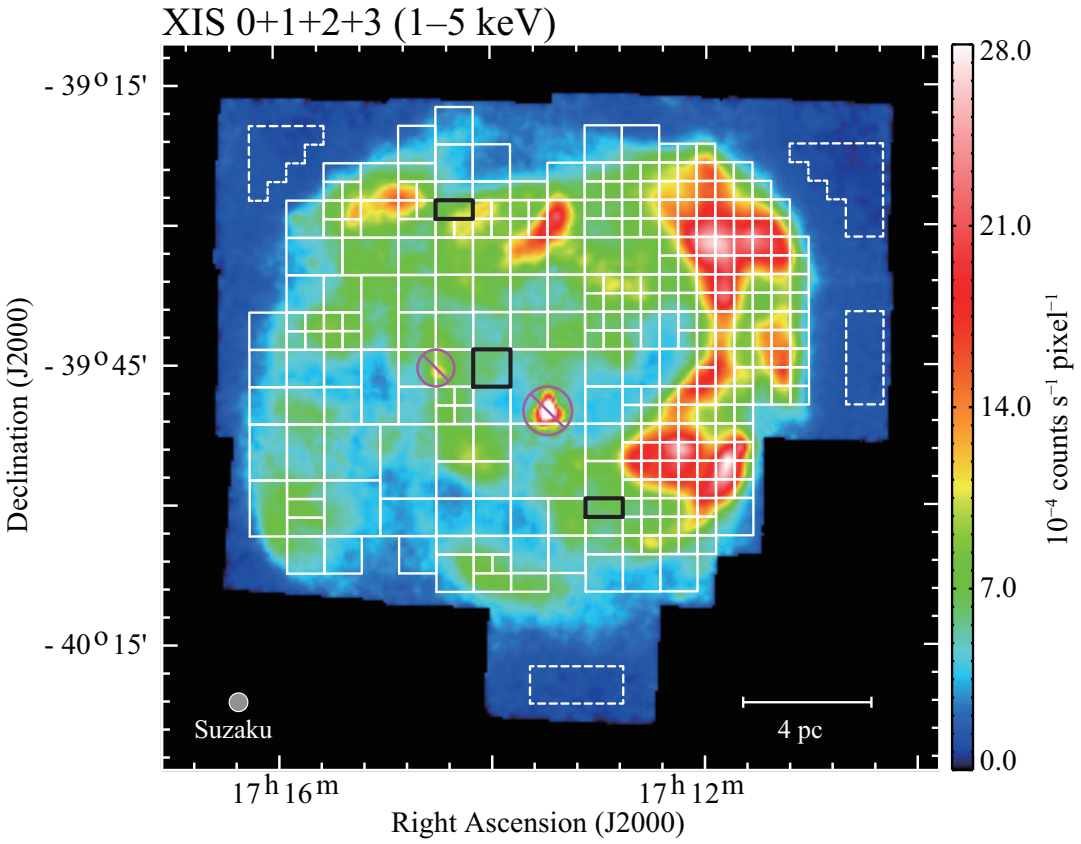

FIGURE 4.1: *Suzaku* XIS mosaic image of RX J1713.7−3946 in the energy band 1–5 keV (Chapter 2.3.1). The color scale indicates count rate on a square root scale and is unit of 10^{-4} counts s^{-1} $pixel^{-1}$. The solid boxes are those used for spectral analysis. We also show the spectra enclosed by the black solid lines (see also Figure 4.2). The dashed boxes correspond to the regions used to extract the background spectrum. The two point sources, 1WGA J1714.4−3945 and 1WGA J1713.4−3949, are circled with magenta and those regions were removed from spectral analysis.

4.2.1.3 Spectroscopy

The X-ray spectra of RX J1713.7−3946 is represented by the absorbed power-law model (e.g., Koyama et al., 1997). This model is for synchrotron X-rays with photoelectric absorption and the model fitting gives three parameters, absorbing column density $N_{\rm H}$(X-ray), and the photon index Γ, in addition to the absorption-corrected X-ray flux. We show typical X-ray spectra in Figure 4.2. We shall explain the method to derive the three parameters above. First, the SNR was divide into ∼600 regions of $2' \times 2'$ grids, where the X-rays are significantly detected. For the ∼600 regions, only the data taken with FI CCD (XIS 0, 2, and 3) were used to derive X-ray spectra. In order to compare with the data of the interstellar medium, CO and HI, the angular resolution was set to the highest value (*Suzaku* HPD ∼$2'$). In addition, the background spectrum was

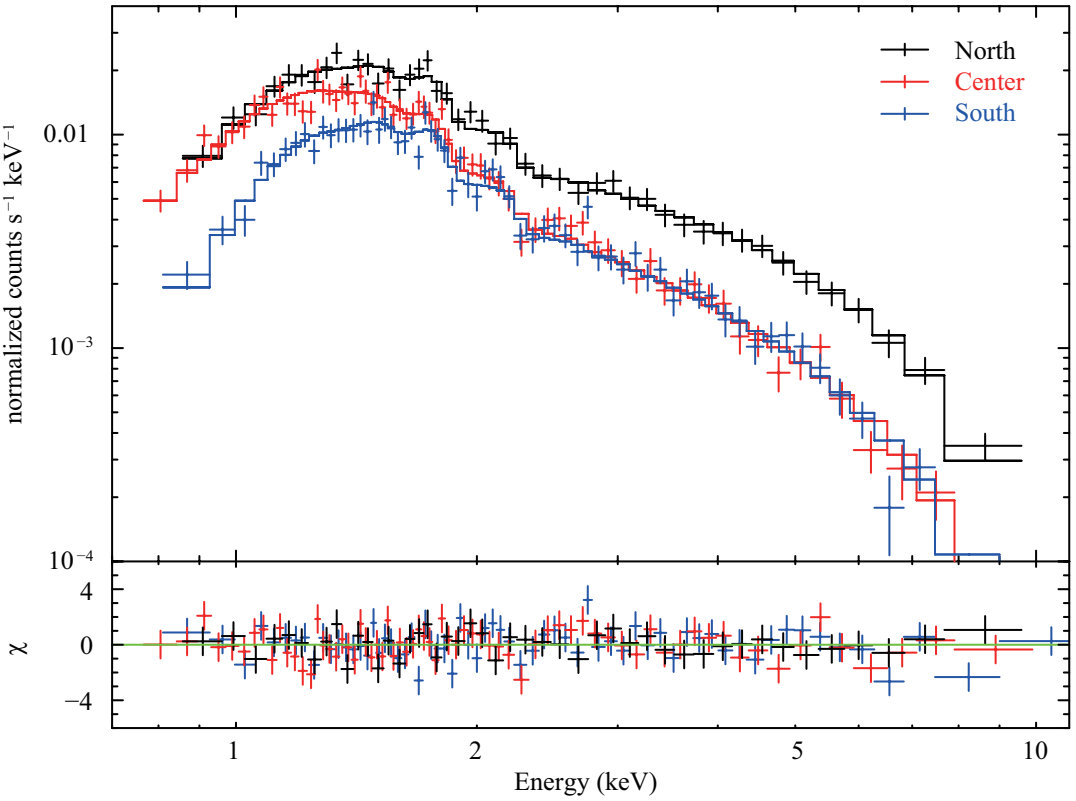

FIGURE 4.2: Typical X-ray spectra of north (black), center (red) and south (blue) regions (for the regions definition see Figure 4.1). The solid lines represent the best-fit absorbed power-law model. The lower part shows the residuals from the best-fit models. The north and center spectra can be fitted by the same absorbing column density ($N_{\rm H}$(X-ray)$\sim$0.5 $\times$ 10^{22} cm^{-2}) but with different photon index (north: Γ=2.1$\pm$0.1, center: Γ=2.7$\pm$0.1). The center and south spectra are the same photon index (Γ $\sim$2.7) but with different absorbing column densities (center: $N_{\rm H}$(X-ray) = $0.45^{+0.06}_{-0.05}$ $\times$ 10^{22} cm^{-2}, south: $N_{\rm H}$(X-ray) = $0.89^{+0.09}_{-0.08}$ $\times$ 10^{22} cm^{-2}).

estimated in the four regions shown in Figure 4.1 and the western background spectrum ($\alpha_{\rm J2000}$ =$17^{\rm h}10^{\rm m}31^{\rm s}$, $\delta_{\rm J2000}$ = $-39°44'22.7''$) was used for every region. The two prominent point sources (1WGA J1714.4−3945 and 1WGA J1713.4−3949) in the field are excluded in the analysis. Subsequently, the spectra of each region taken with XIS 0, 2, and 3 are summed up and was fit by the absorbed power-law model to generate RMF (Redistribution Matrix File) by xisrmfgen and ARF (Ancillary Response File) by xissimarfgen (Ishisaki et al., 2007).

Next, in order to reduce the statistical relative errors in absorbing column density $N_{\rm H}$(X-ray) to less than 30%, some neighboring regions on source were summed up and the spectra were again fit by the absorbed power-law model. Figure 4.1 shows the final spectra with 305 regions as indicated by solid boxes. About one third of the whole SNR is 2′ grid (4 arcmin^2) and 80% of that is better than 4′ grid (16 arcmin^2). These values are much better than the previous studies (e.g., Cassam-Chenaï et al., 2004, 70% of

that is worse than 6′ grid (36 arcmin^2)). Each spectrum is binned to include at least 100 counts. After the binning the energy ranges a below 0.4 keV and above 12 keV bin are excluded in the fitting. The best fit parameters in the fitting were used to derive absorbing column density $N_{\rm H}$(X-ray), photon index Γ, and absorption-corrected flux in 3–10 keV, $F_{3-10{\rm keV}}$, as shown in Figure 4.3. If the background spectrum is changed to that for four to three regions, we see systematic errors of up to 10–20% in $N_{\rm H}$(X-ray). This however does not significantly affect the results in Figure 4.3.

4.2.2 CO and HI

^{12}CO(J=1–0) and HI datasets are NANTEN Galactic Plane Survey (NGPS) and Southern Galactic Plane Survey (SGPS) taken with NANTEN, and ATCA & Parkes telescopes (Moriguchi et al., 2005; McClure-Griffiths et al., 2005), respectively. The angular resolutions are HPBW ∼2.′6 for CO and ∼2.′2 for HI, similar to *Suzaku* XIS HPD ∼2′. The velocity resolutions and typical rms noise fluctuations are (CO) 0.65 km s^{-1} and 0.3 K ch^{-1} and (HI) 0.82 km s^{-1} and 1.9 K ch^{-1}, respectively.

The velocity integrated intensities of CO and HI, W(CO) and W(HI), are converted into molecular column density $N(H_2)$ and atomic column density $N_{\rm H}$(HI) and the total proton column density is obtained as $N_{\rm H}(H_2{+}{\rm HI}) = 2{\times}N(H_2) + N_{\rm H}({\rm HI})$. A relationship $N(H_2)$ (cm^{-2}) = $X_{\rm CO}$ (cm^{-2} (K km s^{-1})$^{-1}$)×W(CO) (K km s^{-1}) is used where $X_{\rm CO}$ = 2.0×10^{20} (cm^{-2} (K km s^{-1})$^{-1}$) (Bertsch et al., 1993). The HI line is generally assumed to be optically thin and a relationship $N_{\rm H}$(HI) = 1.823×10^{18} × W(HI) is used (Dickey & Lockman, 1990). The regions where the HI is optically we need to apply the correction for self-absorption. Details of the method is given by (Fukui et al., 2012) in Section 3.3.3.

4.3 Results

4.3.1 Typical X-ray spectra

Figure 4.2 shows *Suzaku* XIS 0+2+3 spectra in the three typical regions, the north ($\alpha_{\rm J2000}$, $\delta_{\rm J2000}$) = ($17^{\rm h}14^{\rm m}19.95^{\rm s}$, $-39°28'31.11''$), the center ($\alpha_{\rm J2000}$, $\delta_{\rm J2000}$) = ($17^{\rm h}13^{\rm m}59.33^{\rm s}$, $-39°45'31.49''$), and the south ($\alpha_{\rm J2000}$, $\delta_{\rm J2000}$) = ($17^{\rm h}12^{\rm m}56.75^{\rm s}$, $-40°00'31.28''$), and the results of the model fitting. The lower parts show residuals in the fitting indicating that the fitting is reasonably good. We see no sign of thermal X-rays in Figure 4.2. The absorbing column density $N_{\rm H}$(X-ray) is ∼0.5×10^{22} cm^{-2} both in the north and the center, but the photon index is different as Γ = 2.1±0.1 and Γ = 2.7±0.1 for the north and

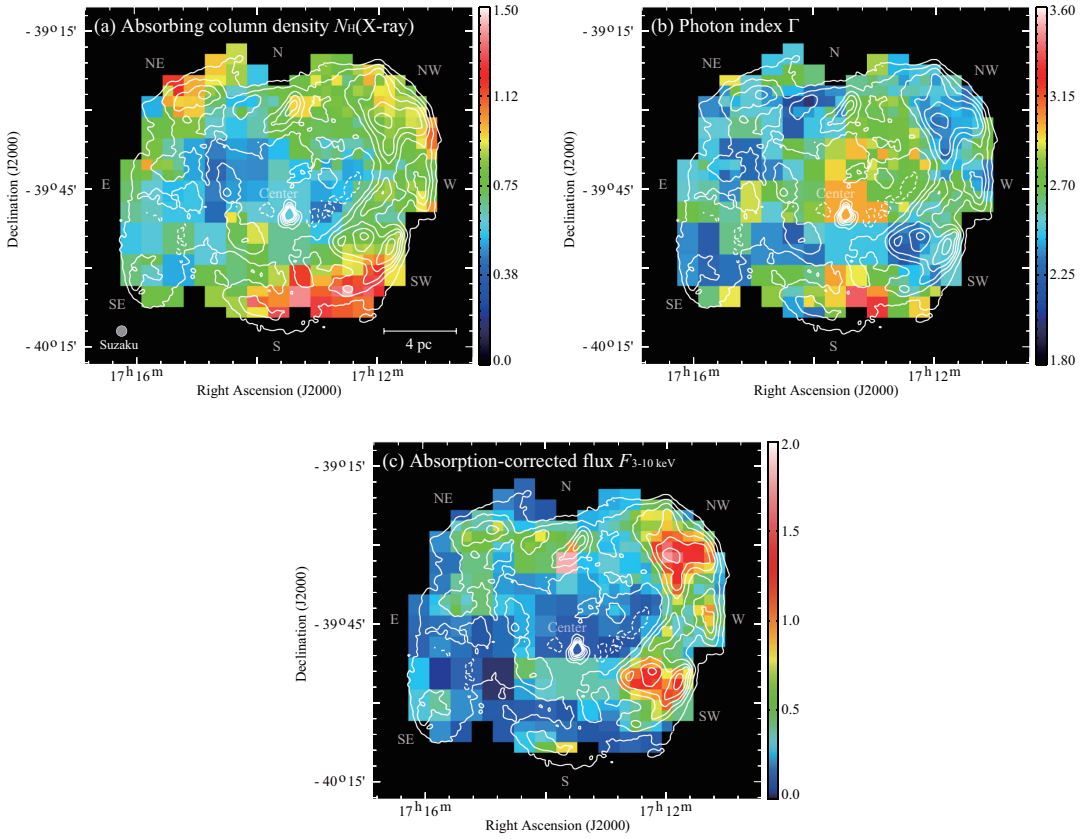

FIGURE 4.3: Maps of the best-fit parameters, (a) absorbing column density $N_{\rm H}$(X-ray), (b) photon index Γ, and (c) absorption-corrected X-ray flux $F_{3-10{\rm keV}}$, for absorbed power-law model. All maps overlaid with smoothed contours of the *Suzaku* XIS mosaic images. The contour levels are from at 3.9×10^{-4} counts s^{-1} pixel^{-1} and are square-root-spaced up to 23.9×10^{-4} counts s^{-1} pixel^{-1} with a pixel size of ∼16.″7. The color schemes in (a–b) and (c) are liner and square-root scale, respectively. The units are 10^{22} cm^{-2} for $N_{\rm H}$(X-ray) and 10^{-12} erg cm^{-2} s^{-1} for $F_{3-10{\rm keV}}$.

the center, respectively. On the other hand, the south has large absorbing column density $N_{\rm H}$(X-ray) $= 0.89^{+0.09}_{-0.08} \times 10^{22}$ cm^{-2} and photon index Γ ∼2.7. These differences are seen as significantly different spectral shapes in Figure 4.2. This confirms that the X-ray spectrum changes significantly from place to place as shown in the previous studies (e.g., Cassam-Chenaï et al., 2004; Tanaka et al., 2008)

4.3.2 Spatial and spectral characterization of the X-rays

4.3.2.1 Absorbing column density

Figure 4.3a shows absorbing column density $N_{\rm H}$(X-ray) in the individual regions, where the *Suzaku* XIS 1–5 keV intensity is overlayed as contours. We aimed at achieving that the relative error is 30% at maximum at the 90% confidence level by tuning the

pixel size. Consequently, the average relative error and its maximum value are confined to be 14% and 30%, respectively, at the 90% confidence level. This accuracy is high enough to assess the spatial variation of the absorbing column density and photon index as discussed later.

We find that the global distribution of $N_{\rm H}$(X-ray) shows a shell-like structure in Figure 4.3a. On the east side of center ($\alpha_{\rm J2000} \sim 17^{\rm h}14.5^{\rm m}$, $\delta_{\rm J2000} \sim -39^\circ40'$) and the west side of center ($\alpha_{\rm J2000} \sim 17^{\rm h}13^{\rm m}$, $\delta_{\rm J2000} \sim -39^\circ49'$), $N_{\rm H}$(X-ray) is as small as 0.4–0.5 $\times 10^{22}$ cm^{-2} (region in blue). On the other hand, two regions in the northeast ($\alpha_{\rm J2000} \sim 17^{\rm h}15^{\rm m}$, $\delta_{\rm J2000} \sim -39^\circ25'$) and the northwest ($\alpha_{\rm J2000} \sim 17^{\rm h}12^{\rm m}$, $\delta_{\rm J2000} \sim -39^\circ30'$) show medium values of $N_{\rm H}$(X-ray) = 0.7–1.0 $\times$ 10^{22} cm^{-2} (region in green), and part of the southwest ($\alpha_{\rm J2000} \sim 17^{\rm h}12.5^{\rm m}$, $\delta_{\rm J2000} \sim -40^\circ5'$) shows the largest $N_{\rm H}$(X-ray) with 1.1–1.4 $\times 10^{22}$ cm^{-2} (region in red). Therefore, the absorbing column density varies from 0.4$\times 10^{22}$ cm^{-2} to 1.4$\times 10^{22}$ cm^{-2} within the SNR. These values are mostly consistent with the previous studies with *XMM-Newton* (Cassam-Chenaï et al., 2004, typical angular resolution $\sim 8'$), while the angular resolution and the source coverage are better in the present study.

Figure 4.4 shows absorbing column density $N_{\rm H}$(X-ray) and visual extinction ($A_{\rm V}$ in unit of mag) derived from the Digitized Sky Survey I (DSS; Dobashi et al., 2005). The visual extinction is smoothed to the same binning with the X-rays. The values of $A_{\rm V}$ in Figure 4.4b are roughly classified into the three levels; low values ($A_{\rm V} < 2$ mag in blue) in the center of the SNR, medium values (2 mag $< A_{\rm V} <$ 3 mag in green) in the northeast and northwest regions, and high values ($A_{\rm V} > 3$ mag in red) in the southwest. The general trend of $A_{\rm V}$ is similar to that of $N_{\rm H}$(X-ray). Figure 4.5 shows a correlation plot between absorbing column density $N_{\rm H}$(X-ray) and visual extinction, showing a good correlation with a correlation coefficient of $\sim$0.83.

4.3.2.2 Photon index and Flux

Figures 4.3b and 4.3c show the distributions of photon index Γ and absorption-corrected flux $F_{3-10{\rm keV}}$, respectively. Their relative errors and maximum errors are $\sim$6% and 13% in Figure 4.3b, and $\sim$7% and 23% in Figure 4.3c at the 90% confidence level, respectively. Like absorbing column density, these quantities show significant spatial variation. In particular, photon index is largest with $\Gamma \sim 3$ (in orange color) toward the center ($\alpha_{\rm J2000} \sim 17^{\rm h}13.5^{\rm m}$, $\delta_{\rm J2000} \sim -39^\circ48'$) and the central south ($\alpha_{\rm J2000} \sim 17^{\rm h}13.5^{\rm m}$, $\delta_{\rm J2000} \sim -40^\circ3'$). On the other hand, six regions with small photon index ($\Gamma <$ 2.4) are distributed as islands inside the SNR; the northwest ($\alpha_{\rm J2000} \sim 17^{\rm h}11^{\rm m}50^{\rm s}$, $\delta_{\rm J2000} \sim -39^\circ32'30''$), the southwest ($\alpha_{\rm J2000} \sim 17^{\rm h}12^{\rm m}30^{\rm s}$, $\delta_{\rm J2000} \sim -39^\circ56'30''$), the

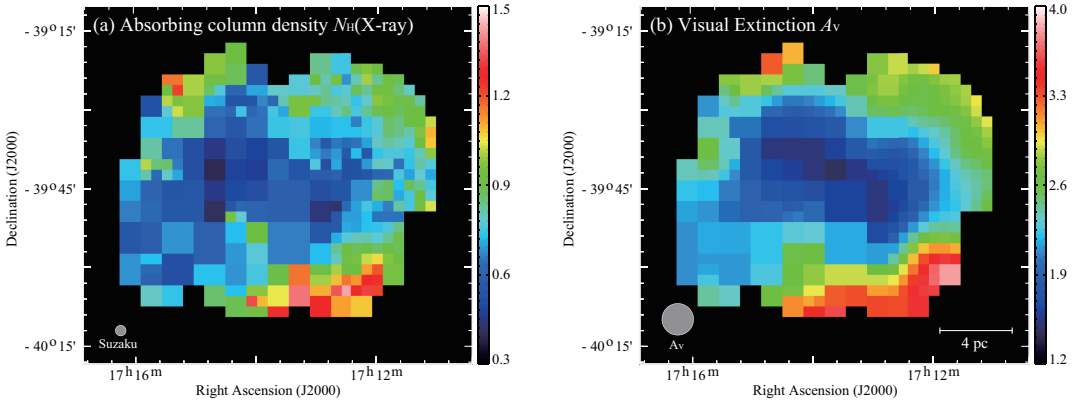

FIGURE 4.4: (a) Distribution of the absorbing column density $N_{\rm H}$(X-ray) as Figure 4.3 (b), but the color scale is changed. (b) Distribution of the visual extinction $A_{\rm v}$ (Dobashi et al., 2005). The grid separations are the same as (a).

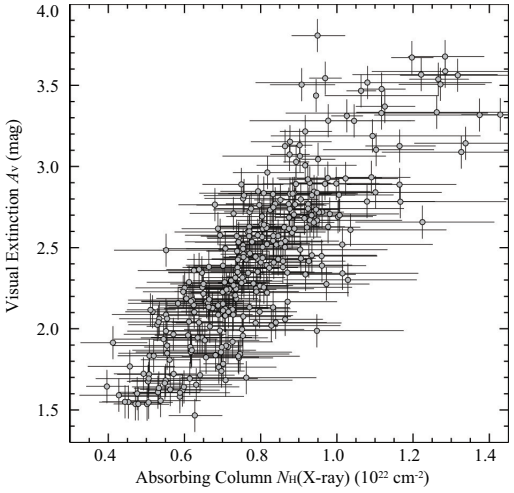

FIGURE 4.5: Correlation plot between the absorbing column density $N_{\rm H}$(X-ray) (in units of 10^{22} cm^{-2}) and the visual extinction $A_{\rm v}$ (in units of mag). The error bars are given at a 90% confidence level in $N_{\rm H}$(X-ray).

north ($\alpha_{\rm J2000}$ ~$17^{\rm h}14^{\rm m}$, $\delta_{\rm J2000} \sim -39°30'$), the east ($\alpha_{\rm J2000}$ ~$17^{\rm h}15^{\rm m}$, $\delta_{\rm J2000} \sim -39°40'$), and two regions in the southeast ($\alpha_{\rm J2000}$ ~$17^{\rm h}14^{\rm m}30^{\rm s}$, $\delta_{\rm J2000} \sim -39°55'$) and ($\alpha_{\rm J2000}$ ~$17^{\rm h}15^{\rm m}$, $\delta_{\rm J2000} \sim -40°00'$). We do not discuss some regions with small photon index in the peripheral of the SNR where the statistics is worse than inside. The absorption-corrected flux $F_{3-10{\rm keV}}$ is similar to the 1–5 keV X-rays contours, especially at the brightest peaks in the northwest, west, and southwest. We also find another strong peak in the north ($\alpha_{\rm J2000}$ ~$17^{\rm h}13^{\rm m}36^{\rm s}$, $\delta_{\rm J2000} \sim -39°37'31.7''$). These flux excesses are not due to a systematic error and are possibly connected with the ISM distribution as discussed in Section 4.4.

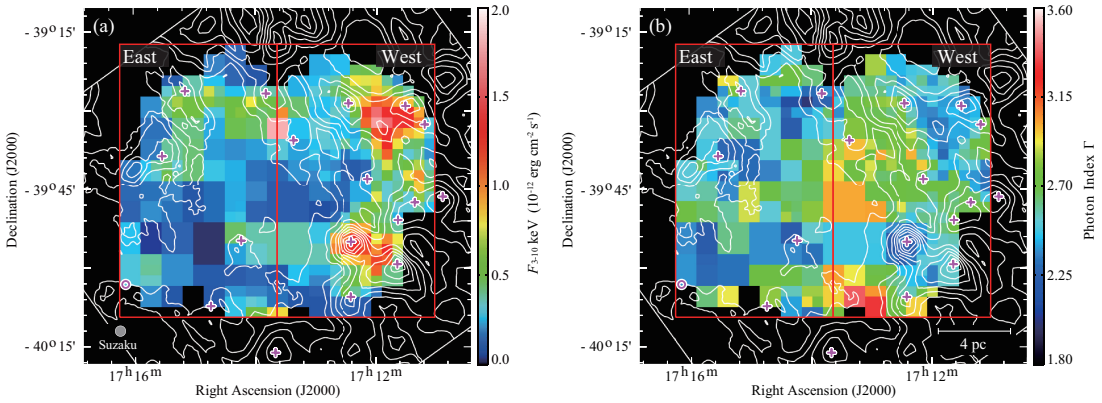

FIGURE 4.6: Distribution of (a) the absorption-corrected flux $F_{3-10\mathrm{keV}}$ and (b) photon index Γ as Figure 4.3. The contours indicate the proton column density $N_{\mathrm{H}}(\mathrm{H_2}+\mathrm{HI})$ in a velocity range from -20 to 2 km s^{-1}. The contour levels are 0.6, 0.75, 0.90, 1.1, 1.3, 1.5, 1.7, 1.9, and 2.1 $\times$ 10^{22} cm^{-2}. The magenta crosses and circle are corresponded to the positions of CO and HI clumps (Section Chapter 2.3.1.

4.3.3 Comparison with the ISM: The X-ray flux, photon index and the ISM

Overlays of the interstellar gas at $V_{\mathrm{LSR}} = -20$ to 2 km s^{-1} with absorption-corrected flux $F_{3-10\mathrm{keV}}$ and photon index Γ are shown in Figure 4.6a and Figure 4.6b, respectively, where the ISM is total proton column density $N_{\mathrm{H}}(\mathrm{H_2}+\mathrm{HI})$ including derived from the CO and HI. The velocity range of the ISM associated is derived by Moriguchi et al. (2005). based on a good correlation between the ISM and X-rays enhanced by the interaction with the SNR. We also annotated the positions (center of gravity) of the molecular clumps (crosses) and the HI clump (circle) defined by Section 2.3.1. Additionally, we will hereinafter refer to the regions between the clumps as "inter-clump". Figure 4.6a shows a trend that the X-rays are enhanced toward the regions with enhanced ISM in a pc scale. This trend is most significant in the west of the SNR, where the ISM is rich. On the other hand, in a sub-pc scale, we find that each bright spot of X-rays is lying around the CO and HI clumps except for the molecular clump in southwest ($\alpha_{\mathrm{J2000}} = 17^{\mathrm{h}}12^{\mathrm{m}}25.3^{\mathrm{s}}$, $\delta_{\mathrm{J2000}} = -39°55'7.4''$; named as "clump C''). These results are consistent with the Chapter 2 and the present work has made it possible to evaluate the trend more quantitatively. Figure 4.7 shows a correlation plot between $F_{3-10\mathrm{keV}}$ and the ISM density; the linear correlation coefficients (hereafter LCC) are ∼0.55 (for the whole), ∼0.19 (the east, on the left side of α_{J2000} ∼$17^{\mathrm{h}}13^{\mathrm{m}}38^{\mathrm{s}}$) and ∼0.54 (west, on the right side of α_{J2000} ∼$17^{\mathrm{h}}13^{\mathrm{m}}38^{\mathrm{s}}$), respectively. The LCC∼ 0.55 does not show strong correlation but the number of sample in the plot ∼300 indicates a positive correlation at a 5% confidence level according to a T-test (e.g., Taylor, 1982).

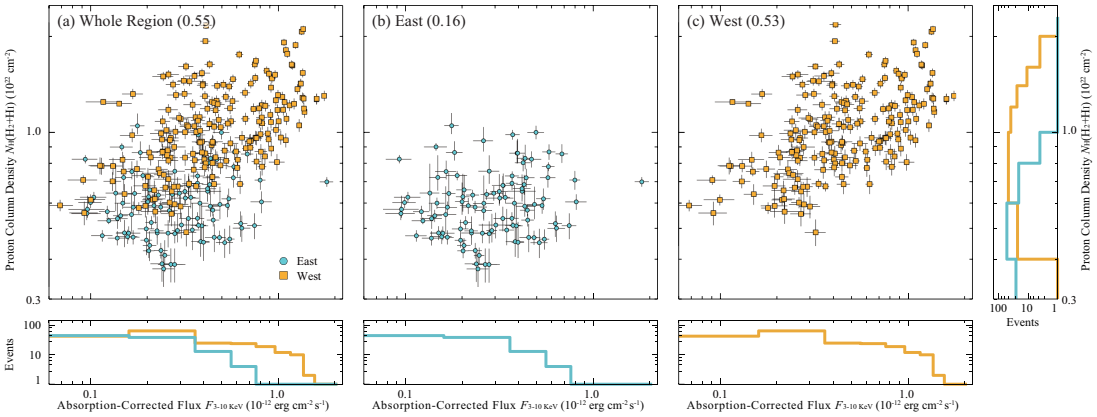

FIGURE 4.7: Correlation plot between the absorption-corrected flux $F_{3-10\mathrm{keV}}$ and the proton column density $N_{\mathrm{H}}(\mathrm{H_2}+\mathrm{HI})$ in (a) whole region, (b) East and (c) West. The regions are defined as follow Figure 4.6: ◯ for East, □ for West. The histograms are also shown at lower or right side of each plot. All plots, the scale is square-root.

In Figure 4.6b, we note that the regions having the hard spectrum are seen toward the enhanced ISM in the west, whereas the regions of the hard spectrum are also found toward the diffuse ISM in the east. Most outstanding are the ISM peaks toward/around the two X-ray peaks in the northwest (α_{J2000} $\sim 17^{\mathrm{h}}11^{\mathrm{m}}50^{\mathrm{s}}$, $\delta_{\mathrm{J2000}} \sim -39^{\circ}32'30''$) and in the southwest ($\alpha_{\mathrm{J2000}}$ $\sim 17^{\mathrm{h}}12^{\mathrm{m}}30^{\mathrm{s}}$, $\delta_{\mathrm{J2000}} \sim -39^{\circ}56'30''$. In addition, we find four regions of the hard spectrum in the east where the ISM is diffuse ($\alpha_{\mathrm{J2000}} \sim 17^{\mathrm{h}}15^{\mathrm{m}}40^{\mathrm{s}}$, $\delta_{\mathrm{J2000}} \sim -39^{\circ}58'00''$). Figure 4.8 shows a correlation plot showing that the relationship between the ISM and photon index is different between the west and east. In the west, the spectrum is hard when the ISM is dense and the spectrum is soft where the ISM is diffuse (LCC ~ -0.41). In the east, the ISM is diffuse and the photon index shows variation (LCC ~ -0.08), where the ISM density is not apparently related to the variation of the photon index for the whole region LCC is estimated to be ~ -0.16. Additionally, we show correlation plots between the photon index Γ and the absorption-corrected flux $F_{3-10\mathrm{keV}}$ in Figure 4.9. LCCs are ~ -0.62 (the whole), ~ -0.53 (the east) and~ -0.81 (the west), respectively. The histograms toward the west and east regions show a similar trend to the photon index distribution with respected the ISM density, while the west region has much higher X-ray fluxes than the east. We shall discuss about these results later in Section 4.4.2.2.

We summarize the main aspects of the present analysis as follows (Figures 4.6, 4.7, 4.8, and 4.9);

1. It is notable that the most intense X-rays are seen in the two region toward or around the CO peaks (Figure 4.6a). In the western half of the SNR, the ISM density is high with significant $\mathrm{H_2}$ and the X-rays are enhanced. In the eastern

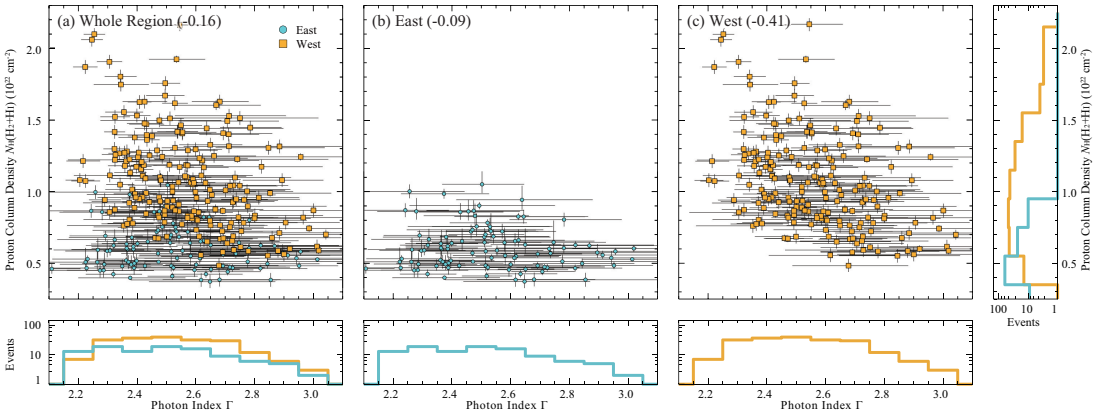

FIGURE 4.8: Correlation plot between the photon index Γ and the proton column density $N_{\rm H}$(H$_2$+HI) in (a) whole region, (b) East, and (c) West. All plots, the scale is linear.

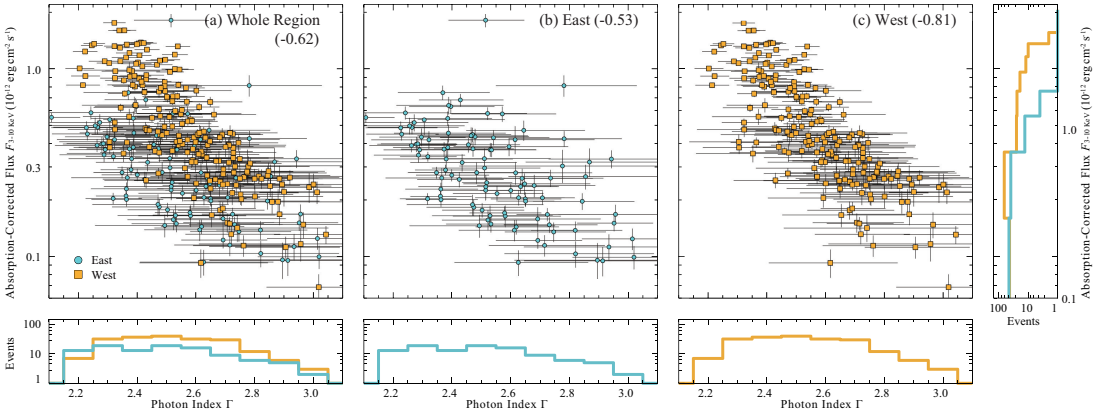

FIGURE 4.9: Correlation plot between the photon index Γ and the absorption-corrected flux $F_{3-10{\rm keV}}$ in (a) whole region, (b) East, and (c) West. The scale is linear in the photon index Γ and is square-root in the absorption-corrected flux $F_{3-10{\rm keV}}$.

half of the SNR, the ISM density is low, being dominated by HI, and the X-rays are weak. The overall correlation between the ISM density and the X-rays is however not significantly high with a correlation coefficient of ∼0.55 (Figure 4.7).

2. The smallest X-ray photon index around 2.3 is seen toward the six regions; around/-toward the two CO peaks in the west, and toward the four regions of low ISM density in the east (Figure 4.6b). The largest X-ray photon index around 3 is found toward the central region of the SNR as well as in the southern edge (Figure 4.6b).

3. The photon index shows a good correlation with the X-rays and the low photon index is seen toward regions of intense X-rays and vice versa (Figure 4.9). There is an offset by 0.3 in this correlation between the eastern and western halves of the SNR in the sense that the X-rays are more intense in the west, where the ISM

is denser than in the east. The overall correlation between the photon index and the ISM density is not high (Figure 4.8).

4.4 Discussion

4.4.1 Spatial variation of the absorbing column density

The observations with *Suzaku* XIS have enabled us to estimate detailed distributions of the absorbing column density $N_{\rm H}$(X-ray) and photon index Γ in RX J1713.7−3946 at a low background level and high photon statics. Here in the discussion, we first discuss the absorbing column density $N_{\rm H}$(X-ray).

The spatial distribution of $N_{\rm H}$(X-ray) delineates the SNR shell as shown in Figure 4.4. This distribution shows a good correspondence with visual extinction. The regression in a straight line calculated from a least-squares fitting gives $N_{\rm H}$(X-ray) (cm^{-2}) = (3±1)×10^{21}·$A_{\rm V}$ (magnitude) for the scatter plot in Figure 4.5. The numerical factor is slightly larger than that of the conventional relation $N_{\rm H}$ (cm^{-2}) = 2.5×10^{21}·$A_{\rm V}$ (magnitude) (Jenkins & Savage, 1974). This is understandable if we consider the distance of RX J1713.7−3946 is 1 kpc, since the visual extinction tends to be under-estimated for a distance larger than a few 100 pc by the foreground stars. It is not necessarily true that all $N_{\rm H}$(X-ray) is physically associated with the SNR. Here we need to take into account the contribution of the local gas between the SNR and the sun (Figure 4.10a). Moriguchi et al. (2005) already estimated the foreground component $N_{\rm H,local}$(H$_2$+HI) (Figure 4.10b). Figure 4.10c shows the distribution of absorbing column density [$N_{\rm H}$(X-ray)−$N_{\rm H,local}$(H$_2$+HI in the SNR, which gives a shell-like distribution of $N_{\rm H}$(X-ray) more clearly than Figure 4.3a. The absorption toward the center of the SNR is ∼0.2×10^{22} cm^{-2}, whereas that toward the outer boundary is shell-like with absorbing column density of ∼0.5–0.8×10^{22} cm^{-2}. This shell represents a cavity wall of the ISM created by the stellar wind of the SNR progenitor. The inside of the cavity is highly evacuated with density lower than ∼ 1 cm^{-3} and the dense clumps in the cavity wall have higher density like ∼10^2–10^4 cm^{-3} (e.g., Inoue et al., 2012).

We shall discuss the absorption toward the southeast-rim. In this region Fukui et al. (2012) identified cold HI gas that corresponds to the VHE γ-ray shell. The cold HI with low spin temperature of ∼40 K has density around 100 cm^{-3}, less than ∼1000 cm^{-3} threshold density for the collisional excitation of the CO emission. The proton column density of the cold HI without CO emission is estimated to be ∼0.5×10^{22} cm^{-2} from the HI self-absorption in the southeast rim of RX J1713.7−3946 (Fukui et al., 2012).

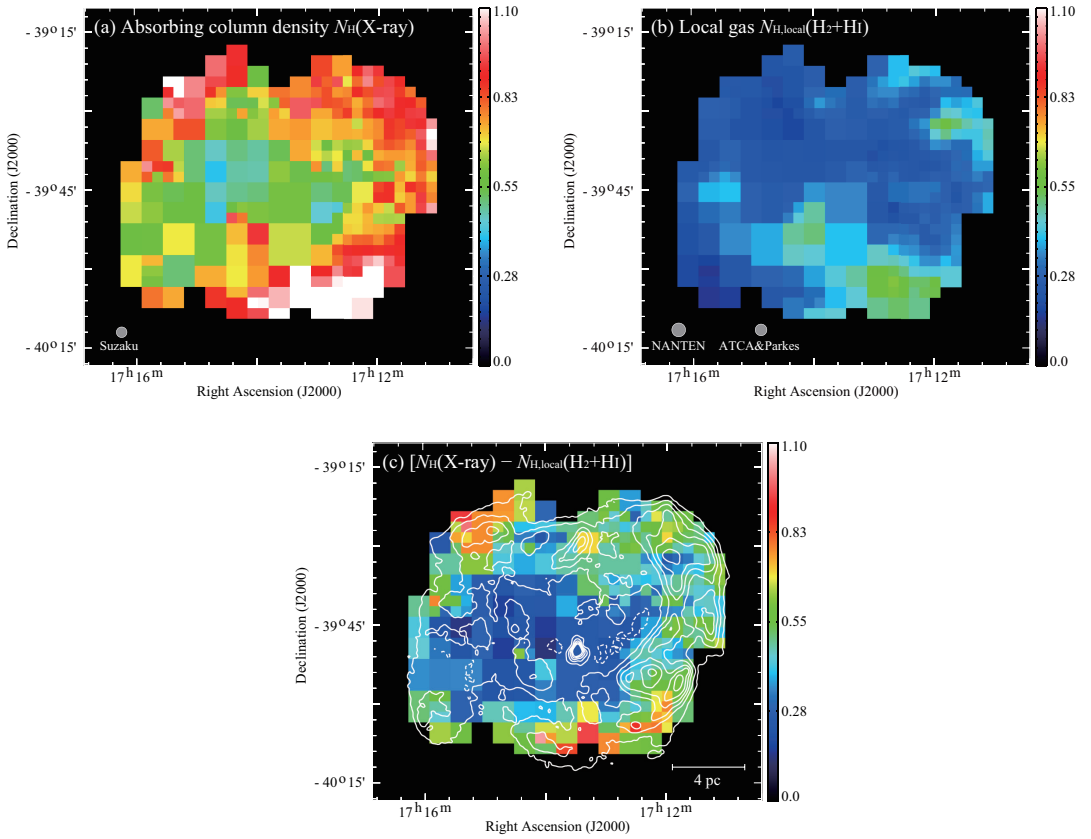

FIGURE 4.10: (a) Distribution of the absorbing column density $N_{\rm H}$(X-ray) as Figure 4.3 (a), but the color scale is changed to stress the region of the low absorbing column density. (b) Distribution of the proton column density in local gas $N_{\rm H,local}(H_2+HI)$ estimated by using the CO and HI data sets. (c) Distribution of the absorbing column density $[N_{\rm H}(\text{X-ray})-N_{\rm H,local}(H_2+HI)]$ overlaid with smoothed contours of the *Suzaku* XIS mosaic images as shown in Figure 4.3. All images are the same color scale.

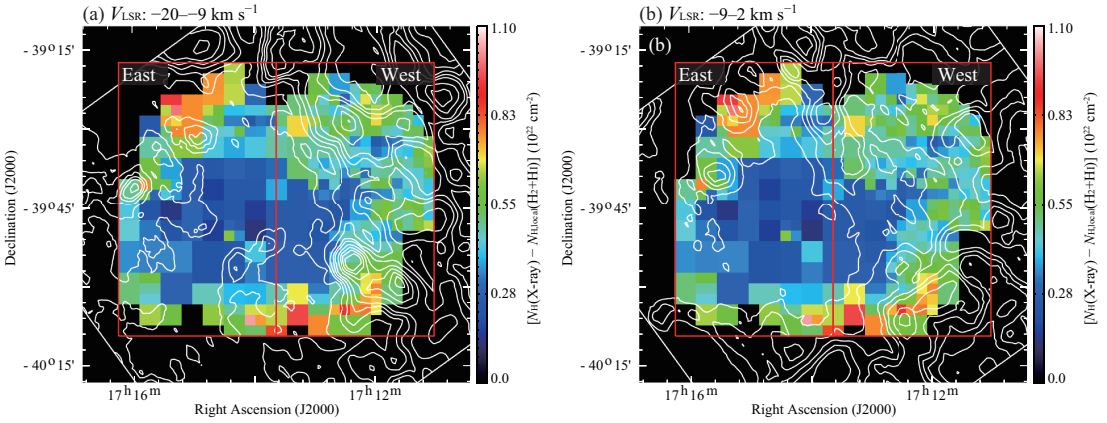

FIGURE 4.11: Distribution of the absorbing column density $[N_{\rm H}(\text{X-ray})-N_{\rm H,local}(H_2+HI)]$ as Figure 4.6 (c) superposed on the proton column density $N_{\rm H}(H_2+HI)$ in the velocity range from (a) −20 to −9 km s^{-1} and from (b) −9 to 2 km s^{-1}, respectively. The contour levels are 0.4, 0.5, 0.6, 0.7, 0.9, 1.1, 1.3, and 1.5 × 10^{22} cm^{-2}. The regions, East and West, where used for the correlation plots (see Figure 4.12).

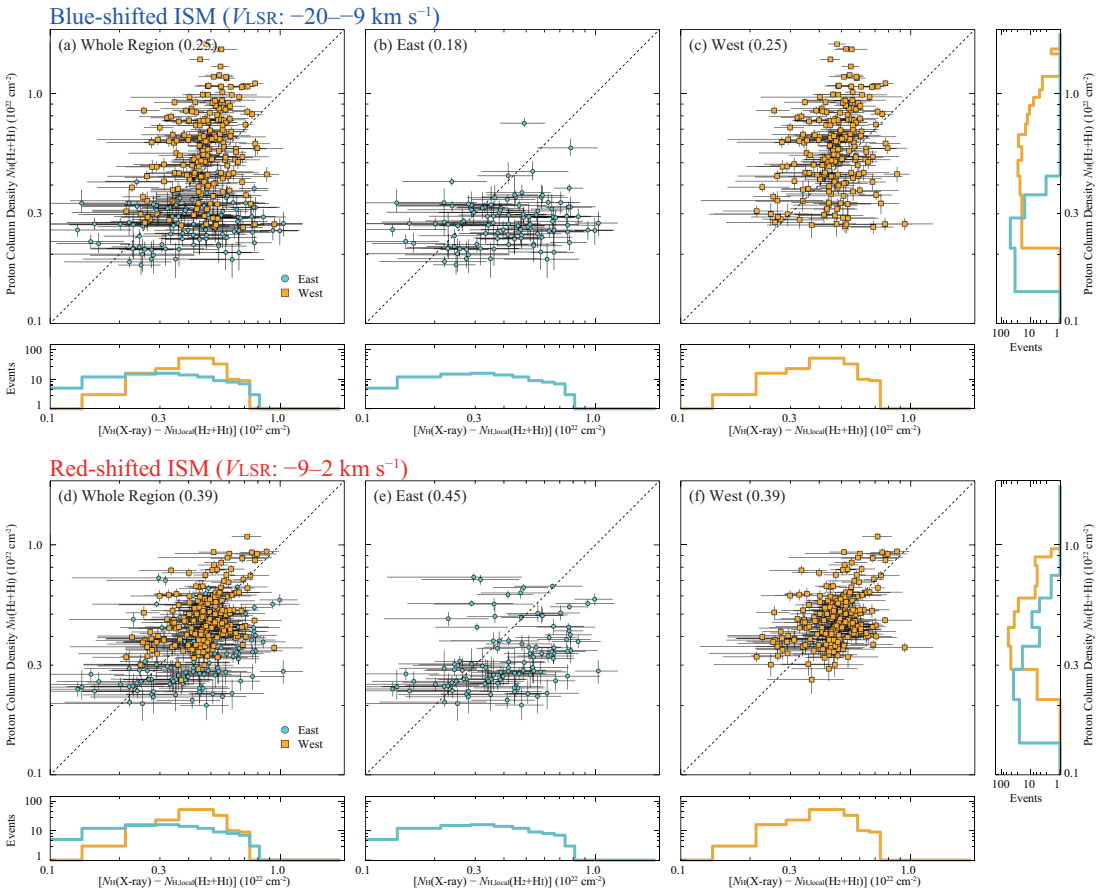

FIGURE 4.12: Correlation plot between the absorbing column density [$N_{\rm H}$(X-ray)−$N_{\rm H,local}$(H$_2$+HI)] and the proton column density $N_{\rm H}$(H$_2$+HI) in the velocity range from (a–c) −20 to −9 km s^{-1} and from (d–f) −9 to 2 km s^{-1}, respectively. The regions indicate (a, d) whole region, (b, e) East, and (c, f) West, respectively. The dashed lines are the bisector for each panel. The histograms are also shown at lower or right side of each plot. All plots, the scale is square-root.

The present absorption in the SNR calculated from X-rays has also column density of 0.4–0.5×10^{22} cm^{-2} (Figure 4.10c) which is consistent with the cold HI.

We compared the absorbing column density [$N_{\rm H}$(X-ray) − $N_{\rm H\_local}$(H$_2$+HI)] (Figure 4.10c) with $N_{\rm H}$(H$_2$+HI), the proton column density physically associated with the X-ray emitting shell, in two velocity ranges of the interacting gas in Figures 4.11 and 4.12. Figures 4.11a and 4.11b show [$N_{\rm H}$(X-ray) − $N_{\rm H\_local}$(H$_2$+HI)] overlayed on the ISM proton column density $N_{\rm H}$(H$_2$+HI) at $V_{\rm LSR}$ ∼ −20 to −9 km s^{-1} and ∼ −9 to 2 km s^{-1}. This comparison shows that the ISM distribution has generally good correspondence with the X-ray absorbing column density. It is however to be noted that the blue-shifted ISM shows a poorer correlation than that of the red-shifted ISM with the X-ray absorbing column density as shown in Figure 4.12, scatter plots between the ISM and the X-ray absorption column density. In Figure 4.12 we divide the plots into the red- and blue-shifted ISM. The blue-shifted ISM in the west shows a poor correlation with

the X-ray absorbing column density of LCC∼0.25, while the red-shifted ISM in the west has a higher correlation of LCC∼0.39 than the blue-shifted ISM. This indicates that the red-shifted ISM is located on the far-side of the SNR, and it is in the opposite sense to what is expected in an expanding motion of the shell-like ISM. The relative position of the ISM is explicable if the pre-existent cloud motion is dominant for the dense CO gas instead of expansion, as already suggested to explain the velocity distribution of the HI self-absorption Fukui et al. (2012).

4.4.2 Relationship between the X-ray flux, the photon index, and the X-ray absorption/the ISM

4.4.2.1 Shock-cloud interaction

Inoue et al. (2012) showed by magnetohydrodynamic (MHD) numerical simulations that the X-ray intensity is closely correlated with the ISM by the enhanced magnetic field around dense clumps due to turbulence in the shock-cloud interaction. The interaction creates correlation between the ISM and X-rays at a pc scale via the magnetic field. Chapter 2 showed that pc-scale correlation is seen between the X-ray intensity and the clump mass interacting with the SNR blast waves, as well as anti-correlation between them in a sub-pc scale due to exclusion of the CR electrons in the dense clumps. The distributions of the X-ray intensity in Figure 4.6a at grid sizes of 2–8 arcmin (0.6–2.4 pc) show their interrelation at a pc scale; we see trend that the X-rays are enhanced in the west where the ISM is rich, and that the X-rays are depressed in the east where the ISM is poor. This is consistent with what is expected in the shock-cloud interaction scheme. The higher dispersion in Figure 4.7 may be in part ascribed to anti-correlation at a sub-pc scale, consistent with the suggestion in Chapter 2.

4.4.2.2 Efficient cosmic-ray acceleration

Based on the present results on the photon index (Figure 4.3b), we discuss the efficient cosmic-ray acceleration in RX J1713.7−3946. As shown by the previous works (Takahashi et al., 2008; Tanaka et al., 2008), the photon index in the 1–10keV range reflects rolloff energy ε_0 of the synchrotron X-rays. The small (large) photon index corresponds to large (small) rolloff energy. According to the standard DSA scheme, the rolloff energy of synchrotron photons ε_0 is given as follows when the synchrotron cooling is effective (Zirakashvili & Aharonian, 2007),

$$\varepsilon_0 = 0.55 \times (v_{\rm sh} \,/\, 3000 \text{ km s}^{-1})^2 \, \eta^{-1} \text{ (keV)}, \tag{4.1}$$

where $v_{\rm sh}$ is the shock speed and $\eta = B^2/\delta B^2$ (>1) a gyro-factor, the degree of magnetic field fluctuations. In particular the limit of $\eta = 1$ is called as Bohm limit corresponding to highly turbulent conditions and, accordingly, the rolloff energy is likely determined by the shock speed and turbulence.

The present results suggest that in the west of the SNR, where the ISM is rich, the shock-cloud interaction is effective and turbulence is enhanced around dense ISM clumps. On the other hand, in the east of the SNR where the ISM is poor the DSA alone is mainly working without shock-cloud interaction. We show a schematic image summarizing the relevant features in Figure 4.13. The shaded regions in blue, white, and orange correspond to the photon index $\Gamma < 2.4$ (small) , $2.4 < \Gamma < 2.8$ (medium), and $\Gamma > 2.8$ (large), respectively. In Chapter 2, we presented that the innermost cavity of 3–4 pc radius is surrounded by the ISM shell consisting of the dense clumps and the inter-clump gas. The inter-clump gas is shown by the shaded gray region around the clumps in Figure 4.13. The dense clumps have density of 10^2 to 10^4 cm^{-3} (see also Section 2.3.1) and are mainly distributed in the west toward the Galactic plane. The inter-clump gas has density < 2 cm^{-3}, as given by the upper limit from no thermal X-rays (Takahashi et al., 2008), and we shall adopt density of the inter-clump gas to be 1 cm^{-3} for discussion. We assume that density in the cavity is $\sim$0.25 cm^{-3}, the same with that estimated toward Gum nebula where the gas is swept up by the strong stellar winds from ζ Pup (Wallerstein & Silk, 1971; Gorenstein et al., 1974). In this scheme, DSA is efficiently taking place in the cavity and the accelerated CRs are injected into the ISM shell. Figure 4.13 show that the shock waves are now interacting with the five dense clumps and has passed through two clumps denoted as "C'' and "L''.

Table 4.1 gives two sets of possible parameters for discussion in the two cases with different ISM density, although they are crude at best (c.f., Tanaka et al., 2008). In the west where the shock-cloud interaction is working, the magnetic field may be amplified up to $\sim$1 mG as indicated by the short time variation of $\sim$1 yr in the synchrotron X-rays by *Chandra*, where the Bohm limit ($\eta = 1$) is a good approximation (Uchiyama et al., 2007). On the other hand, the shock speed $v_{\rm sh}$ is proportional to $1/\sqrt{n}$ and is decreased in the dense ISM, where n is the average number density of the ISM. The observational result shows that vsh is decreased to 4500 km s^{-1} or less, and we shall assume $\sim$3000 km s^{-1} (Uchiyama et al., 2007; Zirakashvili & Aharonian, 2007). It is probable that in the west of the SNR, mainly the shock-cloud interaction causes large rolloff energy and a small photon index. On the other hand, in the east the shock speed is not much decelerated in the lower density. A possible scenario is as follows; the average ISM density in the east is about 1/4 of that in the west and the shock speed $v_{\rm sh}$ becomes larger by a factor of 2. Then, η becomes larger than 1, but the term (the shock speed $v_{\rm sh})^2$ is more effective. If we assume the shock speed is $\sim$6000 km s^{-1} and $\eta \sim 4$, the

TABLE 4.1: An Example of the Physical Parameters for the Rolloff Energy

Region	Gas density n (cm^{-3})	Gyro-factor η	Shock speed $v_{\rm sh}$ ($\mathrm{km\ s}^{-1}$)	Rolloff energy ε_0 (keV)
Inter-clump	1[†]	1[‡]	3000[‡]	0.6[§]
Inside of the cavity	0.25[*]	4	6000	0.6

Notes. [†]Inoue et al. (2012), [*]Wallerstein & Silk (1971); Gorenstein et al. (1974), [‡]Uchiyama et al. (2007); Zirakashvili & Aharonian (2007), [§]Takahashi et al. (2008); Tanaka et al. (2008).

rolloff energy becomes larger as ~ 0.6 keV (Tanaka et al., 2008) and the photon index smaller. The trend in the photon index, therefore, is largely explicable by the DSA scheme with modification due to the ISM gas.

The regions where the photon index is small in the east seem to be located toward the edge of medium density clumps along the outer part of the shell (Figure 4.6b). It is however not likely that this small photon index is due to the shock-cloud interaction, because the spatial extent with $\Gamma < 2.4$ is four times larger than that in the west. It is predicted that the area where the rolloff energy (photon index) is above (below) a certain value becomes small with the increase of the magnetic field if the Sedov-Taylor evolution is assumed (equation (9) in Kishishita et al., 2013). This implies that the field is stronger in the east than in the west, but it is inconsistent with the shock-cloud interaction. It is therefore reasonable that the acceleration is mainly by DSA in the east not by the shock-cloud interaction.

In Figure 4.13, the innermost part of the SNR having the large photon index $\Gamma > 2.8$ is shown by orange color. We suggest that the electrons there have lower rolloff energy due to synchrotron cooling over the last 1000 yrs; for magnetic field of 10 μG the CR electron cooling time at 10 keV is small as $\sim$500 yrs, whereas that at 1 keV is large as $\sim$1500 yrs, leading to low rolloff energy in the central 3–4 pc. We also mention that such spectral softening can be described as energy loss due to adiabatic expansion (e.g., Kishishita et al., 2013).

One would expect that the photon index becomes even larger toward the denser regions, if only $v_{\rm sh}$ determines the photon index. Interestingly, the photon index becomes small toward the clump C and the region between the two dense clumps, D and L in Figure 4.6b. It is also notable that the X-rays are enhanced toward these regions having small photon indexes. In the shock-cloud interaction scheme, the magnetic field is amplified in the interacting region, leading to higher synchrotron loss and smaller rolloff energy. This can lead to lower X-ray intensity and lower rolloff energy toward the dense clumps, while obviously we need a more elaborate work to quantitatively affirm this. It is thus possible that the observed trend may not be explained by only a DSA scheme.

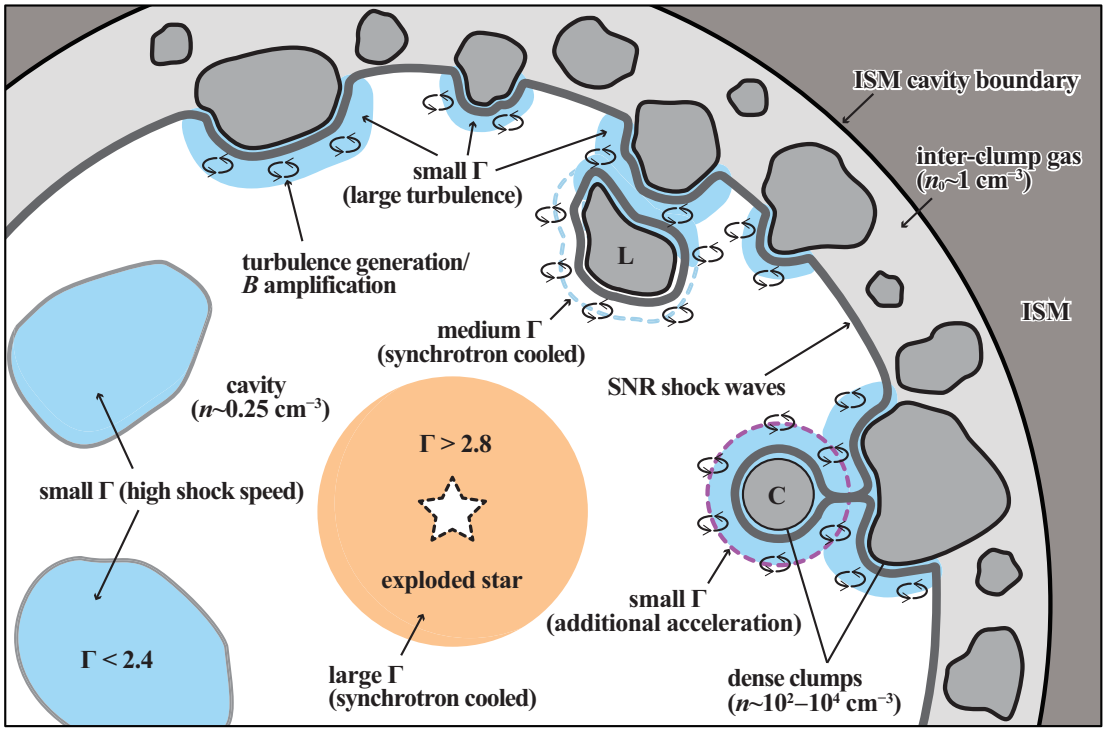

FIGURE 4.13: Schematic image of the efficient cosmic-ray acceleration toward RX J1713.7−3946. The SNR shock waves travel through the cavity (gas density $n \sim 0.25$ cm^{-3}), where cosmic-ray acceleration is working by DSA scheme and the shock speed is not much decelerated in lower density. Propagated shock waves are stalled toward the dense clumps, and are traveling in the inter-clump space. Shock-cloud interaction generates the turbulence ($\eta \sim 1$) and enhances the magnetic field around the dense clumps. The accelerated particles in the innermost cavity and some of clumps are already cooled down due to the synchrotron cooling. The additional acceleration is induced due to the high turbulence and strong magnetic fields around the some of dense clumps (see the text for more details).

We here suggest that some additional acceleration mechanism is working to accelerate CR particles in the west where the ISM is rich. Such mechanisms include the 2nd order Fermi acceleration (Fermi, 1949) and/or magnetic reconnection in the turbulent medium (Hoshino, 2012). In the latter case, compression in the shocked region creates multiple magnetic islands and causes magnetic reconnection that leads to outflow and accelerate high-energy particles emitting enhanced synchrotron radiation. This scenario is consistent with the shock-cloud interaction picture presented for RX J1713.7−3946 (Inoue et al., 2012) and multiple magnetic islands may be formed around the dense ISM clumps.

To summarize, we suggest that the ISM and its distribution have a significant impact on the scheme of the particle acceleration via the shock-cloud interaction. This suggests the tight relationship between the SNR and the ISM. The present study explored the CR electron behavior into significant details not achieved in the previous works, and presented that the ISM density affects significantly the CR electron rolloff energy. In particular, dense molecular clumps excites turbulent in the shock waves, amplifying the

magnetic field. The CR electron rolloff energy is increased in spite of such amplified field, and we suggest that additional electron acceleration may be taking place in such turbulent regimes around the dense clumps.

In near future, Cherenkov Telescope Array (CTA) will provide information on the spectral distribution of γ-rays over the SNR at 1 arcmin resolution and will allow us to investigate the spectra and acceleration of both the CR protons and electrons. In addition, the soft X-ray spectrometer (SXS) of ASTRO-H will probe yet undetected thermal X-rays by sensitive high-energy resolution spectroscopy in RX J1713.7−3946. We can then probe the fraction of the energy of the SNR blast waves used for cosmic-ray acceleration. And the hard X-ray imager (HXI) of ASTRO-H will resolve photon index distribution at 10 keV or higher, possibly allowing us to constrain electron energy spectrum models by comparing that below 10 keV (e.g., Yamazaki et al., 2013). These future instruments will enable more accurate measurements of the efficient cosmic-ray acceleration.

4.5 Conclusions

We summarize the present work as follows.

1. We have estimated the spatial distribution of absorbing column density, photon index, and absorption-corrected flux (3–10 keV) comparable to the scale of the ISM distribution, a few arcmin, by using *Suzaku* archival data with low background.

2. The X-ray flux shows enhancement toward the dense ISM. This is consistent with the shock-cloud interaction model by (Inoue et al., 2012) that X-rays become bright around the dense cloud cores due to turbulence amplification of magnetic field.

3. Photon index shows a large variation within the SNR from $\Gamma = 2.1$–2.9. The photon index shows smallest values around the dense regions of cloud cores as well as toward diffuse regions with no molecular gas. This trend can be described as a rolloff energy variation of CR electrons (Zirakashvili & Aharonian, 2007). We present possible parameters to explain the variation of the rolloff energy under the DSA scheme. The enhanced intensity and harder spectra of the X-rays toward the dense clumps may require additional electron acceleration toward the dense clumps possibly via magnetic reconnection or other mechanism incorporating magnetic turbulence.

4. The absorbing column density shows a good correlation with the visual extinction. We found that the southeast-rim identified by HI self-absorption, which shows

enhanced VHE γ-rays has a clear counterpart in the X-ray absorption too, lending new support to the HI self-absorption interpretation.

Chapter 5

Summary and Future Prospects

5.1 Summary of the Thesis

In this dissertation, I summarize my Ph.D. study on shock-cloud interaction of the young γ-ray SNR RX J1713.7−3946 on the basis of the multi-wavelength study. The datasets of NANTEN/NANTEN2 CO and ATCA & Parkes HI reveal the distribution and physical condition of the total interstellar gas which consists of both molecular and atomic components. We succeeded to obtain evidence that the efficient cosmic-ray acceleration is strongly connected to the interaction between the shock waves and interstellar gas, and the cosmic-ray protons are accelerated close to the *knee* energy in the SNR for the first time. The investigations have been carried out through a comparison among the interstellar gas, the H.E.S.S. VHE γ-rays, and *Suzaku* synchrotron X-rays. Details are summarized as follows.

In Chapter 2, I presented a detailed study of the SNR RX J1713.7−3946 based on NANTEN/NANTEN2 ^{12}CO(J=1–0, 2–1, 4–3), ^{13}CO(J=2–1), ASTE ^{12}CO(J=3–2), ATCA & Parkes HI, and *Suzaku* X-rays. RX J1713.7−3946 is located at (l, b) = (347.°3, −0.°5) and has a large apparent diameter ∼1 deg (∼20 pc at 1 kpc), closer distance ∼1 kpc, and young age ∼1600 yr. The SNR emits strong VHE γ-rays and synchrotron X-rays and hence is a primary candidate of a cosmic-ray accelerator up to the *knee* energy. First, I revealed the spacial distribution of the CO, mainly the ^{12}CO(J=2–1) line is used, HI, and synchrotron X-rays in the energy band 1–5 keV and 5–10 keV toward whole the SNR. I newly identified 9 CO clumps and a HI clump, which is associated with the SNR and derived its physical parameters (peak position, intensity, velocity, mass etc.). I also estimated more details of some physical parameters in the prominent CO peaks of clumps A and C using ^{12}CO(J=2–1, 3–2, 4–3) and ^{13}CO(J=2–1) and revealed that clumps A and C have densities of 0.5–0.8 $\times 10^4$ cm^{-3} and 0.8–1.7 $\times 10^4$

cm^{-3} and temperatures 9–11 K and 11–16 K, respectively. Surprisingly, clump C shows a strong density gradient consistent with an average density distribution of $r^{-2.2\pm0.4}$ (r is the radius of clump C) and clear bipolar outflow structure. Therefore, we have concluded that the clump C is containing protostellar core(s) and survived the SNR shock erosion, since the shock propagation stalled in the dense clump.

In a morphological study between the CO/HI clumps and X-rays, we found that the X-rays are enhanced within ∼1 pc of the CO and HI peaks, whereas at smaller scales down to 0.1 pc the CO peaks tend to be anti-correlated with the X-ray intensity which decreases toward the CO and HI clumps. More detailed analysis shown that all clumps have a radius of 0.04±0.01 degrees and the X-rays are distributed with a separation of 0.07±0.03 degrees from the center of each clump, therefore the X-rays are rim-brightened on the CO/HI clumps. I also investigated the azimuthal distribution of X-rays around each CO clump and revealed that the all X-ray emissions surrounded by CO are enhanced toward the center of the SNR. Some of the clumps also emit X-rays for the all azimuth angle and hence these clumps survived the SNR blast waves, being now embedded within the SNR. I also found the strong correlation (correlation coefficient ∼ 0.85) between the X-ray intensity and the clump mass interacting with the SNR shock waves.

I concluded that the interstellar gas clumps (including the interstellar core clump C) are formed by a strong stellar wind from the progenitor of the SNR at some Myr ago and is now interacting with the SNR shock waves. These CO/HI clumps are not destroyed by the SNR blast waves, but the X-rays are greatly influenced by shock-cloud interaction with a magnetic field amplification. The present findings described above are compared with numerical simulations of MHD assuming a realistic highly inhomogeneous density distribution by Inoue et al. (2009, 2012). These simulations indicate that the magnetic field is amplified around dense CO/HI clumps as a result of enhanced turbulence induced by the shock-cloud interaction. We interpret that therefore amplified magnetic fields enhance the X-ray intensity, which depends on the 1.5-th power of the magnetic field strength. Such enhanced magnetic field may also lead to efficient acceleration additional to the DSA.

In Chapter 3, we have carried out a detailed comparison between the total interstellar gas and the VHE γ-rays. We first tried to reveal the distribution of total interstellar protons using the NANTEN ^{12}CO(J=1–0) and ATCA & Parkes HI datasets. To our surprise, we found the atomic gas (HI) component which corresponds to the VHE γ-ray distribution toward southeast-rim of the SNR where the CO counterpart had not been found in the previous studies (e.g., Aharonian et al., 2006b). Even more interestingly, the HI component is discovered as cold HI in self-absorption dip, not as a line emission. The self-absorbed structure is considered that the high density region of HI, but it

is not dense enough to significant detection (either creation or excitation) of the CO molecules (Goldsmith et al., 2007). Therefore, we assumed the background level of HI and estimated the total interstellar proton column density $N_{\rm p}$(H$_2$+HI) containing with absorption-corrected HI. As a result, we revealed that the total mass of the interstellar protons is 2.0 $\times$ 10^4 $M_\odot$; the mass of molecular component is 0.9 $\times$ 10^4 $M_\odot$ and that of atomic component is 1.1 $\times$ 10^4 $M_\odot$. Most of the neutral gas was likely swept up by the stellar wind of an OB star prior to the supernova explosion to form a low-density cavity and a dense wall. Therefore, the distribution of the interstellar gas is highly inhomogeneous; the inner region of the SNR is very low density ($N_{\rm H}$ $\sim$0.01 cm^{-3}), and the outer region formed with the molecular wall ($N_{\rm H}$ $\sim$100–10000 cm^{-3}). Finally, we obtained an extremely well spacial correspondence with the total interstellar proton column density $N_{\rm p}$(H$_2$+HI) and VHE γ-ray emission, comparing both in azimuthal and radial plots and concluded the VHE γ-rays are hadronic origin. We also estimate the total energy of cosmic-ray protons $W_{\rm tot}$ = (0.8–2.3) $\times$ 10^{48} erg, 0.1% of the total energy of typical supernova explosion, with the averaged interstellar gas density of $\sim$ 130 cm^{-3}.

In addition to above, I also investigated the penetration depth, $l_{\rm pd}$, of cosmic-ray protons to the dense interstellar clumps. According to the numerical simulation, $l_{\rm pd}$ is proportional to the square root of the cosmic-ray proton energy and SNR age but is inversely proportional to the square root of magnetic field strength (Inoue et al., 2012). Therefore, high-energy cosmic-ray protons as VHE γ-ray emitter penetrate into the dense clumps, however the lower-energy cosmic-ray protons such as GeV γ-rays emitter do not. Therefore, the γ-ray spectrum is (a) highly energy dependent when (b) the magnetic field is strong enough ($\sim$ 100μ G). (a) is consistent with the *Fermi* LAT GeV spectrum which has very hard photon index Γ = 1.5, and (b) is as shown in Chapter 2. Consequently, we concluded that the GeV to VHE γ-rays are both hadronic origin and our observational results are an evidence for the cosmic-ray acceleration close to the *knee* energy.

In Chapter 4, I estimated the detailed physical parameters of synchrotron X-rays (absorbing column $N_{\rm H}$(X-ray), photon index Γ ,and absorption-corrected flux $F_{3-10{\rm keV}}$) using *Suzaku* archival datasets. Thanks to the low background level of the *Suzaku* XIS, we carried out the spacial distribution of the physical parameters at angular resolution of 2–8 arcmin, which is comparable to the scale of the ISM distribution. The X-rays are dominated by non-thermal component and can be fitted by a simple absorbed power-law model.

First, we revealed that absorbing column density $N_{\rm H}$(X-ray) varies from 0.4$\times$$10^{22}$ cm^{-2} to 1.4$\times$$10^{22}$ cm^{-2} within the SNR and is exhibits cavity like structure of the interstellar material. The distributions of $N_{\rm H}$(X-ray) and visual extinction $A_{\rm V}$ show an excellent positive correlation (correlation coefficient $\sim$0.83). Intriguingly, $N_{\rm H}$(X-ray) value in

southeast-rim also is consistent with the cold HI estimated in Chapter 3.3.3.3. I have also shown the flux distribution very similar to the *Suzaku* XIS count maps. In order to understand the relationships between the X-ray flux and interstellar gas density, we investigated the correlation of the two. As a result, we obtain the correlation coefficient $\sim$0.55, which is not a strong correlation but a large number of samples ($\sim$300). Therefor, the correlation significant. The results quantitatively support the strong connection between the X-rays and interstellar gas.

Next, I have provided the photon index Γ map, which also varies from 2.1 to 2.9 within the SNR and has prominent six dips (low Γ value positions) located not only in gas rich regions in the west, but also gas poor regions in the east. In order to understand the spatial variation of the X-ray photon index (=acceleration efficiency of cosmic-ray electrons), we compared it with the interstellar gas distribution and concluded that the photon index varies with two reasons; It is probable that gas rich part of the SNR in the west the shock-cloud interaction dominates turbulent excitation ($\eta \sim 1$) leading to the large rolloff energy and small photon index. On the other hand, the gas poor region in the eas the shock speed $v_{\rm sh}$ is not decelerated well due to lower density. The photon index is inversely proportional to the rolloff energy of X-rays and is only proportional to the shock speed $v_{\rm sh}$ and η^{-1}. Therefore, regard the gas is rich or poor, cosmic-ray electrons can accelerate efficiently by different mechanism. Interestingly, the photon index becomes small toward the some dense clumps. In the shock-cloud interaction scheme, the magnetic field is amplified in the interacting region, leading to higher synchrotron loss and smaller rolloff energy. This can lead to lower X-ray intensity and lower rolloff energy toward the dense clumps, while obviously we need a more elaborate work to quantitatively affirm this. Therefore, we proposed to need the additional acceleration mechanize such as the second order Fermi acceleration (Fermi, 1949) and/or the magnetic reconnection (Hoshino, 2012).

These results in this dissertation are summarized concisely as:

- we obtained evidence for the acceleration of cosmic-ray protons close to the *knee* energy in the young SNR RX J1713.7−3946 for the first time.
- we quantitatively revealed a strong connection between the SNR shock waves, interstellar gas, and efficient acceleration of cosmic-rays in the SNR.

Finally, we conclude that *the interstellar gas plays an essential role in producing the γ-rays , X-rays and efficiently accelerate cosmic-rays in the SNR RX J1713.7−3946 and probably in other young γ-ray SNRs.*

5.2 Future Prospects

The present study has revealed the shock-cloud interaction and its importance for the understanding of efficient cosmic-ray acceleration and its origin in the young SNR RX J1713.7−3946. The our methods are a revolutionary approach and opened a new possibility in a science field of astrophysics. However, evidence is not enough to reveal universality in the Galactic and/or extra-galactic SNRs. Additionally, we need to further reinforce and deepen our studies, in order to achieve better understanding of the phenomena of the universe. In this section, we present some of the future works or on going studies.

(1) Further expansion our studies into other SNRs

The target of the present study is limited to the SNR RX J1713.7−3946 alone. We should expand our study to other SNRs using the present methods in order to investigate the universality of our idea. Additionally, it is important to investigate whether the present cosmic-ray acceleration and the γ-ray production is applicable to other SNRs with large range of physical parameters (e.g., SNR age, radius, interacting interstellar gas, photon index of X-rays) for a better understanding of the evolution of the SNRs and unified view of the origin of the VHE cosmic-rays.

The target for the achievement of the purpose as mentioned above, can be divided into three categories as follows:

[Category I.] Young SNRs
(e.g., RX J0852.0−4622, RCW 86, HESS J1731−347, SN1006, Cas A, Tycho)

[Category II.] Middle-aged SNRs
(e.g., Puppis A, W28, W44, W51C, IC443, W41)

[Category III.] Magellanic SNRs
(e.g., N132D, N23, N49, N157B, N186D)

The young SNRs are the most important targets because they emit in high energy X-rays and γ-rays and hence are actively accelerating the cosmic-rays close to the *knee* energy. In particular, RX J0852.0−4622 (hereafter Vela Jr.) is the best target of study because the SNR has the same characteristics (bright in VHE γ-rays and synchrotron X-rays) as RX J1713.7−3946. We already started comparative studies between the high energy radiations and interstellar gas and showed that Vela Jr. is in similar condition to RX J1713.7−3946, namely, the VHE γ-rays correspond well with the interstellar gas in

distribution, and the hadronic origin is suggested (Fukui, 2013). In addition, we are now observing the Vela Jr. with *Suzaku* (AO8: PI H. SANO) and will reveal the efficient acceleration of cosmic-ray electron through the detailed spectral analysis of the X-ray data. Studies on other SNRs are also under way by our NANTEN team (e.g., HESS J1731−347, Fukuda et al., 2014 submitted to the Astrophysical Journal; Cas A, CO observations with Nobeyama 45-m telescope (PI: H. SANO); SN1006, HI observations with ATCA (PI: T. FUKUDA); RCW 86, CO observation with Mopra (PI: Y. FUKUI)).

The middle-aged SNRs are also essential targets for the advanced stage of shock interaction. In this case, the non-thermal X-rays had already disappeared due to the cooling with high energy radiation (see Chapter 1.4)[4]. On the other hand, GeV–VHE γ-rays are still bright owing to the long cooling time scale (see Equation 1.45) and are predicted to be converted to the lower energy photon with the passage of time due to escape of cosmic-rays (e.g., Gabici et al., 2009; Ohira et al., 2010). Moreover, the shock waves will slow down and will heat up the surrounding interstellar gas, where strong thermal X-ray is emitted. Therefore, we are able to understand the physical conditions of shocked/ionized gas and escaped cosmic-rays for a long lapse of time evolution after the primary interaction. We have already started the comparison between the GeV γ-rays and interstellar gas distribution in middle-aged SNRs (see Chapter 1.5.1 and Yoshiike et al., 2013).

It is not easy to identify an interacting interstellar gas with the SNRs, because the CO/HI clumps are overlapped on the line of sight, particularly toward the Galactic plane in our galaxy. On the other hand, the interacting gas and the SNRs in the extra galaxy with face-on angle can be well separated free from the contamination. In this case, the SNRs located in the Magellanic clouds, "Large Magellanic Cloud" (LMC) and "Small Magellanic Cloud" (SMC), are the most suitable for the present studies. Most recently, we found that the molecular cloud associate with SNR N132D in the Magellanic (see Figure 5.1; Sano et al., 2014, in preparation). The detailed physical properties will be revealed with the observations by using Atacama Large Millimeter/submillimeter Array (ALMA).

In the future, the Cherenkov telescope array (CTA) will discover ∼1000 VHE γ-ray SNRs with 10 times higher sensitivity than current Cherenkov telescopes (e.g., H.E.S.S., MAGIC, VERITAS). At that time, the spectral index of γ-rays will be able to compared with the interstellar gas and that of X-rays directory with the same spatial resolution

[4]Most recently, however, the non-thermal X-rays are detected in middle-aged SNR W44 (Uchida et al., 2012). The authors also found that the hard X-rays are enhanced around the CO clumps similar to the present studies. Therefore, the relativistic cosmic-ray electrons are probably being accelerated in the middle-aged SNRs.

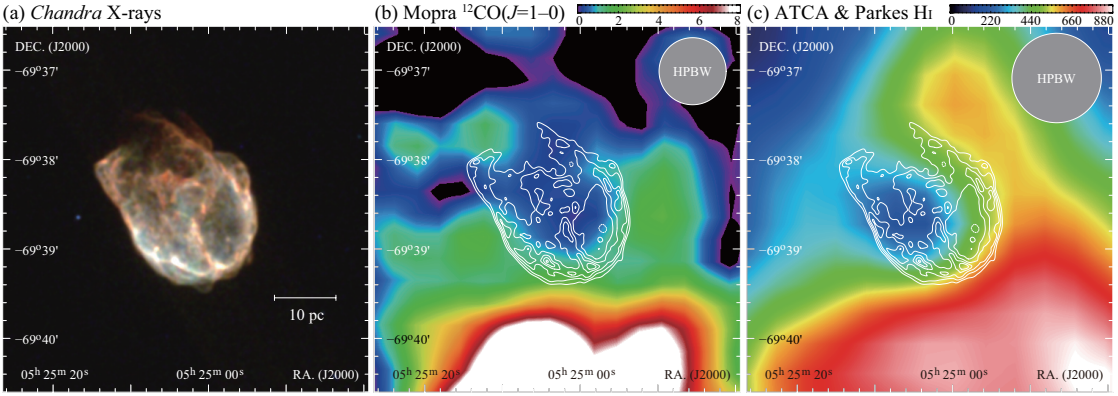

FIGURE 5.1: (a) The *Chandra* three color image of SNR N132D. Red, green, and blue correspond to 0.5–1.2 keV, 1.2–2.0 keV, and 2.0–7.0 keV intensity distributions, respectively. (b) Integrated intensity map of the Mopra ^{12}CO(J=1–0) data in a velocity range of $V_{\rm LSR}$ = 257.0–269.7 km s^{-1} is shown in color. The color scale indicates integrated intensity on a square root scale in unit of K km s^{-1}. The white contours indicate the X-ray intensity in (a). The lowest contour level and intervals are 6.50×10^{-7} and 2.89 ×10^{-7} counts s^{-1} pixel^{-1}, respectively. (c) Integrated intensity map of ATCA & Parkes HI. The velocity range and contours are same as in (b). The color scale also indicates integrated intensity on a liner scale and its unit is same as (a).

and hence it is no doubt that the decisive evidence for the acceleration of the cosmic-ray protons will brought to us by these future projects.

(2) Resolving a small scale structure of the SNR RX J1713.7−3946

According to the numerical simulations, the molecular clumps which enhance the turbulence and amplified the magnetic fields through the shock-cloud interaction have a smaller size than the current by identified CO clumps ($\sim$ 1 pc) in RX J1713.7−3946 by a factor of $\sim$3 (Inoue et al., 2009, 2012). The authors have pointed out the existence of small scale structure of interstellar gas ($\sim$ 0.3 pc) which create the $\sim$ 1 mG spots at $\sim$0.05 pc scale. This suggestion is supported by X-ray observation (e.g., Uchiyama et al., 2007) which have shown a year-scale flux variation of X-ray filaments ($\sim$ 0.05 pc) due to a strong synchrotron cooling and is consistent with the magnetic field amplification around the small ($\sim$0.1 pc) gas clumps. Therefore, we are now observing the small scale structure of CO in the SNR RX J1713.7−3946 with the Mopra radio telescope. This observation will detect the CO clumps at $\sim$0.2 pc angular resolution and will allow us a direct comparison between the results of numerical simulations and CO structures.

(3) More detailed analyses from a viewpoint of numerical simulations

In addition to the future prospect in (1), we should be reanalyzed the results of numerical simulations (Inoue et al., 2009, 2012). Specifically, the numerical results, it is

required to derive the physical parameter directly comparable to the CO observables (e.g., line width, intensity, velocity fields) in order to investigate detailed physics in the shocked regions. Additionally, we need advanced simulations with more realistic initial conditions.

(4) Shock speed measurement toward southeast-rim of RX J1713.7−3946

In the discussion of Chapter 4, I noted that the shock speed of eastern region is faster than that of western region in the SNR RX J1713.7−3946. The measurement of shock speed is an important parameter to our model as described Chapter 4.4.2.2. The western shock speed $v_{\rm sh,west}$ is estimated by previous study (e.g., Uchiyama et al., 2007, and by private communications with Prof. Yasunobu Uchiyama), $v_{\rm sh,west} \sim$ 3000–4000 km s^{-1}. In addition, the southeast-rim of the SNR has two clear filaments that had been observed in 2005 with *Chandra*. Therefore, the shock speed of southeast-rim $v_{\rm sh,southeast}$ can be obtained by additional *Chandra* observation and to measure the proper motion of the filament. For example, if the $v_{\rm sh,southeast} \sim$ 6000 km s^{-1}, the filaments move to the southeast by $\sim 10''$ ($\sim$ 0.05 pc) until 2014, which is detectable significantly with *Chandra*'s high spatial resolution.

(5) Search for a thermal X-rays in the synchrotron dominant SNRs

The thermal X-ray emissions provide us many physical informations such as electron temperature, ionization parameter, and ion temperature. The parameters are the essential physical quantities to understand the thermal balance between the shock heating and the cosmic-ray acceleration[5]. In the site of efficient cosmic-ray acceleration, such as RX J1713.7−3946, the shock heating will suppress the thermal emission cased by the huge dynamical pressure of accelerated cosmic-ray particles (e.g., Helder et al., 2009). RX J1713.7−3946 candidate of above case, which is now accelerating cosmic-rays efficiently and has not been detected in the thermal X-rays. There are only two SNRs in addition to RX J1713.7−3946 that show such pure non-thermal X-rays, Vela Jr. and HESS J1731−347, known to date. We will perform deep observations with *Suzaku* XIS toward the SNRs in oder to detect the thermal X-rays. In RX J1713.7−3946, our proposal has accepted and we will observe soon the by the *Suzaku* XIS with 100 ks exposure (AO8, PI: H. SANO). The observations will provide us the electron temperature and ionization parameter in RX J1713.7−3946 for the first time.

[5]We can derive the total energy of shock waves $E_{\rm shcok} = kT_{\rm e} = m_{\rm e}v^2_{\rm shcok}$, where $T_{\rm e}$ is the electron temperature, $m_{\rm e}$ is the electron mass, and $v_{\rm shcok}$ is the shock speed. Therefore, we can compare the shock heated energy $kT_{\rm e}$ with the total energy of shock waves $m_{\rm e}v^2_{\rm shcok}$ using two parameters of $v_{\rm shcok}$ and $T_{\rm e}$.

Appendix A

Velocity Channel Distributions in RX J1713.7−3946

A.1 CO and Non-thermal X-Rays (J2000 Coordinate)

In order to clarify a relationship between X-rays and CO clumps in Chapter 4, it is necessary to identify all the CO clumps interacting with the SNR blast waves. The previous studies (e.g., Fukui et al., 2003; Moriguchi et al., 2005) identified most of the CO clumps, but it was not complete because a velocity range was limited (e.g., $V_{\rm LSR}$: -12–-3 km s^{-1} in Moriguchi et al., 2005). We therefore identified all the CO clumps interacting with the SNR blast waves for a wide velocity range, such as in Fukui et al. (2012) ($V_{\rm LSR}$: -20–$+2$ km s^{-1}). We used the velocity channel maps and appropriate criteria to identify other CO clumps. Figure A1 shows the velocity channel distribution of ^{12}CO(J=1–0, 2–1) every 2 km s^{-1} from -24 km s^{-1} to 8 km s^{-1} superposed on the *Suzaku* X-ray distribution (1–5 keV). We also plotted the position of each CO clump interacting with the SNR. The clumps, C$_{\rm E}$, D$_{\rm W}$, G$_{\rm E}$, O$_{\rm b}$, O$_{\rm SW}$, Q$_{\rm W}$, Z, Z$_{\rm NW}$ and Z$_{\rm NE}$, are newly identified in present work.

A.2 CO, HI and VHE γ-Rays (Galactic Coordinate)

We show velocity channel distributions of ^{12}CO(J=1–0, 2–1) and HI data every 1 km s^{-1} from -20 km s^{-1} to 0 km s^{-1} superposed on the VHE γ-ray distribution in Figure A2.

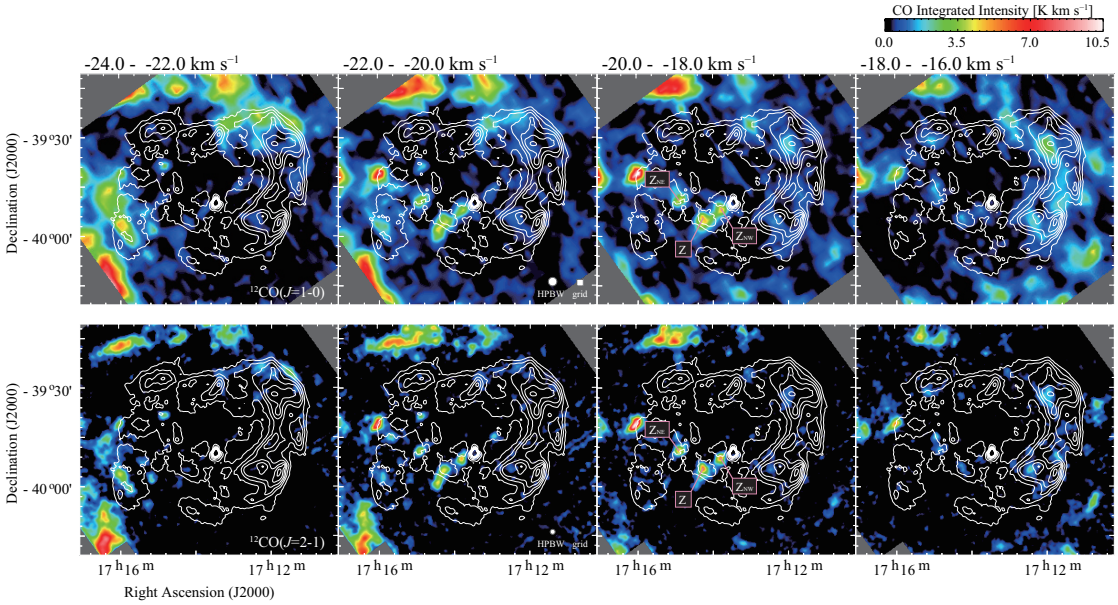

FIGURE A1: Velocity channel distributions of the ^{12}CO(J=1–0) (*top panels* in false color) and ^{12}CO(J=2–1) (*bottom panels* in false color) emissions overlaid on the *Suzaku* X-ray contours for the energy band 1–5 keV. Each panel of CO shows intensity distributions integrated every 2 km s^{-1} in a velocity range from −24 to 8 km s^{-1} following the color code shown on the upper right. In the X-ray distribution, the lowest contour level and the contour interval are 2.1 and 0.6 $\times$ 10^{-4} counts s^{-1} pixel^{-1}, respectively. The CO clumps shown in Table 2.3 are also plotted.

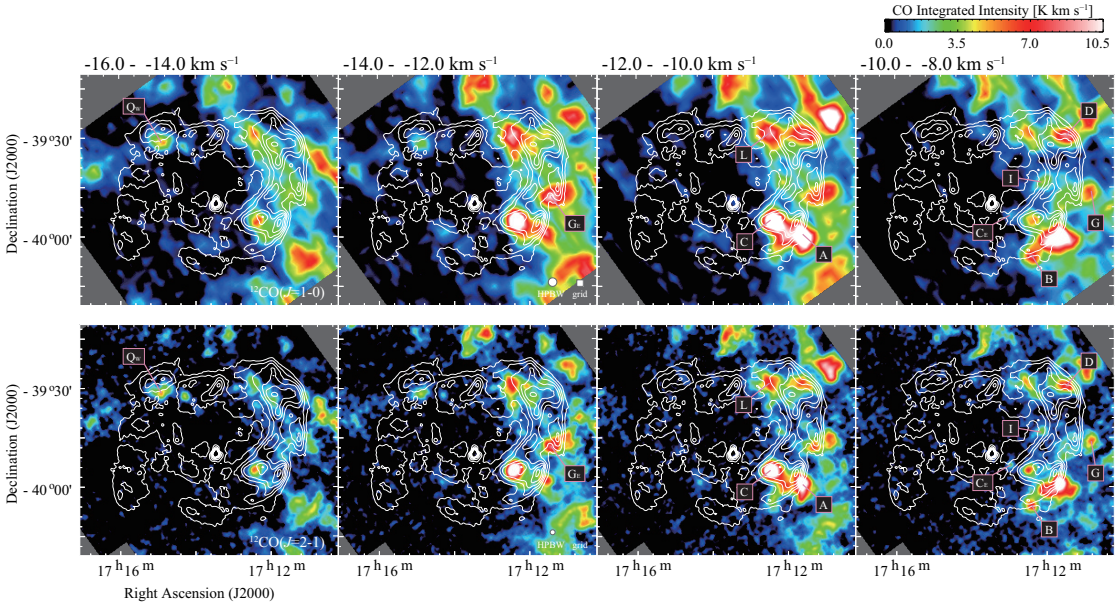

FIGURE A1: (Continued)

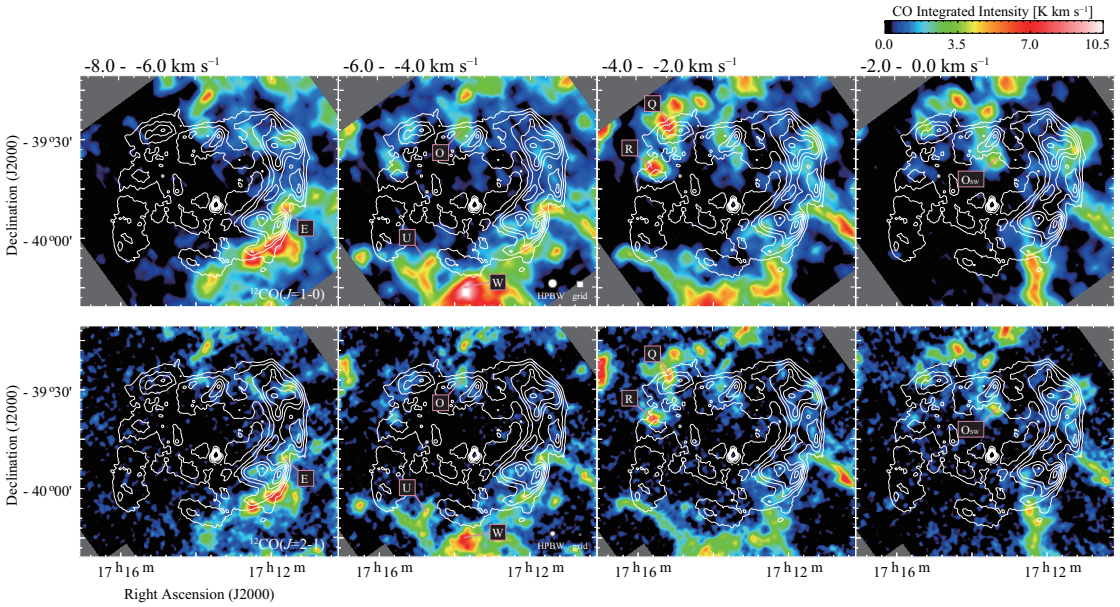

FIGURE A1: (Continued)

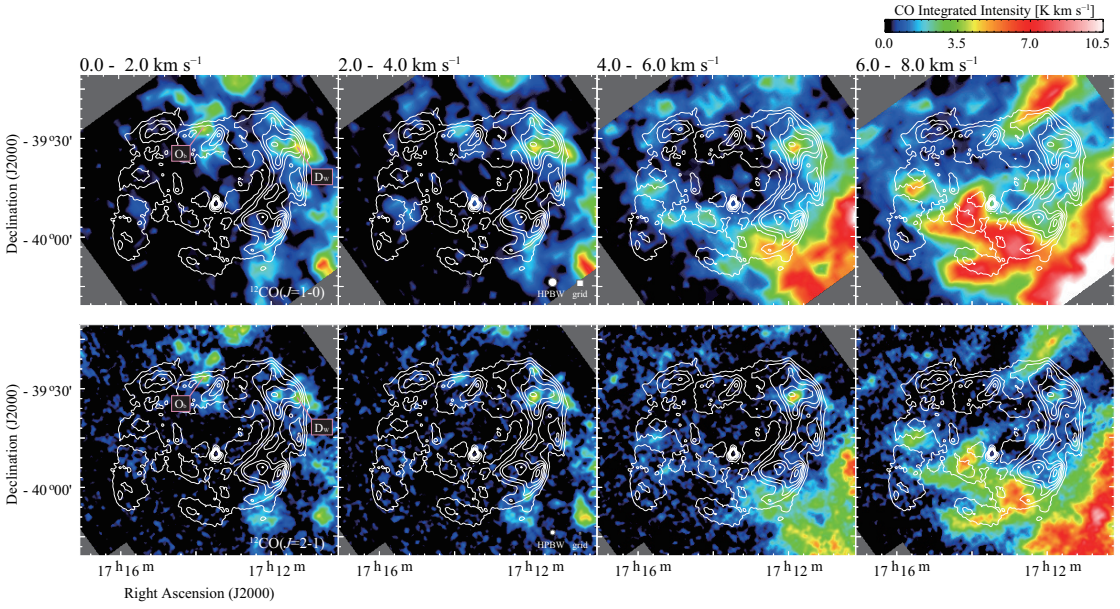

FIGURE A1: (Continued)

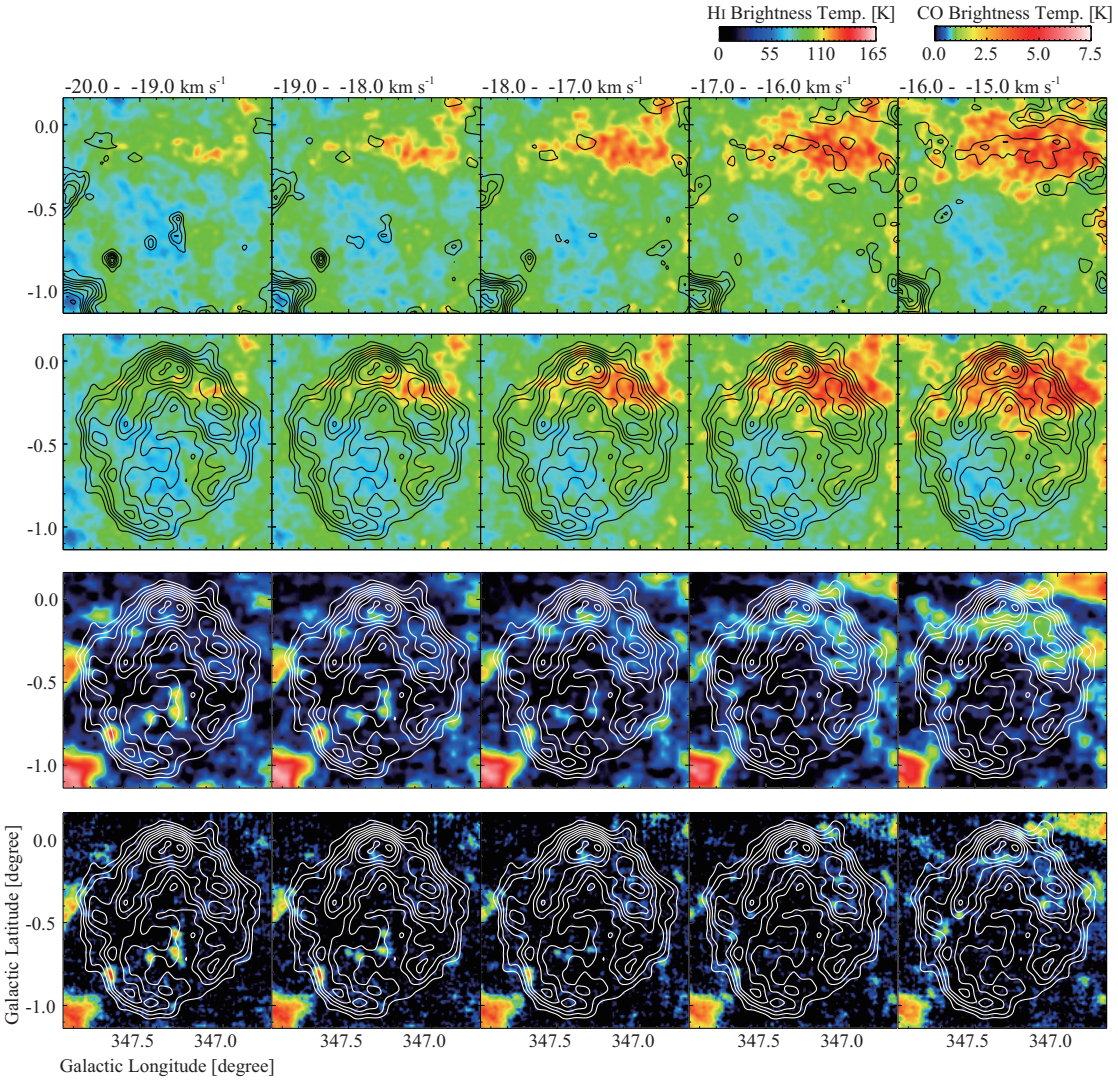

FIGURE A2: Velocity channel maps of ^{12}CO(J=1–0, 2–1) line emission and HI brightness temperature overlaid on the VHE γ-ray distribution. First-row panels (top): HI image and ^{12}CO(J=1–0) contours. Second-row panels: HI image superposed on the VHE γ-ray contours. Third-row panels: ^{12}CO(J=1–0) image superposed on the VHE γ-ray contours. Fourth-row panels: ^{12}CO(J=2–1) image superposed on the VHE γ-ray contours. Each panel shows CO and HI distributions every 1 km s^{-1} in a velocity range from -20 to 0 km s^{-1} . The lowest contour levels of CO and VHE γ-rays are 0.73 K ($\sim 3\sigma$) and 20 smoothed counts, and contour intervals of CO and VHE γ-rays are 0.73 K ($\sim 3\sigma$) and 10 smoothed counts, respectively.

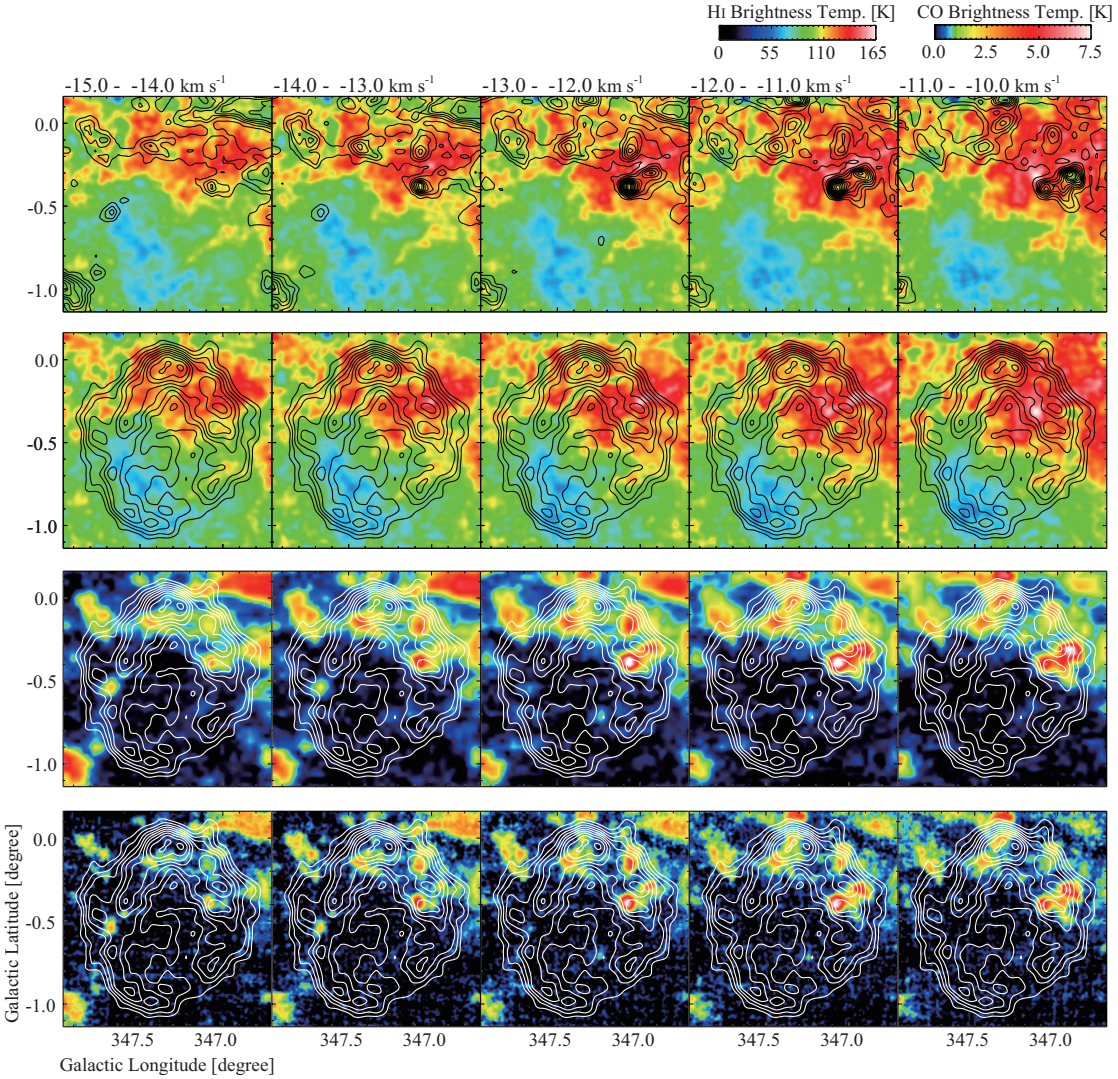

FIGURE A2: (Continued)

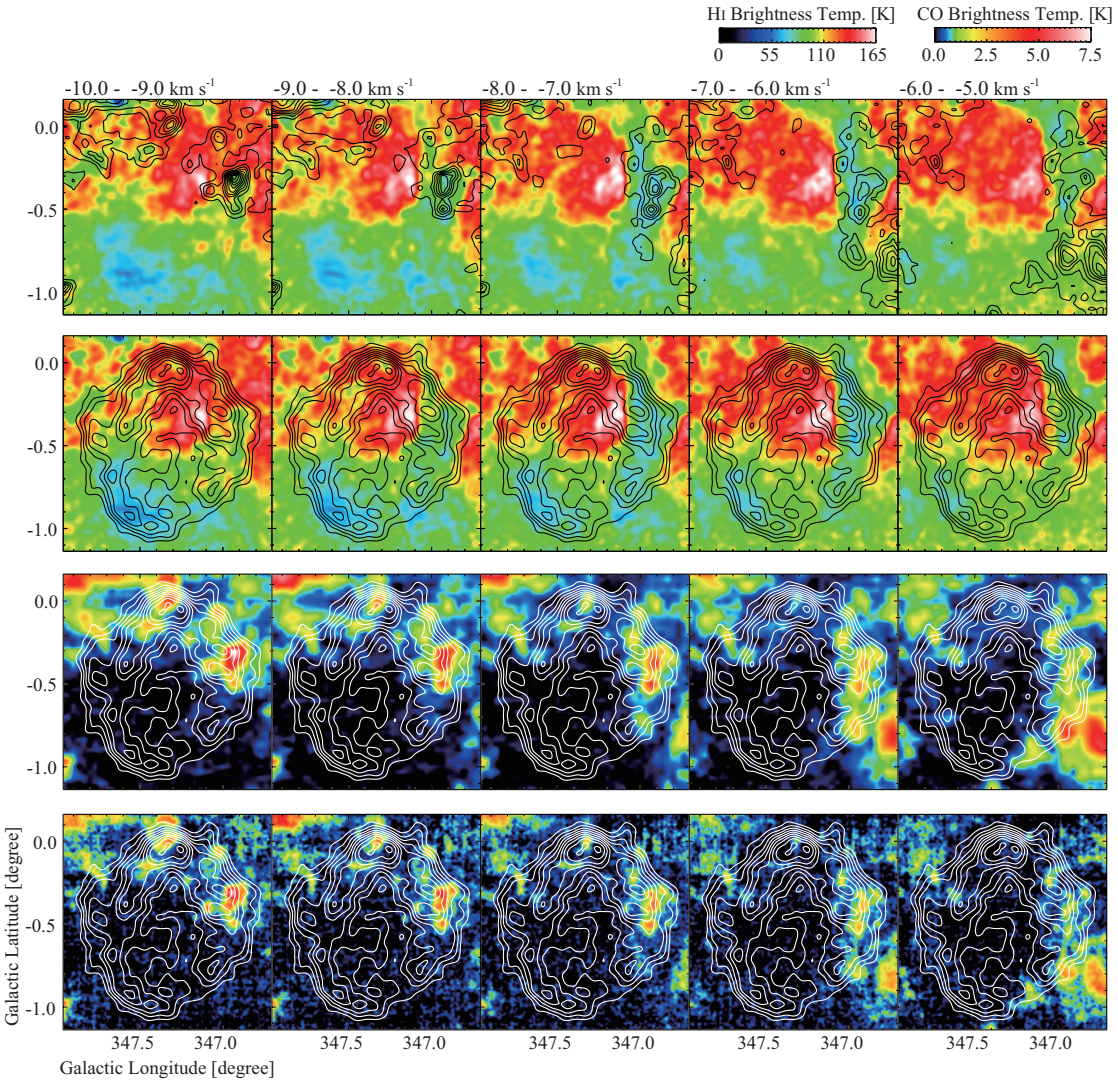

FIGURE A2: (Continued)

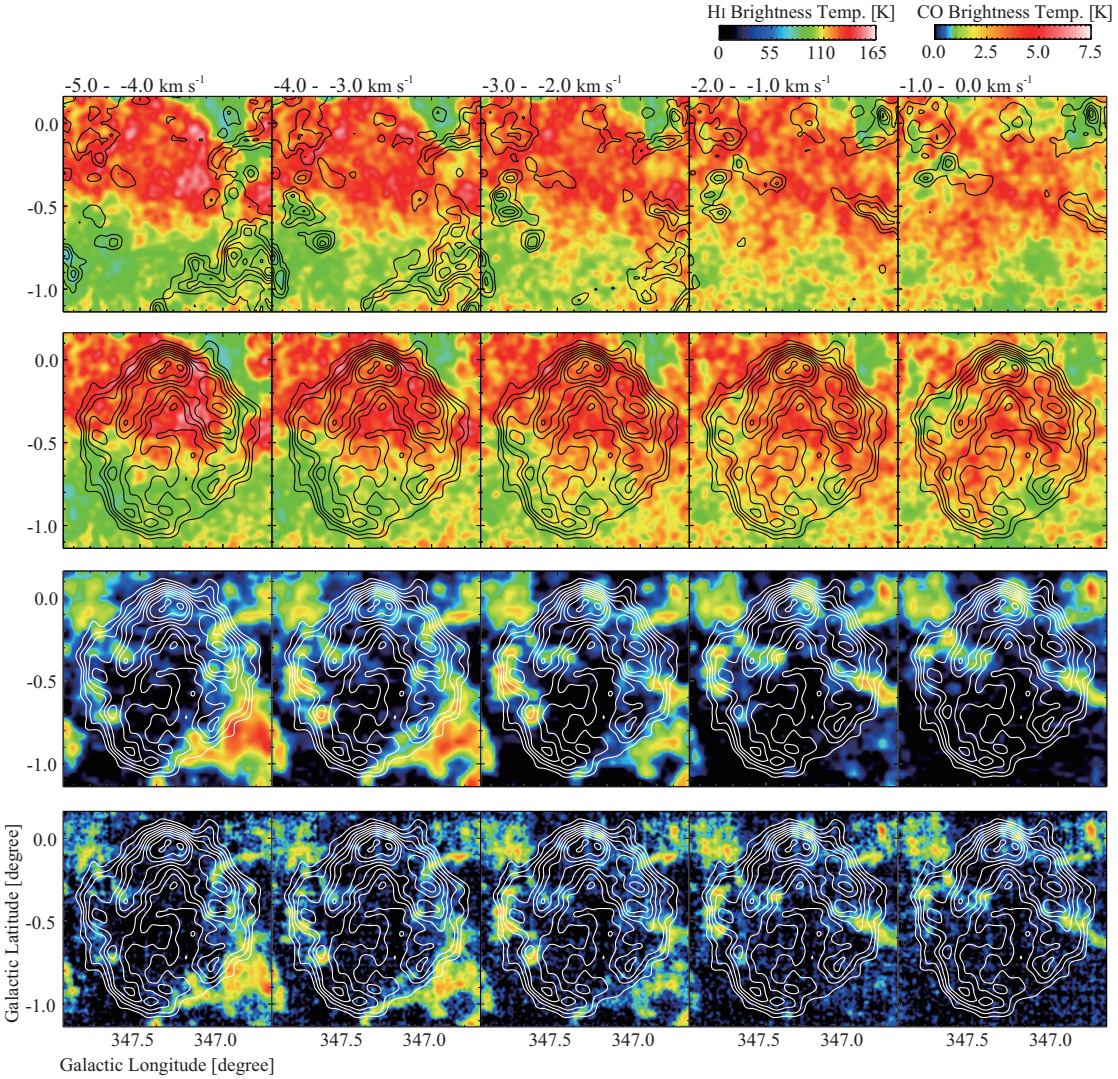

FIGURE A2: (Continued)

Appendix B

Expanding Motion of the Dark HI SE Cloud

Figure B1, left shows schematically an expanding spherical shell of radius $R_0 = 9$ pc and uniform expansion velocity $V_0 = 10$ km s^{-1}, and Figure B1, right a position–velocity diagram of the shell, where the ellipsoidal nature of the shell is not taken into account for simplicity.

Figure B2 shows three representative velocity channel distributions of the dark HI SE cloud for a velocity range from -20 to -10 km s^{-1} and shows that the SE cloud is extended to the north. The extension shifts toward the northwest with velocity decrease from -10 to -20 km s^{-1} as is consistent with the iso-velocity contours expected from the shell model in Figure B1.

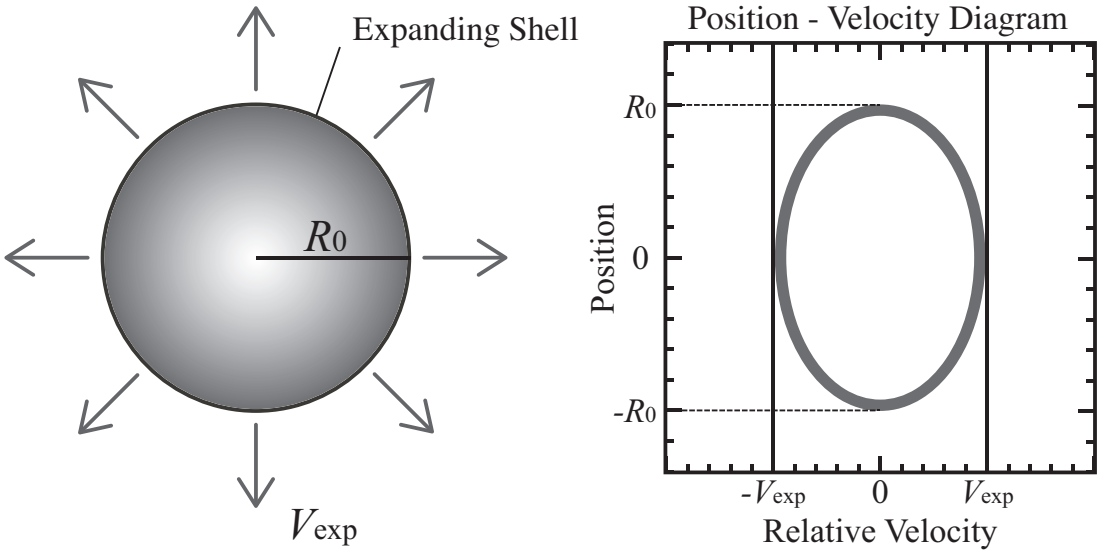

FIGURE B1: Schematic image of a uniformly expanding shell and its velocity distribution in the position–velocity plane. Here, we assume a radius of the shell R_0 and an expansion velocity $V_{\rm exp}$ of 9 pc and 10 km s^{-1}, respectively.

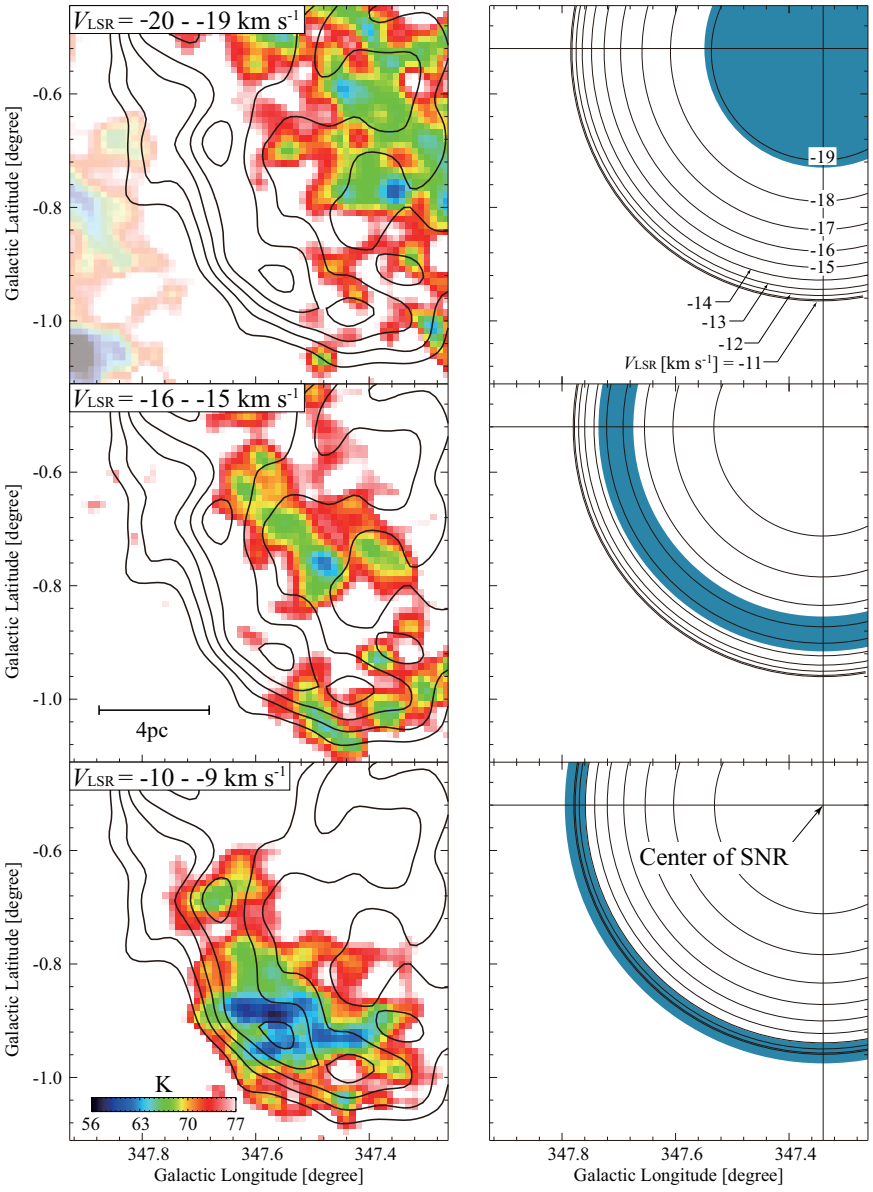

FIGURE B2: Left: velocity channel distributions of HI integrated intensity toward the SE cloud superposed on the VHE γ-ray contours. VHE γ-ray contours are plotted every 10 smoothed counts from 20 smoothed counts. The faded area in the upper panel is a component unrelated to the SNR. Right: model velocity distributions of an expanding shell shown in Figure B1. Iso-velocity lines are shown here, and blue areas show the corresponding velocity range shown in the left panels.

Figure B3 shows another presentation of kinematical details of the SE cloud in position–velocity diagrams. We choose a line AB passing through the center of the SNR and the SE cloud, and another line CD passing through the SE cloud in the north–south (Figure B3a). We show a position-velocity distribution of HI along the line AB (Figure B3b) and HI profiles along the two lines AB and CD (Figure B3c). We find that the SE cloud is extended to the northwest with a large velocity gradient of 10 km s^{-1} per 0.5 deg, or $\sim$1.2 km s^{-1} pc^{-1}. The HI profiles in Figure B3c shows that the dips are deep and clear at b less than -0.5 deg but becomes shallower above $b = -0.5$ deg. The shallower dips make it nontrivial to quantify the dips at b higher than -0.5 deg; we note that, even when the dips are not clearly seen, the HI probably suffers from self-absorption to some extent as suggested by the weaker HI brightness at -12 km s^{-1} toward $b = -0.^{\circ}52$ than toward $b = -0.^{\circ}35$ (line AB).

We note that the strong velocity gradient in Figures B2 and B3 is consistent with the blueshifted part of an expanding shell. The strong velocity gradient is interpreted in terms of the expanding shell as depicted by a white circle in the position–velocity diagram (Figure B3b). The blue shift by 10 km s^{-1} toward the center of the SNR indicates that this part of the shell is in the foreground. This is consistent with that the dips are due to self-absorption against the background HI emission. We also infer that the swept-up shell is highly non-uniform since the broad HI dips are seen only in a quarter of the shell.

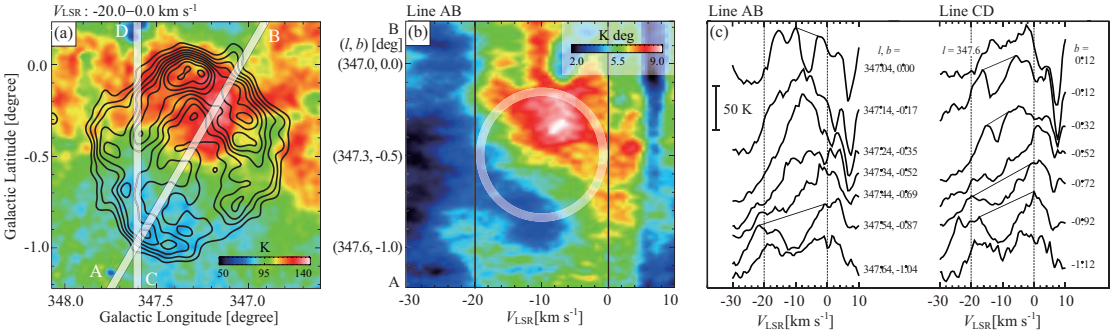

FIGURE B3: (a) Averaged brightness temperature distribution of HI in a velocity range from -20 km s^{-1} to 0 km s^{-1}. Contours show the H.E.S.S. VHE γ-rays and are plotted every 10 smoothed counts from 10 smoothed counts. The line AB is inclined by 60 deg to the Galactic plane and the line CD passes the center of the SNR. (b) Position–velocity distribution of HI along the line AB in (a). The velocity resolution is smoothed to 1 km s^{-1} and the integration interval is 200 arcsec. The white circle shows a schematic image of an expanding spherical shell (Figure B1). (c) HI spectra along the lines AB and CD in Figure (a). Expected profiles of HI self-absorption are shown by straight lines in the spectra with significant HI dips.

Appendix C

Analysis of the HI Emission; the Optically Thin Case

The present analysis has shown that the HI is self-absorbed in part of the SNR as indicated by the HI dips, and the HI column density is estimated by taking into account the self-absorption (Figure 3.7). In order to see the effects of the self-absorption quantitatively, we here show for comparison the ISM proton distribution in the optically thin case, which does not take into account the self-absorption. Figure C1, equivalent to the self-absorption case in Figure 3.7, includes the HI column density distribution for the optically thin assumption smoothed to the H.E.S.S. resolution (Figure C1b and Figure C1c), where the SE cloud is not seen. Figure C1a and C1d are the same with those in Figure 3.7. Figure C2 is equivalent to Figure Figure 3.8. Figure Figure C2a is the total ISM proton column density for the optically thin HI at NANTEN resolution overlaid on the VHE γ-ray distribution. Figure C2b is the corresponding azimuthal distribution of ISM protons and VHE γ-rays, where the ISM protons is deficient in azimuthal angle from -90 to 0 deg as compared to Figure 3.8b. Figure C3 is equivalent to Figure 3.10, and shows the radial distribution of ISM protons for the optically thin HI without correction for the HI self-absorption. In the smoothed radial distribution, the effect of the self-absorption is not so obvious.

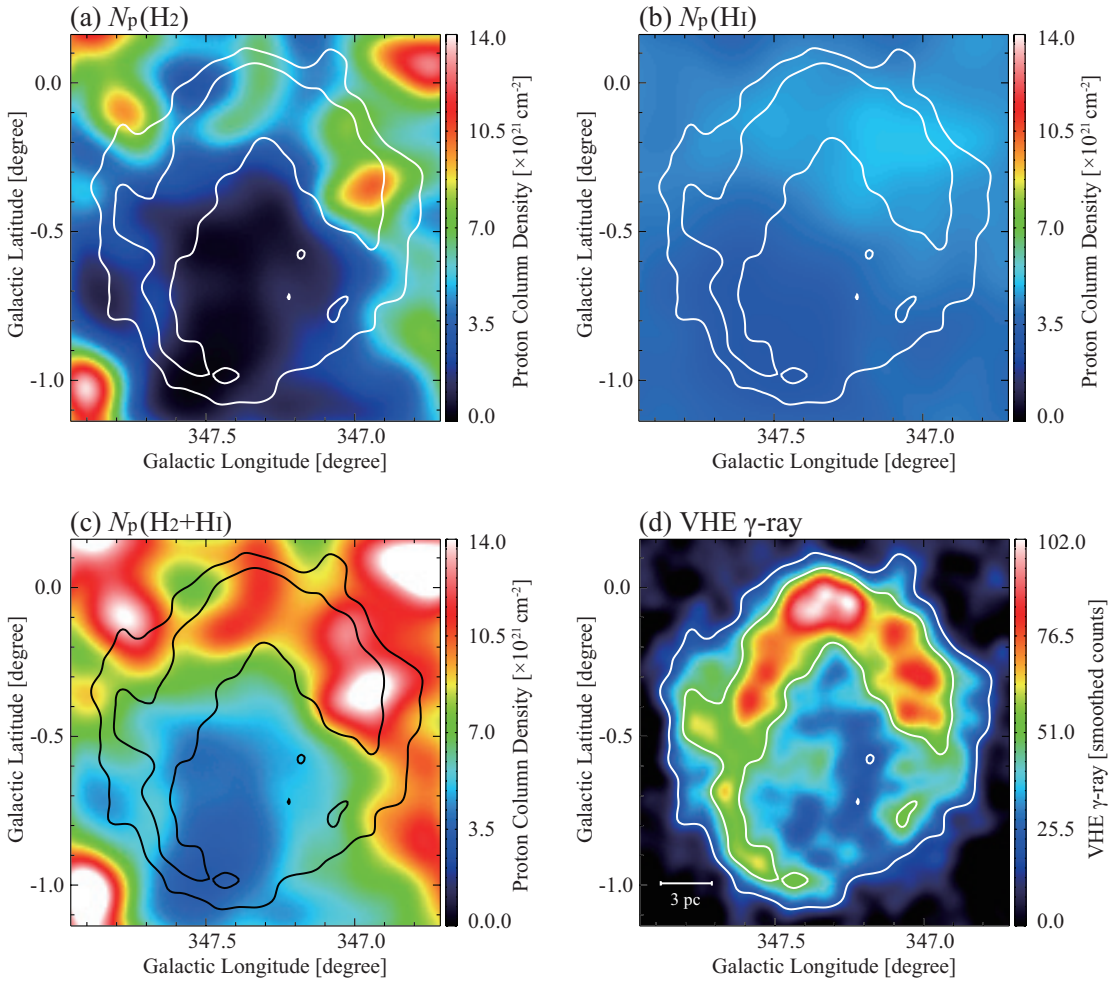

FIGURE C1: (a) Distributions of column density of the ISM protons N_p estimated from ^{12}CO(J=1–0) $N_p(H_2)$, (b) HI emission without correction for the self-absorption N_p(HI) and (c) sum of $N_p(H_2)$ and N_p(HI). Here, we assume for reference that the HI emission is optically thin and the HI self-absorption is not taken into account. All datasets used here are smoothed to an HPBW of the VHE γ-ray distribution with a Gaussian function. (d) VHE γ-ray distribution. Contours are plotted every 50 smoothed counts from 20 smoothed counts.

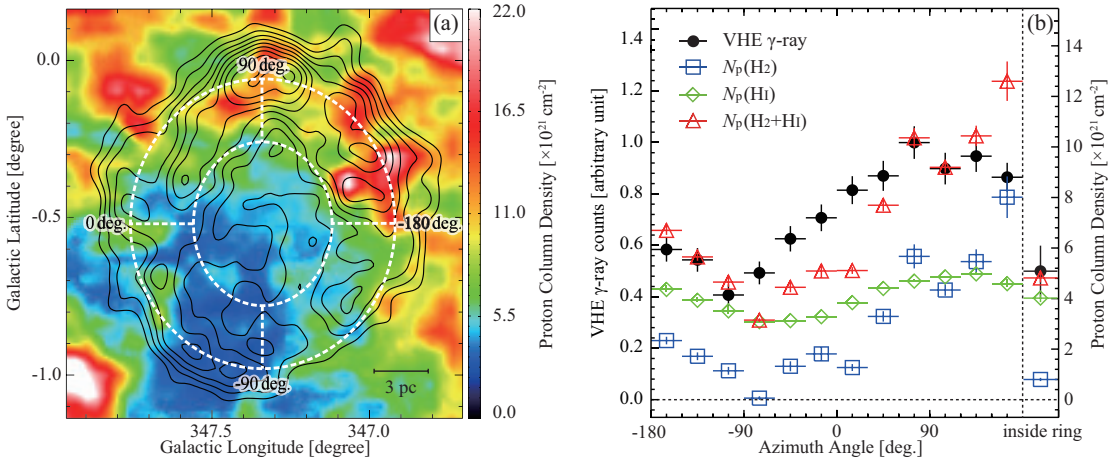

FIGURE C2: (a) Distribution of column density of ISM protons $N_{\rm p}({\rm H_2+HI})$ in a velocity range from -20 km s^{-1} to 0 km s^{-1}, where the HI is assumed to be optically thin and without self-absorption. Contours and two elliptical rings are the same as in Figure 3.8a. (b) Azimuthal distributions of $N_{\rm p}({\rm H_2})$, $N_{\rm p}({\rm HI})$, $N_{\rm p}({\rm H_2+HI})$, and VHE γ-ray smoothed counts per beam in the two elliptical rings in (a). The same plots inside of the inner ring are shown on the right side in (b).

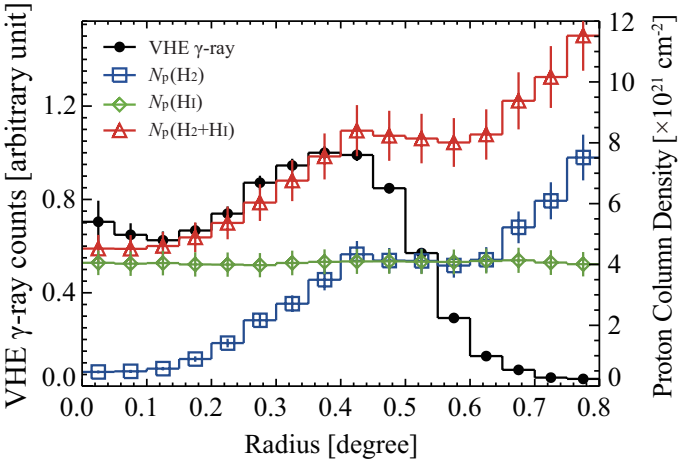

FIGURE C3: Radial distributions of averaged values of VHE γ-rays, $N_{\rm p}({\rm H_2})$, $N_{\rm p}({\rm HI})$, and $N_{\rm p}({\rm H_2+HI})$, where the HI is assumed to be optically thin as in Figure C1. $N_{\rm p}({\rm H_2})$ and $N_{\rm p}({\rm HI})$ show column densities estimated from ^{12}CO(J=1–0) and HI, respectively, and $N_{\rm p}({\rm H_2+HI})$ shows the total ISM column density, the sum of $N_{\rm p}({\rm H_2})$ and $N_{\rm p}({\rm HI})$.

Appendix D

The Background Level of X-rays

In order to estimate the azimuth distribution of the X-rays in Figure 2.8, we estimated the background level of the X-rays in the energy band 1–5 keV inside the SNR. Figure D1 shows two histogram of the X-rays. One is that extracted from the whole area observed as shown in Figure 2.1, and the other the typical inner part of the SNR. The latter is extracted from nine circles of $6'$ diameter which include no significant peaks of the X-rays. The central circle is at $(\alpha_{\rm J2000}, \delta_{\rm J2000}) = (17^{\rm h}\ 13^{\rm m}\ 52.8^{\rm s}, -39^\circ\ 49'\ 12.0'')$ and the other eight have offsets $\pm 11'$ from the center in $\alpha_{\rm J2000}/\delta_{\rm J2000}$ as shown in Figure D1b. We consider that the peak of the histogram for the whole ($\sim$1.16 $\times$ 10^{-4} counts s^{-1} pixel) is the typical background level outside the SNR, and that the primary peak of the histogram for the inner part ($\sim$3.86 $\times$ 10^{-4} counts s^{-1} pixel) indicates the background level of the SNR interior. We used the excess counts from the background level as those of the individual X-ray features in deriving the azimuthal distribution in Figure 2.8.

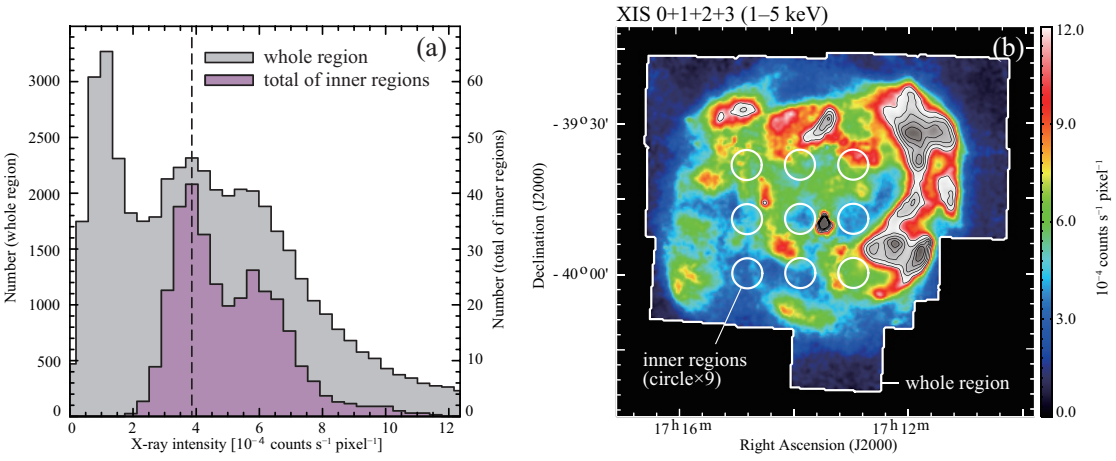

FIGURE D1: (a) Histograms of X-rays intensity in the energy band 1–5 keV. The gray and magenta histograms show the contributions of the whole observed region and of the typical inner region of the SNR, respectively. (b) Same XIS mosaic image (1–5 keV) as Figure 2.2 (c). The region enclosed by the broken solid lines and that enclosed by the nine circles represent the whole and typical inner region used for (a), respectively.

Appendix E

X-ray absorption by the ISM affects the X-ray images

We shall here test if the X-ray absorption by the ISM affects the X-ray images. The X-ray counts in 1–5 keV are generally about 8 times higher than in 5–10 keV and the distributions in the two bands are fairly similar with each other (Figures 2.5 and 2.7). The ratio 8 is consistent with an X-ray photon index of ∼2.3 typical to the SNR (e.g., Tanaka et al., 2008). Only clump L shows the largest difference from 8 by a factor of more than two in the plot, indicating a softer spectrum. The similarity of the two bands suggests that X-ray absorption is not significant, because the X-rays should show a much harder spectrum if absorption is significant. The optical depth due to the ISM at X-rays is proportional to the $(-8/3)$-th power of the energy and is expressed as follows (Longair, 1994);

$$\tau_{\rm x} = 2 \times 10^{-22} \ N_{\rm H} \ ({\rm cm}^{-2}) \cdot \varepsilon^{-8/3} \ ({\rm keV}), \tag{E.1}$$

where $N_{\rm H}$ (cm^{-2}) is the ISM column density and ε (keV) is X-ray photon energy. The maximum ISM column density in the SNR is estimated to be 1×10^{22} cm^{-2} toward the brightest CO peak, clump C. Even for this column density absorption optical depths are 2, 0.3, 0.03 and 0.004 at 1 keV, 2 keV, 5 keV, and 10 keV, respectively, as calculated by equation (1), and absorption is not likely affect the X-ray distribution significantly. We made a test on the X-ray absorption toward clump C, where the X-rays show depression which may be possibly due to absorption. The X-ray intensity ratio toward clump C is ∼8.6 between the 1–5 keV and 5–10 keV bands as observed by *Suzaku* (see Chapter 4.3.2). By using Xspec we calculated the X-ray intensity integrated over the two energy bands for three different values of absorbing column density, i.e., 0.3, 1 and 3×10^{22} cm^{-2}, for an X-ray photon index of 2.3, and found that the intensity ratios between the two bands are ∼11.1, 7.0, and 3.5, respectively. Column density slightly less than

$1{\times}10^{22}$ cm^{-2} fits the X-ray observations reasonably well as is consistent with the CO observations.

References

Abdo, A. A., Ackermann, M., Ajello, M., et al. 2010, Science, 327, 1103

Abdo, A. A., Ackermann, M., Ajello, M., et al. 2010, ApJ, 718, 348

Abdo, A. A., Ackermann, M., Ajello, M., et al. 2011, ApJ, 734, 28

Abramowitz, M., & Stegun, I. A. 1965, Dover Books on Advanced Mathematics, New York: Dover, —c1965, Corrected edition, edited by Abramowitz, Milton; Stegun, Irene A.,

Acero, F., Ballet, J., Decourchelle, A., et al. 2009, ApJ, 505, 157

Ackermann, M., Ajello, M., Allafort, A., et al. 2012, ApJ, 756, 4

Ackermann, M., Ajello, M., Allafort, A., et al. 2013, Science, 339, 807

Aharonian, F. A., & Atoyan, A. M. 1996, A&A, 309, 917

Aharonian, F. A., Akhperjanian, A. G., Aye, K.-M., et al. 2004, Nature, 432, 75

Aharonian, F., Akhperjanian, A. G., Bazer-Bachi, A. R., et al. 2006a, ApJ, 636, 777

Aharonian, F., Akhperjanian, A. G., Bazer-Bachi, A. R., et al. 2006b, A&A, 449, 223

Aharonian, F., Akhperjanian, A. G., Bazer-Bachi, A. R., et al. 2007, A&A, 464, 235

Aharonian, F., Akhperjanian, A. G., Bazer-Bachi, A. R., et al. 2008, A&A, 481, 401

Allen, M., & Robinson, G. W. 1977, ApJ, 212, 396

Arikawa, Y., Tatematsu, K., Sekimoto, Y., & Takahashi, T. 1999, PASJ, 51, L7

Ballet, J. 2006, Advances in Space Research, 37, 1902

Bamba, A., Pühlhofer, G., Acero, F., et al. 2012, ApJ, 756, 149

Beatty, J. J., & Westerhoff, S. 2009, Annual Review of Nuclear and Particle Science, 59, 319

Bell, A. R. 1978, MNRAS, 182, 147

Bell, A. R. 2004, MNRAS, 353, 550

Berezhko, E. G., & Völk, H. J. 2008, A&A, 492, 695

Bertsch, D. L., Dame, T. M., Fichtel, C. E., et al. 1993, ApJ, 416, 587

Blake, G. A., Sutton, E. C., Masson, C. R., & Phillips, T. G. 1987, ApJ, 315, 621

Blandford, R. D. & Ostriker, J. P. 1978, ApJ, 221, L2

Brogan, C. L., Gelfand, J. D., Gaensler, B. M., Kassim, N. E., & Lazio, T. J. W. 2006, ApJ, 639, L25

Burgay, M., Rea, N., Israel, G. L., et al. 2006, MNRAS, 372, 410

Bykov, A. M., Uvarov, Y. A., & Ellison, D. C. 2008, ApJ, 689, L133

Casanova, S., Aharonian, F. A., Fukui, Y., et al. 2010a, PASJ, 62, 769

Casanova, S., Jones, D. I., Aharonian, F. A., et al. 2010b, PASJ, 62, 1127

Cassam-Chenaï, G., Decourchelle, A., Ballet, J., et al. 2004, A&A, 427, 199

Cutri, R. M., Skrutskie, M. F., van Dyk, S., et al. 2003, VizieR Online Data Catalog, 2246, 0

Dame, T. M., Hartmann, D., & Thaddeus, P. 2001, ApJ, 547, 792

Denoyer, L. K. 1979, ApJ, 232, L165

Denoyer, L. K. 1979, ApJ, 232, L165

Desai, K. M., Chu, Y.-H., Gruendl, R. A., et al. 2010, AJ, 140, 584

Dickey, J. M. & Lockman, F. J. 1990, ARA&A, 28, 215

Dobashi, K., Uehara, H., Kandori, R., et al. 2005, PASJ, 57, 1

Draine, B. T. 2011, Physics of the Interstellar and Intergalactic Medium by Bruce T. Draine. Princeton University Press, 2011. ISBN: 978-0-691-12214-4,

Dubner, G. M., Velázquez, P. F., Goss, W. M., & Holdaway, M. A. 2000, AJ, 120, 1933

Ellison, D. C., & Vladimirov, A. 2008, ApJ, 673, L47

Ellison, D. C., Patnaude, D. J., Slane, P., & Raymond, J. 2010, ApJ, 712, 287

Emerson, J. P. 1988, NATO ASIC Proc. 241: Formation and Evolution of Low Mass Stars, 193

Fang, J., Tang, Y., & Zhang, L. 2011, ApJ, 731, 32

Fermi, E. 1949, Physical Review, 75, 1169

Fixsen, D. J. 2009, ApJ, 707, 916

Fukuda, T., Yoshiike, S., Sano, H., et al. submitted to ApJ

Fukui, Y., & Kawamura, A. 2010, ARA&A, 48, 547

Fukui, Y., Iwata, T., Mizuno, A., Bally, J., & Lane, A. P. 1993, Protostars and Planets III, 603

Fukui, Y., Onishi, T., Abe, R., et al. 1999, PASJ, 51, 751

Fukui, Y., Moriguchi, Y., Tamura, K., et al. 2003, PASJ, 55, L61

Fukui, Y., Sano, H., Sato, J., et al. 2012, ApJ, 746, 82

Fukui, Y. 1989, European Southern Observatory Conference and Workshop Proceedings, 33, 95

Fukui,Y. 2008, in AIP Conf. Proc., Vol. 1085, Proc. of 4th International Meeting on High-Energy Gamma-Ray Astronomy, ed. F. A. Aharonian, W. Hofmann, & F. Rieger (Melville, NY: AIP), 104

Fukui, Y. 2013, in Astrophysics and Space Science Proc. 34, 2nd Session of the Sant Cugat Forum on Astrophysics, ed. Diego F. Torres & O. Reimer (Berlin: Springer), 249

Funk, S. 2012, APS April Meeting Abstracts, 3002

Güsten, R., & Philipp, S. D. 2004, The Dense Interstellar Medium in Galaxies, 253

Gabici, S., Aharonian, F. A., & Blasi, P. 2007, Ap&SS, 309, 365

Gabici, S., Aharonian, F. A., & Casanova, S. 2009, MNRAS, 396, 1629

Gabici, S. 2013, Cosmic Rays in Star-Forming Environments, 34, 221

Ginzburg, V. L., & Syrovatskii, S. I. 1964, The Origin of Cosmic Rays, New York: Macmillan, 1964,

Giuliani, A., Tavani, M., Bulgarelli, A., et al. 2010, A&A, 516, L11

Giuliani, A., Tavani, M., Bulgarelli, A., et al. 2010, A&A, 516, L11

Goldreich, P., & Kwan, J. 1974, ApJ, 189, 441

Goldsmith, P. F., Li, D., & Krčo, M. 2007, ApJ, 654, 273

Gorenstein, P., Harnden, F. R., Jr., & Tucker, W. H. 1974, ApJ, 192, 661

Gottwald, M., Parmar, A. N., Reynolds, A. P., et al. 1995, A&AS, 109, 9

Grenier, I. A., Casandjian, J.-M., & Terrier, R. 2005, Science, 307, 1292

Hayakawa, S. 1952, Progress of Theoretical Physics, 8, 571

Heiles, C., & Crutcher, R. 2005, Cosmic Magnetic Fields, 664, 137

Helder, E. A., Vink, J., Bassa, C. G., et al. 2009, Science, 325, 719

Helder, E. A., Vink, J., Bykov, A. M., et al. 2012, Space Sci. Rev., 173, 369

Hillas, A. M. 1984, ARA&A, 22, 425

Hiraga, J. S., Uchiyama, Y., Takahashi, T., & Aharonian, F. A. 2005, A&A, 431, 953

Hoshino, M. 2012, Physical Review Letters, 108, 135003

Inoue, T., Yamazaki, R., & Inutsuka, S.-i. 2009, ApJ, 695, 825

Inoue, T., Yamazaki, R., & Inutsuka, S.-i. 2010, ApJ, 723, L108

Inoue, T., Yamazaki, R., Inutsuka, S.-i., & Fukui, Y. 2012, ApJ, 744, 71

Ishisaki, Y., Maeda, Y., Fujimoto, R., et al. 2007, PASJ, 59, 113

Jenkins, E. B., & Savage, B. D. 1974, ApJ, 187, 243

Jones, F. C., & Ellison, D. C. 1991, SSRv., 58, 259

Jun, B.-I., & Norman, M. L, 1996, ApJ, 465, 800

Katz, B., & Waxman, E. 2008, JCAP., 01, 018

Keohane, J. W., Rho, J., Pannuti, T. G., Borkowski, K. J., & Winklery, P. F. 2005, X-Ray and Radio Connections

Kishishita, T., Hiraga, J., & Uchiyama, Y. 2013, A&A, 551, A132

Koo, B.-C., McKee, C. F., Lee, J.-J., et al. 2008, ApJ, 673, L147

Koyama, K., Petre, R., Gotthelf, E. V., et al. 1995, Nature, 378, 255

Koyama, K., Kinugasa, K., Matsuzaki, K., et al. 1997, PASJ, 49, L7

Koyama, K., Tsunemi, H., Dotani, T., et al. 2007, PASJ, 59, 23

Krčo, M., & Goldsmith, P. F. 2010, ApJ, 724, 1402

Kulesa, C. A., Hungerford, A. L., Walker, C. K., Zhang, X., & Lane, A. P. 2005, ApJ, 625, 194

Lada, C. J. 1985, ARA&A, 23, 267

Landt, H., & Bignall, H. E. 2008, MNRAS, 391, 967

Larson, R. B. 1969, MNRAS, 145, 271

Lazarian, A., & Vishniac, E. T. 1999, ApJ, 517, 700

Lazendic, J. S., Slane, P. O., Gaensler, B. M., et al. 2003, ApJ, 593, L27

Lazendic, J. S., Slane, P. O., Gaensler, B. M., et al. 2004, ApJ, 602, 271

Lizano, S., & Shu, F. H. 1989, ApJ, 342, 834

Longair, M. S. 1994, High Energy Astrophysics, Vol. 2 (2nd ed.; Cambridge: Cambridge Univ. Press)

Lu, F. J., Li, T. P., Sun, X. J., Wu, M., & Page, C. G. 1996, A&AS, 115, 395

Malkov, M. A., & O'C Drury, L. 2001, RPPh., 64, 429

McClure-Griffiths, N. M., Dickey, J. M., Gaensler, B. M., Green, A. J., Haverkorn, M., & Strasser, S. 2005, ApJS, 158, 178.

Mizuno, A., & Fukui, Y. 2004, Milky Way Surveys: The Structure and Evolution of our Galaxy, 317, 59

Mizuno, Y., Kawamura, A., Onishi, T., et al. 2010, PASJ, 62, 51

Moriguchi, Y., Tamura, K., Tawara, Y., et al. 2005, ApJ, 631, 947

Morlino, G., Amato, E., & Blasi, P. 2009, MNRAS, 392, 240

Muraishi, H., Tanimori, T., Yanagita, S., et al. 2000, A&A, 354, L57

Nakajima, H., Yamaguchi, H., Matsumoto, H., et al. 2008, PASJ, 60, 1

Nakamura, R., Bamba, A., Dotani, T., et al. 2012, ApJ, 746, 134

Ohama, A., Dawson, J. R., Furukawa, N., et al. 2010, ApJ, 709, 975

Ohira, Y., Murase, K., & Yamazaki, R. 2010, A&A, 513, A17

Onishi, T., Mizuno, A., & Fukui, Y. 1999, PASJ, 51, 257

Patnaude, D. J., Slane, P., Raymond, J. C., & Ellison, D. C. 2010, ApJ, 725, 1476

Penston, M. V. 1969, MNRAS, 145, 457

Pfeffermann, E., & Aschenbach, B. 1996, in Proc. Roentgenstrahlung from the Universe, ed. H. U. Zimmermann, J. H. Trümper, & H. Yorke, 267

Pineda, J. L., Mizuno, N., Stutzki, J., et al. 2008, A&A, 482, 197

Planck Collaboration, Ade, P. A. R., Aghanim, N., et al. 2011, A&A, 536, A19

Porter, T. A., Moskalenko, I. V., & Strong, A. W. 2006, ApJ, 648, L29

Reynolds, A. P., Parmar, A. N., Hakala, P. J., et al. 1999, A&AS, 134, 287

Rho, J., & Borkowski, K. J. 2002, ApJ, 575, 201

Rybicki, G. B., & Lightman, A. P. 1979, Radiative Processes in Astrophysics (New York: Wiley-Interscience)

Sato, F., & Fukui, Y. 1978, AJ, 83, 1607

Schneider, N., Stutzki, J., Winnewisser, G., & Block, D. 1998, A&A, 335, 1049

Scoville, N. Z., & Solomon, P. M. 1974, ApJ, 187, L67

Serlemitsos, P. J., Soong, Y., Chan, K.-W., et al. 2007, PASJ, 59, 9

Sano, H., Yoshiike, S., Fukuda, T., et al. in preparation

Seta, M., Hasegawa, T., Dame, T. M., et al. 1998, ApJ, 505, 286

Slane, P., Gaensler, B. M., Dame, T. M., et al. 1999, ApJ, 525, 357

Slane, P., Hughes, J. P., Edgar, R. J., et al. 2001, ApJ, 548, 814

Takahashi, T., Abe, K., Endo, M., et al. 2007, PASJ, 59, 35

Takahashi, T., Tanaka, T., Uchiyama, Y., et al. 2008, PASJ, 60, 131

Tanaka, T., Uchiyama, Y., Aharonian, F. A., et al. 2008, ApJ, 685, 988

Taylor J. R. 1982 An introduction to error analysis (2nd ed.; California: USB)

Tian, W. W., Li, Z., Leahy, D. A., et al. 2010, ApJ, 712, 790

Torii, K., Enokiya, R., Sano, H., et al. 2011, ApJ, 738, 46

Uchida, H., Koyama, K., Yamaguchi, H., et al. 2012, PASJ, 64, 141

Uchiyama, Y., Aharonian, F. A., & Takahashi, T. 2003, A&A, 400, 567

Uchiyama, Y., Aharonian, F. A., Tanaka, T., Takahashi, T., & Maeda, Y. 2007, Nature, 449, 576

Uchiyama, H., Ozawa, M., Matsumoto, H., et al. 2009, PASJ, 61, 9

van den Berg, M., Penner, K., Hong, J., et al. 2012, ApJ, 748, 31

van der Hucht, K. A. 2001, New A Rev., 45, 135

Wallerstein, G., & Silk, J. 1971, ApJ, 170, 289

Wang, Z. R., Qu, Q.-Y., & Chen, Y. 1997, A&A, 318, L59

Weaver, R., McCray, R., Castor, J., Shapiro, P., & Moore, R. 1977, ApJ, 218, 377

Wootten, H. A. 1977, ApJ, 216, 440

Wootten, H. A. 1977, ApJ, 216, 440

Wootten, A. 1981, ApJ, 245, 105

Wootten, A. 1981, ApJ, 245, 105

Yamamoto, H., Kawamura, A., Tachihara, K., et al. 2006, ApJ, 642, 307

Yamazaki, R., Ohira, Y., Sawada, M., & Bamba, A. 2013, arXiv:1301.7499

Yoshiike, S., Fukuda, T., Sano, H., et al. 2013, ApJ, 768, 179

Yoshiike, S., Fukuda, T., Sano, H., et al. in preparation

Zirakashvili, V. N., & Aharonian, F. 2007, A&A, 465, 695

Zirakashvili, V. N., & Aharonian, F. A. 2010, ApJ, 708, 965